The High-Energy Emission of Low-Mass Stars

by

Girish M. Duvvuri

B.A., Wesleyan University, 2017

M.S., University of Colorado Boulder, 2019

A thesis submitted to the

Faculty of the Graduate School of the

University of Colorado in partial fulfillment

of the requirements for the degree of

Doctor of Philosophy

Department of Astrophysical and Planetary Sciences

2023

Committee Members:

Zachory K. Berta-Thompson

J. Sebastian Pineda

Meredith MacGregor

Kevin France

Mike Chaffin

Duvvuri, Girish M. (Ph.D., Astrophysical and Planetary Sciences)

The High-Energy Emission of Low-Mass Stars

Thesis directed by Prof. Zachory K. Berta-Thompson and Dr. J. Sebastian Pineda

The high-energy emission from low-mass stars is a product of stellar magnetism and turbulent convection as well as an input to the dynamics of planetary atmospheres. Observing this high-energy emission and understanding its formation are vital to understanding the physics of both stars and planets. One limitation to our knowledge of planetary atmospheric escape is the lack of observed extreme ultraviolet spectra for most stars, and to overcome this obstacle I present a method to use more accessible observations to infer the unobserved extreme ultraviolet. Then I measure the variability of emission from the upper layers of the stellar atmosphere for a number of stars across a range of rotation periods to characterize one aspect of how magnetic heating processes seem to collectively wane as stars age and spin down. That spin-down over time takes place after an initial phase of high activity during a star's youth, an important period of time for early planetary evolution, and so I combine my method of extreme ultraviolet inference with existing studies of solar-type stars to estimate the cumulative irradiation of planets orbiting the young Solar analog V1298 Tau. Finally, I extend this approach of using stars across time and rotation period to map out how the high-energy spectrum evolves for M dwarfs, the most common type of star and exoplanet host.

Dedication

To the people who taught me by example, a group larger than I ever dared to hope for.

Acknowledgements

There were many people along this path that I was fortunate to meet along the way, but I was most fortunate for the two advisors besides me for most of it. Thank you Zach Berta-Thompson and Sebastian Pineda for somehow managing to get me here. I've talked to and learned from you about what kind of teacher and scientist I want to be and I'm not sure I've made it obvious how much I value you, am grateful to you, and aspire to be a similar exemplar for others one day.

Kevin France may not have been my formal advisor, but I am grateful for his guidance on our papers together and for welcoming me into his meta-group (this is what I still call it in my head even though it's named CUSP now) which became a scientific home more than a collaborative network. Within that meta-group were two friends and colleagues whom I had encountered very early in this academic journey and I was lucky enough to deepen those friendships during my time here. Nicole Arulanantham was one of my first TAs and is still one of the first people I turn to for both advice and company. I met Wilson Cauley when I was starting to learn how to do research and a good chunk of this thesis exists because of him. Allison Youngblood and Fernando Cruz Aguirre, are also friends found through CUSP science who are a part of this dissertation.

Alexander Brown and Tom Ayres have indulged many irregularly timed interrogations that made their way in here. Steve Cranmer taught courses that were masterclasses in both content and the technique of constantly refining teaching material. Meredith MacGregor is kind of terrifyingly good putting together an exciting research program and making people around her want to jump on board. Jessica Libby-Roberts was an excellent senior grad student to follow and I'm sorry I didn't manage to run CUBE nearly as well as she did for the brief time I was supposedly in charge.

Going a bit further back in time, I also want to acknowledge Khachig Tölölyan, for being a professor who moved between the sciences and humanities without losing appreciation for either; Lutz Hüwel, for teaching the first physics course that made me care about the subject material along with the instructor instead of in opposition to them; Meredith Hughes, for an astronomy course that took a single lecture to convince me to reshape my college plans around this major; and Seth Redfield, my first advisor.

Thank you to Daniel David Sega Neuman, roommate and friend through the best and worst of this place. Thank you to friends from before: Julian Dann, who seems eternally excited by science; Rachel Aronow, who tolerates my random musings; Sarah Corner, who is responsible for more of my few good decisions than I think she knows; and Roxie/Yun Ju Chuang, who is probably the single best person in the world at making me do things. Thank you to a friend from long ago, Nikhil Chowdri, who has always been unnervingly and unreasonably confident in my abilities. And yes, I acknowledge the fool of a cat who kept yelling at me while I was either procrastinating or trying to finish this thing. He lost ten pipe cleaners in the last two days and kept asking for me to throw more.

Contents

Chapter

Tables

Table

Figures

Figure

Chapter 1

Introduction

The majority of all the worlds we know of are illuminated by a star whose mass does not significantly exceed our Sun's and whose radiation places it along a bounded path within a color-magnitude diagram (Hertzsprung, 1911; Russell, 1913), identifying it as a main-sequence star primarily powered by the fusion of hydrogen into helium (see Figure 1.1). These low-mass main sequence stars possess magnetic fields, those fields transport some fraction of the internal energy up and out to the plasma of the outer layers of the stellar atmosphere, that plasma emits high-energy photons, and some of those photons interact with the atmospheres of the planets orbiting these stars. High-energy radiation is an observable phenomenon that is both an effect of stellar magnetic processes and a cause of planetary atmospheric processes. This dissertation characterizes some aspects of the high-energy radiation from low mass stars to improve our collective understanding of stellar atmospheric structure, stellar magnetism, and planetary atmospheres.

The success of exoplanet detection surveys has placed us in an era of exoplanet demographics and comparative exoplanetology. Bryson et al. (2021) has stated that G dwarfs like our Sun are expected to host 0.38 – 0.63 rocky planets at an instellation where they could have liquid surface water under an Earth-like atmosphere according to calculations in Kopparapu et al. (2014)[1] and 0.32 – 0.42 rocky planets in the liquid water zone for K dwarfs. A similar analysis by Hsu et al. (2020) using the liquid water zone defined in Kopparapu et al. (2013) and slightly different radius boundaries for rocky planets found an occurrence rate of 0.33 – 0.44 such planets per star for

[1] this orbital region is often referred to as the habitable zone, although this work will refer to this as the "liquid water zone" instead to avoid over-interpretation

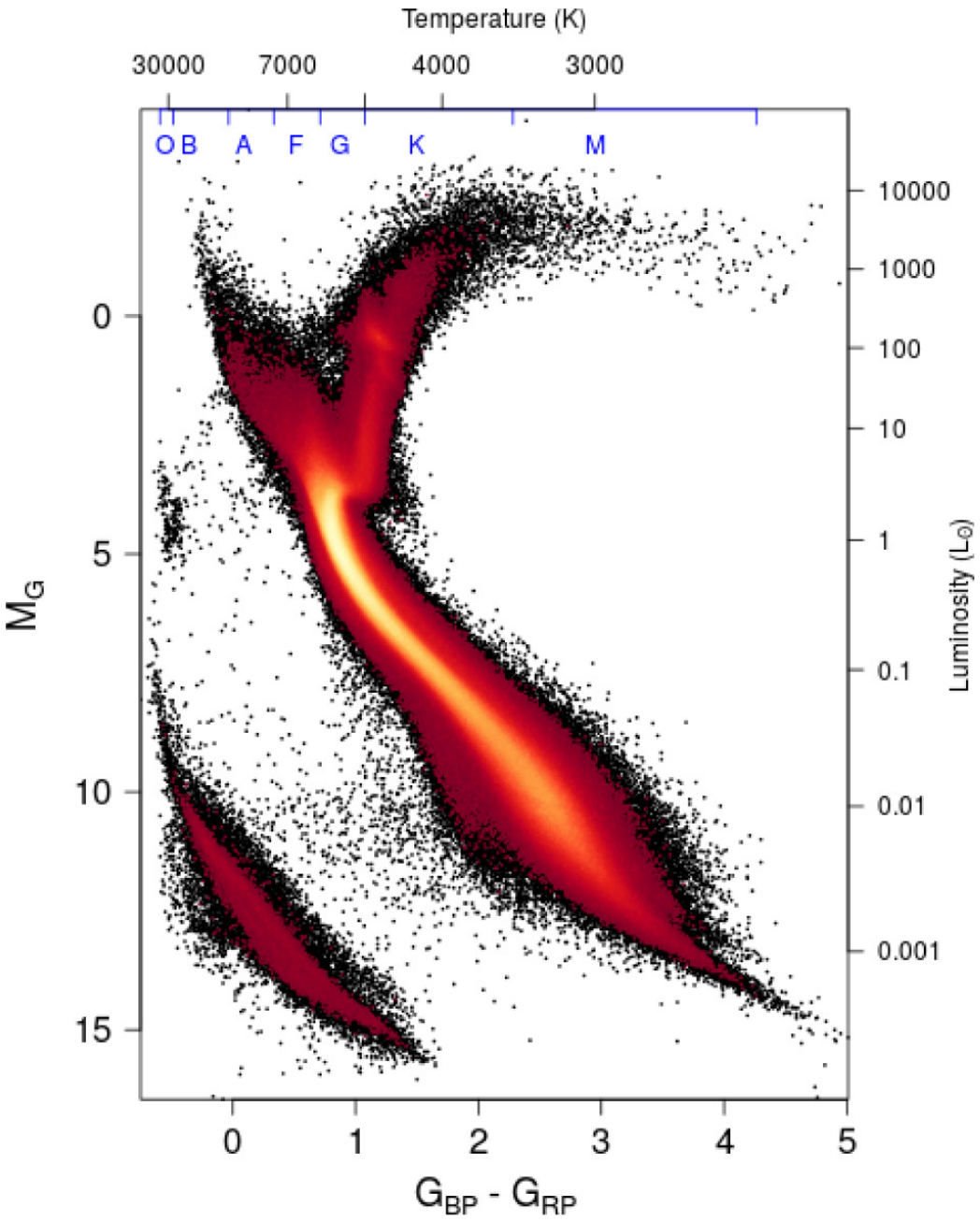

Figure 1.1: Figure 5 of Gaia Collaboration et al. (2018a). The bottom x-axis shows the $G_{\rm BP} - G_{\rm BP}$ color measurement of the difference between two *Gaia* photometric filters, while the top x-axis approximately transforms the colors to stellar effective temperature and the tick marks separate spectral types. The left y-axis uses *Gaia* parallax measurements to transform photometric measurements in the *Gaia* G-band to absolute magnitude and the right y-axis transforms this quantity to stellar luminosity. The sample of stars has been filtered by signal-to-noise, low interstellar reddening $E(B-V) < 0.015$, and other quality criteria described in Section 2 of Gaia Collaboration et al. (2018a), so it should be noted that this sample is not statistically complete. The color scales with the square root of the density of stars at that point in parameter space. The stars this work focuses on are within the region traced by the brightest overdensity path to the right of the "G" tick mark on the temperature axis.

M dwarfs. The physical distance and orbital periods for the liquid water zone depend on the bolometric luminosity of an exoplanet host star, a quantity that decreases by a factor of > 1000 from a star like our Sun to a M7.5V star like TRAPPIST-1 (Gonzales et al., 2019), which hosts 7 planets (Gillon et al., 2016, 2017) including 4 in the liquid water zone (Hill et al., 2023).

While the total energy irradiating a planet is an important quantity, it is insufficient to determine the composition or structure of a planetary atmosphere. We can glean some information about a planetary atmosphere by directly imaging it to measure its emission, or by the indirect measurements of transmission and secondary eclipse spectroscopy, but interpreting the signal we observe to understand the physical properties of that atmosphere requires a knowledge of the incident stellar radiation field that goes beyond the luminosity to the spectral energy distribution (SED) F_λ, which also changes dramatically across the mass-interval of $0.2 - 1\ M_\odot$, as demonstrated in Figure 1.2 which compares the SEDs of TRAPPIST-1 and the Sun after scaling them to the same bolometric instellation (Wilson et al., 2021).

For convenience, we will divide the wavelength interval this work treats as "high-energy" 1 – 3200 Å into four sub-intervals, schematically described in Figure 1.3, by a combination of where the emission is formed in the stellar atmosphere and absorbed in the planetary atmosphere: X-ray (1 – 100 Å), which is mostly emitted from the corona and heats the upper exosphere of a planet; the extreme ultraviolet (EUV, 100 – 912 Å)[2] , which is emitted from all three upper layers and is also mostly absorbed by heating the exosphere and ionizing H and He; the far ultraviolet (FUV, 912 – 1700 Å), which is formed in the chromosphere and transition region and photodissociates molecules further into a planet's atmosphere; and the near ultraviolet (NUV, 1700 – 3200 Å), which is emitted by the photosphere and chromosphere and also photodissociates molecules (France et al., 2016).

[2] practically this interval and the boundaries of its neighbors will be redefined in the context of the data available for individual systems

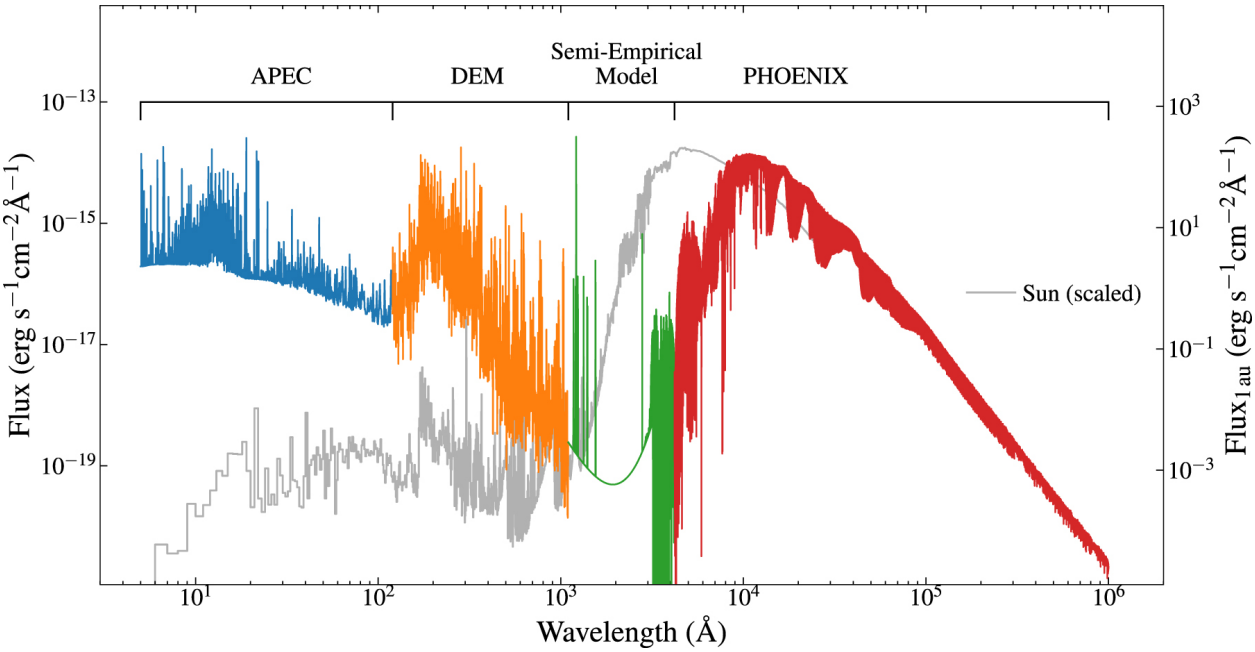

Figure 1.2: Spectral energy distribution of TRAPPIST-1 (M8V) compared to the Sun (G2V), scaled so that the integrated flux of both spectra matches the insolation received at 1 AU from the Sun, taken from Figure 8 of Wilson et al. (2021). The cooler TRAPPIST-1 has significantly more high-energy emission from wavelengths < 2000 Å compared to the Sun in this scaling, which approximately reflects the flux received in the liquid water zone, leading to different atmospheric properties and spectroscopic signatures given the same initial atmospheric composition.

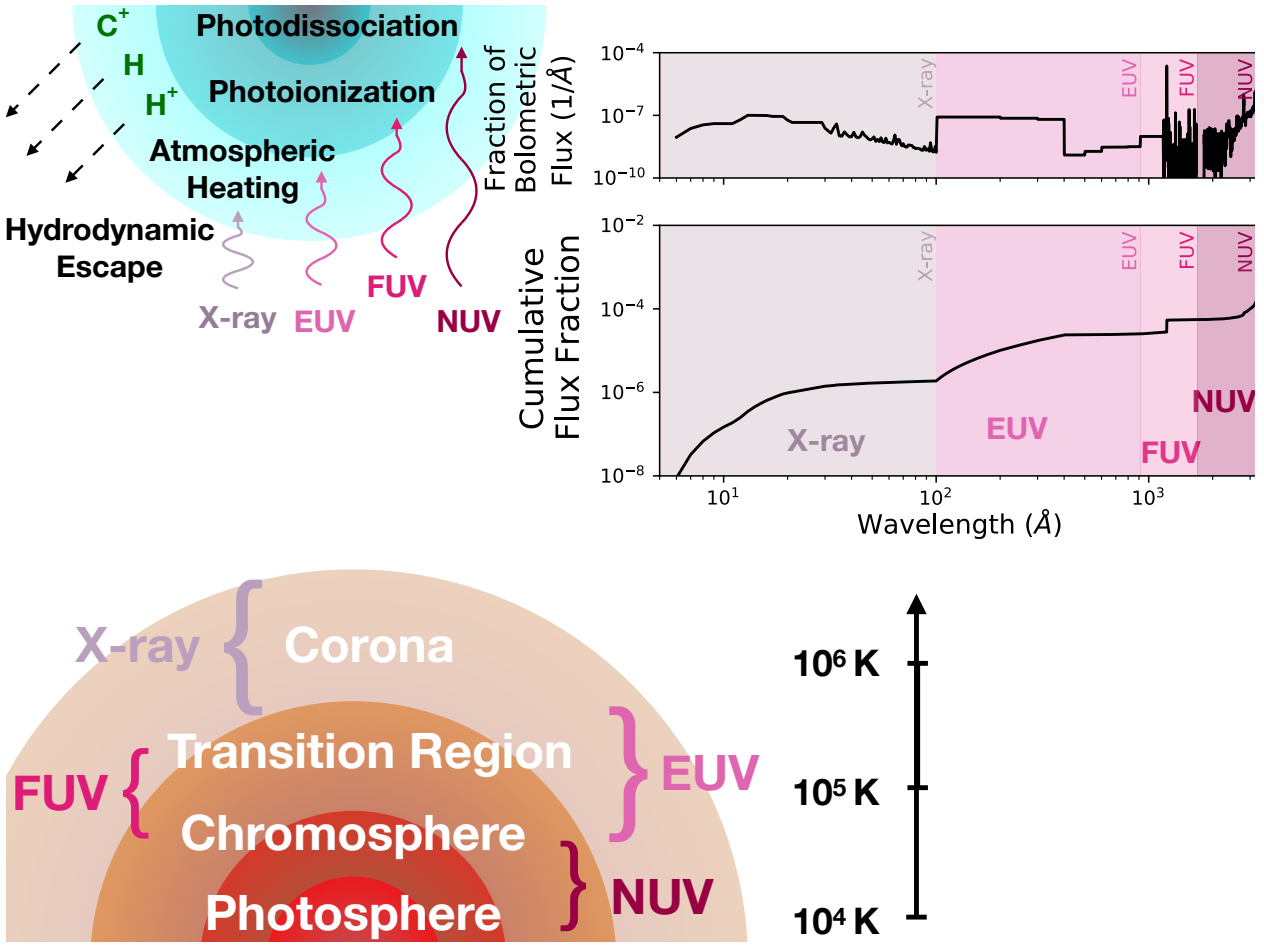

Figure 1.3: The sub-intervals we are defining for high-energy emission are formed in different layers of a star and each have distinct impacts on planets: X-ray (1 – 100 Å), extreme ultraviolet (EUV, 100 – 912 Å), far ultraviolet (FUV, 912 – 1700 Å), and near ultraviolet (NUV, 1700 – 3200 Å).

R

Mihalas (1978) describes a simple set of assumptions required to construct a "classical model atmosphere": the atmosphere is time-steady and can be described by a series of homogeneous layers (either plane-parallel slabs or spherical shells of finite thickness), momentum balance is achieved by a combination of hydro-static equilibrium and steady flows, and the internal energy produced by the star is transported out to space by a combination of radiation and convection (see Figures 1.7 and 1.8 for such one-dimensional model structures). Combining these physical assumptions with an equation of state and some specific information about the opacity of the constituent atoms and molecules of the star yields a spectrum that (more or less) matches the optical and infrared emission of observed stars, as seen in Figure 1.4. Most of this emission is well-described by the Planck curve of a perfectly emitting or absorbing sphere (Planck, 1901) with a radius approximately equal to the star's, and a particular temperature[3] , the "effective temperature" $T_{\rm eff}$, with significant deviations where atomic processes introduce additional lines or continua. The success of this simplicity is admirable, but additional physical processes are required for model stellar atmospheres to be able to match the data < 3200 Angstroms for cooler stars, as shown in Figure 1.5, taken from Figure 12 of Loyd et al. (2016), which shows a more recent model atmosphere code from Husser et al. (2013) compared to data from GJ 832 (M1.5V).

Differential rotation and convection within the stellar interior churn magnetic fields that emerge on the surface with structure and heterogeneity at many scales (Mestel, 1953; Spruit, 1999), transporting energy via non-thermal processes that begin to dominate above the photosphere (Linsky, 1980). While the net effects of these spatially and temporally varying structures can be approximated by a one-dimensional model representing some ill-defined average over the stellar disk and some timescale, the physical processes require all three spatial dimensions and time-variable components to accurately describe. A (perhaps deliberately) overwhelming display of the magnetic fields emerging above the photosphere is shown in Figure 1.6, taken from Figure 16 of Wedemeyer-Böhm et al. (2009).

[3] this definition collapses many historical developments that arguably start with Stefan (1897)

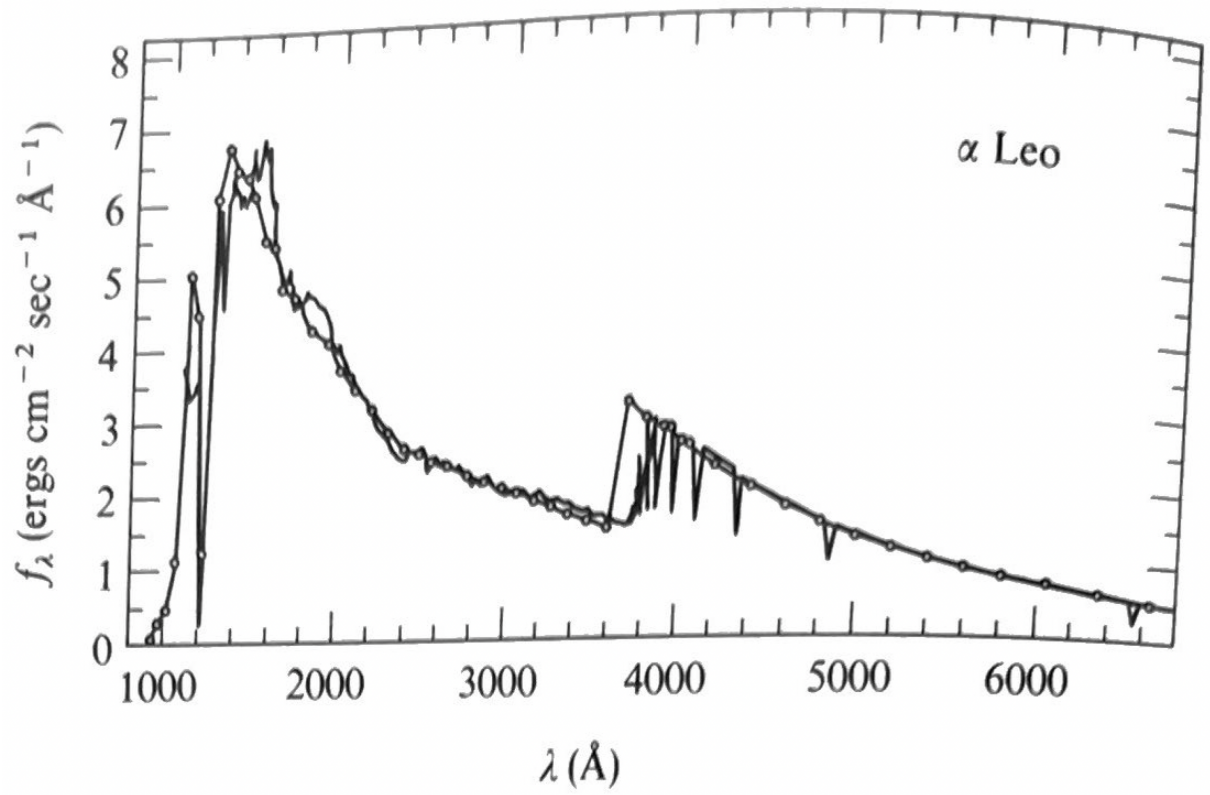

Figure 1.4: Figure 7-8 from Mihalas (1978), comparing the spectrum of α Leo (B7V) observed by Philip et al. (1975) to a line-blanketed model atmosphere from Kurucz et al. (1974), where the y-axis is 10^9 f_λ as observed at Earth. The data are plotted as open circles connected by black lines while the model is plotted as a smoother second black line beneath the data.

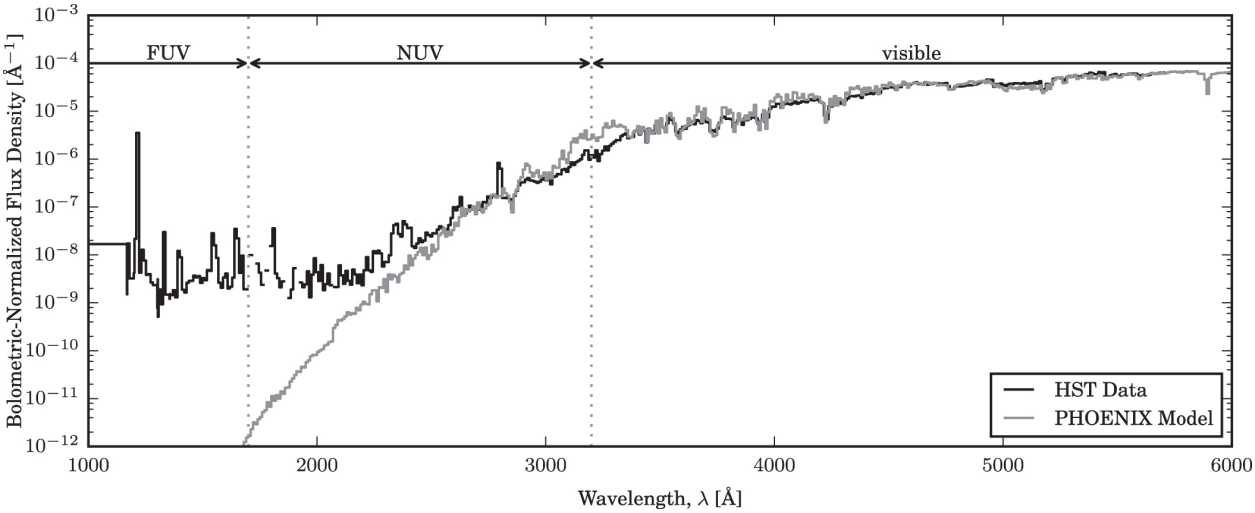

Figure 1.5: Figure 12 from Loyd et al. (2016), comparing a model atmosphere from Husser et al. (2013) to data for GJ 832, a M1.5V star. The Husser et al. (2013) model does not include emission from layers above the photosphere, and therefore does not produce the high-energy emission from the chromosphere, transition region, and corona.

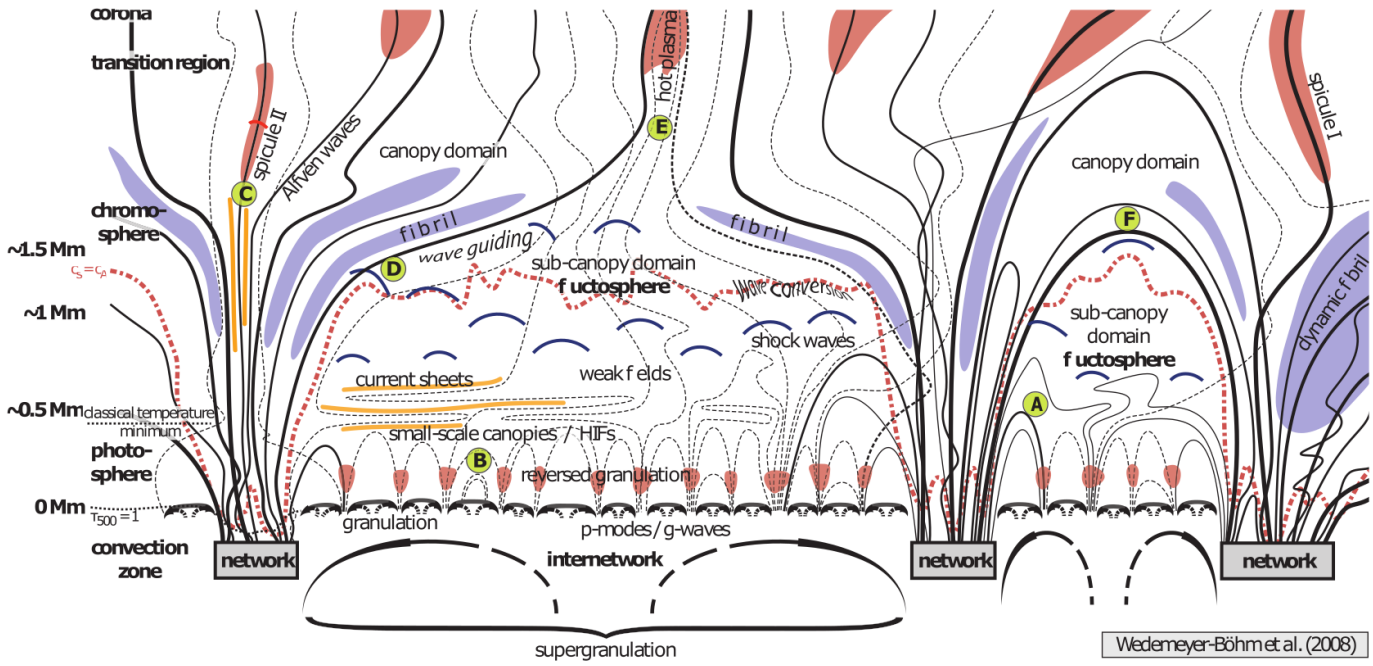

Figure 1.6: The magnetic field structure and spatial flows emerging from the convection zone to the upper atmosphere of the quiet Sun, not at all to scale, taken from Figure 16 of Wedemeyer-Böhm et al. (2009).

1.1 Structure Above the Photosphere

The dominance of magnetic energy transport marks a shift in the stellar atmosphere, and the definitions for upper layers are not strict, so we follow a schematic approach from Linsky (1980) to delineate layers by significant structural changes. Above the photosphere is a layer called the chromosphere, where the temperature begins to rise as the density falls and the plasma's non-radiative heating is opposed by radiatively cooling through the Lyman-α line at 1216 Å and the Lyman-continuum < 912 Å. That radiative cooling is insufficient to keep up with the combination of decreasing density and the non-thermal energy being dumped here and so the temperature continues to rise with altitude.

As the plasma gets hotter, more hydrogen atoms get ionized and the effectiveness of the Lyman-α and Lyman-continuum cooling fades. The only radiative cooling mechanisms left are weak, mostly just emission lines where the strongest ones are resonance lines of species like C, N, O, and Si. The abundance of these species' nuclei is not high enough to maintain the same temperature gradient as the chromosphere, so the next layer of the stellar atmosphere is a thin little transition region where the temperature shoots up real high real fast until it gets hot enough for free electrons to recombine with ionized hydrogen and this bound-free continuum opacity stabilizes the temperature gradient along with a host of emission lines in the X-ray and EUV.

At these temperatures and densities, roughly a stellar radius above the photosphere, the plasma can also balance the energy equation by launching particles out into space. In this region the plasma density is extremely low and the pretense of spherical symmetry has completely fallen apart as the plasma gets organized along magnetic field structures and forms a wispy halo or crown extending from the photospheric surface, granting this region, the corona, its name.

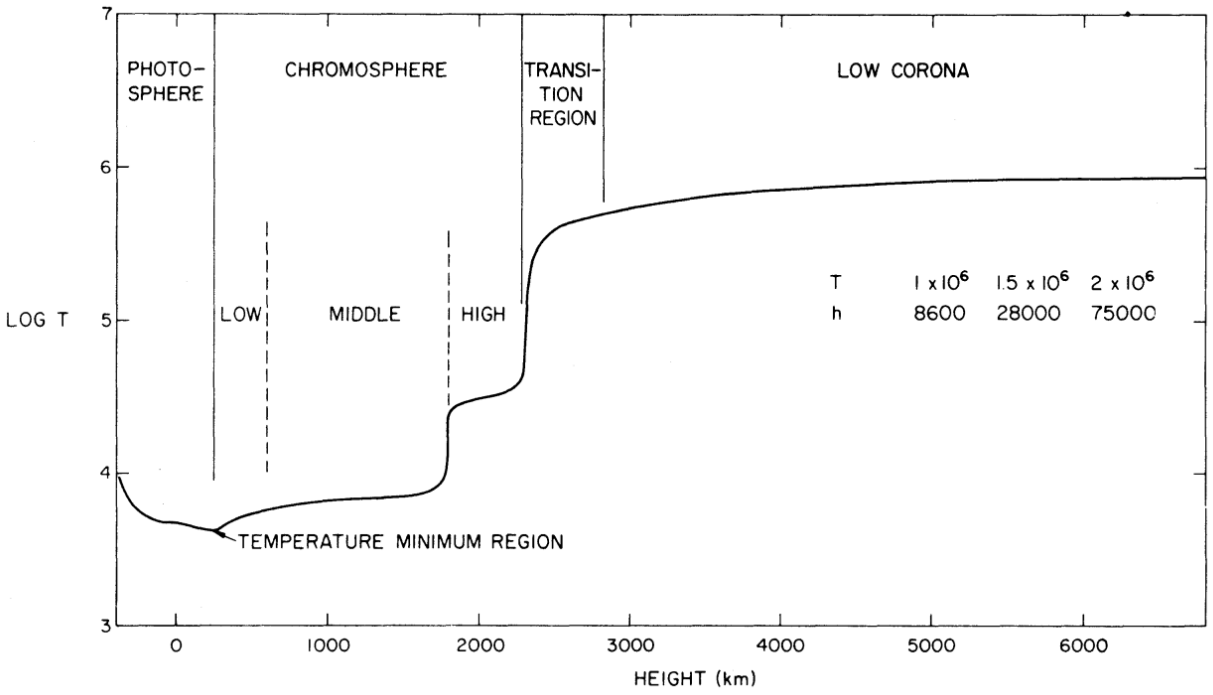

Figure 1.7: An illustrative view of the temperature structure of the Sun as a function of altitude above the polar limb, taken from Figure 1-1 of Athay (1976).

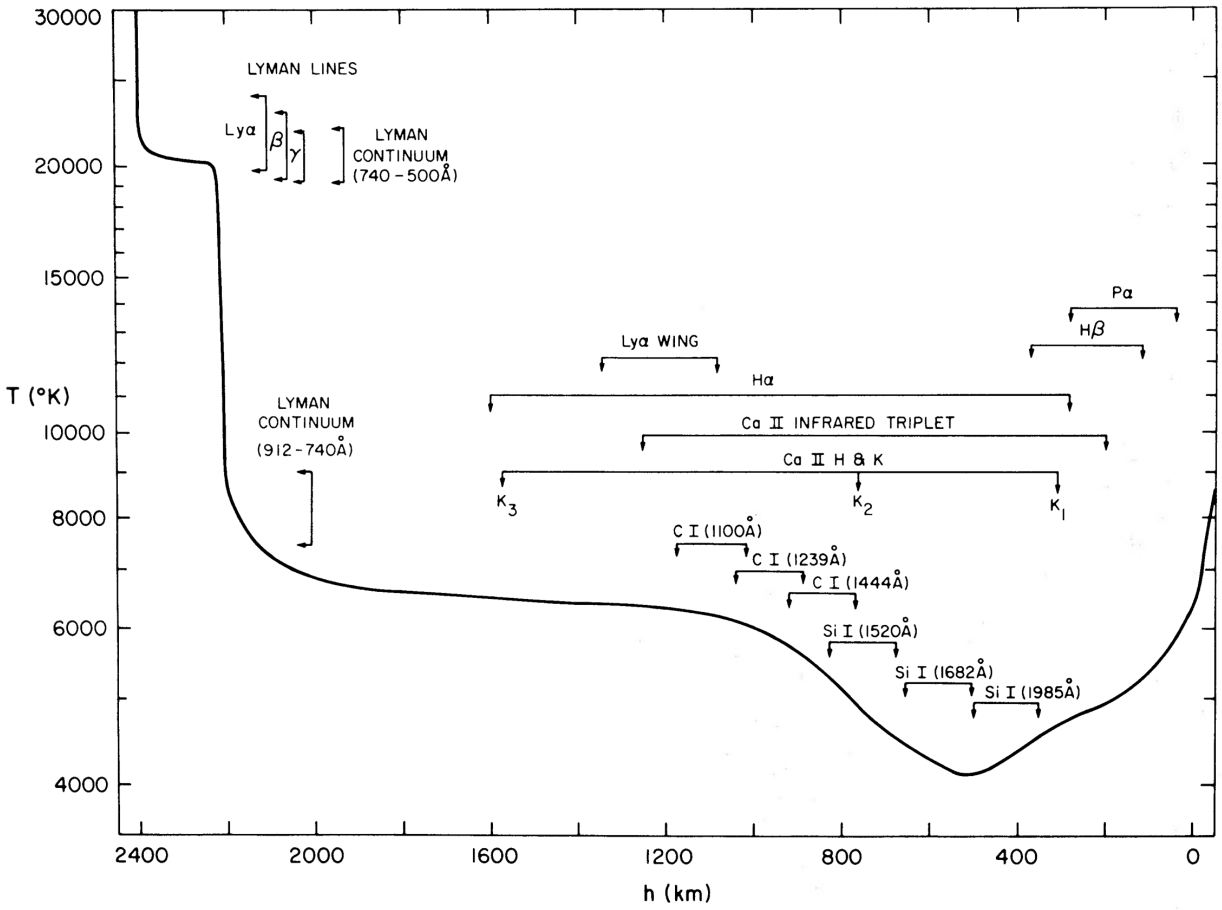

Figure 1.8: Figure 1 from Vernazza et al. (1973) showing the temperature-altitude structure from a semi-empirical model atmosphere of the Sun, labelling different regions with where spectral lines and continua are formed.

1.2 Heating Mechanisms Above the Photosphere

This summary of heating from the photosphere is largely adapted from Cranmer et al. (2015). The simplest form of non-radiative heating is present in the photosphere: acoustic waves carrying mechanical energy associated with convection up to the photospheric surface. These waves propagate to some extent upwards until they finally damp out, and the lower density of the chromosphere is what allows the energy associated with these waves to become an appreciable fraction of the energy budget. Observations of the Sun's magnetic field at the photospheric surface show bright points between cells or granules of plasma, so we can infer that magnetic energy is transported by convection from the solar interior to these flux tubes that pop up between the cells that are moving around via convection. These magnetic field measurements are correlated to surface heterogeneities: cool dark sunspots and hot plages and faculae. Observations of sunspots show structure in CO absorption lines that suggest a cool component to the chromosphere that co-exists with the hotter temperature inversion so the energy transport in this layer must be able to maintain this separation of temperature components (Ayres & Rabin, 1996). There are observational limits to magnetic field measurements that prevent us from directly tracing their progress up to the corona, but some measurements have confirmed the existence of Alfvén waves throughout the chromosphere which must transport some of this energy. These waves display both time-steady and turbulent behaviors but there are open questions as to whether they can damp out enough at the appropriate altitudes to be responsible for the non-radiative heating throughout the upper stellar atmosphere. Magnetic fields in the corona are more obvious because the magnetic pressure greatly exceeds the gas pressure and plasma is organized into structures that trace the magnetic field lines. The ambient temperature of the $T > 10^6\,\mathrm{K}$ corona also produces X-ray radiation, some of which back-heats the layers below.

1.3 Temperature to Simplify the Relationship Between Structure and Spectrum

Although the altitudes and densities for all these different regions differ from star to star, the physical dynamics of the plasma associated with these structural changes is fairly consistent from a temperature perspective. This is useful, since the radiation of low-density material is mostly explained by temperature, and so we can point to how different contributions to the spectrum are associated with stuff at different temperatures and we don't have to know everything about where the material is spatially to talk about what it's doing to produce emission. The following discussion of emission processes is adapted from Rybicki & Lightman (1986). The contributions of atomic processes in the upper stellar atmosphere to producing a photon can be grouped into 3 categories:

- Bound-Bound transitions: these are transitions of an electron from one energy state to another while remaining bound to a nucleus. This emits a photon with a characteristic energy/wavelength/frequency $E_{ul} = \frac{hc}{\lambda_{ul}} = h\nu_{ul}$ when the transition is from a higher energy "upper" state u to a "lower" energy state l corresponding to the difference in energies between states and can take place by:
    - spontaneous emission: where there is always some probability of this transition occurring, translating to a frequency in an ensemble population, denoted by the Einstein A coefficient A_{ul}.
    - stimulated emission: where the presence of the external electromagnetic field of a passing photon makes the production of a similar photon more likely by modifying the electron's wave-function, and so the product $B_{ul}J_\lambda$ of the Einstein B coefficient and ambient radiation intensity J_λ is an additional probability or frequency term for the production of a photon.
    - collisional de-excitation: a collision with another particle, most likely a free electron, where the exchange of energies between particles is close enough to E_{ul} to kick the bound electron down from u to l.

The energy of the interaction and resulting photon need not be exactly E_{ul} but within some interval depending on a combination of factors:

  * the intrinsic energy uncertainty of the transition, which is inversely proportional to the expected lifetime of an electron occupying u in its current environment
  * the perturbation of the energy of the electronic state by collisions, which depends on the density and velocity distribution
  * the velocity distribution of particles Doppler shifting the emitted photon relative to the central energy of the transition

- Free-bound continua: these transitions produce a photon when a free electron is captured by a particle into a particular electronic state if the electron is at an appropriate energy such that the sum of the electronic state energy and the energy of the emitted photon is equal to the kinetic energy transferred during the collision. The discontinuity of the minimum energy of the photon being the ionization energy relative to the occupied electronic state and the decreasing probability of the free-bound transition at higher energies results in a "recombination edge" ramp-shaped structure in the spectrum like the H I 912 Å visible in the spectrum of the Sun from 600 – 912 Å in Figure 1.2. The shape of this edge depends on the velocity distribution of the recombining species relative to the free electrons.

- Free-free continua: the acceleration of charged particles (typically a free electron) in the presence of an electromagnetic field (typically from the presence of an ion) results in the emission or absorption of photons depending on the energy exchanged. This depends on the plasma's ambient electromagnetic field and the velocity distributions of ions and electrons.

- Two-photon continua: An infrequent process by which a bound-bound transition from u to l is extremely unlikely but occurs by dropping down from u to an intermediate state and producing one photon, and then in quick succession dropping down to l and producing a second photon.

In the upper stellar atmosphere, particularly above the lower chromosphere, the densities are low enough that it is typically safe to assume that all photons produced either safely escape without interacting with any particles if they are emitted up and out of the stellar atmosphere, or are absorbed by the denser optically thick plasma if emitted down towards the stellar surface. If all the baryonic particles are colliding with each other often enough to share a common thermal Maxwellian velocity distribution with a characteristic temperature T, the particles can be considered to be in local thermodynamic equilibrium "LTE" which simplifies many of the calculations required to determine the shape of spectral lines and recombination continua. In this case, the populations of different ions, electronic states, and free electrons all become simpler functions of density and temperature because all electronic states and ionization stages are produced by collisional excitation via free electrons. The combination of these two approximations is referred to as the "coronal" or "nebular" assumption for the two major astrophysical contexts in which these approximations are most valid. Under these conditions, the populations of electronic states is given by,

$$\frac{n_u}{n_l} = \frac{g_u}{g_l} \exp\left(-\frac{E_u - E_l}{k_\mathrm{B} T}\right) \tag{1.1}$$

where n_i refers to the number density of state i (either u or l), g_i refers to the statistical degeneracy of the state (how many valid electronic configurations correspond to the same energy level), k_B is the Boltzmann constant, and $\frac{E_u - E_l}{k_\mathrm{B} T}$ is the Boltzmann factor and its inverse exponential represents the probability of a free electron colliding with the correct kinetic energy to excite a bound electron from l to u. Similarly, the ion populations are well-described by the Saha ionization equation (Saha, 1920, 1921),

$$\frac{n_{j+1} n_e}{n_j} = \frac{2 U_{j+1}}{U_j} \left(\frac{2\pi m_e k_\mathrm{B} T}{h^2}\right)^{3/2} \exp\left(-\frac{\chi_{j,\,j+1}}{k_\mathrm{B} T}\right) \tag{1.2}$$

where n_j represents the number density of an ionization stage j, $U_j(T)$ is the partition function of j, $\chi_{j,\,j+1}$ is the ionization energy from j to $j+1$, and $e^{-\frac{\chi_{j,\,j+1}}{kT}}$ is the probability of a free electron colliding with the appropriate Boltzmann factor just like in Equation 1.1.

CHIANTI is a database of atomic data that was collated for the analysis of optically thin plasma under the coronal approximation, where the ionization equilibrium populations incorporate effects beyond the Saha equation (Dere et al., 1997; Del Zanna et al., 2021). Given an assumed electron density and a range of temperatures, CHIANTI can calculate contributions to the spectrum at a wavelength λ from a parcel of plasma with an electron density n_e and a temperature T from different processes for a given ion. Figure 1.9 shows the contribution functions of a set of strong emission lines and some X-ray spectral bins as a function of temperature. Taking a 2-dimensional view of the contribution functions for H I, the top two panels of Figure 1.10 show a heat-map where the color of a pixel corresponds to the value of the contribution function at a wavelength λ (x-axis) from plasma at a temperature T (y-axis). The top panel displays contributions from bound-bound transitions of H I (the discrete vertical lines corresponding to different electronic transitions), free-bound continua (the swath of higher intensity near 912 Å and temperatures $10^4 < T < 10^5$ K, the ionization edge of neutral hydrogen referenced above and apparent in Figure 1.2), and the free-free continuum (the swath of high intensity at high temperatures and short wavelengths). The bottom panel shows the flux density of the spectrum produced by weighting this contribution function for a pure neutral hydrogen gas by a differential emission measure model of the structure of the Sun's upper atmosphere (discussed further in Chapter 2). Even though the free-free continuum has a high contribution function comparable to the free-bound continuum, the Sun's atmosphere has much less material at 10^7 K than 10^5 K and so the observed emission from the free-bound continuum is higher.

The use of CHIANTI to produce this 2D view of how plasma at a particular temperature contributes to the observed intensity at a particular wavelength will be used frequently in this dissertation, while the expressions for and physical meaning of the contribution function is elaborated upon in Chapter 2.

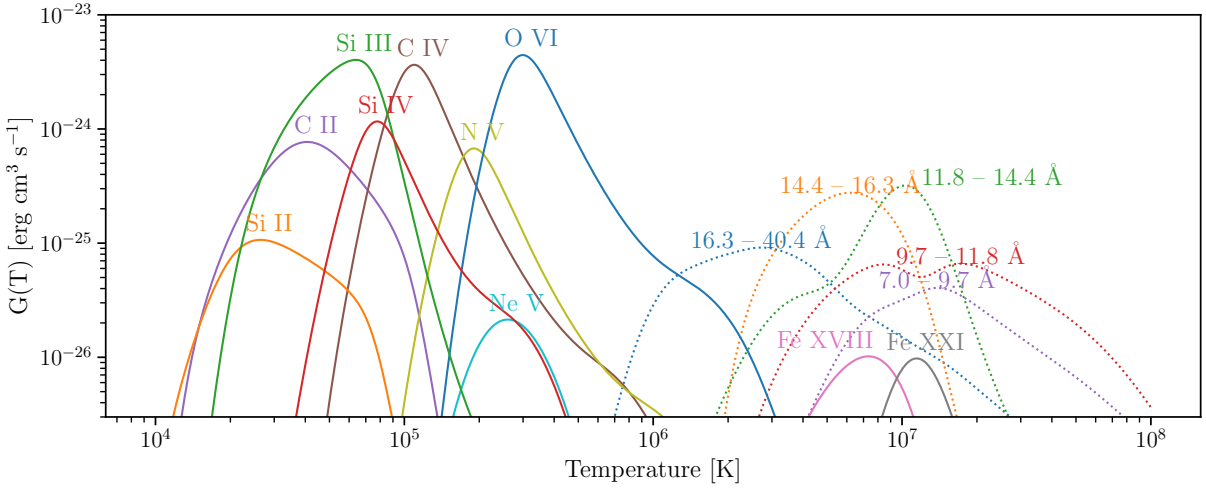

Figure 1.9: A sample of the contribution functions $G_{ul}(T)$ and $G_\lambda(T)$ discussed further in Sections §2.3 and §2.4. The solid lines show the summed contribution functions for some of the strongest transitions of the labeled ion observable by *Hubble* with STIS and COS. The dotted lines show the summed contribution functions $G_\lambda(T)$ for typical wavelength bins in a *Chandra* spectrum of an M dwarf, adding up the $G_{ul}(T)$ functions of all emission lines that fall within the wavelength bin.

1.4 Time Variability of High-Energy Emission

Now we relax the assumption of time-steadiness and look beyond the spectrum as it exists in a single moment in time. The links between magnetism, convection, interior structure, and angular momentum result in a combination of variability timescales for the non-radiative heating and the consequent emission.

- Impulsive – Flares and coronal mass ejections are sudden changes that can be as brief as seconds or sustained for longer by some superposition of these events. Figure 1.11 shows one proposed mechanism for flares: a magnetic reconnection event that accelerates a beam of electrons down towards the chromosphere while Figure 1.12, taken from Figure 1 of Mendoza et al. (2022), shows a lightcurve that illustrates the changes in brightness associated with flares.

- Rotation period – The presence of surface features like starspots results in variation associated with these features rotating in and out of view, leading to the sinusoidal behavior that the flares sit on top of in Figure 1.12. Depending on the stellar surface area covered by these features, more or less high-energy emission will be emitted in a particular direction because of the spectral distinctions between any surface feature and the "typical" photosphere. It is important to note that the combination of spot and faculae fractions for cool stars like TRAPPIST-1 can be $> 60\%$ (Rackham et al., 2018) which sort of breaks the assumption of these features as minor perturbations to the mean behavior of the photosphere.

- Spot evolution – Surface features do not persist indefinitely but emerge, grow, and fade over a timescale that depends on their position, size, and the stellar mass. Differential rotation as a function of latitude is an example of one factor in the destruction of a spot.

- Activity cycles – The Sun displays an 11 years activity cycle during which the spot fraction, typical spot latitude, high-energy emission, and flare frequency all vary together (Maunder, 1904), some aspects of which can be seen in "butterfly diagrams" as shown in Figure 1.13.

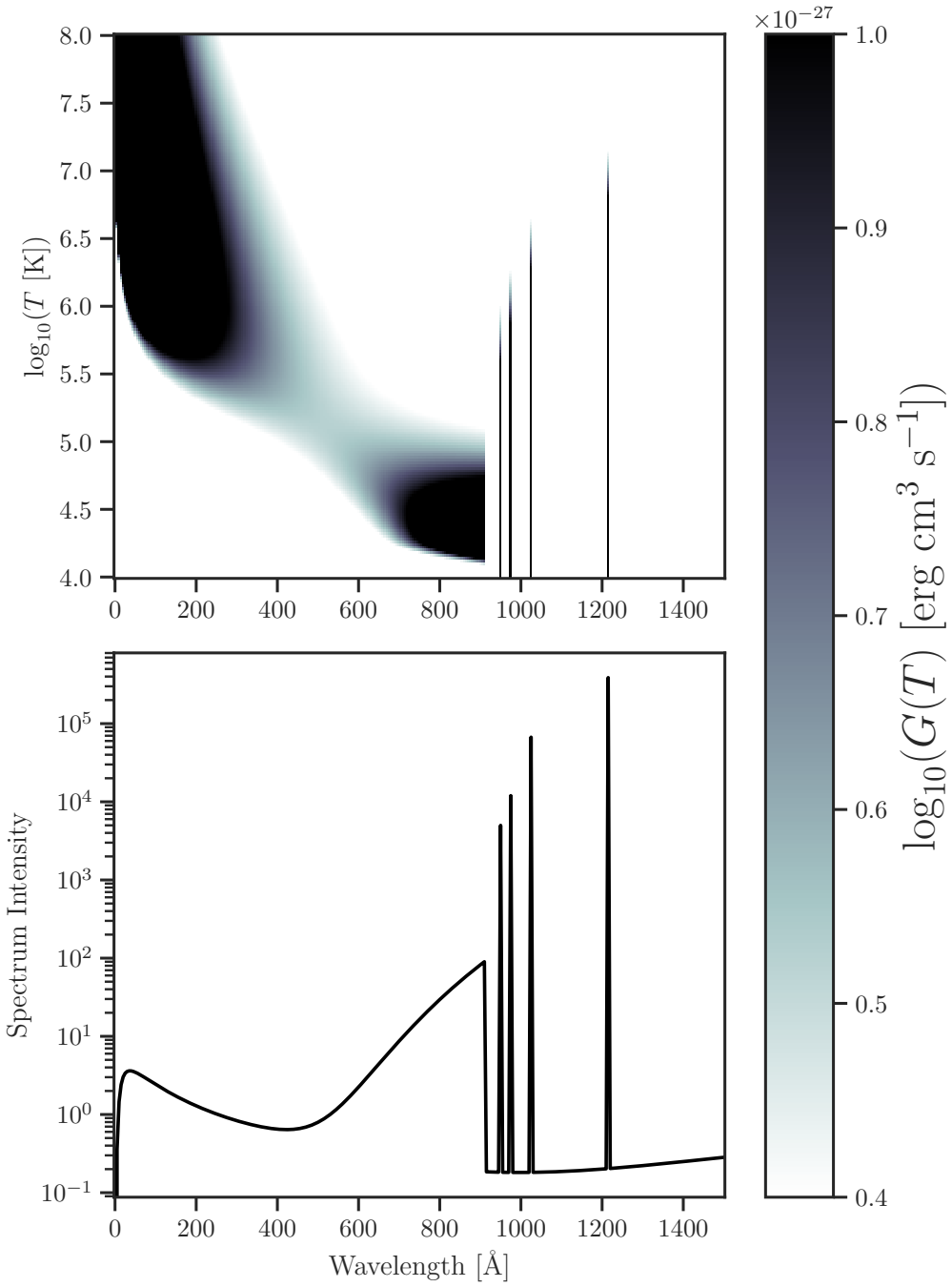

Figure 1.10: The top panel shows a 2D view of the contribution function of emission from neutral hydrogen, where the y-axis corresponds to temperature, the x-axis corresponds to wavelength, and the color scale corresponds to the value of the contribution function according to the color-bar on the right side of the plot. The color scale is linear between cutoff values chosen to emphasize both the lines and continua. The bottom panel shows the spectrum produced by a plasma with this contribution function when weighted by the temperature and density structure of the Sun's upper atmosphere, de-emphasizing the contribution from free-free emission $\lambda < 300$Å because there is less material at $T > 10^6$ K.

Wilson (1968) measured the Ca II H and K emission lines of multiple solar-type stars over decades and found that they also showed activity cycles via the periodic variation of the strength of these chromospheric lines.

- Maunder minima – While there is a fairly smooth continuous behavior within the Sun's activity cycle, these cycles are not identical to each other. Spoerer & Maunder (1890) found that 1645 to 1716 showed an unusually low activity level, a behavior now known as a Maunder minimum, with very few sunspots observed at all. Baum et al. (2022) identified a possibly similar minimum for HD 166620, a K2V star with a 16 year activity cycle that has appeared to have entered a very low and flat activity behavior some time around 2004.

- Rotation/Activity/Age evolution – Skumanich (1972) put together multiple studies of four open clusters to make claim that stellar lithium abundance, rotation period, Ca II H and K emission, all followed the same t^{-2} power law decay as a function of age (see Figure 1.14). This functional form was later modified to a broken power-law relationship, where the activity level in a particular indicator remains constant at a saturation level until some break-point when it begins to decline. Some recent examples in the X-ray and Hα are Wright et al. (2011) and Newton et al. (2016) respectively. While the value of the slope has varied between studies and a dependence on stellar mass has been introduced, the core idea that these properties have closely related evolutionary behavior has held up over the last fifty years.

- Stochastic – I am treating this as a catch-all for the wiggles in time-variability of various spectral features that cannot be attributed to measurement uncertainty but have no clearly identifiable periodicity or structure and elaborate on this type of variability in Chapter 3.

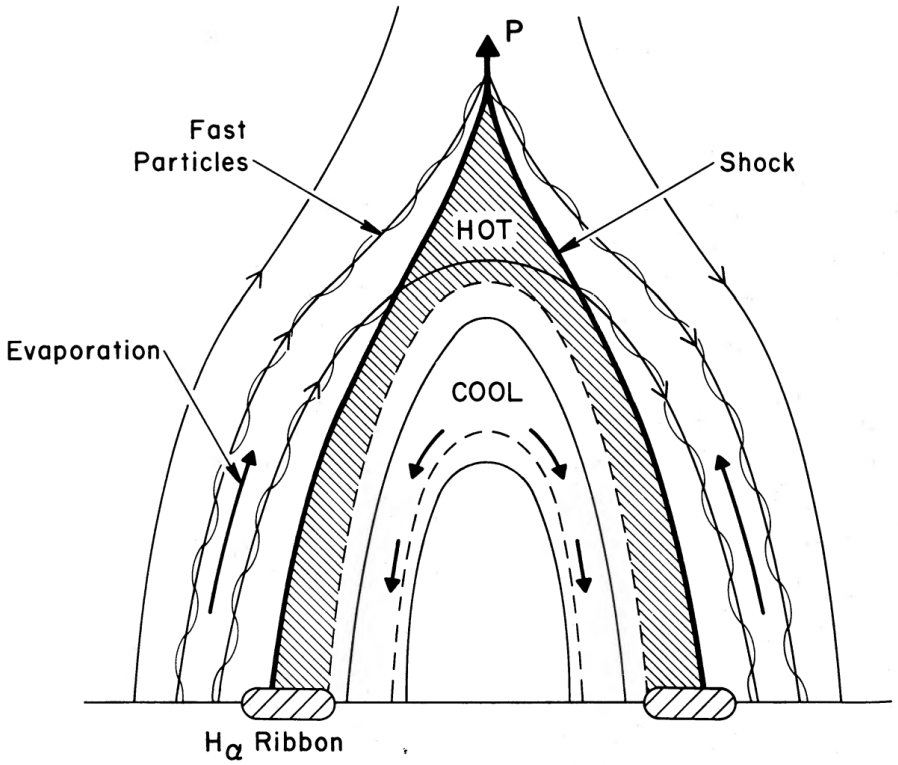

Figure 1.11: Figure 1 from Cargill & Priest (1983) showing a sketch of post-flare loops after a reconnection event. The shaded region shows the distribution of heated material that is falling down as inferred from time-resolved Hα observations of flares.

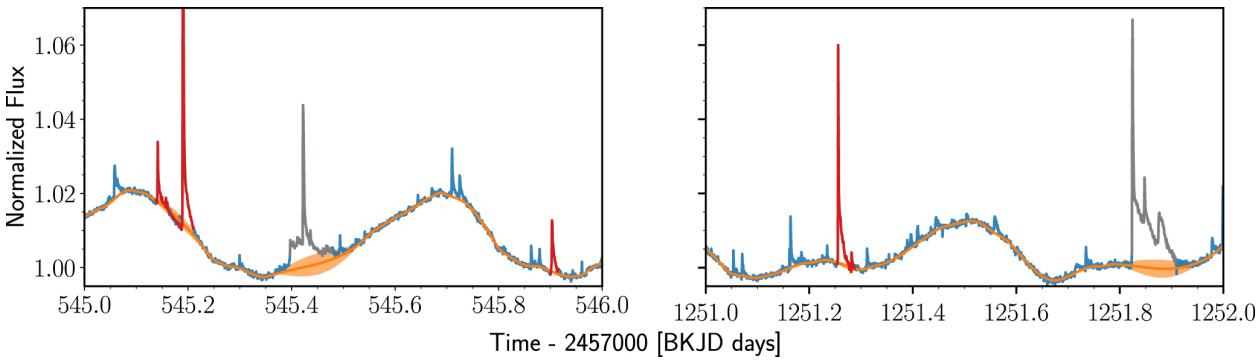

Figure 1.12: Figure 1 from Mendoza et al. (2022) showing two days of *Kepler* observations of the flare star GJ 1243. Many of the flares show a similar shape overall, with variation in both amplitude and duration, but there are also more complicated superpositions of flares and individual flares can deviation from the default shape. The sinusoidal behavior is from the rotation of surface features changing the overall flux received from the face of the star in view.

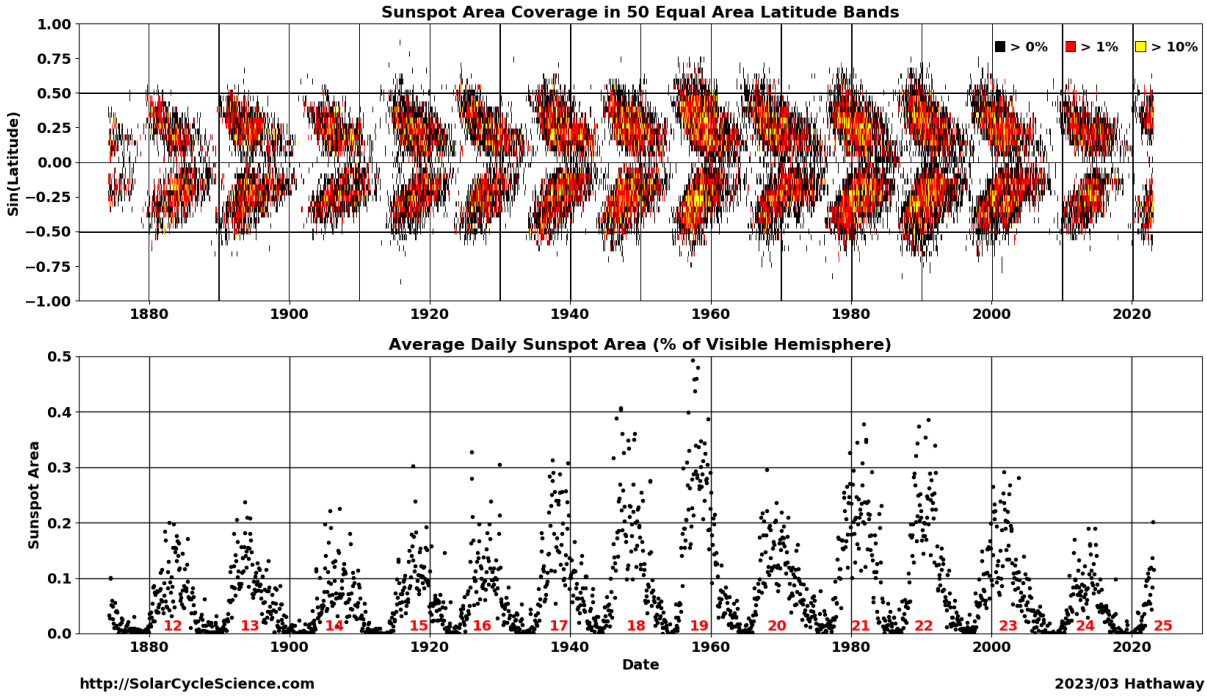

Figure 1.13: Obtained from http://solarcyclescience.com/solarcycle.html. The top panel shows a color-coded scale for where sunspots occurred as a function of latitude and time while the bottom panel collapses the position information. There is a periodic rise and fall of total sunspot area that coincides with sunspots occurring closer to the equator over the course of the cycle.

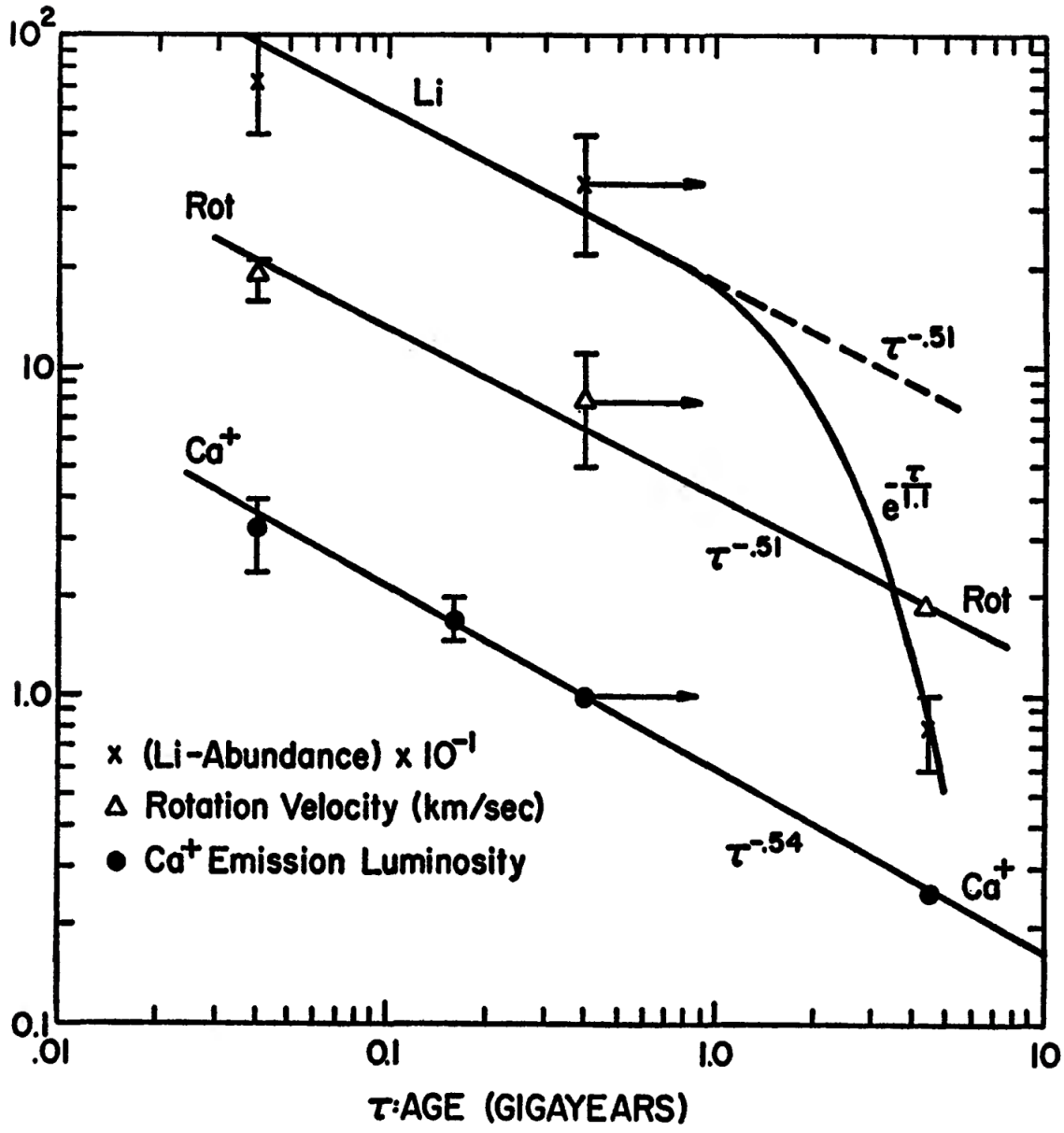

Figure 1.14: Figure 1 from Skumanich (1972) showing multiple properties for four clusters following a similar trend with age.

1.5 Impact of High-Energy Radiation on a Planetary Atmosphere

When high-energy photons come into contact with the atmosphere of a planet, they can produce photo-electrons by ionizing atomic or molecular species, photodissociate molecules, or excite electronic states. Any of these interactions donates the photon's energy to the system and can trigger cascading interactions that distribute the energy; for example the free photo-electrons can collide with enough particles to thermalize the system and increase the temperature in the vicinity of their production or recombine with ions to produce photons at various energies depending on which species they come into contact with. At the highest energies and highest altitudes of the atmosphere however, the donated energy can enable the escape of particles, particularly the lightest elements, by providing enough kinetic energy to overcome the gravitational energy binding the particle to the planet. Which interactions take place depends on the incident stellar radiation at a particular altitude, and the combination of absorption, emission, and chemical reaction processes of the various species present at that altitude. A net consequence of these effects is that the deeper a photon manages to get into the planetary atmosphere, the more likely it is to affect the temperature structure and chemical network than drive escape (Youngblood et al., 2019).

X-ray photons heat gas by ionizing metals, but the gas heated to 10^6 K also cools by emission lines produced by the same metals (typically carbon and oxygen), resulting in a temperature balance determined by the abundance and ionization of these metals (Owen & Jackson, 2012). EUV photons are predominantly absorbed by ionizing hydrogen and helium while they are the most abundant species present at a particular altitude, and in radiative equilibrium a temperature balance is achieved between the ionization and recombination of hydrogen and helium. In thinner and heavier atmospheres dominated by other molecules like N_2 and CH_4 (Titan) or CO_2 (Mars) however, the lack of hydrogen allows EUV flux to go deeper into the thermosphere and photodissociate these molecules to heat the atmosphere, drive their escape, and affect organic chemistry(Lavvas et al., 2011; Amerstorfer et al., 2017). Simplified model atmospheres in radiative and chemical equilibrium still need high-resolution absorption cross-sections and EUV spectra to describe these interactions.

Radiatively driven atmospheric escape of a particular species can take place through a ballistic process like Jeans escape, or a hydrodynamic pressure-driven wind. The Jeans parameter, which compares the thermal kinetic energy to the escape velocity, is often used to determine which category of loss mechanisms dominates,

$$\lambda_J = \frac{GM_p m}{k_B T_{\rm exo} r_{\rm exo}} \tag{1.3}$$

where λ_J is the Jeans parameter, M_p is the mass of the planet, m is the mass of a particle in the exosphere, $T_{\rm exo}$ is the temperature of the exobase, and $r_{\rm exo}$ is the radial coordinate of the particle within the exosphere. Jeans (1904) first described this thermal process whereby the kinetic motion of a particle within a gas of temperature T has some probability of moving fast enough in the right direction to escape the gravitational potential. A higher Jeans parameter indicates the Jeans escape mechanism is more dominant, so the escape probability is limited to a few particles at the upper-end of the velocity distribution making their way out. At lower Jeans parameter values, the hydrodynamic regime, there are enough particles moving together that they constitute a pressurized wind described by fluid equations. In both cases, the solution depends on the altitudes at which photons get absorbed.

Watson et al. (1981) introduced a framework where all the radiative heating by EUV flux is assumed to take place within some thin slice of the atmosphere and defined an effective radius for this altitude beyond the exobase, simplifying the problem significantly and descendants of this approach like Erkaev et al. (2007) and Kubyshkina et al. (2018) also defined a net mass-loss efficiency to collapse all the calculations of escape probability into a single factor, yielding a mass-loss rate

$$\dot{M} = F_{\rm XUV} \frac{\pi \eta R_{\rm eff}^2}{K} \frac{R_p}{G M_p m} \tag{1.4}$$

where $F_{\rm XUV}$ integrates the incident flux density at the planet's position from 0 – 912 Å[4] , η is the mass-loss efficiency, $R_{\rm eff}$ is the effective radius, K is a factor from Erkaev et al. (2007) to account

[4] individual authors set slightly different bounds for this "XUV" = X-ray + EUV regime

for Roche-lobe overflow effects, M_p and R_p are the mass and radius of the planet respectively, and m is the mass of the particle species being considered, typically neutral hydrogen. This type of expression is useful for comparison between systems by translating the more abstract quantity of integrated XUV flux to a mass-loss rate, but the tunable parameters make it difficult to interpret any particular value unless there are external constraints like observations of escape and/or the atmospheric composition via transmission spectroscopy.

Deeper into the atmosphere, as photons are spent on chemistry rather than escape, many molecular species relevant to habitability and biosignature detection are dissociated by high-energy photons, some of which are shown with their photo-dissociation cross-sections as a function of wavelength in Figure 1.15, taken from Figure 8 of Loyd et al. (2016). Since ozone can be abiotically produced depending on the stellar irradiation, its use as a biosignature must be contingent on the presence/absence of other species like CO, CO_2, and CH_4 (Meadows, 2017). Looking at habitability itself instead of biosignature detection, the wavelength dependence of a photosynthesising species has to complement the received radiation in a way that prevents overheating to the point of denaturing proteins (Shields et al., 2016). A number of proposed pathways for prebiotic chemistry leading to abiogenesis require NUV flux to reach the surface, and so a planet in the liquid water zone may not be exposed to enough NUV flux if the host star's spectrum is too faint in that regime (Ranjan et al., 2017). Richey-Yowell et al. (2022) positions K dwarfs as the most promising target for habitable planet discoveries because they benefit from the small star advantages for exoplanet discovery and characterization without risking the complete loss of an atmosphere that may accompany the higher XUV fluxes of M dwarfs.

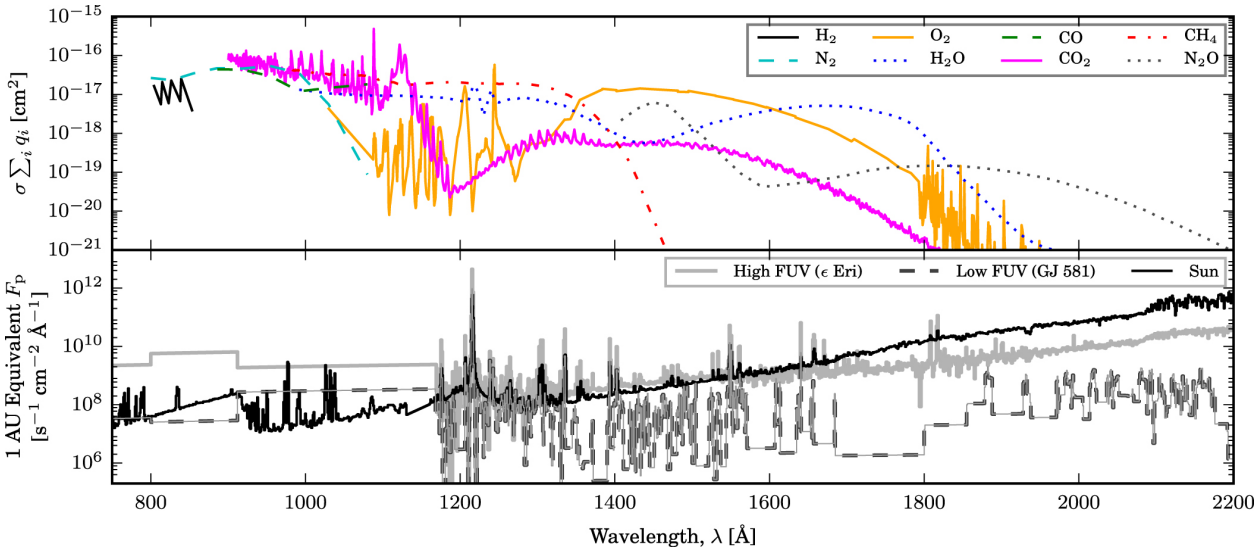

Figure 1.15: Figure 8 from Loyd et al. (2016) showing the photo-dissociation cross-sections of significant molecules in the top panel compared to the very different SEDs of the Sun and ϵ Eridani in the bottom panel.

1.6 Dissertation Structure

The chapters in this dissertation each address the characterization of a particular aspect of high-energy emission. Chapters 2 and 3 are published work while Chapter 4 is close to submission. Chapter 5 is a first foray into a much longer project that will build on the foundation laid by this dissertation, and concludes the dissertation by considering avenues for further investigation.

1.6.1 Chapter 2: Inferring the Extreme Ultraviolet Emission of Low-Mass Dwarfs

The EUV interval is the most defined by observational constraints, and any analysis of the high-energy irradiation of a planetary atmosphere needs to come up with a way to deal with those observational constraints. While targets with observable EUV flux exist, there is no currently operational facility observing between 150 and 912 Å. Inferring the spectra of exoplanet hosts in this regime is critical to studying the evolution of planetary atmospheres because the EUV heats the top of the thermosphere and drives atmospheric escape. In Chapter 2 I present my implementation of the differential emission measure technique to reconstruct the EUV spectra of cool dwarfs. I characterize this implementation's accuracy and precision by applying it to the Sun and AU Mic and then apply it to three fainter M dwarfs: GJ 832, Barnard's Star, and TRAPPIST-1.

1.6.2 Chapter 3: Stochastic Chromospheric Variability Across Stellar Rotation Period

In Chapter 3 I analyze the ultraviolet and optical spectra of 9 M dwarfs across a range of rotation periods to determine whether they showed stochastic intrinsic variability distinguishable from flares. The ultraviolet spectra were observed during the Far Ultraviolet M Dwarf Evolution Survey *Hubble Space Telescope* program using the Space Telescope Imaging Spectrograph and the optical observations were taken from the Apache Point Observatory 3.5-meter telescope using the Dual Imaging Spectrograph and from the Gemini South Observatory using the Gemini Multi-Object Spectrograph. We used the optical spectra to measure multiple chromospheric lines: the Balmer

series from Hα to H10 and the Ca II H and K lines. We find that after excising flares, these lines vary on the order of $1 - 20\%$ at minute-cadence over the course of an hour. The absolute amplitude of variability was greater for the faster rotating M dwarfs in our sample. Among the 5 stars for which we measured the weaker Balmer lines, we found a tentative trend that the fractional amplitude of the variability increases for higher order Balmer lines. Similarly, we measured the integrated flux of multiple ultraviolet emission features formed in the transition region: the N V, Si IV and C IV resonance line doublets, and the C II and He II multiplets. Unfortunately, the signal-to-noise (S/N) ratio of the UV data was too low for us to detect non-flare variability at the same scale and time cadence as the optical. We consider multiple mechanisms for the observed stochastic variability, propose both observational and theoretical avenues of investigation to determine the physical causes of intrinsic variability in the chromospheres of M dwarfs and advocate for similar analyses of higher mass stars.

1.6.3 Chapter 4: The High-Energy Emission of A Young Sun-like Star

Since the high-energy emission is strongest during the saturation stage of rotation-activity-age evolution, and the initial conditions for magnetic activity and high-energy emission seem to persist for a long period of time, it is important to anchor our study of the rotation-age-activity evolution by empirically measuring the properties of young stars. V1298 Tau is a young 23 Myr old 1.1 $M_{\odot}$ T Tauri star with four known transiting exoplanets amenable to atmospheric characterization with current-generation instruments capable of transmission spectroscopy. In Chapter 4, I piece together observations from the *NICER* X-ray telescope, the Space Telescope Imaging Spectrograph and Cosmic Origins Spectrograph instruments aboard *Hubble Space Telescope*, and empirically informed models to create a panchromatic spectrum data product for V1298 Tau spanning 1 – 10^5 Å. I use the data product for this young Solar analog to characterize the long-term evolution of high-energy radiation from solar-mass stars and compare the lifetime cumulative high-energy irradiation of the V1298 Tau planets to other exoplanets orbiting solar mass stars.

1.6.4 Chapter 5: The Evolution of High-Energy Emission for M Dwarfs

Shifting from the individual to the collective, I describe the collation of a sample of 115 GKM stars with FUV and X-ray data that will allow me to attempt to fit differential emission measure models. I select nine M dwarfs from this larger sample to explore trends in their atmospheric structure as a function of rotation period, then use five similarly massive M dwarfs to interpolate the evolution of their EUV spectra over time, and describe an approach for an interpolation scheme across the entire 115 GKM dwarf sample.

1.6.5 Chapter 6: Future Work

The dissertation concludes by exploring future research that builds on the methods, datasets, and questions that emerge from the work discussed here.

Chapter 2

Inferring the Extreme Ultraviolet Emission of Low-Mass Dwarfs

2.1 Preface

This chapter is a lightly edited reproduction of work published in Duvvuri et al. (2021), where the majority of the analysis was conducted by myself with advice and input from the paper's co-authors, using data collected by the MUSCLES (France et al., 2016) and MegaMUSCLES (Wilson et al., 2021) *Hubble* observing programs. The methods described in this paper were updated in later work for Chapters 4 and 5.

2.2 Introduction

The discovery and characterization of exoplanets has been accompanied by an increased interest in the properties of M dwarf stars as potential hosts for habitable planets. M dwarf planetary systems are abundant, not only because M dwarfs are $\gtrsim 70\%$ of all stars in the Milky Way (Henry et al., 2006; Winters et al., 2015), but also because M dwarfs also have an intrinsically high planet occurrence rate compared to their hotter and more massive siblings (Dressing & Charbonneau, 2015). Moreover, these systems' physical properties benefit their detection and characterization: once for their abundance, twice for the large transit depths of terrestrial planets projected against small stellar radii, and thrice for the short orbital periods of planets with Earth-comparable instellation. The *Transiting Exoplanet Survey Satellite* (*TESS*) is predicted to find 1300 planets orbiting M dwarfs (Ballard, 2019), roughly 10 of which will be terrestrial worlds suitable for atmospheric characterization with the *James Webb Space Telescope* (Barclay et al., 2018).

These M dwarf planetary systems provide a useful sample for study, but some caution that the "habitability" potential of these systems may be poor or non-existent (Scalo et al., 2007; Shields et al., 2016). An M dwarf is a tempestuous host, prone to flaring (Hawley, 1993; Kowalski et al., 2009; Loyd et al., 2018a,b), particularly when young, where a mid-to-late M dwarf's definition of "young" lasts for billions of years (West et al., 2008). Compared to the Sun, M dwarfs emit a much higher fraction of their bolometric flux in the ultraviolet regime (West et al., 2004; Jones & West, 2016). The extreme ultraviolet region (EUV, defined here as 100 - 912 Å) is particularly responsible for heating and ionizing the upper atmosphere of planets, dumping energy into the system and potentially driving atmospheric escape (Sekiya et al., 1980; Sanz-Forcada et al., 2010; Owen & Jackson, 2012; Tian & Ida, 2015; Zahnle & Catling, 2017, e.g.). Any attempt to study an exoplanet atmosphere's evolution must be informed by the radiation field it is subject to over the entirety of its lifetime (Penz & Micela, 2008; Claire et al., 2012; Peacock et al., 2020). But directly measuring the EUV flux is impeded by the same mechanism that makes it important for planet atmospheres: its interactions with atomic hydrogen and helium mean that the interstellar medium blocks some of the flux from this spectral region for most stars (Cox & Reynolds, 1987; France et al., 2019). This problem is exacerbated for M dwarfs since the closest M dwarfs with observable EUV flux either have noisy data from the *Extreme Ultraviolet Explorer* (*EUVE*) or no data at all (Craig et al., 1997; Linsky et al., 2014; France et al., 2016), and there is no presently available dedicated EUV observatory to remedy the situation (France et al., 2019).

In the absence of direct observation, we must turn to theoretical inference. Peacock et al. (2019a) and Peacock et al. (2019b) use the `PHOENIX` 1D stellar atmosphere code (Hauschildt, 1993; Hauschildt & Baron, 2006; Baron & Hauschildt, 2007) to model the non-LTE radiative transfer through the chromospheres and transition regions of M dwarfs but do not include a corona. Fontenla et al. (2016) adjusts the temperature and pressure profiles of a 1D stellar atmosphere until the model agrees with the available spectral data, but this takes time to do well and has to be specific to each star. These semi-empirical methods require quasi-simultaneous observations from optical to X-ray wavelengths, a reliable atomic database, and laborious fine-tuning to be successful.

Taking a more empirical approach, Linsky et al. (2014) identifies correlations between Lyman-α and EUV flux, while Youngblood et al. (2017) identifies correlations between far-ultraviolet (FUV, 912 to 1700 Å) lines and the Lyman-α flux, chaining these correlations to the Linsky et al. (2014) relations to predict the EUV flux in turn. A drawback of this method is that the uncertainty on each correlation introduces scatter into the predicted EUV flux while the sample is insufficiently large to investigate the effects of both effective temperature $T_{\rm eff}$ and stellar activity. France et al. (2018) correlates certain FUV lines with the EUV flux between 90 and 360 Å directly, leading to much less scatter in the predicted flux and accounting for both $T_{\rm eff}$ and stellar activity in their sample, but this still leaves us with ~ 600 Å of EUV flux to estimate.

These limitations of existing methods lead us to use the differential emission measure (DEM), a technique for EUV spectral synthesis adapted from an earlier technique called the emission measure distribution. Pottasch (1963) defined the emission measure distribution $\equiv \frac{n_{\rm O}}{n_{\rm H}} \int n_e^2 \, ds$ as the integral of the electron number density squared (n_e^2) along the line of sight s weighted by the relative abundance of oxygen to hydrogen ($\frac{n_{\rm O}}{n_{\rm H}}$), to describe the plasma environment of the upper layers of the Sun's atmosphere. This assumed that the Sun's upper atmosphere could be approximated as a series of spherical shells of increasing temperature, and all emission lines were produced by collisional excitation and spontaneous radiative decay within restricted spatial regions.

As this picture of spherical symmetry broke down, the differential emission measure was developed to keep the same 1-dimensional simplification to temperature but account for the spatial ambiguity of a photon's origin (see Mariska 1992 for a detailed overview of the method's history). The differential emission measure uses a similar integral expression over a limited temperature range to estimate the density and temperature environment of ions emitting an observed line, allowing one to then use those environmental conditions to estimate the flux from emission lines that cannot be observed but should be emitted by the same parcel of plasma. When UV detector technology was in its infancy and instruments had poor flux calibration, differing by factors of $\gtrsim 2$ in different wavelength regimes, the DEM could be used to estimate the subset of solar emission line fluxes with poor data from other lines that were thought to have more accurate and precise data (Warren

et al., 1998). While the state of solar EUV data has improved, the opacity of the interstellar medium and low sensitivities of previous and current EUV-capable observatories present a similar spectral synthesis problem for distant stars. Variations of the DEM have been applied to other stars like AU Mic by Pagano et al. (2000), α Centauri A and B by Ayres (2014), and HD 209458 by Louden et al. (2017) to infer the EUV flux from these stars. Sanz-Forcada et al. (2011) developed scaling relations between X-ray and EUV fluxes by applying the DEM method to a large sample of stars, but the paper's sample had few M dwarfs and lacked enough UV data to constrain the lower temperature end of the DEM for most of their stars.

In this chapter we characterize our uncertainties in fitting the DEM and propagate them to our predictions of the EUV flux from M dwarfs. Our physical assumptions and setup are similar to the methods of Warren et al. (1998) to model the EUV irradiance of the Sun, described in Section §2.3. The specifics of our implementation are described in Section §2.4 and we test our method against data from the Sun in Section §2.5. In Section §2.6 we apply our method to AU Mic, a $\sim 10-20$ Myr old M1 star at a distance of 9.979 pc (MacGregor et al., 2013; Plavchan et al., 2020). We compare our DEMs of the Sun and AU Mic to previous DEMs published in the literature and available in the `CHIANTI` atomic database (Dere et al., 1997; Del Zanna et al., 2015) in Section §2.7.

We compare our predicted spectra for the Sun and AU Mic to data in detail in Section §2.8 and in Section §2.9 we apply our method to different case studies: GJ 832, a planet-hosting M2 V that has predicted EUV fluxes from Linsky et al. (2014) and semi-empirical models from both Fontenla et al. (2016) and Peacock et al. (2019b); Barnard's Star, a $\sim$ 10 Gyr old M4 with a candidate planet (Ribas et al., 2018), with contemporaneous X-ray and FUV data during quiescence and a flare (France et al., 2020b); and TRAPPIST-1, an ultracool dwarf which hosts at least seven planets (Gillon et al., 2017) and tests our ability to fit the DEM in an extremely low S/N regime (Wilson et al., 2021). Our work shows that with *Hubble Space Telescope* (*Hubble* or *HST*) measurements of a few FUV emission line fluxes and a coarse X-ray spectrum from *Chandra* or *XMM-Newton*, we can estimate the EUV spectrum with meaningful uncertainties for any star whose EUV flux is dominated by emission lines from the optically thin regions of the star's upper atmosphere.

2.3 Differential Emission Measure

The following description of the DEM is adapted from Warren et al. (1998). Many other formulations of the DEM and similar techniques exist, and Mariska (1992) explains them in more detail. Given an optically thin plasma in a collisionally dominated time-independent equilibrium with negligible collisional de-excitation, the radiance of a wavelength transition is given by

$$I_{ul} = \frac{1}{4\pi} \int_{\text{line-of-sight}} n_u A_{ul} \frac{hc}{\lambda_{ul}} \, ds \; [\text{erg}\,\text{s}^{-1}\,\text{cm}^{-2}\,\text{sr}^{-1}], \tag{2.1}$$

where ul signifies a transition from an upper state u to a lower state l, A_{ul} is the Einstein rate coefficient of the transition, λ_{ul} is the wavelength of the transition, h is Planck's constant, and c is the speed of light in a vacuum. This quantity is not a spectral density because it captures all of the emission from the spontaneous radiative decay without describing a line profile. We can rewrite this integral as

$$I_{ul} = \int_T G_{ul}(T) \cdot \Psi(T) \, dT \; [\text{erg}\,\text{s}^{-1}\,\text{cm}^{-2}\,\text{sr}^{-1}], \tag{2.2}$$

where

$$G_{ul}(T) = \frac{n_u}{n_{\text{ion}}} \frac{n_{\text{ion}}}{n_{\text{element}}} \frac{n_{\text{element}}}{n_{\text{H}}} \frac{1}{n_e} \frac{A_{ul} hc}{4\pi\lambda_{ul}} \; [\text{erg}\,\text{s}^{-1}\,\text{cm}^{3}\,\text{sr}^{-1}] \tag{2.3}$$

is the transition's emissivity contribution function and the differential emission measure is

$$\Psi(T) = n_e n_{\text{H}} \frac{ds}{dT} \; [\text{cm}^{-5}\,\text{K}^{-1}]. \tag{2.4}$$

$G_{ul}(T)$, the emissivity contribution function, describes the volume integrated power of a parcel of gas as a function of temperature. The function can be computed with a few ingredients: a stellar abundance to give us the ratio of the number density of any particular element's atoms to the number density of hydrogen atoms $\frac{n_{\text{element}}}{n_{\text{H}}}$, the assumption of collisionally dominated equilibrium

(i.e. coronal equilibrium) and `CHIANTI` to give us the population fraction of any particular upper state of an ion $\frac{n_u}{n_{\rm ion}}$ and the population fraction of each ion per element $\frac{n_{\rm ion}}{n_{\rm element}}$, an assumed local density n_e, and laboratory measurements or theoretical calculations of the atomic data A_{ul} and λ_{ul}. We follow Del Zanna et al. (2002) in using a constant electron pressure P_e to define $n_e(T) = \frac{P_e}{k_B T}$, where k_B is the Boltzmann constant. This single pressure will not be applicable to the entire temperature domain, but errors in the $G(T)$ function can be partially compensated for by the $\Psi(T)$ function as long as the errors are largely a function of temperature and do not vary significantly across lines formed at the same temperature.

The differential emission measure, $\Psi(T)$, describes the density and temperature structure along the line of sight, common to all transitions we observe from the chromosphere, transition region, and corona. Under our assumptions that the ions are predominantly populated by collisions and depopulated by spontaneous emission, the flux observed is proportional to the collision rate. The differential emission measure resembles a reaction rate, $n_e \cdot n_{\rm H}$, weighted by $\frac{ds}{dT}$ which measures how much of the path length s is at a temperature T. In emission measure studies of other stars, a volume emission measure is commonly employed that predicts a flux and includes factors of the stellar radius and solid angle filling factor of the emitting plasma. We adopt the line-of-sight approach to be able to compare the DEMs of very different stars to each other and to solar surface features.

For each emission line there is a formation temperature T_f that maximizes the product $G_{ul}(T) \cdot \Psi(T)$, and since the emissivity function $G_{ul}(T)$ tends to be very narrowly peaked, the bulk of of the observed line flux is emitted by plasma at $\approx T_f$. By measuring the observed line intensities of transitions with a known $G_{ul}(T)$, we can constrain the value of $\Psi(T)$ within the vicinity of the lines' formation temperatures T_f. Amassing a list of observable transitions over a sufficiently wide range of T_f allows us to fit for the parameters of an assumed functional form describing $\Psi(T)$ across the temperature domain of the upper stellar atmosphere. With $\Psi(T)$ in hand and atomic data to construct $G_{ul}(T)$ for the transitions we have not observed but seek to estimate, we can reconstruct the optically thin emission of the chromosphere, transition region, and corona. With the exception

of the recombination continua addressed in Section §2.5.3, optically thin emission lines contribute the majority of the EUV flux from an M dwarf.

2.4 Implementation

We use `CHIANTI 8.0.7` (Dere et al., 1997; Del Zanna et al., 2015) to calculate the $G_{ul}(T)$ functions for all the transitions in the database assuming the elements have a solar coronal abundance (Schmelz et al., 2012). We calculate these emissivity contribution functions across a temperature range from 10^4 to 10^8 K for multiple assumed electron pressures ranging from $P_e = 10^{12}$ to 10^{25} k_B cm^{-3} K. The majority of coronal emission lines are not strongly sensitive to density, but we test the variation in the predicted flux as a function of the P_e used to calculate $G_{ul}(T)$ in Section §2.5.1. We assume that $\Psi(T)$ is well-described by

$$\log_{10} \Psi(T) = \sum_{n=0}^{5} c_n \mathbf{T_n} \left(\frac{\log_{10} T - 6}{2} \right) \tag{2.5}$$

where $\mathbf{T_n}(x)$ are the Chebyshev polynomials of the first kind, and their argument is shifted and scaled to transform the domain to the interval $[-1, 1]$. We use the Chebyshev polynomials following the previous work of Louden et al. (2017) and because they form an orthonormal basis. Given the coefficients c_n, and the list of emissivity contribution functions $G_{ul}(T)$, we can generate a full spectrum by summing the contribution functions of all emission lines within a wavelength bin centered on a wavelength λ with a width $\Delta\lambda$ to get a wavelength-specific contribution function

$$G_\lambda(T) = \sum_{\text{transitions}} G_{ul}(T) \textbf{ if } [|\lambda_{ul} - \lambda| \leq \Delta\lambda] \,. \tag{2.6}$$

We then scale the temperature integral of Equation 2.2 to predict the observed flux density in each wavelength bin, assuming the bin is wide enough to contain the entire line profile

$$F_\lambda = \frac{\pi}{\Delta\lambda} \left(\frac{R_\star^2}{d^2} \right) \int_T G_\lambda(T) \cdot \Psi(T) \, dT \; [\text{erg s}^{-1} \text{ cm}^{-2} \text{ Å}]. \tag{2.7}$$

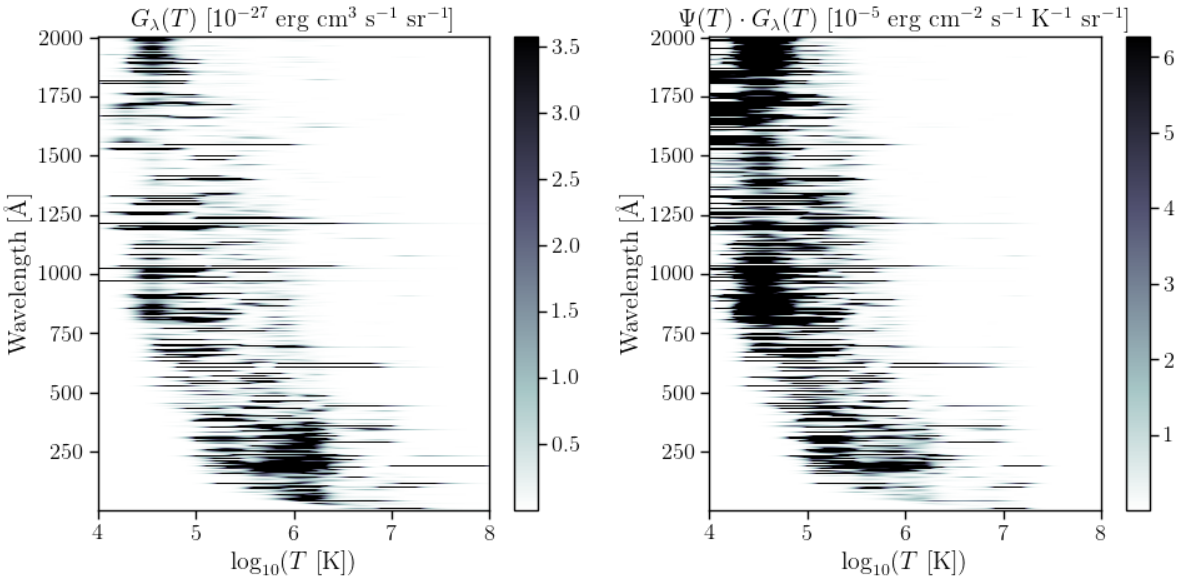

Figure 2.1: The left panel is a heatmap where the shading represents the value of the emissivity contribution function $G_\lambda(T)$ as a function of temperature along the horizontal axis and as a function of wavelength along the vertical axis. This matrix is generated from the `CHIANTI` atomic database by specifying the atomic abundances and the electron density as a function of temperature $n_e(T)$. The right panel multiplies the $G_\lambda(T)$ matrix by the DEM, $\Psi(T)$, of the Sun shown as a blue line in Figure 2.6. The colorbars of both panels are cut off at the 60^{th} and 95^{th} percentiles to highlight the strongest lines. While the $G_\lambda(T)$ matrix shows the atomic data, the right panel represents the temperature integrand for which lines are actually emitted by stars. EUV lines are largely formed at temperatures between 10^5 and $10^{6.5}$ K, requiring FUV measurements to constrain the low temperature end and X-ray measurements and/or coronal FUV semi-forbidden transitions of highly ionized iron to constrain the high temperature end.

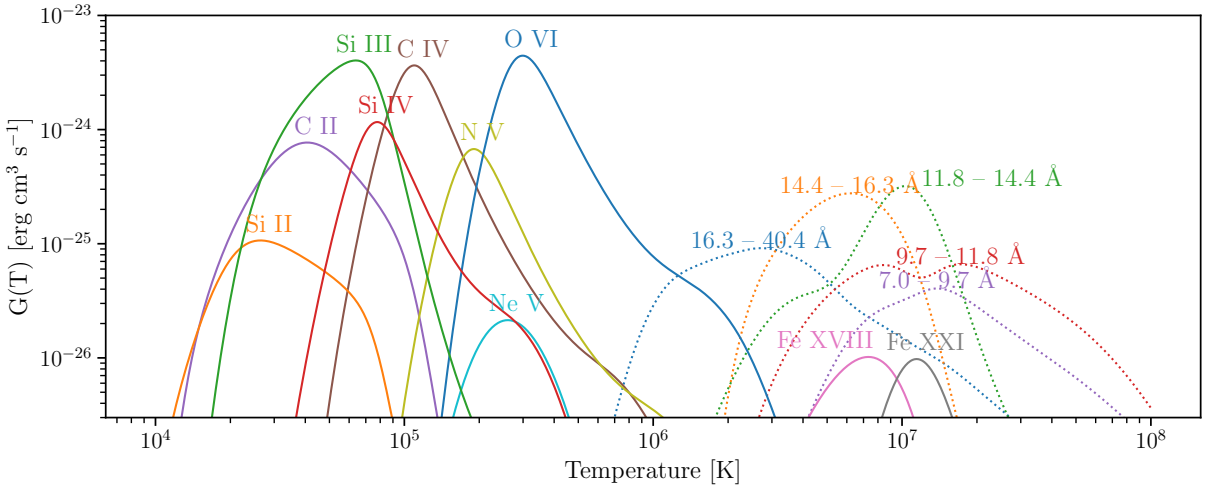

Figure 2.2: A sample of the emissivity functions $G_{ul}(T)$ and $G_\lambda(T)$ described in Sections §2.3 and §2.4. The solid lines show the summed emissivity functions for some of the strongest transitions of the labeled ion observable by *Hubble* with STIS and COS. The dotted lines show the summed emissivity functions $G_\lambda(T)$ for typical wavelength bins in a *Chandra* spectrum of an M dwarf, adding up the $G_{ul}(T)$ functions of all emission lines that fall within the wavelength bin. The ion emissivities are constructed by adding together the emissivities of all lines emitted by that ion, for example both lines of the N V 1239/1243 doublet. The X-ray wavelength bin emissivities are constructed similarly by adding together the emissivities of lines from multiple ions that are emitted at similar wavelengths. This lets us use coarser resolution X-ray spectra for fainter stars but weakens the temperature specificity of individual flux measurements. Note the contribution function for a semi-forbidden transition of Fe XXI at 1354 Å with a formation temperature at $\sim 10^7$ K. Its emissivity peaks at a factor of 10^3 times less than other typically observable FUV lines, making it unobservable for most quiescent M dwarfs. Observing or obtaining an upper limit for the flux of this line provides an additional constraint on $\Psi(T)$ at high temperatures.

The scaling factor assumes that the solid angle emitting the flux is $\approx \pi \left(\frac{R_\star}{d}\right)^2$ steradians, which is approximate because the corona extends beyond the stellar radius. We create a matrix of $G_\lambda(T)$ with the wavelength axis at a constant resolving power $R = \frac{\lambda}{\Delta\lambda} = 500$ between 1 and 2000 Å, and the temperature axis as 2000 logarithmically spaced points between 10^4 and 10^8 K (see Figure 2.1). Fitting for the coefficients c_n and combining the $\Psi(T)$ model with this matrix allows us to generate a high-resolution spectrum, but since the DEM makes no prescription for line shape, the line profiles are all Dirac-δ functions, which is why we then divide by the wavelength bin width $\Delta\lambda$ to get the observed flux density. Comparing this model to a real stellar spectrum is only reasonable at a low enough resolution such that the entirety of the line profile is contained within each resolution element. The $R = \frac{\Delta\lambda}{\lambda} = 500$ $G_\lambda(T)$ matrix can be downsampled to whatever resolution is required to contain the line widths of any spectral data used for comparison.

By combining either the $G_{ul}(T)$ functions or the $G_\lambda(T)$ matrix with the polynomial coefficients c_n, we have a generative model for a list of integrated line fluxes or a low-resolution spectrum respectively. To get a usefully constrained model, we need data that covers the full temperature domain. Figure 2.2 shows the $G_\lambda(T)$ functions for the wavelength bins of a typical *Chandra* spectrum, where each bin peaks at a slightly different temperature but spans 10^6 and $10^{7.5}$ K, and the $G_{ul}(T)$ functions for the strongest optically thin FUV lines accessible in a *Space Telescope Imaging Spectrograph* (STIS) and *Cosmic Origins Spectrograph* (COS) spectrum from *Hubble*. There is significant overlap in the contribution functions of these transitions near 10^5 K, but they spread out far enough to constrain $\Psi(T)$ between 10^4 and $10^{5.5}$ K. Each line flux measurement can be used to derive an average value of $\Psi(T)$ near the formation temperature T_f of the transition

$$\overline{\Psi}(T_f) = \frac{F_{\text{line}}}{\pi \left(\frac{R_\star^2}{d^2}\right) \int_T G_{ul}(T) dT} \tag{2.8}$$

and any individual wavelength bin's flux density can provide a similar constraint by substituting $G_\lambda(T)$ in for $G_{ul}(T)$ and dividing by the wavelength bin width $\Delta\lambda$. We do not fit to these averages because we can directly compare our predicted fluxes to the data, but the averages are useful for

visualizing how an individual flux measurement constrains the DEM.

Using the affine-invariant Markov Chain Monte Carlo sampler implemented in the Python package `emcee` (Foreman-Mackey et al., 2013), we fit the coefficients c_n (see Equation 2.5) using a combination of the available X-ray data and integrated FUV line fluxes. Since the uncertainties on the emissivities are unknown and we have little a priori information on how to characterize the systematic uncertainties associated with this method, we assume that the variance is boosted by a scaled multiple of the predicted flux, making our log-likelihood

$$\ln \mathcal{L} = \sum_i \ln \left(\frac{1}{\sqrt{2\pi \left(\sigma_{y_i}^2 + (s \cdot f(x_i))^2 \right)}} \right) - \left(\frac{y_i - f(x_i)}{2\sqrt{\sigma_{y_i}^2 + (s \cdot f(x_i))^2}} \right)^2 \tag{2.9}$$

where $f(x_i)$ is the model prediction, y_i is the data, σ_{y_i} is the Gaussian uncertainty of the data, and s is the free parameter that characterizes these unknown systematic uncertainties (which are assumed to be independent of the data and temperature). Some contributions to s are likely to be errors in stellar parameters like the stellar abundance, deviations of level populations from true collisional equilibrium or variations in the relative abundances along the line of sight, the departure from being perfectly optically thin $\tau = 0$, and the spatial inhomogeneity of the emitting plasma. This form of the likelihood is independent of the two types of data described above, allowing us to mix together combinations of line fluxes and spectra in different wavelength regimes, so long as we ensure that these do not overlap to count the same data twice.

We incorporate Bayesian priors on individual parameters to modify the likelihood evaluated in Equation 2.9. We sample $\log_{10}(s)$ uniformly between -2 and 2. The mean value of the DEM is set by c_0, which is sampled uniformly between 20 to 26 and then exponentially cut off beyond those bounds. These boundary values were chosen to limit the DEM to physical expectations for $10^5 \lesssim n_e \lesssim 10^{17}$ cm^{-3}, and path-length $10^8 \lesssim ds \lesssim 10^{11}$ cm. The remaining coefficients c_n are sampled uniformly within the bounds ± 100, and then we also require that the base-10 logarithm of the final polynomial be positive at $\log_{10} T = 6$ to prevent unphysically small DEMs and that the derivative be negative at the lower bound $T = 10^4$ K to reflect the higher amount of material in

the photosphere compared to the chromosphere. These priors extend generously beyond physically realistic DEM shapes, for example they do not require the DEM to go to 0 at high temperatures, allowing for an infinitely extended corona. Data constrain the parameter distributions to factors of a few at most, with the $s-$factor systematic uncertainty typically restricted to the interval $0.1 < s < 1$.

2.5 Testing the DEM Method Against the Sun

To test our implementation of the DEM on solar data, we use the Solar Irradiance Reference Spectra (SIRS) published by Woods et al. (2009). This is a disk-integrated spectrum of the quiescent Sun assembled from measurements collected during the 2008 minimum of the solar activity cycle at 1 Å resolution. Referring to a list of the lines used for the DEM fitting in Warren et al. (1998), and making a point to select the FUV lines most likely to be detected in *Hubble* observations of M dwarfs, listed in Table 2.1, we measure their fluxes in this spectrum by subtracting the continuum and integrating line profiles. Then we selected the X-ray data between 5 and 50 Å, comparable to the regions observed by the *Chandra-X-ray Observatory* and *XMM-Newton*, and left the spectrum at its original resolution of 1 Å wavelength bins, $R = \frac{\lambda}{\Delta\lambda} \leq 50$. This combination of line fluxes and an X-ray spectrum is the same type of data we use for M dwarfs discussed later in this work. Table 2.1 also lists the integrated fluxes of EUV lines measured from the Woods et al. (2009) spectrum, used in the test described in Section §2.5.3. The SIRS did not provide error bars, but we assigned errors such that we had three versions of the data with S/N = 1, 10, and 100 to test the sensitivity of the fitting to S/N. The true errors vary across the observations from different instruments and wavelength ranges assembled by Woods et al. (2009), but never exceed 10% at instrument native resolutions which are much finer than the 1 Å bins used here.

Table 2.1. Integrated fluxes of optically thin lines measured in the Solar Irradiance Reference Spectrum (Woods et al., 2009) compared to the DEM predictions.

Ion	Wavelengths [Å]	$\log_{10} T_f$ $\log_{10}([\mathrm{K}])$	Observed Flux $[10^{-2}\ \mathrm{erg\,s^{-1}\,cm^{-2}}]$	FUV/X-ray $[10^{-2}\ \mathrm{erg\,s^{-1}\,cm^{-2}}]$	No Anomalous Ions $[10^{-2}\ \mathrm{erg\,s^{-1}\,cm^{-2}}]$
C II	1335.7	4.4	14.9	11.0	11.9
C III	1175.7	4.8	4.73	7.78	3.36
C IV [a]	1548.2, 1550.7	5.0	12.0	7.95	2.17
N V [a]	1238.8, 1242.8	5.3	1.56	1.56	0.419
Ne VII[b]	465.2	5.7	1.47	3.07	1.60
Ne VIII[b]	770.4, 780.3	5.8	1.80	2.83	1.92
O III[b]	508.2, 525.8, 599.6, 703.9	4.9	2.71	6.63	2.09
O IV[b]	554.5, 787.7, 790.2	5.2	5.85	19.9	4.95
O V[b]	629.7, 760.4	5.4	6.47	21.4	5.77
Si III	1206.5	4.5	6.83	22.6	18.4
Si IV[a]	1393.8	4.9	3.72	2.24	0.827
Si XII[b]	499.4	6.3	0.699	0.921	1.03

Note. — In cases where multiple transitions are listed for the same ion, the reported flux is the summed flux across all listed transitions.

[a]These FUV transitions were not used to fit the "Fit with EUV Lines and without Anomalous Ions" model shown in Figure 2.6 as a red solid line.

[b]These EUV transitions were used to fit the "'Fit with EUV Lines and without Anomalous Ions" model shown in Figure 2.6 as a red solid line.

2.5.1 Pressure Sensitivity

Across this broad range of temperatures, no single electron density or pressure will accurately describe the environmental conditions of the plasma emitting the observed flux we are using to fit the DEM or the unobserved EUV flux we are trying to predict. However we must assume some function for the electron density $n_e(T)$ to calculate emissivities if we want to fit the DEM at all. Updating the emissivity calculation iteratively would be computationally prohibitive and still fail to accurately describe detailed non-equilibrium physics. By generating multiple emissivity matrices across a broad range of electron pressures, $P_e = 10^{12}$ to 10^{25} k_B cm^{-3} K, and fitting a DEM to the solar data with each matrix, we test the sensitivity of the DEM shape and calculate the variation in the predicted EUV flux as a function of assumed pressure. Figure 2.3 shows a representative sample of these DEMs, which vary only slightly for pressures lower than 10^{20} k_B cm^{-3} K and are consistent with each other to within 1σ variations of the DEM shape. The horizontal lines are the average $\overline{\Psi}(T_f)$ values. To test if any particular model is a statistically significant improvement over the others, we compare the models' values of the Bayesian Information Criterion (BIC, Schwarz 1978). Kass & Raftery (1995) demonstrates that the BIC is related to the natural logarithm of the Bayes factor, such that a $\Delta BIC = 1$ implies the more negative model is e times more likely than the higher one. The BIC is evaluated with the equation

$$\mathrm{BIC} = k\ln(n) - 2\ln(\hat{\mathcal{L}}) \tag{2.10}$$

where k is the number of model parameters, n is the number of datapoints, and $\hat{\mathcal{L}}$ is the maximum-likelihood of the model. This criterion penalizes a higher number of parameters, and the model significance increases as the BIC decreases. All models in this comparison have the same number of parameters, but we also use the BIC later in Section §2.5.5 to test our method's sensitivity to polynomial degree.

Table 2.2 compares each pressure model's BIC, estimated systematic uncertainty characterized by the s-factor, and EUV flux integrated from 100 to 912 Å. In the middle of our pressure range, from 10^{17} to 10^{20} k_B cm^{-3} K, the predicted integrated fluxes are consistent with each other

to within 1σ, but the BIC clearly favors the 10^{19} model. We adopt the $P_e = 10^{19}$ k_B cm^{-3} K emissivity matrix for other tests of the Sun DEM model moving forward. At pressures higher than 10^{21} k_B cm^{-3} K, the DEM shape and predicted fluxes change drastically, likely because the plasma is optically thick and collisional de-excitation can no longer be ignored. The base of the solar chromosphere is at a pressure of $\sim 10^{20}$ k_B cm^{-3} K (Mariska, 1992), so a model DEM that assumes the entire upper atmosphere is at photospheric pressure is bound to be unphysical.

For all other stars, we adopt the same approach of fitting the star's DEM with each pressure separately and choosing the model with the best likelihood. We caution that it is unphysical to interpret these "best" pressures as representative of a specific region in the stellar atmosphere, and that they should be seen as the most useful average for implementing the DEM and nothing more. Future work could involve testing the DEM with temperature-pressure profiles from stellar atmosphere models to see if this improves the accuracy and precision of the estimated spectrum.

2.5.2 Sensitivity to S/N

Figure 2.4 compares our DEMs fit to the Sun's data with S/N = 1, 10, and 100. For higher S/N models, the variance is dominated by the uncertainty on the predicted flux, parameterized by the $s-$factor and independent of the DEM's shape, so changing the S/N of the data used to fit the DEM has little consequence. At S/N = 1, the data uncertainty dominates and the model percentile ranges shift dramatically, with no overlap with the higher S/N models until the higher temperatures constrained by many X-ray fluxes. As mentioned earlier, s is a measure of our average temperature-independent systematic uncertainty that combines the uncertainties on the emissivities with anything else intrinsic to our method's assumptions and approximations. Figure 2.5 shows us that $s = 0.63$ in the solar case with S/N= 100. This indicates that we should assume the systematic uncertainty on any predicted line flux is roughly 60% of the predicted value. Some of the systematic uncertainty may be attributed to fact that the Woods et al. (2009) spectrum combines observations of quiescence from different instruments taken at different times, which is a problem that will affect most stellar observations and needs to be accounted for in modelling uncertainties.

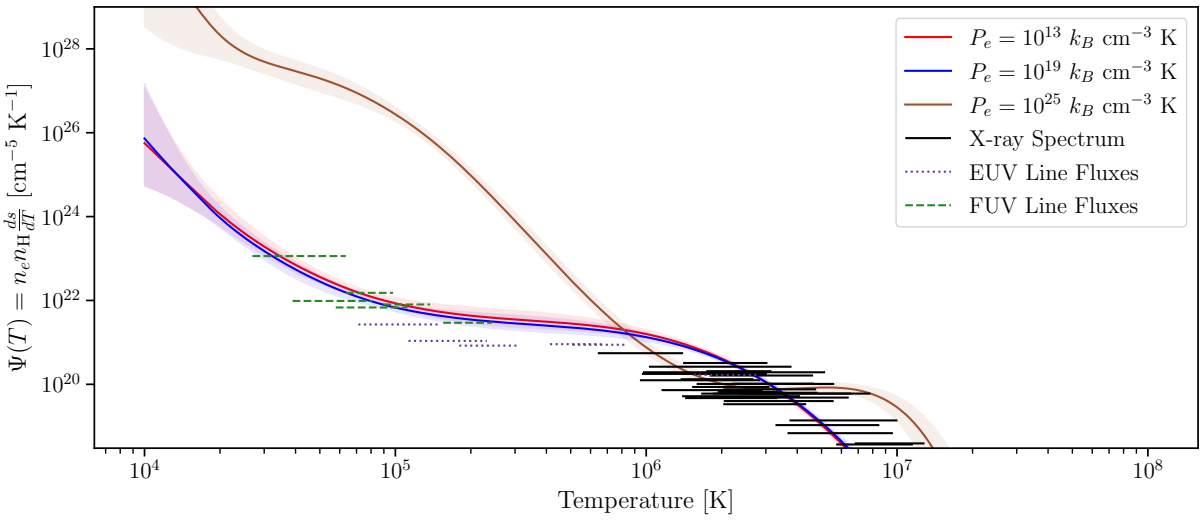

Figure 2.3: The DEMs of the Sun fit to the same data, a combination of FUV emission lines and X-ray spectra, but with emissivity functions calculated at different electron pressures P_e. The horizontal bars represent constraints on the average DEM value $\overline{\Psi}(T_f)$ in the vicinity imposed by the emissivity functions $G(T)$ for ion line fluxes or wavelength bins as described in Section §2.4, with the horizontal extent of the lines representing the full width at half maximum for the emissivity function. These constraints transformed from a flux to an average DEM value are only approximately illustrative of the fit quality. For a true comparison of the DEM prediction to the data used to fit the model, see plots of the predicted line fluxes and X-ray spectra in Figures 2.7 and 2.8 respectively. The solid lines represent the median DEM value as a function of temperature from the posterior samples for $\Psi(T)$ while the shaded region encloses the 16^{th} to 84^{th} percentile values of the DEM. The red, blue, and brown models correspond to DEM models with emissivities evaluted at electron pressures $P_e = 10^{13}$, 10^{19}, and $10^{25}\ k_B\ \mathrm{cm}^{-3}\ \mathrm{K}$ respectively. The green dashed bars and black solid bars represent the flux constraints from the FUV lines and X-ray spectra used to fit these models, while the dotted purple bars represent the flux constraints from EUV lines listed in Table 2.1 but were not used to fit these models. For visualizing these constraints we use the emissivities calculated by assuming the electron pressure $P_e = 10^{19}\ k_B\ \mathrm{cm}^{-3}$.

Table 2.2. The Bayesian Information Criterion (BIC) for models using different electron pressures evaluated against the FUV line fluxes and the X-ray spectrum used to fit the model.

Log Electron Pressure $\log_{10} P_e$ $\log_{10}\left([k_B\ \mathrm{cm}^{-3}\ \mathrm{K}]\right)$	BIC —	Integrated EUV Flux [ergs s^{-1} cm^{-2}]	$\log_{10} s_{\mathcal{L}_{\max}}$ —	$\log_{10} s$ —
12	−447.8	$4.9^{+4.2}_{3.4}$	−0.2090	$-0.1671^{+0.0739}_{-0.0632}$
13	−448.6	$4.6^{+4.3}_{-3.1}$	−0.1852	$-0.1699^{+0.0731}_{-0.0626}$
14	−450.1	$4.3^{+4.5}_{-2.8}$	−0.1929	$-0.1757^{+0.0735}_{-0.0619}$
15	−449.8	$4.5^{+4.2}_{-3.1}$	−0.2166	$-0.1741^{+0.0726}_{-0.0624}$
16	−452.3	$4.1^{+3.6}_{-2.8}$	−0.2249	$-0.1783^{+0.0733}_{-0.0631}$
17	−456.2	$3.6^{+3.5}_{-2.3}$	−0.2137	$-0.1909^{+0.0720}_{-0.0619}$
18	−460.7	$3.5^{+3.3}_{-2.1}$	−0.2311	$-0.2019^{+0.0697}_{-0.0615}$
19	−464.7	$3.5^{+3.1}_{-2.1}$	−0.2424	$-0.2178^{+0.0692}_{-0.0596}$
20	−463.3	$3.8^{+3.3}_{-2.4}$	−0.2515	$-0.2125^{+0.0709}_{-0.0603}$
21	−455.1	$6.2^{+6.1}_{-4.1}$	−0.2108	$-0.1804^{+0.0729}_{-0.0623}$
22	−426.2	20^{+20}_{-17}	−0.0881	$-0.0591^{+0.0873}_{-0.0725}$
23	−376.7	59^{+94}_{-59}	0.0828	$0.1254^{+0.1199}_{-0.0962}$
24	−367.6	140^{+220}_{-140}	−0.0113	$0.0413^{+0.1069}_{-0.0826}$
25	−364.1	200^{+370}_{-200}	0.0244	$0.0473^{+0.1067}_{-0.0809}$

Note. — The BIC penalizes model parameters by $k \ln(n)$ where k is the number of parameters being fit and n is the number of data points being fit to. An increasingly negative BIC indicates a better fit. In this case, the most preferred models are the $P_e = 10^{19}$ and 10^{20} k_B cm^{-3} K models respectively. We also show the value of $\log_{10} s$ for the maximum likelihood sample from the posterior and the median $\pm 1\sigma$ confidence interval for $\log_{10} s$.

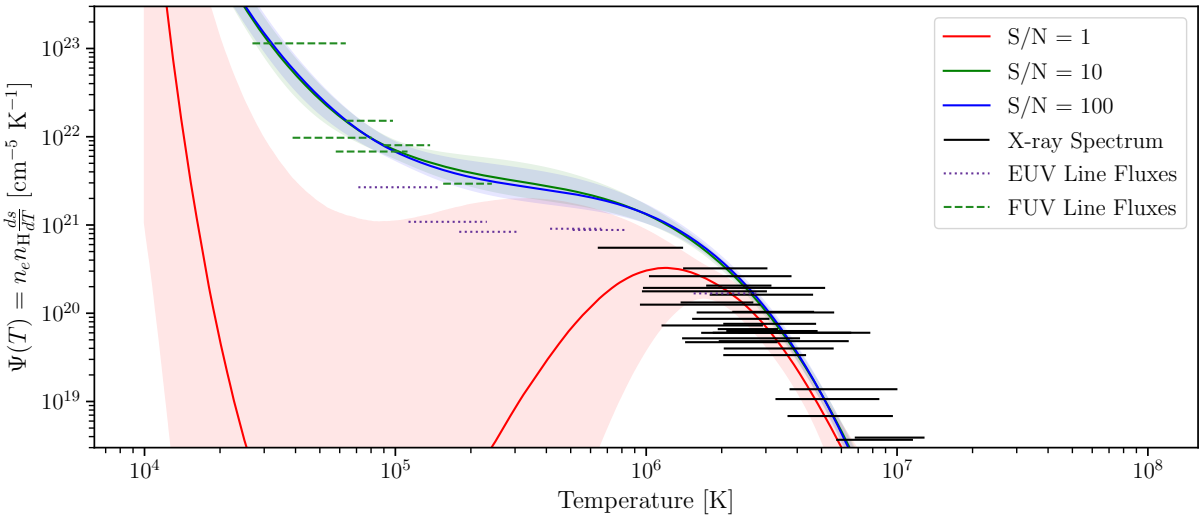

Figure 2.4: A comparison of fitting the DEM to the same data, a combination of FUV line fluxes and X-ray spectra from the Woods et al. (2009) quiescent Sun spectrum, but with different errors assigned to vary the signal-to-noise ratio (S/N). As shown before in Figure 2.3, the solid lines and shaded regions represent the different DEM models while the horizontal bars represent constraints imposed by the flux measurements. The red, green, and blue models represent fitting the DEM at S/N values of 1, 10, and 100 respectively. As shown previously in Figure 2.3, the green dashed bars and black solid bars represent the flux constraints from the FUV lines and X-ray spectra used to fit these models. The dotted purple bars represent the flux constraints from EUV lines listed in Table 2.1 and which were not used to fit these models.

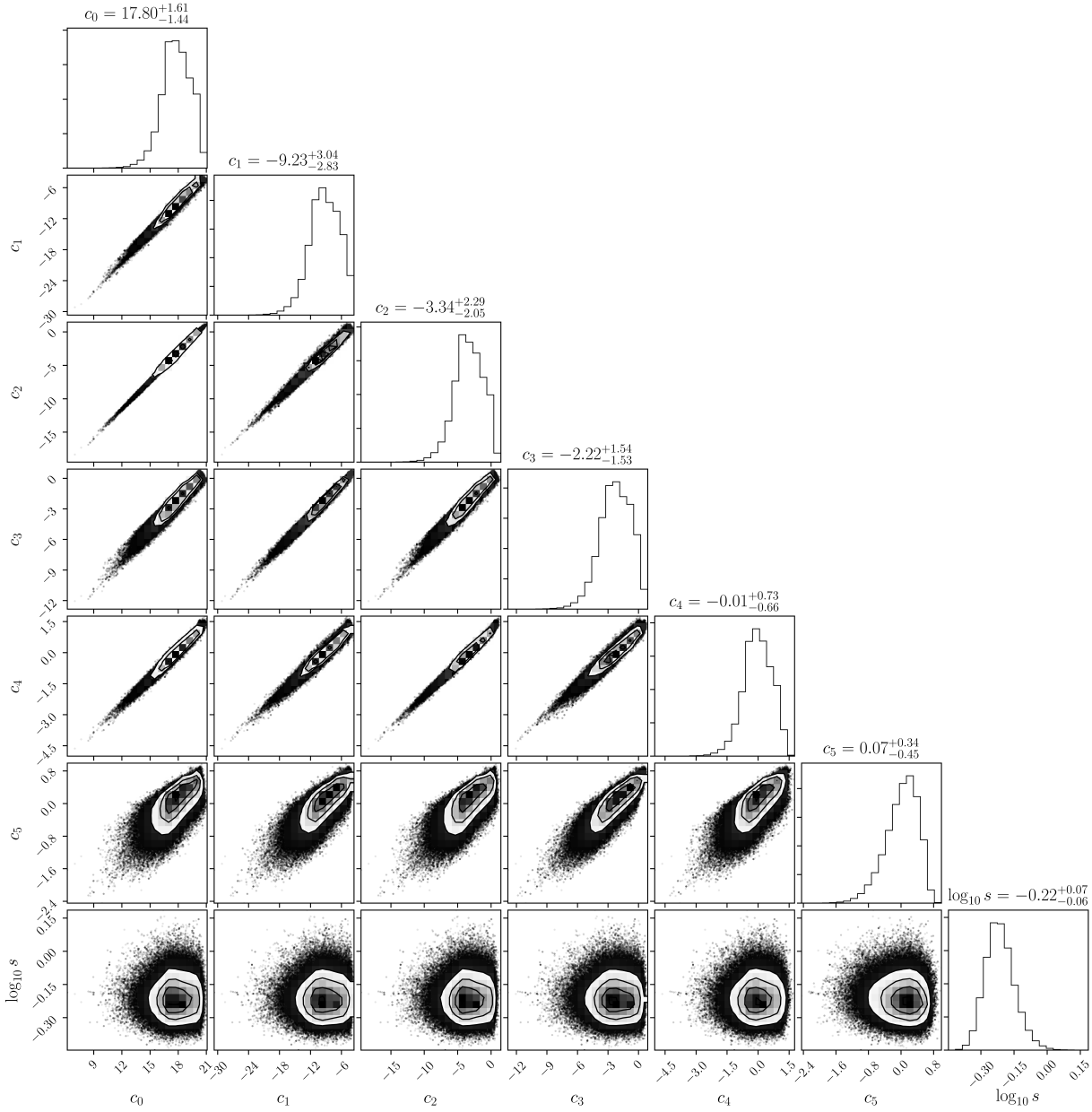

Figure 2.5: The corner plot for the parameter distributions when fitting the Sun at S/N = 100 shows the median value of $\log_{10} s$ to be $-0.22^{+0.07}_{-0.06}$ which translates to a model uncertainty of 60% for the predicted flux. This uncertainty dominates the fitting over the uncertainty associated with the data itself.

2.5.3 Including EUV Data in the Fitting and Excluding Anomalous Ions

With the Sun, we can refer to the EUV lines observed by Woods et al. (2009) in the SIRS, allowing us to see how much information we are losing about the DEM in the stellar case where EUV data is not available. Including the EUV lines gives us more temperature coverage and allows us to exclude three ions from the Na-like and Li-like isolectronic sequences: N V, C IV, and Si IV. Del Zanna et al. (2002) showed that a DEM informed by these ions significantly overpredicts the flux of other transitions because of an anomaly in the `CHIANTI` ionization equilibrium calculations for these isoelectronic sequences compared to other ions for the same plasma environmental conditions. The factor of discrepancy is not constant across all transitions and densities, so it cannot be corrected for by a consistent known number. This discrepancy constitutes a significant systematic uncertainty that cannot be avoided when fitting the DEM to faint stars with few strong measurable lines that are not from these anomalous ions. Including line fluxes from multiple transitions of other ions can help mitigate the influence of the anomalous ions, but upper limits can still help if the star is too faint to measure these lines.

To help characterize the magnitude of these discrepancies, we include EUV lines from 7 ions that are currently unobservable for our M dwarf sample of interest, listed in Table 2.1, and drop the anomalous ions (retaining some of the FUV lines and the X-ray spectrum) when fitting the model labeled "Fit with EUV Lines and without Anomalous Ions" in Figures 2.6, 2.7, 2.8, and 2.9. This new DEM model shifts down by a factor of ~ 5 in between 10^5 and 10^6 K (see Figure 2.6) to match the EUV line fluxes (see Figure 2.7) that are not informing our stellar-analogous DEM. The DEMs agree with each other at the higher temperatures constrained by the X-ray spectra resulting in nearly identical predictions in that spectral regime (see Figures 2.6 and 2.8). The predicted line fluxes from both models are compared to the data in Table 2.1 and Figure 2.7, and highlight the problem of the anomalous ions. The model without EUV lines and including the anomalous ions predicts the FUV fluxes reasonably well, adopting a compromise position between FUV lines formed at similar temperatures that have discrepant DEM constraints (see Figure 2.6),

but this compromise still overestimates the flux of the EUV lines by up to a factor of 5. When applying the DEM to M dwarfs without EUV data, we include the ions with anomalous `CHIANTI` emissivities because these are the strongest lines available and we cannot afford to simply exclude them. Measuring upper limits for the fluxes of other transitions formed at similar temperatures can mitigate the influence of the anomalous ions when combined with the $s-$factor uncertainty, as demonstrated in our modeling of AU Mic in section 2.6.

In Figure 2.7, the error bars associated with the plotted data point incorporate both the posterior distributions of the DEM shape and the $s-$factor uncertainty of the "Fit with EUV Lines and without Anomalous Ions" model. We do this by drawing randomly from the posterior sample of the MCMC fitting to generate a sample $\Psi(T)$ using the Chebyshev coefficients c_n (see Equation 2.5) with an associated $s-$factor. The $\Psi(T)$ is combined with $G(T)$ to predict the flux of an observed data point, y_i, giving a model flux $f(x_i)$. Multiple sample draws in this fashion would only represent the uncertainty associated with the DEM shape and exclude the $s-$factor. To include the model-intrinsic uncertainty, we draw randomly from the Gaussian distribution $\mathcal{N}(\mu = f(x_i), \sigma = s \cdot f(x_i))$ and record the prediction from the flux distribution parameterized by a single MCMC posterior sample. This process is executed with $N = 5 \times 10^4$ draws from the model parameters' posterior distribution to describe the full range of the model's predicted flux. The errorbar for a particular datapoint represents the width of the 16^{th} to 84^{th} percentile interval for this distribution built up of random draws. Figures 2.8 and 2.9 show the uncertainties of both models as errorbars on the models' respective predicted spectra using the same method. The $s-$factor dominating the uncertainty results in errorbars that scale according to the magnitude of the flux predicted by the model.

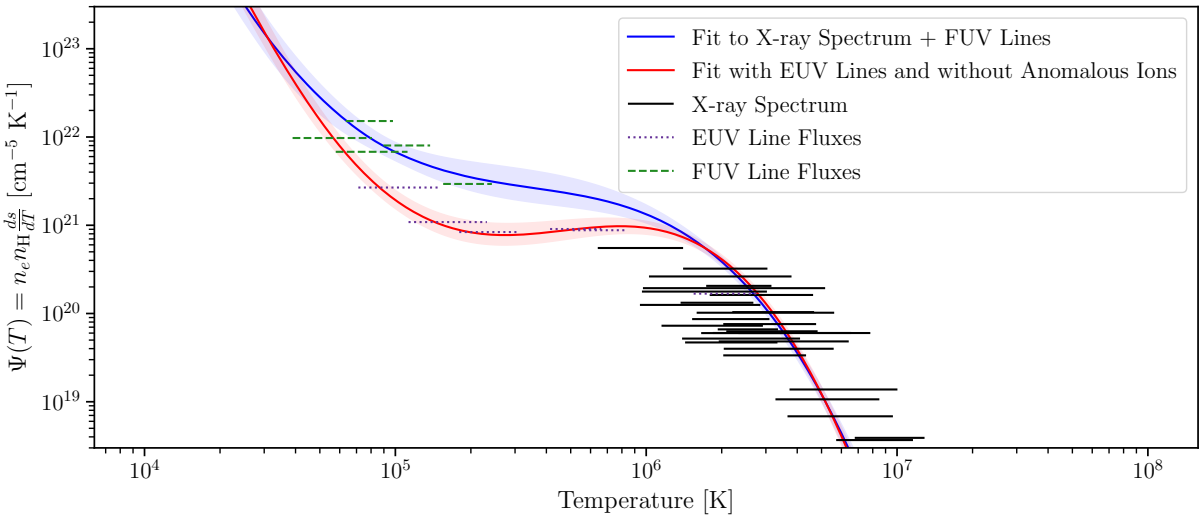

Figure 2.6: A comparison of the DEM fit using FUV lines and the X-ray spectrum to a new DEM that excludes N V, C IV, Si IV from the FUV data and includes a number of EUV lines listed in Table 2.1. As in Figures 2.3 and 2.4, the solid lines and regions represent the median DEM and 1σ confidence intervals while the horizontal bars represent constraints imposed by the measured fluxes.

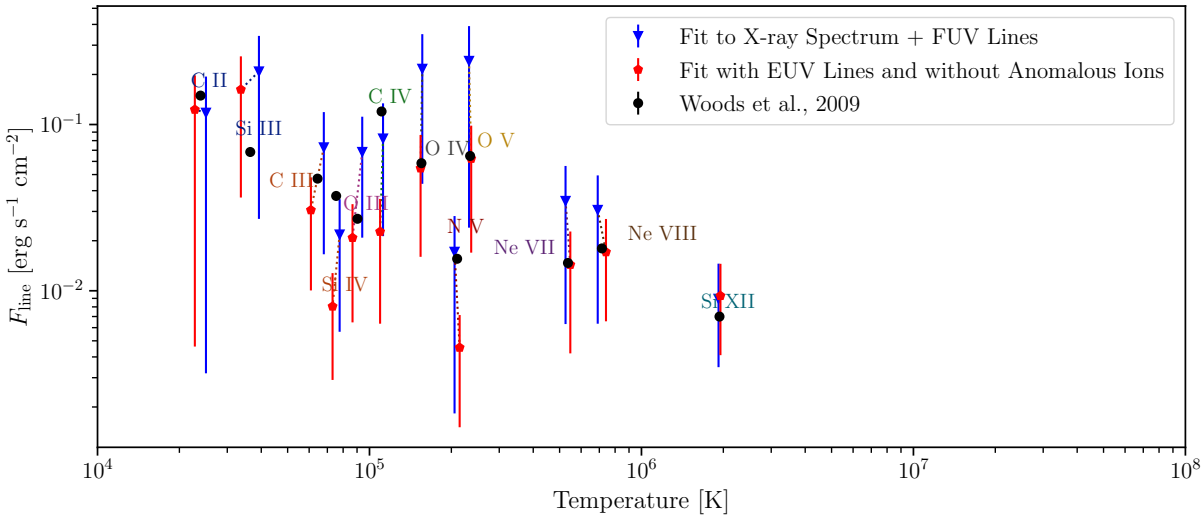

Figure 2.7: A comparison of the predicted line fluxes from the DEM models shown in Figure 2.6 to the lines listed in Table 2.1. The color scheme is the same as Figure 2.6, with the red pentagons marking predictions from the model including EUV lines and the blue triangles marking predictions from the model excluding EUV lines. The black points represent the line flux measurements with errorbars for their measurement uncertainties while the model predictions have errorbars for the *s*-factor model intrinsic uncertainty. The high S/N assigned to the Woods et al. (2009) data makes the errorbars nearly invisible. Note how the red model accurately predicts the fluxes of O III, O IV, O V formed at roughly the same temperatures as N V, C IV, Si IV but drastically underestimates the flux of these anomalous ions. Conversely, the blue model is caught in a compromise that slightly underestimates the flux of these ions and overestimates the flux of other FUV ions, but this compromise results in significantly overestimating the flux of EUV ions.

When we compare the predicted EUV flux of the Sun from both fits to the observed spectrum itself, the DEM prediction fit without EUV lines overestimates the data by 80% (see Figure 2.9 and Table 2.5). The $s-$factor uncertainty for this model estimates that each line's predicted flux has an uncertainty 60% of the predicted value, so the 1σ confidence interval of the model still encompasses the observed data. The DEM prediction including EUV lines and excluding anomalous ions underestimates the integrated flux by only 0.01%, but does have a significant 57% $s-$factor uncertainty. Within the EUV regime, there are 3 different recombination continuum regions that form from excess kinetic energy emitted when an ion captures a free electron into a bound state. Only one of them, the H I 912 Å continuum, is a significant contributor to the total EUV flux integrated from 100 to 912 Å, accounting for 15% in the Woods et al. (2009) spectrum of the Sun. The other two regions, He II 229 Å and He I 504 Å, contribute 3% and 2 % respectively. This falls within our uncertainties on the predicted flux, but it would be worth investigating if it is possible to incorporate these recombination continua in the DEM model without added parameters. The reconstruction of the EUV spectrum only used the emissivities of optically thin emission lines in the $G_\lambda(T)$ emissivity matrices and does not account for any contribution from continuum processes. The data required to incorporate free-bound, free-free, and two-photon continua exist in `CHIANTI`, but as of this work we have not included these sources of emissivity in the $G_\lambda(T)$ emissivity matrices. In future work we hope to include these processes for both fitting the DEM to X-ray spectra and reconstructing the EUV spectrum.

2.5.4 Abundance Sensitivity

We use the solar coronal abundances from Schmelz et al. (2012) stored in `CHIANTI` and an ionization equilibrium calculated at those abundances to get the $G_{ul}(T)$ functions for each emission line. Then for every $G_{ul}(T)$ function, we multiply by the stellar abundance if the ion's atomic number $Z > 2$. A higher metal abundance should shift the ionization equilibrium, which would have some effect on the self-consistency of the emissivity calculations. To verify whether or not this effect would be significant, we tested how the DEM fitting was sensitive to abundance in this

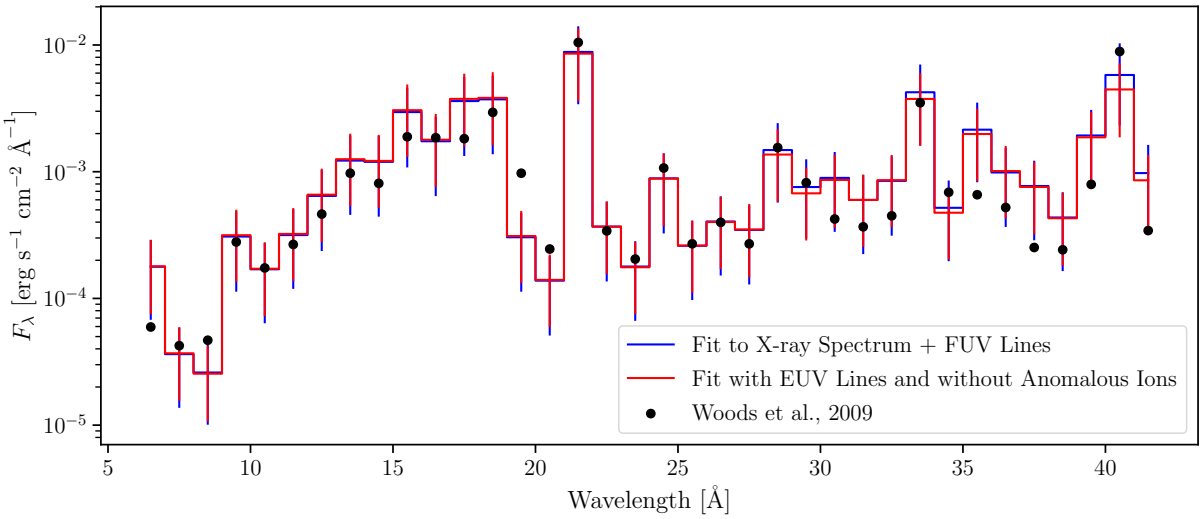

Figure 2.8: The predicted X-ray spectra from both models discussed in Section §2.5.3 compared to each other and the Woods et al. (2009) SIRS data used to fit the DEM. The solid lines represent models according to the same color scheme as Figure 2.6, blue for the model without EUV lines and red for the model with EUV lines and without the anomalous FUV ions. The errorbars on each model incorporate both the uncertainty in DEM shape and the $s-$factor uncertainty of their respective models in the manner described in Section §2.5.3. The DEMs do not differ significantly in the temperature regime associated with emitting at X-ray wavelengths, so the spectra for both models are nearly identical. A more complete look at the X-ray spectral data, including data not used to fit the DEM, and our DEM prediction is shown in the top-left panel of Figure 2.16.

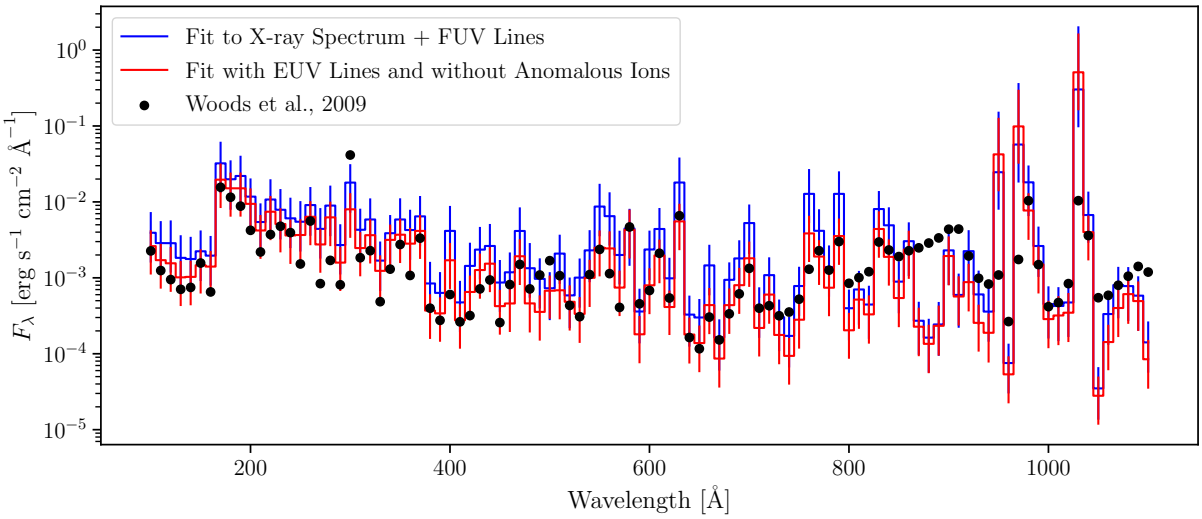

Figure 2.9: The predicted EUV spectra of both DEM models discussed in Section §2.5.3 with errorbars representing the uncertainties derived in the manner described in that section. The color scheme follows that of Figures 2.6 and 2.8, with the solid blue line representing the predicted spectrum and uncertainty of the model fit without EUV lines and the solid red line representing the predicted spectrum and uncertainty of the model fit with EUV lines and without the anomalous ions. The black points are the data from Woods et al. (2009). Both model spectra show nearly the same spectral shape as the data, excepting the ramp feature at wavelengths between 800 and 912 Å, discussed in Section §2.5.3. The blue model consistently overestimates the spectrum although the 1σ errorbars usually include the data.

crude framework. When we fit to stars other than the Sun we can refer to the literature and use the best abundance available, but we should not expect to always have an accurate and precise abundance measurement for the stars we are fitting the DEM to. Fitting the Sun with emissivity matrices generated using a super-solar [Fe/H] = 1 and a sub-solar [Fe/H] = −1 abundance resulted in the overall DEM shifting up or down to compensate. The predicted EUV fluxes obtained by combining each model DEM with their respective emissivity matrix differed by $< 15\%$.

This makes sense since the $G_{ul}(T)$ of an emission line from any metal is linearly proportional to the abundance. In fact, this harks back to the original implementation of the emission measure distribution in Pottasch (1963), where the author determined the relative abundances of elements by shifting them around to minimize the scatter in the emission measure distribution. This abundance adjustment is contingent on the assumption of the relative abundances being constant throughout the optically thin plasma, but everything else about this implementation of the DEM hinges on this assumption as well. This will also let us compare the DEM shapes of stars with different abundances by modifying the temperature independent coefficient c_0 to shift the overall DEM shape, marginalizing over the stellar abundance for any future study of the DEMs of a population of stars. However, if the relative abundances of an M dwarf corona differ from the Sun, the ions of an affected element will be consistently discrepant from the final DEM fit, and this is likely our greatest source of systematic uncertainty for stars other than the Sun. In the Sun, heavy elements with a first ionization potential < 9 keV tend to be enhanced in the corona relative to the photosphere (Drake et al., 1995). There is evidence to suggest that this first ionization potential effect varies with spectral type and may even be reversed in M dwarfs (Drake et al., 1995; Wood et al., 2012; Laming, 2015).

A single line from a species constrains the DEM near its ionization temperature, but many lines from an element across multiple ionization stages can constrain the element's relative abundance by fitting an element-specific DEM and shifting it to match the DEM fit without that element. This will only be possible for the brightest stars and the C, O, or Si species, since this requires bright lines from at least three ionization stages formed at conditions valid for the DEM method. Fitting

DEMs for as many nearby main-sequence stars as possible may allow us to generate this stellar coronal abundance library. A future and intermediate improvement would be to use the sample of stars for which *EUVE* allowed papers like Drake et al. (1995) to determine coronal abundances and select the most appropriate analog for a target we are fitting the DEM to. We intend to use this approach for future work.

2.5.5 Polynomial Degree

Higher polynomial degrees allow more flexibility between the well-constrained temperatures. The spread of FUV and X-ray formation temperatures constrains the slopes in their respective regimes (2×10^4 K < FUV < 2×10^5 K, 10^6 K < X-ray < 2×10^7 K), and this rigidly constrains lower order polynomials. The models show the most agreement with each other around $T = 10^5$ K, where there are a number of FUV lines with overlapping emissivities to anchor the fit (see Figures 2.2 and 2.10), while there are significant discrepancies at temperatures lower than the constraints imposed by the FUV lines and higher than the constraints imposed by the X-ray spectrum. Table 2.3 compares the BIC values for the different polynomial order and since the Sun's DEM shows very little curvature, the BIC prefers the $3^{\rm rd}$ order model and penalizes the complexity of higher order polynomials. Table 2.3 also shows that the models predict values consistent within 1 σ for the EUV flux integrated between 100 to 912 Å, and the $s-$factor uncertainty decreases slightly for higher order polynomials. This consistency is a product of both the low curvature of the Sun's DEM and the fact that the FUV and X-ray data constrain either end of the temperature interval responsible for EUV emission lines. When we ran a similar test with AU Mic, we found that orders below 5 were unable to match the complexity of the data, so we move forward with the $5^{\rm th}$ order as our standard approach for fitting other stars. Most targets will have too few data points to merit a model with many more parameters than a $5^{\rm th}$ order polynomial.

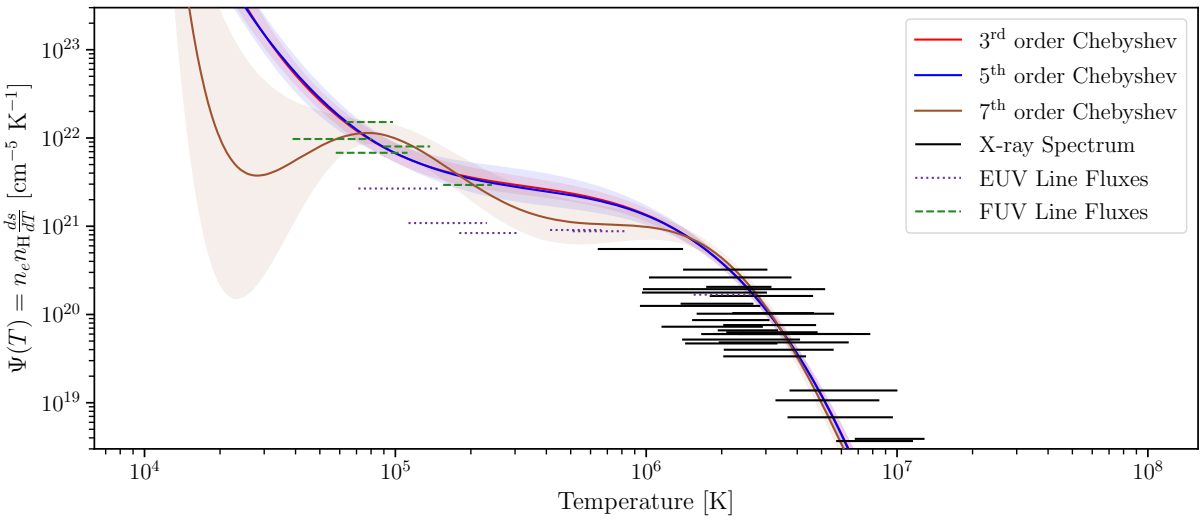

Figure 2.10: This plot compares the Sun's DEMs fit with different polynomial orders to each other and the flux constraints imposed by the observed FUV lines and X-ray spectrum used to fit the data according to the same scheme described in the caption of Figure 2.3. The red model is a 3$^{\rm rd}$ order polynomial, the blue model is the 5$^{\rm th}$ order polynomial we adopt as our standard approach, and the green is a 7$^{\rm th}$ order polynomial. The spread in FUV line formation temperatures sets a slope for the DEM to match between 2×10^4 and 2×10^5 K, while the X-ray spectrum sets the slope between 10^6 and 2×10^7 K. Table 2.3 compares the different order models to show that the different models predict consistent EUV fluxes.

Table 2.3. The BIC for different polynomial order models.

Chebyshev Polynomial Order —	BIC —	Integrated EUV Flux [ergs s^{-1} cm^{-2}]	$\log_{10} s_{\mathcal{L}_{\rm max}}$ —	$\log_{10} s$ —
3	−472.0	$3.8^{+2.6}_{-2.3}$	−0.2438	$-0.2182^{+0.0696}_{-0.0600}$
4	−468.4	$3.7^{+2.7}_{-2.3}$	−0.2516	$-0.2173^{+0.0690}_{-0.0610}$
5	−464.7	$3.5^{+3.1}_{-2.1}$	−0.2515	$-0.2177^{+0.0696}_{-0.0603}$
6	−464.7	$3.4^{+2.9}_{-2.1}$	−0.2372	$-0.2208^{+0.0692}_{-0.0597}$
7	−464.9	$3.0^{+2.4}_{-1.8}$	−0.2662	$-0.2348^{+0.0706}_{-0.0599}$
8	−461.1	$2.9^{+2.4}_{-1.8}$	−0.2852	$-0.2350^{+0.0698}_{-0.0600}$
9	−457.1	$2.9^{+2.5}_{-1.8}$	−0.2709	$-0.2337^{+0.0709}_{-0.0593}$
10	−454.0	$3.1^{+3.0}_{-1.9}$	−0.2858	$-0.2307^{+0.0717}_{-0.0616}$

Note. — The Sun's DEM shows very little complexity, so the 3$^{\rm rd}$ order polynomial model is most preferred, with each subsequent order scoring a worse BIC. This was not true for the AU Mic test for which orders below 5 were too inflexible to match the constraints of the prior and the data.

2.6 Applying Our DEM Method to AU Mic

AU Mic is a nearby young and active M dwarf with an observable debris disk, 9.979 ± 0.04 pc away and 22 ± 3 Myr old (MacGregor et al., 2013; Ibañez Bustos et al., 2019; Plavchan et al., 2020). The system also hosts at least one confirmed planet and possibly a second planet candidate (Plavchan et al., 2020), making it a rare case of an M dwarf planetary system with a precisely known young age. Despite being nearby, and having been observed multiple times with *EUVE*, the quiescent EUV spectrum of AU Mic is poorly constrained (see Section 2.8 and Figure 2.16), so some method of reconstructing the EUV spectrum is required to study this planetary system in detail. On the other hand, the X-ray and FUV data for this star are extremely precise considering how intrinsically faint the star is, allowing us to fit a very well-constrained DEM and compare our implementation to earlier work published in Del Zanna et al. (2002). Pagano et al. (2000) published a very thorough list of emission line fluxes measured from spectra taken during quiescence, a subset of which we use to fit the DEM for AU Mic and list in Table 2.4. Redfield et al. (2002) published separate quiescent and flare FUSE measurements of FUV lines and Redfield et al. (2003) reported the quiescent coronal line fluxes listed in Table 2.4. The bandpass for *FUSE* overlaps with that of COS, so we fit separate DEMs including and excluding the *FUSE* measurements to demonstrate the usefulness of transitions observed between 900 and 1100 Å in constraining the high-temperature end of the DEM, motivating future COS observations of cool dwarfs.

The majority of the lines listed in Table 2.4 will be unobservable for other fainter cool dwarfs, but having the ground truth of which lines are emitted from the upper atmospheres of cool dwarfs is immensely useful for future DEM fitting. If a line is observed for AU Mic, we can place upper limits on the flux from that line for another star, constraining the DEM near that line's formation temperature. We fit the DEM assuming solar coronal abundances from Schmelz et al. (2012), using the FUV lines listed in Table 2.4 and an X-ray spectrum from the Reflection Grating Spectrometer (RGS, den Herder et al. 2001) on *XMM-Newton*, observed in October 2018 (Kowalski et al., 2019). The spectrum was resampled at 1 Å resolution before fitting. The lightcurve for this observation

showed multiple flares and we use the quiescent X-ray spectrum from the work of Kowalski et al. (in prep) and Tristan et al. (in prep). This observation was not concurrent with the data obtained by Pagano et al. (2000) and Redfield et al. (2003), so it is possible that the X-ray and FUV data are not from identical levels of quiescence. Very few targets will be likely to have concurrent X-ray and FUV observations, so this issue will plague most of the stars needing EUV reconstruction. We compare our fit using FUV lines and an X-ray spectrum to another fit using the same FUV lines and X-ray line flux measurements reported by Wood et al. (2018). We also note that whenever possible, a line flux measurement is more useful than a spectral bin, and if high temperature emission line strengths can be measured, these should be favored over the use of spectral bins.

In Figure 2.11 we compare two fits for AU Mic to the constraints imposed by the data, with the red model using only line flux measurements and the blue model using the combination of FUV lines and an X-ray spectrum that will be applicable to fainter M dwarfs. AU Mic has a higher DEM than the Sun across the entire temperature domain, and significantly higher at temperatures greater than 2×10^6 K, corresponding to the corona. The presence of detectable coronal iron lines, formed at $T > 10^6$ K, places a strong constraint that lifts AU Mic's DEM far higher than the Sun's which had many X-ray spectrum points depressing the DEM in the vicinity of this temperature. The iron emission lines are not solely responsible for the differences, as the constraints from the X-ray spectra set a slope at these high temperatures leading toward the iron lines. The shape of AU Mic's DEM beyond $T = 2 \times 10^5$ K demonstrates the importance of including a corona in calculating the total EUV flux. Peacock et al. (2019b) finds significant differences in the total flux and spectral shape between the `PHOENIX` models without a corona and the semi-empirical SRPM model from Fontenla et al. (2016). Peacock et al. (2019b) also simulates the addition of a corona to their models by using the DEM of AU Mic available in `CHIANTI` from Del Zanna et al. (2002), showing potential opportunities for supplementing stellar atmosphere models with DEMs fit to observations of specific stars.

Figure 2.12 compares the predicted X-ray spectra to the observed spectrum and Figure 2.13 compares the predicted line fluxes to the FUV line profile measurements listed in Table 2.4. Both

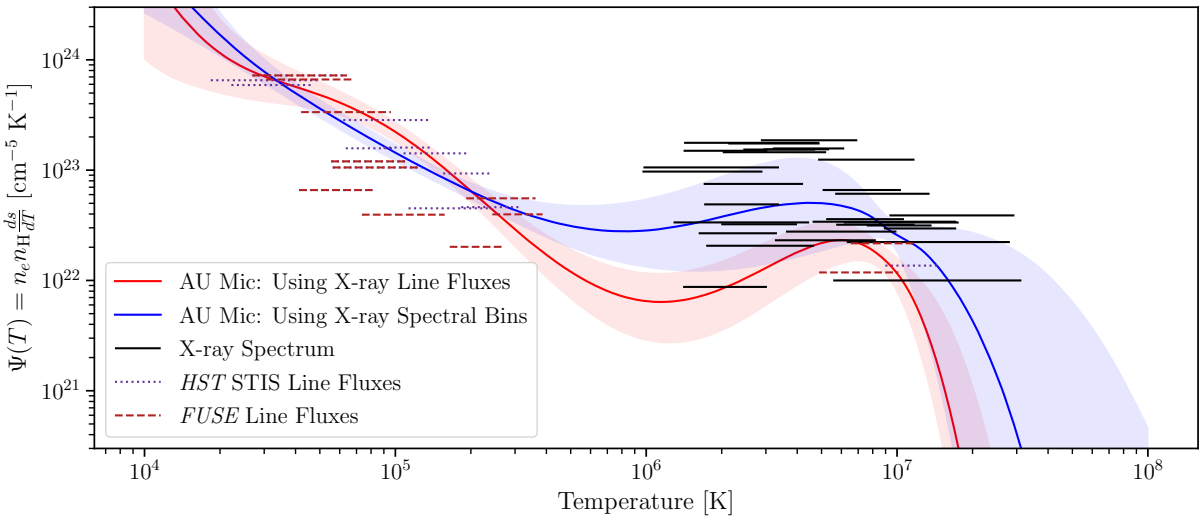

Figure 2.11: Comparing the DEM of AU Mic fit to a combination of FUV line fluxes from STIS (published in Pagano et al. 2000) and *FUSE* (published in Redfield et al. 2002 and Redfield et al. 2003) and either a coarsely sampled X-ray spectrum or a list of X-ray line fluxes reported in Wood et al. (2018). The red line and region correspond to the median DEM value and 1σ confidence intervals for AU Mic fit using only line flux measurements, while the blue line and region are the model for AU Mic constrained by the X-ray spectrum instead of line fluxes. The horizontal bars represent constraints from the FUV lines listed in Table 2.4 and from the *XMM-Newton* X-ray spectrum. The dotted purple bars correspond to the STIS lines published in Pagano et al. (2000) while the dashed red bars correspond to *FUSE* lines published in Redfield et al. (2003) and the black solid bars are from the quiescent *XMM-Newton* spectrum presented in Kowalski et al. (2019) (to be published in Kowalski et al. in prep, and Tristan et al. in prep). There were too many X-ray lines listed in Wood et al. (2018) to represent in this figure.

figures incorporate the $s-$factor uncertainties and DEM shape variation (Section §2.5.3) and show that the model predictions are typically consistent with the data to 1σ. Figure 2.14 shows the parameter distributions for the DEM fit to line fluxes, and we find that the $s-$factor for AU Mic is 0.4, comparable to that of the Sun. At lower wavelengths the red model, which was not fit to the spectrum itself, significantly underestimates the flux. This may be a consequence of the higher energy emission including flux from free-free or free-bound continuum sources, creating the discrepancies between both these DEMs. To reproduce the flux in these bins without accounting for this extra emissivity, the DEM fit to the spectrum must enhance the amount of material at these high temperatures. Including free-free and free-bound continuum emissivities in the $G_\lambda(T)$ matrices should mitigate or eliminate these discrepancies.

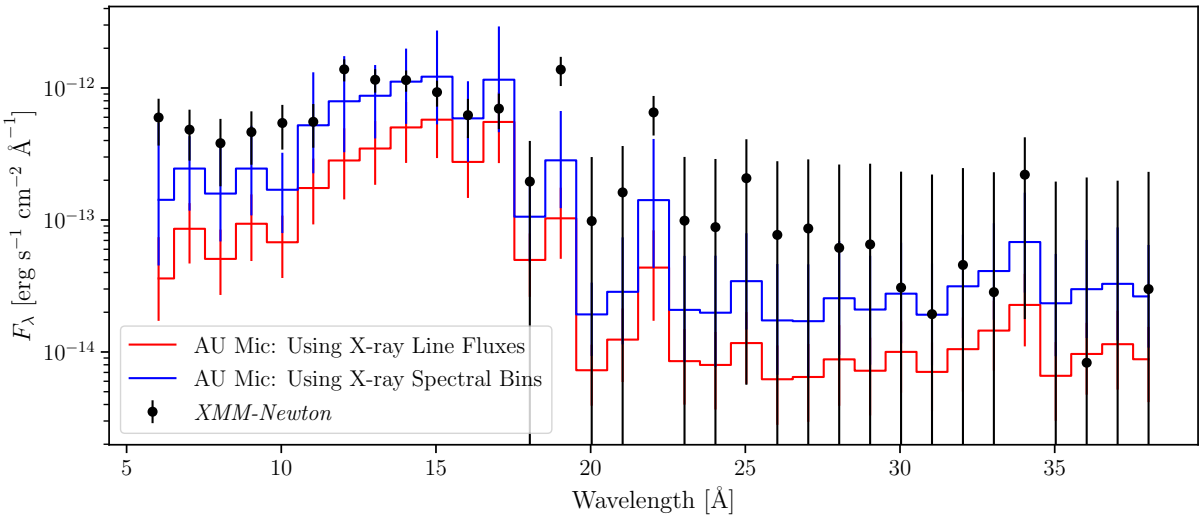

Figure 2.12: The X-ray data used to fit the DEM compared to the predicted spectra for the DEM models of AU Mic shown in Figure 2.11. The black points represent the downsampled RGS X-ray spectrum at a 1 Å wavelength resolution while the red and blue lines show the DEM prediction for the flux density in the same wavelength bins, incorporating the $s-$factor uncertainty in their error bars, for the models fit with X-ray lines and the X-ray spectrum respectively. They are consistent with each other, although the median prediction of the DEM fit to the spectrum is consistently above the DEM fit to X-ray line fluxes.

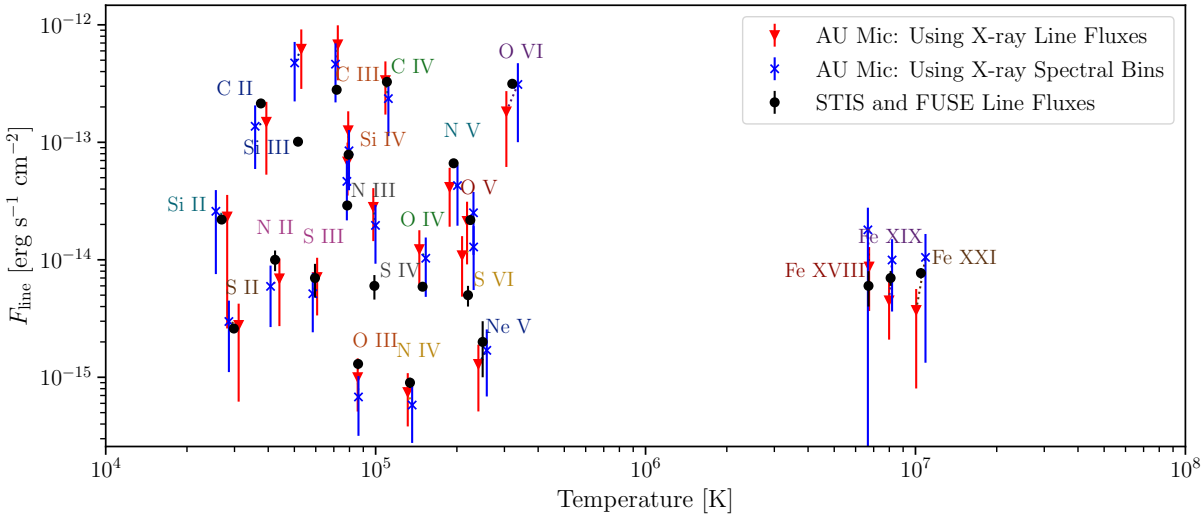

Figure 2.13: The FUV line fluxes predicted by the AU Mic DEM models shown in Figure 2.11 compared to the data from Pagano et al. (2000) and Redfield et al. (2003). Following the color scheme of Figures 2.11 and 2.12, the red triangles represent the predictions from the DEM model fit using only line fluxes while the blue pentagons represent the predictions from the DEM model using the X-ray spectrum. The black points represent the combined fluxes of lines emitted by the ion annotating the point, with errorbars for the measurement uncertainty while the model predictions have errorbars representing the $s-$factor model intrinsic uncertainty.

2.7 Our DEMs Compared to Published Literature

Differential emission measure techniques are primarily applied in the solar context to resolved regions, highlighting individual structures like coronal holes or flare loops. Vernazza & Reeves (1978) fit DEMs to many such structures, including "quiet regions" with minimal observed activity during the 9-month interval from 1973 May to 1974 August, shortly before the solar minimum of Cycle 21. This is not perfectly analogous to our quiescent Sun DEM fit to data integrated over the entire solar disk, but it is the best comparison for which we had access to a published DEM via `CHIANTI` (Dere et al., 1997; Del Zanna et al., 2015). The left panel of Figure 2.15 compares the Vernazza & Reeves (1978) quiet region DEM to our disk-integrated quiescent Sun DEM, fit under the assumptions applicable to observing the Sun as a star (albeit with much higher signal-to-noise): the few FUV lines listed in Table 2.1 and the X-ray spectrum at a low resolution of $R \leq 50$. We also include the solar DEM fit excluding anomalous ions and including EUV lines.

Similarly, the right panel of Figure 2.15 compares our DEM for AU Mic to the DEM published by Del Zanna et al. (2002), which combined *FUSE*, STIS, and *EUVE* observations. `CHIANTI` has a volume differential emission measure version of the Del Zanna et al. (2002) DEM which needed to be divided by $\frac{4\pi R_\star^2}{d^2}$ to match our formulation of a column differential emission measure, and we use the stellar radius and distance assumed by Del Zanna et al. (2002), $R_\star = 0.68 R_\odot$ and $d = 9.94$ pc, for consistency in the scaling factor. Like our dataset, they did not have access to simultaneous observations from these different instruments. Unlike our dataset, they included the integrated fluxes of lines observed with *EUVE*, but we believe the *EUVE* observations they used were flare contaminated for reasons discussed later in Section §2.8. We also compare our AU Mic DEM to the active solar region DEM of Vernazza & Reeves (1978), demonstrating a small resemblance between the active region and the active star AU Mic. The active region DEM seems to shift the shape of the quiet sun DEM to a higher temperature and dramatically enhance the DEM near 10^6 K. AU Mic, a star more active than the Sun, has more material at nearly all temperatures.

Both panels show that our DEMs are significantly higher than their literature counterparts

Table 2.4. Ion fluxes of AU Mic compared to the predictions from the red DEM model shown in Figure 2.11.

Ion	Wavelengths [Å]	$\log_{10} T_f$ $\log_{10}([\mathrm{K}])$	Observed Flux $[10^{-15}\ \mathrm{erg\,s^{-1}\,cm^{-2}}]$	DEM Prediction $[10^{-15}\ \mathrm{erg\,s^{-1}\,cm^{-2}}]$
C II	1324, 1336[a]	4.6	214 ± 16.0	$149^{+71.7}_{-96.2}$
C III	977, 1176[a]	4.9	280 ± 16.0	681^{+309}_{344}
C IV	1548, 1551	5.0	327 ± 24.2	208^{+164}_{-174}
N II	1086	4.6	10.0 ± 2.00	$6.94^{+3.33}_{-4.21}$
N III	990, 992	4.9	29.0 ± 2.24	$68.6^{+30.9}_{-33.3}$
N IV	1487	5.1	0.90 ± 0.09	$0.747^{+0.337}_{-0.366}$
N V	1238.8, 1242.8	5.3	66.3 ± 4.99	$41.6^{+19.1}_{-22.5}$
O III	1666	4.9	1.30 ± 0.13	$1.00^{+0.448}_{-0.489}$
O IV	1400, 1401, 1407	5.1	5.90 ± 0.423	$12.3^{+5.55}_{-6.17}$
O V	1218, 1371	5.3	21.8 ± 1.86	$21.4^{+9.84}_{-12.2}$
O VI	1032, 1038	5.5	315 ± 26.4	$183^{+89.7}_{-121}$
Ne V	1146	5.4	2.00 ± 1.00	$1.30^{+0.599}_{-0.784}$
Si II	1260, 1265, 1304, 1527, 1533	4.3	22.0 ± 1.06	$23.3^{+12.3}_{-20.7}$
Si III	1108, 1110, 1113, 1206, 1295, 1297, 1299, 1301, 1303	4.8	101 ± 8.11	624^{+289}_{-340}
Si IV	1394, 1403	4.9	78.5 ± 5.73	$126^{+57.3}_{-62.8}$
S II	1253.8, 1259.5	4.4	2.60 ± 0.18	$2.78^{+1.45}_{-2.16}$
S III	1016, 1021,	4.8	7.00 ± 2.24	$7.11^{+3.29}_{-3.75}$
S IV	1063, 1073	5.0	6.00 ± 1.41	$28.2^{+12.6}_{-13.7}$
Fe XVIII	975	6.9	6.00 ± 2.00	$8.75^{+4.10}_{-5.08}$
Fe XIX	1118	7.0	7.00 ± 1.00	$4.51^{+2.05}_{-2.42}$
Fe XXI	1354	7.0	7.70 ± 0.77	$3.73^{+1.91}_{-2.93}$

Note. — All entries are from STIS line fluxes reported in Pagano et al. (2000) and/or *FUSE* measurements reported in Redfield et al. (2002) and Redfield et al. (2003).

[a]multiplet

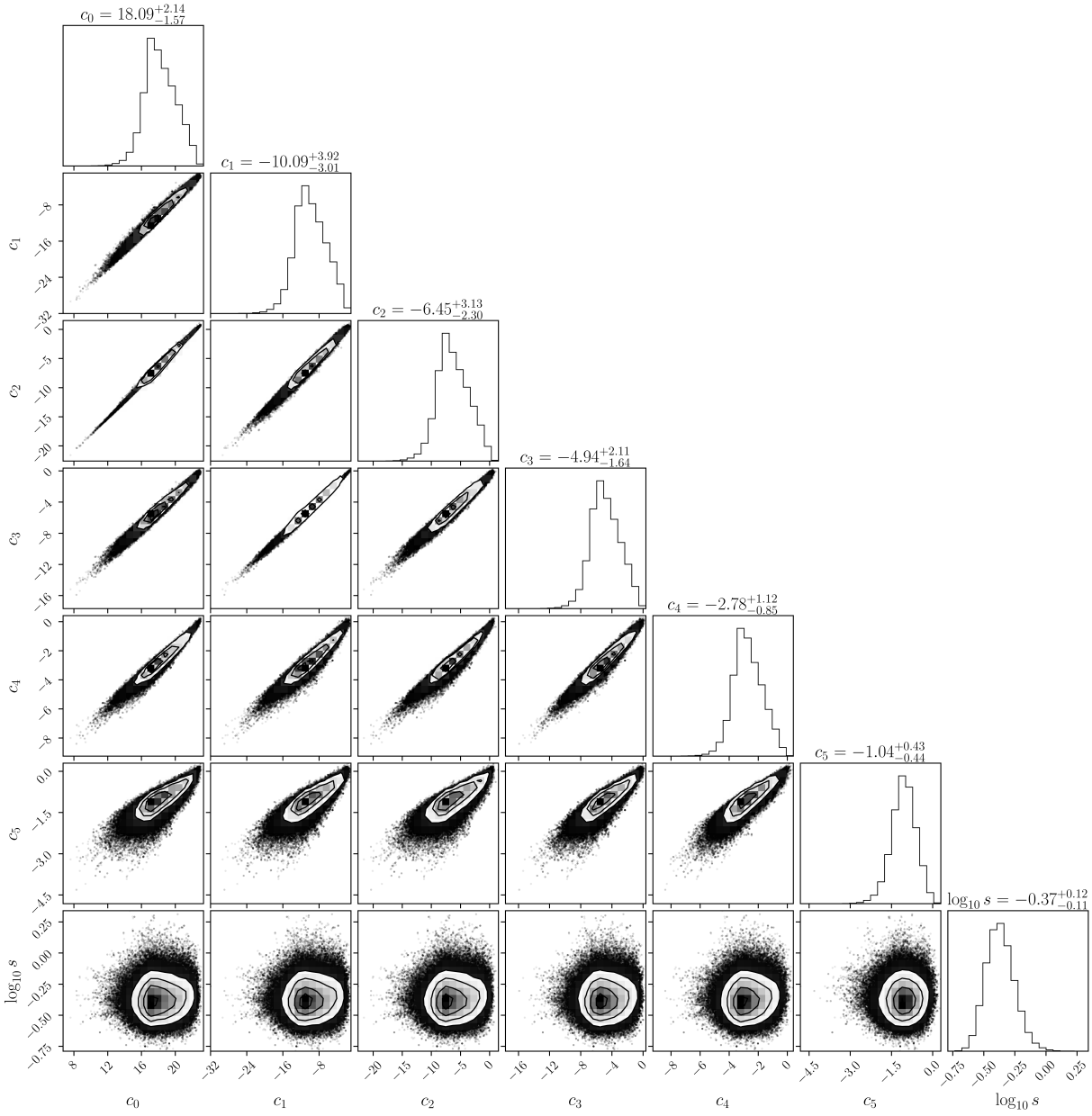

Figure 2.14: The corner plot showing the parameter distributions when fitting AU Mic with a 5^{th} order polynomial to FUV lines and the X-ray spectrum. The model uncertainty for AU Mic is slightly better than that of the Sun, with $s = 0.4$ instead of 0.6.

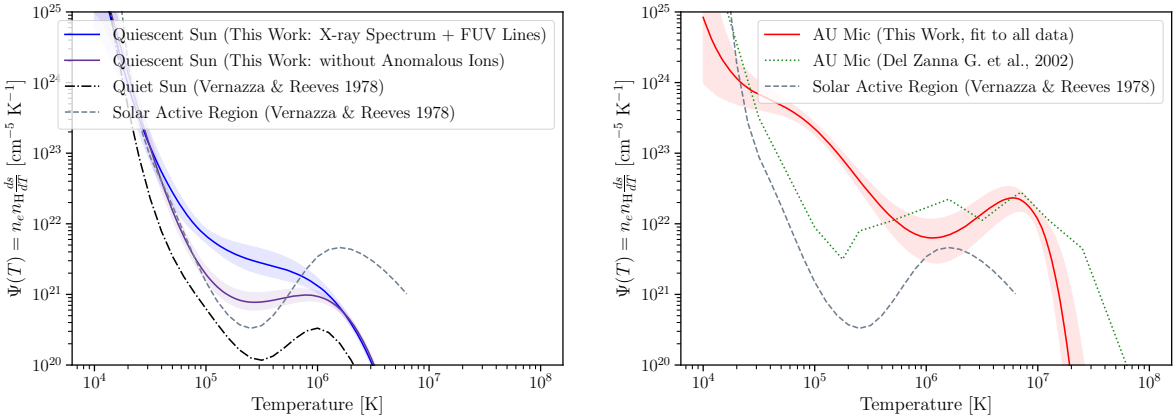

Figure 2.15: The left panel compares both of our DEMs for the quiescent disk-integrated Sun described in Section §2.5.3 to the "quiet Sun" DEM derived by Vernazza & Reeves (1978) from observations of quiet regions of the Sun, while the right panel compares our DEM for AU Mic to the AU Mic DEM published by Del Zanna et al. (2002) and the DEM of an active region published by Vernazza & Reeves (1978). These DEMs used for comparison were available in the CHIANTI database (Dere et al., 1997; Del Zanna et al., 2015).

at temperatures near 10^5 K, roughly corresponding to the transition region. For the AU Mic panel on the right, the Del Zanna et al. (2002) DEM is significantly lower than ours between 3×10^4 and 3×10^5 K. Monsignori Fossi et al. (1996) published the time-evolution of the AU Mic DEM during a flare observed by *EUVE* in July 1992, and while they use a slightly different formulation of the DEM $= n_e^2 \frac{dV}{dT}$, the shape of our DEM strongly resembles theirs published in panels a and g of their Figure 9, which correspond to quiescent phases, while multiplying our DEM by $4\pi R_\star^2 \approx 3 \times 10^{22}$ cm^2 scales to the approximately the same order of magnitude as their DEM. Unfortunately, their DEM was not available in `CHIANTI` for direct comparison.

The discrepancy at temperatures below 10^6 K is largely driven by the line list we are using to fit the DEM, where our strongest lines are from Na-like and Li-like species N V, Si IV, and C IV, and the solar DEM excluding these ions is much closer to the Vernazza & Reeves (1978) quiet region DEM. Del Zanna et al. (2002) fits the DEM of AU Mic without these lines and has enough individual lines to constrain the DEM in this temperature regime without them. We will not be able to afford this luxury for nearly every other M dwarf unless we are observing a strong flare. Instead we fit our DEM including these lines and use the $s-$parameter boost to our variance to account for the systematic uncertainties involved. As long as some other ions formed in the same region are included in the line list, even with just upper limits on their fluxes, the DEM will shift down to accommodate these lines. In the future, we plan to test dividing the observed fluxes of these lines by a corrective factor ~ 5 before fitting the DEM to see how this improves the fit and affects the predicted EUV spectrum.

Working in a data-limited regime is also why we fit for the DEM using an assumed functional form instead of interpolating between the emission measure loci estimated from individual lines (Pagano et al., 2000), or fitting for the value of the DEM in discrete temperature bins (Del Zanna et al., 2002, 2015). Without measured lines in the temperature regime corresponding to most EUV lines, we must use our assumption of a continuous function anchored on both ends of the inaccessible temperature/wavelength regime. The DEM for AU Mic derived by Del Zanna et al. (2002) is poorly constrained between $10^6 < T < 10^{6.7} K$ because they do not use X-ray line fluxes

or a coarse spectrum, but our DEMs agree on the position and magnitude of the coronal peak DEM ($T = 10^7$ K), if not the shape of the decline. Other contributions to the discrepancies between DEMs are differences in the atomic data and calculations for abundances and the ionization equilibrium and level populations. While the DEMs created by Sanz-Forcada et al. (2011) were not available in `CHIANTI`, we expect significant discrepancies at the lower temperature end of the DEM because the majority of their cool dwarfs did not have UV data available.

2.8 Comparing Model EUV Spectra to Data

With our implementation of the DEM well-characterized, we can move on to the main objective of this project: generating EUV spectra in a format useful to the astronomical community with errorbars that self-consistently account for both statistical and systematic uncertainties. Our model spectra range from 1 to 2000 Å at a constant $R = \frac{\Delta\lambda}{\lambda} = 500$, but we advise using data instead of our model in the regimes where that is possible. The model spectrum files include uncertainties derived according to the method described in Section §2.5.3. Figure 2.16 compares our model spectrum of the Sun to the Woods et al. (2009) data and our model spectrum of AU Mic to an *EUVE* observation from July 1992 and quiescent *FUSE* data from a different time described in Redfield et al. (2002, 2003). This *EUVE* observation was during the calibration phase of the mission and happened to catch a flare, first reported by Cully et al. (1993) and later studied in more detail in Monsignori Fossi et al. (1996). We compare our DEM-generated spectrum to data from the quiescent time segment before the flare, extracted using standard *EUVE* Guest Observer Center IRAF procedures. The spectral resolution of the 3 spectrometers is $\sim$ 0.5, 1.0, and 2 Å , which corresponds to 7 pixels per resolution element on the detectors. The photon event data were screened to eliminate high background times and times when the detectors were switched off. The IRAF routine "`apall`" was used for the spectral extraction with a 14 pixel wide spectral region and two 85 pixel wide background regions measured above and below the stellar spectrum. The count rate spectra were converted to flux densities using the effective areas established by the *EUVE* mission and the oversampled spectra were smoothed to the intrinsic spectrometer resolution. The

large background area sampled allowed precise monitoring of the time dependent background. Del Zanna et al. (2002) used a 1993 *EUVE* observation which has no published lightcurve to verify the absence of flares and the time-averaged 1993 spectrum shows more flux than the quiescent 1992 data at all wavelengths indicating possible flare contamination.

Our DEM prediction for the EUV luminosity of AU Mic is $L_{\rm EUV} = 9.0^{+6.1}_{-4.6} \times 10^{28}$ erg s^{-1}, while the Linsky et al. (2014) relations give 1.2×10^{29} erg s^{-1}, Sanz-Forcada et al. (2011) relation gives 1.4×10^{30} erg s^{-1}, and Chadney et al. (2015) finds $L_{\rm EUV} = 8.4 \times 10^{28}$ erg s^{-1} using a coronal emission measure distribution model. We use the Lyman-α flux reported by Wood et al. (2005) for the Linsky et al. (2014) relations, and the X-ray luminosity obtained by multiplying the integrated flux of our EPIC-MOS spectrum with $4\pi d^2$, $L_{\rm X\text{-}ray} = 3.0 \times 10^{29}$ erg s^{-1}, for the Sanz-Forcada et al. (2011) relation. To convert the surface EUV flux reported by Chadney et al. (2015) to luminosity we use their assumed radius for AU Mic $= 0.68 R_\odot$. The major advantages of our DEM approach are a well-characterized uncertainty and a balance between ease of implementation and specificity to each star. Using Equation 3 of Sanz-Forcada et al. (2011) has a minimum uncertainty of 1.99 dex in predicting the EUV flux, but our method can do significantly better than this empirical relation even for very faint targets like TRAPPIST-1, with only a few FUV line measurements and an integrated X-ray flux or coarse spectrum. The DEM method also provides a low-resolution spectral shape in addition to a total flux, which may be useful for those who wish to model more detailed effects of high energy stellar radiation on a planet, disk, or the local interstellar medium.

2.9 Case Studies

Thus far, we have demonstrated our method on targets with extremely good data, which are not representative of the majority of stars for which the astronomical community needs reconstructed EUV spectra to enable other science. In this section we apply our method to three M dwarfs of interest to the exoplanet community, all fainter and less active than AU Mic, and show that their coronae are hotter than the Sun and will seriously affect the atmospheric evolution of planets orbiting in their respective habitable zones.

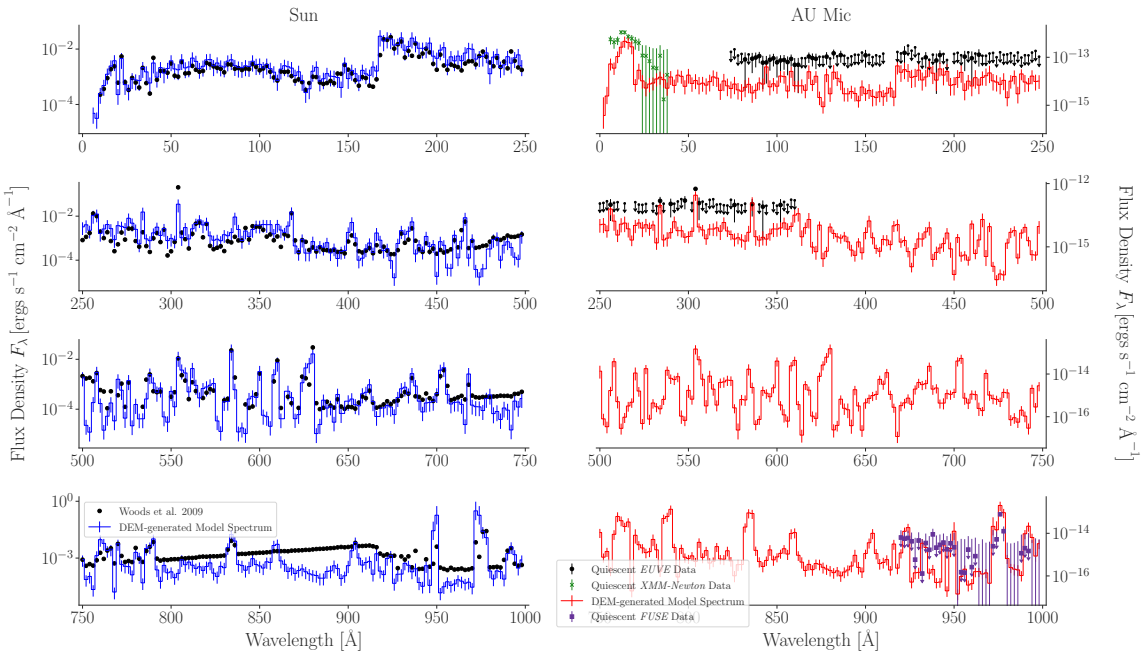

Figure 2.16: The individual rows of this figure show 250 Å chunks of the X-ray, extreme ultraviolet, and a portion of the far ultraviolet regimes. The left side compares to the Woods et al. (2009) spectrum shown as black points to the DEM-generated model spectrum for the Sun in blue, where the DEM was fit to EUV lines, FUV lines excluding anomalous ions, and X-ray data. The right side shows the DEM-generated model spectrum for AU Mic in red, compared to both *EUVE* data shown as black points and *FUSE* data shown as purple squares. The model spectrum for the Sun is largely consistent with the data, except for a recombination continuum associated with the H I 912 Å line spanning $\sim$ 800 to 912 Å. The AU Mic *EUVE* data is almost entirely consistent with zero, but our model does not predict flux significantly higher than these upper limits, while roughly matching some of the clearly detected emission lines.

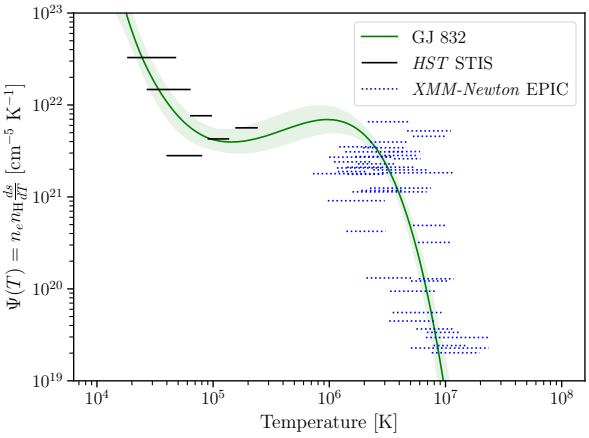

Figure 2.17: Comparing the DEM of GJ 832 fit to a quiescent X-ray spectrum from *XMM-Newton* EPIC and line fluxes from STIS, with $\overline{\Psi}(T)$ constraints shown as horizontal dotted blue and solid black bars respectively.

2.9.1 GJ 832

GJ 832 was included in the original MUSCLES survey (France et al., 2016) with its EUV flux estimated by the Linsky et al. (2014) correlations and semi-empiricaly modeled by both Fontenla et al. (2016) and Peacock et al. (2019b). We fit our DEM model to the line fluxes published in Youngblood et al. (2016) and X-ray data hosted on *MAST* as part of the MUSCLES data products. The line fluxes were measured using STIS data while the X-ray spectrum is from *XMM-Newton* EPIC (France et al., 2016). Comparing our model spectra to the semi-empirical models and the EUV fluxes predicted by the Linsky relations in Figure 2.18 shows that the different models agree with each other in different wavelength regimes. The data we used to fit GJ 832 was not perfectly quiescent, so some of the model discrepancy may be due to flare contamination (Youngblood et al., 2016). The DEM inferred from fitting the data is shown in Figure 2.17.

The DEM model tends to predict higher fluxes than the other three models at wavelengths shorter than 600 Å. Below 400 Å all models except for the Peacock et al. (2019b) `PHOENIX` model coincide quite closely, with the outlier lacking a coronal contribution. Between 400 to 600 Å both the DEM and semi-empirical models predict higher fluxes than the Lyman-α correlations. The biggest discrepancies between models are between 800 to 1100 Å where the semi-empirical models

include the recombination continuum at the H I 912 Å line and the blue wing of the Lyman-α 1216 Å line, both of which are unaccounted for by the DEM model and which the Lyman-α correlation fluxes seem to underestimate. Tilipman et al. (2020) updates the Fontenla et al. (2016) SSRPM model of GJ 832, and when all these EUV reconstruction methods have been applied to a larger sample of stars we may have more insight into the conditions under which each is more likely to be accurate.

2.9.2 Barnard's Star

Barnard's Star is old and inactive compared to most M dwarfs (Ribas et al., 2018), but it still flares occasionally (Paulson et al., 2006). France et al. (2020b) obtained X-ray (*Chandra* ACIS-S) and FUV (*HST* STIS/COS) data of this star both during quiescence and during a flare. We used these data to prepare both a quiescent DEM and a flare DEM, under the assumptions that the system is still in a collisionally dominated equilibrium and with solar coronal abundances scaled by the stellar metallicity [Fe/H] $= -0.32$. This is a very low S/N regime in the quiescent data but not nearly as low as TRAPPIST-1, discussed in Section 2.9.3. A more physically accurate flare DEM would require adjusting the emissivity matrix to account for the magnetic reconnection's influence on the level populations. In the current framework, we see that the flaring state has more material than quiescence at temperatures between $\sim 10^5$ to 10^7 K, but both the flare and quiescent DEMs agree beyond 3×10^7 K (see Figure 2.19). France et al. (2020b) uses our quiescent and flaring model EUV spectra to investigate the influence of EUV variability on a hypothetical planet orbiting in the habitable zone of Barnard's star, demonstrating the applicability of our low-resolution spectra to models of atmospheric escape more complicated than simple energy-limited photoevaporation. We note that this DEM shape is very unusual compared to past published DEMs, but emphasize that the wide error intervals are likely to encompass the true DEM shape. If more data become available, perhaps the model constraints will narrow to something more familiar.

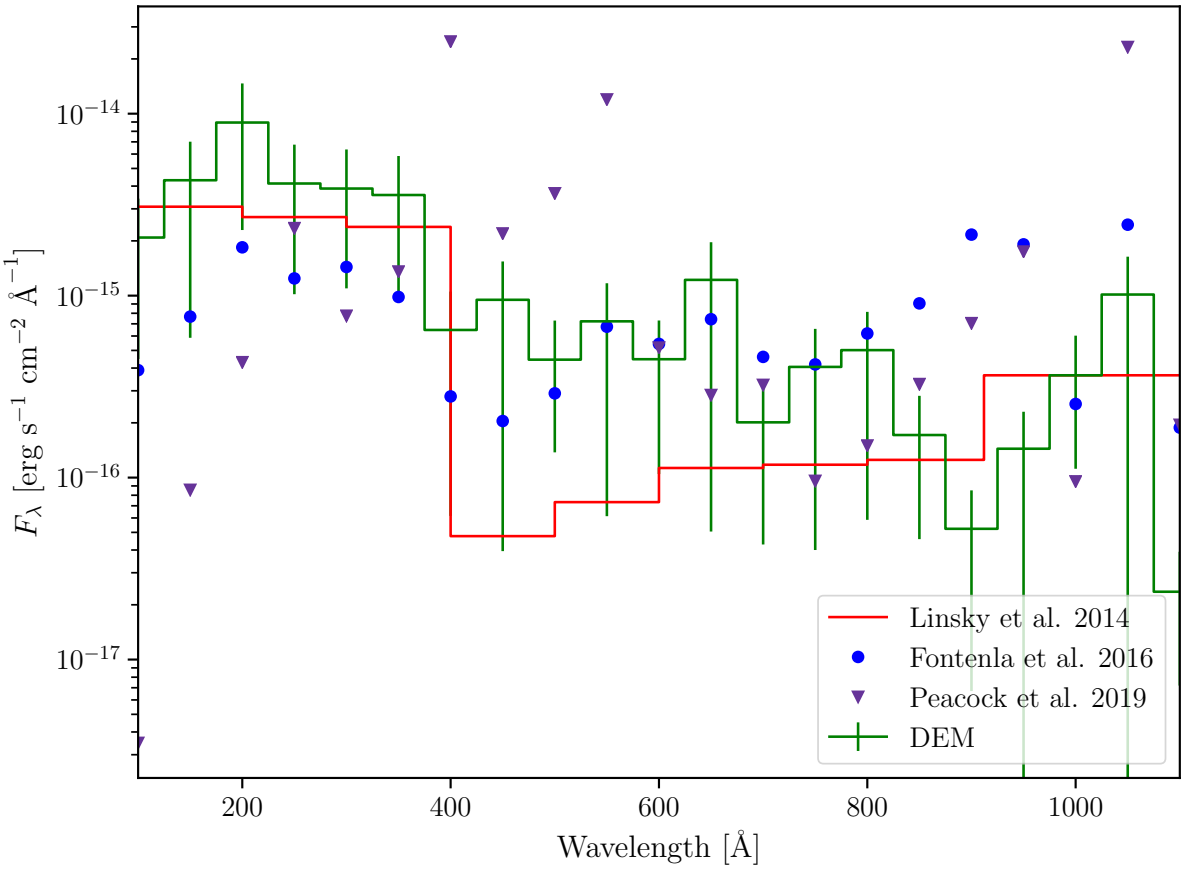

Figure 2.18: Comparing four methods of reconstructing the EUV spectrum of GJ 832. The green line and errorbars represent the spectrum predicted by our DEM model with the errors enclosing the 16$^{\text{th}}$ to 84$^{\text{th}}$ percentile intervals for the predicted flux according to the method described in Section §2.5.3. The red lines show the predicted EUV flux in 100 Å bandpasses according to the Lyman-α correlations published in Linsky et al. (2014), available in the MUSCLES dataset. The blue points represent the semi-empirical model published by Fontenla et al. (2016), also available in the MUSCLES dataset. The purple triangles show the `PHOENIX` model published in Peacock et al. (2019b) and hosted on *MAST*. These four methods of predicting the EUV spectrum appear to have different regions of mutual agreement, discussed in Section 2.9.1.

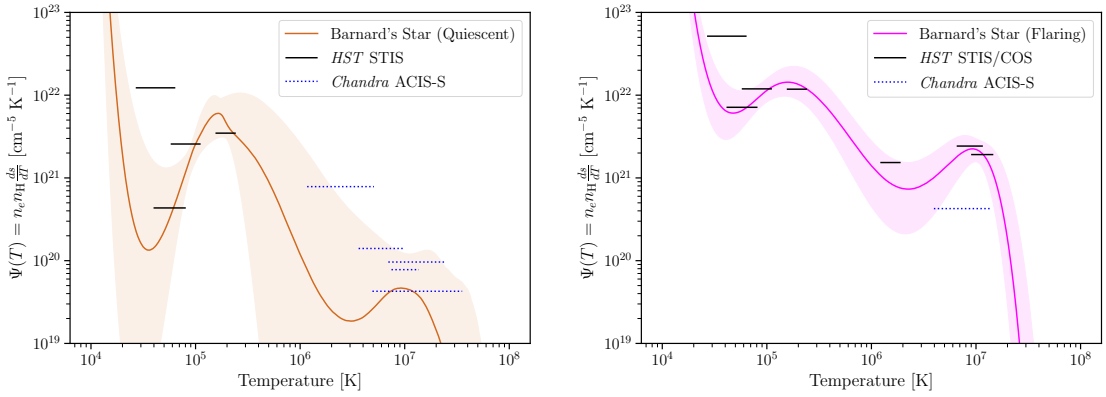

Figure 2.19: The left panel compares the DEM of Barnard's Star fit to a coarse X-ray spectrum from *Chandra* ACIS-S and line fluxes measured from *HST* STIS. The right panel compares the DEM of Barnard's Star fit to an integrated X-ray flux from *Chandra* ACIS-S and line fluxes from STIS/COS during a flare. For both panels, the dotted blue and solid black bars represent the $\overline{\Psi}(T)$ constraints for the X-ray and FUV data respectively.

2.9.3 TRAPPIST-1

TRAPPIST-1 is an ultracool dwarf with a gaggle of seven planets discovered through transits (Gillon et al., 2017). It is included in the Mega-MUSCLES survey, an extension of the original MUSCLES survey from France et al. (2016), and the measured FUV line fluxes (*HST* STIS) and X-ray spectrum (*XMM-Newton* EPIC) are published in Wilson et al. (2021), where we discuss the implementation of our DEM method for this specific target. Wilson et al. (2021) also compares the MegaMUSCLES spectral energy distribution of TRAPPIST-1 to the `PHOENIX` model published in Peacock et al. (2019a). TRAPPIST-1 tests the fitting in a very low S/N regime constrained by a few FUV lines and a very faint X-ray spectrum, but we still get meaningful fits and constraints on the EUV flux (see Figures 2.20 and 2.22).

2.9.4 Comparing the Entire Sample

Figure 2.21 shows the DEMs of all the stars considered within this work and shows some preliminary trends with activity and spectral type: more active stars have a higher mean DEM while the decline in the DEM associated with the move from the transition region to the corona appears to shift to higher temperatures at cooler spectral types. With a more complete sample, we could go a step further to interpolate the EUV flux of cool dwarfs that lack observed FUV and X-ray data by relating the DEM to the more accessible stellar parameters $T_{\rm eff}$ and age, as traced by rotation and/or activity indicators from optical spectra. Determining the best method for this interpolation and testing its accuracy and precision is left to future work.

We summarize the data products of this chapter by plotting all of our DEM-generated EUV spectra scaled to the flux density observed at a distance of 1 AU from the host star in Figure 2.22. The slope of the spectra across the EUV seems to vary as a function of both spectral type and activity. The hotter stars seem to have more EUV flux between 800 to 900 Å while the more active stars have more EUV flux between 100 to 600 Å. These wavelength regions correspond to lines formed roughly at temperatures 2×10^5 and 3×10^6 K respectively (see Figure 2.1). AU Mic,

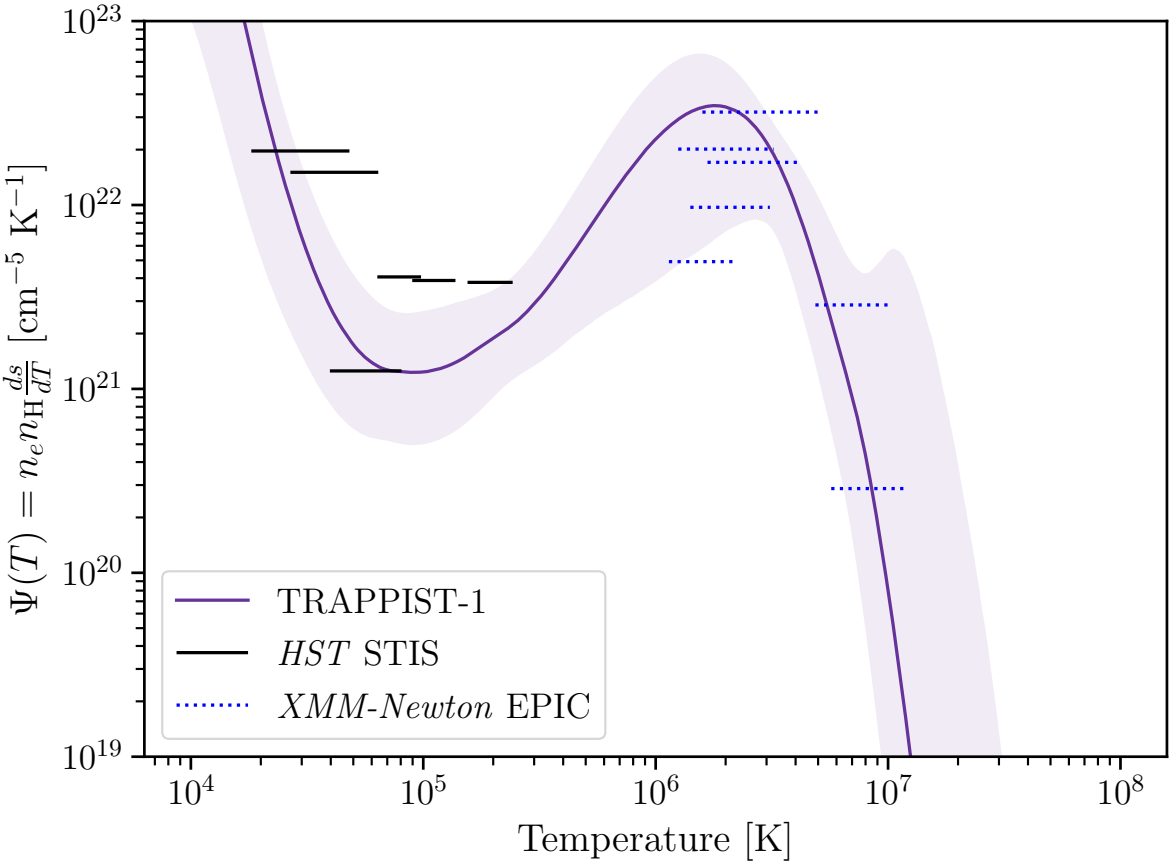

Figure 2.20: Comparing the DEM of TRAPPIST-1 fit to a quiescent X-ray spectrum from *XMM-Newton* EPIC and line fluxes from STIS, with $\overline{\Psi}(T)$ constraints shown as horizontal dotted blue and solid black bars respectively.

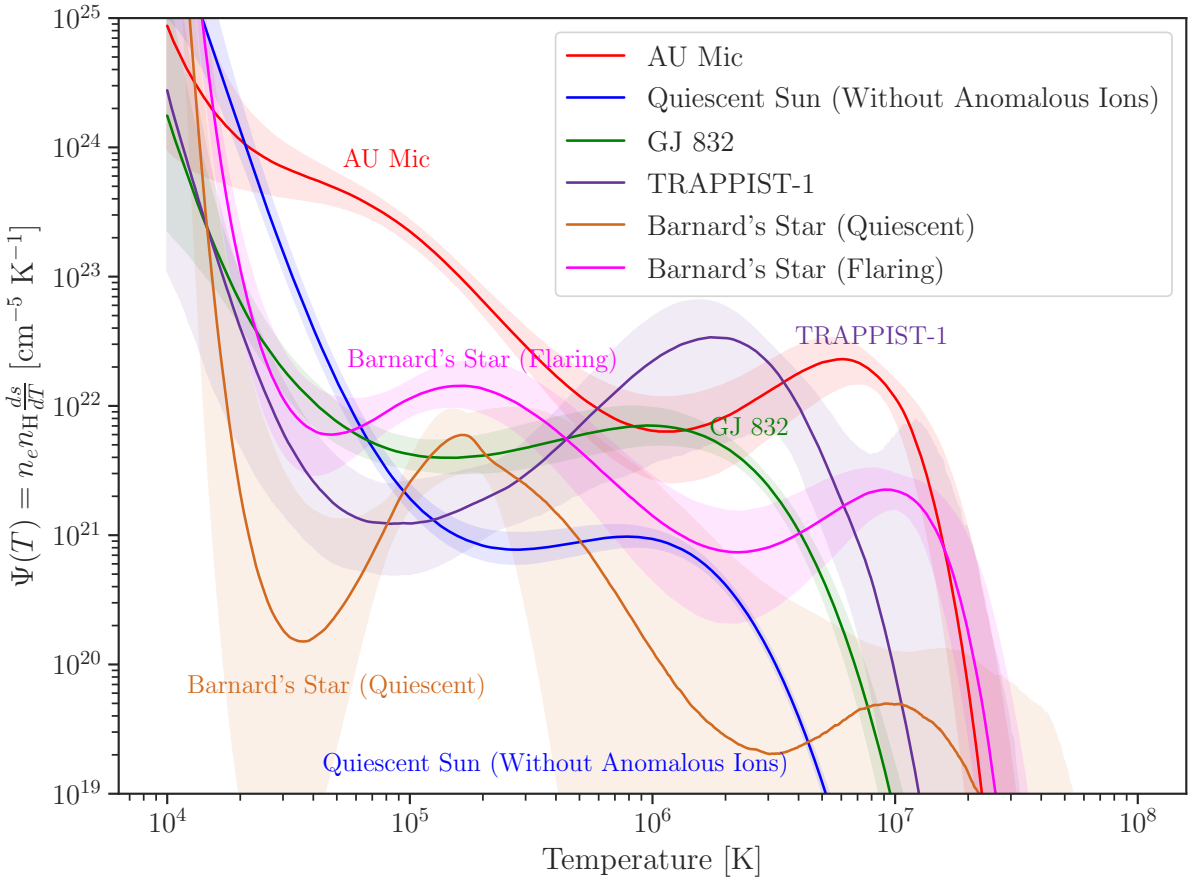

Figure 2.21: The DEMs of all stars considered in this chapter are plotted here with the solid line representing the median predicted value of $\Psi(T)$ and shaded intervals enclosing the 16^{th} to 84^{th} percentile intervals. Filling out this plot with more stars across a grid of effective temperature and stellar activity will allow us to investigate trends in the DEM and EUV spectra of cool dwarfs across the entire population.

which is one of the more active stars and also one of the hotter stars in this sample, has a roughly flat EUV spectrum. TRAPPIST-1, which is also very active but much cooler, shows a strong negative slope from 100 to 1000 Å. The spectral shape of the EUV is controlled by the relative strengths of the corona and chromosphere, and these preliminary observations of our EUV spectra conceptually agree with the findings of Linsky et al. (2020). Linsky et al. (2020) measured the relationship between X-ray and Lyman-α flux for a large sample of FGKM dwarfs and found that for older and relatively inactive stars, the inverse relationship between coronal emission and effective temperature is much stronger than the inverse relationship between chromospheric emission and effective temperature. Trends in the shape of the EUV spectrum generated by the DEM should be investigated along with trends in the DEM and the data used to inform the fitting, and our current sample is simply too small to make stronger claims than these extremely tentative observations. Furthermore, the overall shape of the EUV spectrum may be significantly altered by the inclusion of continuum processes and an analysis of trends without this source of emissivity is premature. Table 2.5 lists the integrated EUV flux at 1 AU, median $s-$factor, effective temperature, stellar radius, and distance for each star considered in this work.

2.10 Conclusions and Future Work

Our tests with the Sun show that with a low-resolution X-ray spectrum and the strongest FUV emission lines, we can predict the EUV flux to within a factor of 2 across the entire EUV region. Furthermore, our characterization of the uncertainties in our method show that our predicted EUV spectra are consistent with the data for the Sun. We have demonstrated that our choice of functional form is able to describe the DEM within the temperature region relevant to predicting EUV flux, and that uncertainties in the abundance and average electron pressure can be accounted for and propagated to the final output spectra. While our approach to fitting the DEM has serious limitations discussed in Sections §2.5.3 and §2.7, our tradeoff exchanging precision for simplicity allows us to fit DEMs and estimate EUV spectra for many more stars than methods which require laborious iterations, both manual and computational. The method can be refined in the future to

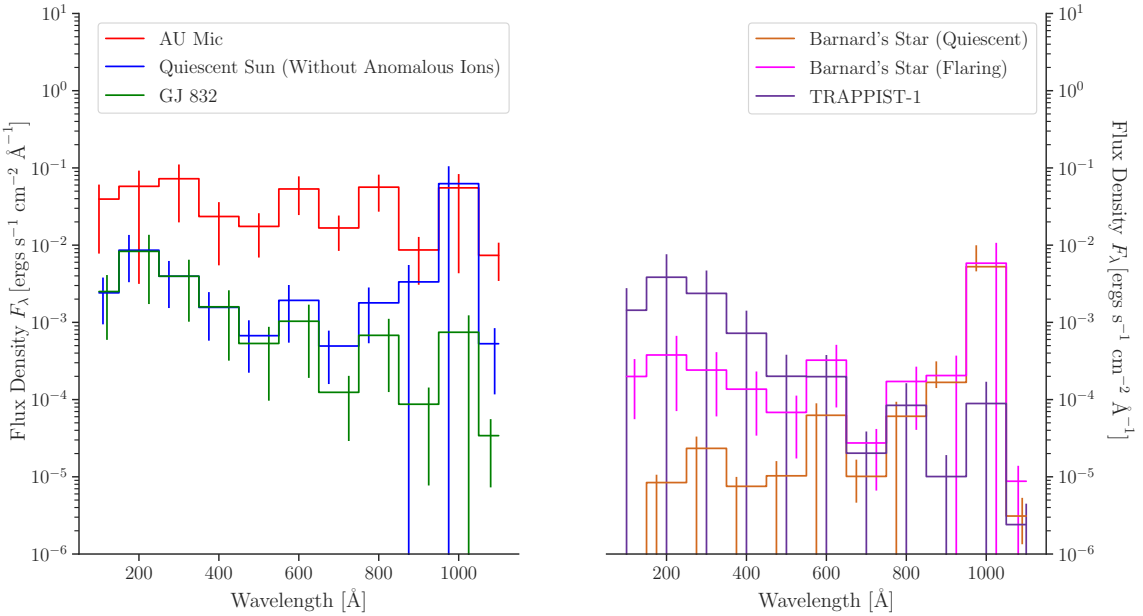

Figure 2.22: A comparison of all of our model spectra generated for the stars considered in this work, downsampled from a resolution of $R = \frac{\Delta\lambda}{\lambda} = 500$ to 100 Å wavelength bins, scaled to the flux received at 1 AU. The distance and radius assumed for each star is listed in Table 2.5, and can be scaled to surface flux or habitable zone distances by multiplying with the appropriate factor. On the left panel, we have the hotter stars of the sample: the Sun (spectrum generated from the DEM model without anomalous ions discussed in Section §2.5.3) in blue, AU Mic in red, and GJ 832 in green. On the right panel we have Barnard's Star in quiescence represented by the brown line, Barnard's Star while flaring shown in pink, and TRAPPIST-1 in dark purple. All the spectra shown have errorbars determined by the method described in Section §2.5.3.

handle different stellar abundances, to use temperature-pressure profiles from stellar atmosphere models, and to find a better way to handle the discrepant `CHIANTI` ionization equilibrium of the Na-like and Li-like isoelectronic sequences. Including the free-free and free-bound emission of hydrogen and helium species is possible with existing `CHIANTI` data and these emissivity sources will be accounted for in future DEM fits and EUV spectral reconstructions. The greatest problem with our current approach is the lack of elemental abundances tailored to individual stars based on their effective temperature and age. Updating the abundances we use and refitting the DEM may dramatically improve our precision, but this is left to future work.

Hubble is the only observatory with FUV spectroscopy and the capability to observe a large sample of M dwarfs, but its lifetime is limited and there will be no replacement in the next few decades. Given the interest in M dwarf planetary systems, a number of survey programs have proposed using *Hubble* to build up a spectral atlas of M dwarfs across the broad range of effective temperature and activity level represented within the spectral type. MUSCLES (France et al., 2016), HAZMAT (Shkolnik & Barman, 2014), FUMES (Pineda et al., in prep), and Mega-MUSCLES (Froning et al., 2019) are completed programs with available data while observations for MEATS, a *Hubble* survey targeting cool dwarf exoplanet hosts scheduled to be observed by *Webb* (HST-GO-16166, PI-France), are forthcoming. Between all these surveys and archival data, we will have enough FUV and X-ray data of cool dwarfs to start characterizing them as a population: fitting DEMs to all nearby cool dwarf stars with sufficiently available data and estimating their EUV flux. With a sufficiently comprehensive DEM library, it may be possible to interpolate DEMs for stars too faint for FUV or X-ray observations, and build on the work of Sanz-Forcada et al. (2011) to calculate the EUV luminosities of all known planet-hosting main-sequence stars. Until stellar atmosphere models become sophisticated enough to have a grid of models varying both effective temperature and stellar activity across the entire cool dwarf regime, or an EUV observatory (France et al., 2019, e.g.) is able to provide directly observed EUV spectra of nearby stars, differential emission measure techniques can satisfy the need for stellar EUV spectra which are physically informed and empirically calibrated.

Table 2.5. The DEM predictions for the integrated EUV flux at 1 AU and median $s-$factor uncertainty for each star considered in this chapter.

Star	EUV Flux at 1 AU	Median s	Effective Temperature	Stellar Radius	Distance
—	[erg s^{-1} cm^{-2}]	—	[K]	[$R_\odot$]	[pc]
Sun (Woods et al., 2009)	1.99	—	5772 [1]	1	4.848×10^{-6}
Sun (DEM fit to FUV + X-ray)[a]	$3.54^{+3.12}_{-2.12}$	0.60	5772[1]	1	4.848×10^{-6}
Sun (DEM fit without anomalous ions)[b]	$1.99^{+1.28}_{-1.15}$	0.57	5772[1]	1	4.848×10^{-6}
AU Mic	$31.9^{+21.8}_{-16.2}$	0.42	3700[2]	0.75[2]	9.979[2]
GJ 832	$1.66^{+1.30}_{-1.06}$	0.62	3657[3]	0.499[4]	4.965[5]
TRAPPIST-1	$0.762^{+1.30}_{-0.744}$	0.74	2516[6]	0.121[6]	12.43[6]
Barnard's Star (Quiescent)	$0.0183^{+0.109}_{-0.00860}$	0.43	3278[7]	0.178[7]	1.83[5]
Barnard's Star (Flaring)	$0.146^{+0.112}_{-0.0965}$	0.45	3278[7]	0.178[7]	1.83[5]

Note. — To enable scaling the spectrum to other quantities, we also list the stellar effective temperature, radius, and distance assumed in this work.

[a]This integrated flux is from the DEM fit to the Sun using the X-ray spectrum and FUV lines.

[b]This integrated flux is from the DEM fit to the Sun using the X-ray spectrum, EUV lines, and FUV lines excluding the anomalous ions N V, C IV, and Si IV.

References. — [1] Mamajek et al. (2015), [2] Plavchan et al. (2020), [3] Bailey et al. (2009), [4] Houdebine (2010), [5] Gaia Collaboration (2018), [6] Van Grootel et al. (2018), [7] Ribas et al. (2018)

Chapter 3

Stochastic Chromospheric Variability Across Stellar Rotation Period

3.1 Preface

This chapter is a lightly edited reproduction of work published in Duvvuri et al. (2023), where the majority of the analysis was conducted by myself with advice and input from the paper's co-authors, using data collected by the FUMES (Pineda et al., 2021a) observing program. The line-fitting process described in this work was updated for the work described in Chapter 5.

3.2 Introduction

Stellar activity is a catch-all term for various behaviors in the stellar atmosphere produced by non-thermal heating processes, processes which create distinct layers above the photospheres of most stars: the chromosphere, transition region, and corona (Linsky, 2017). For low-mass stars, nearly all the high-energy emission (from wavelengths $< 2000\,\text{Å}$) is a product of stellar activity, varying over time as the stellar magnetic and atmospheric structures interact. One category of magnetic activity is the presence of surface inhomogeneities (spots, faculae, plages) which contribute emission distinct from the rest of the photosphere on varying timescales: cycling in and out of view over the rotation period of the star which can be anywhere between a few hours and a year (Newton et al., 2016); waxing and waning over weeks as the surface features erupt, evolve, and dissipate (Basri & Shah, 2020); and growing or fading over decades as the distribution, frequency, and strength of the surface features are changed by the cycling of the stellar magnetic field (Wilson, 1968). Another category is flaring, which is a seconds-to-hours burst of emission produced by magnetic reconnection

events depositing energy. Flare emission can manifest as broadband enhancements to the optical, ultraviolet, and X-ray continua, radio synchrotron/gyrosynchrotron emission, and/or enhancements to emission lines that grow in amplitude, broaden, and sometimes blue/redshift during the flare (Kowalski et al., 2013; MacGregor et al., 2021). Finally, all forms of stellar activity are subject to evolution over the megayear timescales of angular momentum evolution (Skumanich, 1972).

As the study of M dwarfs has been intensified by the interest in their terrestrial exoplanets, the time-variability of magnetic activity has been studied both for its effects on exoplanet observations (Llama & Shkolnik, 2015; Rackham et al., 2019) and for its physical impact on the formation, evolution, and retention of exoplanetary atmospheres (Shields et al., 2016). This motivates studying the high-energy emission of low mass stars across a wide range of rotation periods, which implicitly correspond to a wide range of activity levels and ages.

The Far Ultraviolet M-dwarf Evolution Survey (FUMES) collected FUV spectra between $1100-1736$ Å of a sample of intermediate activity stars (whose stellar properties are listed in Table 3.1) to complement existing datasets and enable new studies of the rotational evolution of magnetic activity for M-dwarfs. Pineda et al. (2021a), FUMES I, measured the flux of FUV emission lines formed in the transition region to study the rotation-activity relation in this wavelength/structural regime. Youngblood et al. (2021b), FUMES II, reconstructed the intrinsic Lyman-α emission for the FUMES sample and demonstrated that the wings of the Lyman-α line can be used to infer the density of the chromosphere. This work, FUMES III, complements the UV data with optical spectroscopic measurements of the Balmer series and Ca II H and K emission lines to study the stochastic variability of the chromosphere and transition region on short timescales comparable to exoplanet observations. When we use the term "stochastic", we are referring to brief changes that cannot be clearly identified as flares based on their amplitude or light curve structure. This analysis builds on existing literature examining the stochastic emission line variability of low mass stars in the ultraviolet (Loyd & France, 2014) and the optical (Lee et al., 2010; Kruse et al., 2010; Medina et al., 2022), but extends it by applying similar analytical techniques to both of these disparate wavelength (and implicitly structural) regimes for a common sample of stars on similar timescales.

Section §3.3 discusses the optical observations and their reduction (§3.3.1), and the measurement of equivalent widths and creation of spectral line light curves to look for variability (§3.3.2). Section §3.4 describes our analysis of the UV data to create similar spectral line light curves for transition region emission lines. In Section §3.5 we quantify the significance of observed variability and compare the variability of different lines to each other and for each line as a function of Rossby number. Finally in Section §3.6 we summarize our findings, discuss the physical and observational implications of our work, and conclude by recommending some observational and theoretical work that could help determine the origin of the stochastic variability described in this study.

3.3 Optical Spectra

The bulk of the optical emission from low mass stars originates from the photosphere, which can be thought of as the "surface" of the star, but the Balmer series and Ca II H and K lines are prominent optical emission features that are formed higher in the magnetically heated chromosphere. The red tinge of the Hα Balmer line coloring the solar limb near the endpoints of an eclipse is how the chromosphere was first identified and named as a distinct stellar atmospheric structure (Lockyer, 1868). The Balmer series lines form through a combination of photoionization, recombination, and collisional excitation while the Ca II H and K lines are collisionally dominated (Cram & Giampapa, 1987). Observing multiple optical chromospheric emission lines and comparing them to the photospheric continuum traces the physics of magnetic heating in the chromosphere relative to the local thermodynamic equilibrium of the photosphere.

While most M dwarfs display chromospheric Ca II H and K emission, only a fraction of these also show the Hα line in emission (Stauffer & Hartmann, 1986). The least active M dwarfs show shallow Hα absorption, and an increase in chromospheric density first deepens the Hα absorption, then fills in the absorption feature with emission, and finally exceeds the photospheric continuum level to become an emission line (Cram & Giampapa, 1987). Shallow Hα absorption can therefore correspond to either an extremely inactive or intermediately active M dwarf, requiring another activity indicator like Ca II emission, flare frequency, or UV emission to break the degeneracy.

Table 3.1. These are the stellar parameters for the subset of the FUMES sample considered in this chapter. All parameters are from Table 2 of Pineda et al. (2021a) as determined in Pineda et al. (2021b). The column titled "Hα EW$_{\rm quiescent}$ lists the photospheric contribution to the Hα equivalent width of the star, calculated using Equation 2 in Newton et al. (2017) and the listed stellar masses as inputs.

Name	Mass	Radius	$T_{\rm eff}$	$P_{\rm rot}$	Rossby Number	Hα EW$_{\rm quiescent}$
–	$[M_\odot]$	$[R_\odot]$	[K]	[days]	–	Å
HIP 112312	$0.247^{+0.018}_{-0.015}$	$0.688^{+0.015}_{0.016}$	3173^{+25}_{-22}	2.355	0.0249	0.157
LP 247-13	0.495 ± 0.013	0.49 ± 0.02	3511^{+79}_{-76}	1.289	0.0278	0.252
CD-35 2722	0.572 ± 0.002	0.561 ± 0.003	3727^{+8}_{-6}	1.717	0.0459	0.299
HIP 17695	$0.435^{+0.011}_{-0.014}$	$0.502^{+0.008}_{-0.007}$	3393^{+20}_{-21}	3.87	0.0708	0.226
HIP 23309	$0.785^{+0.009}_{-0.01}$	0.932 ± 0.014	3886^{+28}_{-27}	8.6	0.379	0.558
GJ 410	0.557 ± 015	0.549 ± 0.024	3786^{+89}_{-83}	14	0.385	0.289
GJ 49	0.541 ± 0.015	0.534 ± 0.023	3713^{+86}_{-81}	18.6	0.472	0.278
G 249-11	0.237 ± 0.006	0.255 ± 0.01	3277^{+71}_{-68}	52.76	0.571	0.152
LP 55-41	0.41 ± 0.01	0.416 ± 0.017	3412^{+75}_{-73}	53.44	0.905	0.216

Table 3.2. APO/ARC 3.5m DIS/1.5”

UT Date	Star	Initial Airmass	Exposure Duration [s]	$N_{\text{exposures}}$
2017-05-01	GJ 410	1.03	180	40
2017-05-01	Feige 56*	1.22	360	1
2017-09-14	LP 247-13	1.13	360	9
2017-09-14	G 191B2B*	1.26	360	1
2017-09-14	LP 55-41	1.33	420	4
2017-09-14	G 249-11	1.32	480	5
2017-09-20	GJ 49	1.16	180	2
2017-09-20	GJ 49	1.15	150	21
2017-09-20	G 191B2B*	1.26	360	1
2017-09-20	GJ 4334	1.28	360	3
2017-09-20	GJ 4334	1.3	420	13

*These stars were used as flux standards for their respective observing nights.

3.3.1 Observations and Reduction

We observed 6 northern FUMES targets with the Dual Imaging Spectrograph (DIS) on the Astrophysical Research Consortium (ARC) 3.5 meter telescope at the Apache Point Observatory (APO). DIS is a dual-channel spectrograph with a resolving power $R = \frac{\lambda}{\Delta\lambda}$ ranging from 7000 at the bluest wavelengths to 12000 at the reddest wavelengths for our observing settings. We used the B1200 and R1200 gratings centered on 4400 and 6400 Å, covering the wavelength ranges 3770 – 5030 Å and 5880 - 7000 Å for the blue and red arms respectively. We observed 4 southern FUMES targets with the Gemini Multiple Object Spectrograph on the Gemini South telescope (GMOS-S) at the southern site of the Gemini Observatory using the B600 grating centered on either 5200 or 5300 Å with a 0.5” mask. The GMOS-S covered wavelengths from 3640 – 6780 with the 5200 setting and 3740 – 6880 with the 5300 setting, with a resolving power of 7000 (blue end) $< R <$ 13000 (red end) across the observed wavelength regime. All APO/ARC 3.5m DIS observations are listed in Table 3.2, and all Gemini GMOS-S observations are listed in Table 3.3.

We reduced the spectral data from both Gemini and DIS by adapting the pyDIS package (Davenport et al., 2016). We bias-subtracted, flat-fielded, and then traced the spectrum with a

Table 3.3. Gemini South GMOS-S/0.5" B600 Grating

UT Date	Star	Central Wavelength [nm]	Initial Airmass	Exposure Duration [s]	$N_{\text{exposures}}$
2017-09-24	HIP 112312	520	1.00	120	6
2017-09-24	HIP 112312	530	1.00	120	6
2017-09-24	LTT 9239*	530	1.02	90	1
2017-09-24	CD-35 2722	520	1.17	120	6
2017-09-24	CD-35 2722	530	1.13	120	6
2017-11-24	HIP 23309	520	1.65	120	6
2017-11-24	HIP 23309	530	1.55	120	6
2017-11-24	EG 21*	520	1.34	50	1
2017-12-27	LTT 1020*	520	1.41	90	1
2017-12-27	HIP 17695	520	1.27	120	6
2017-12-27	HIP 17695	530	1.33	120	6

*These stars were used as flux standards for their respective observing nights.

cubic spline. We fit a low-order polynomial to manually identified lines in a CuAr lamp for Gemini data and a HeNeAr lamp for APO data to wavelength calibrate the spectra. We treated the blue and red detector arms of DIS separately as their own datasets. For the Gemini data, we adapted the pyDIS code to match the nature of the raw data; stitching together the multiple chips into one 2D image, filling in the gaps across chips with NaN values, and saving the read noise and gain properties of each chip into a corresponding 2D array instead of the singular float values assumed by the standard pyDIS package. For both the Gemini and DIS data we extracted the spectra using simple aperture box extraction. The code for both reduction pipelines has been included in separate subdirectories of the Zenodo repository associated with this chapter[1] . We used the spectral standard stars from the IRAF Spec50Cal catalog (identified in Tables 3.2 and 3.3 with an asterisk*) to flux calibrate the spectra, referring to data files included in `pydis` (Davenport et al., 2016).

3.3.2 Analysis

While reducing the optical spectra we noticed a significant flare in the GJ 4334 data and excluded this star from this work's analysis of short-term stochastic variability. For the remaining targets we restricted our analysis to lines that were clearly identifiable in the spectrum, limiting the lowest activity stars to just measurements of Ca II H and K and/or Hα.

3.3.2.1 Equivalent Widths

We measured equivalent widths (EWs) for all optical lines following the convention that negative values correspond to emission

$$\mathrm{EW} = \int_{\lambda_{\mathrm{low}}}^{\lambda_{\mathrm{upp}}} \left(1 - \frac{\mathrm{F}_\lambda}{\mathrm{F}_{\mathrm{continuum}}}\right) \mathrm{d}\lambda \qquad \mathrm{Note: EW} < 0 \Rightarrow \text{ emission} \tag{3.1}$$

where the interval [λ_{low}, λ_{upp}] defines a narrow wavelength window centered on the spectral line and $F_{\mathrm{continuum}}$ is the median flux density value evaluated across all datapoints falling within two

[1] https://doi.org/10.5281/zenodo.6909473 (European Organization For Nuclear Research & OpenAIRE, 2013)

continuum regions defined by wavelength intervals on either side of the spectral line. The typical windows for each line are listed in Table 3.4, although some exposures or targets required individually shifting or restricting windows to ensure the continuum value matched the base of the emission line. These changes to the positions of the windows were < 3 Å and always chosen such that the median continuum intensity value was at the base of the emission line. Changes to the width of the line windows were more significant and chosen with respect to each target to capture the entirety of the line. The shape of the spectrum beneath the Balmer lines changes significantly across the range of effective temperatures in our sample and any choice of windows that is consistent across all stars would fail to accurately capture the true equivalent widths for some of the sample. All wavelength windows were internally consistent for each star to avoid interfering with the measurement of variability.

We assume that the error on the continuum value is negligible when propagating the errors on the numerically measured equivalent widths because it is averaged over many datapoints. We did not fit the lines using Gaussian profiles and a polynomial continuum for a combination of two reasons. The first is that some of the intermediate activity stars in our sample have Balmer lines that are not well described by a Gaussian profile because the combination of line formation processes yields something close to a flat line. The second is that the bluer Balmer lines are in spectral regions that do not have a clearly identifiable continuum, but rather appear to be a superposition of many molecular absorption features that cannot be easily described by a spline or polynomial function during fitting. Equivalent widths were a more stable measurement across all lines, exposures, and targets and therefore more useful for assessing and comparing variability.

3.3.2.2 Optical Emission Line Variability

With time series measurements of multiple emission lines for the majority of the FUMES sample we were able to assess the minute-to-hour variability of chromospheric emission in these low-mass stars and look for trends between lines and across stars. Figure 3.1 shows the variability of LP 247-13's spectrum in three $800\,\mathrm{km\,s^{-1}}$ wide regions centered on the continuum-normalized

Table 3.4. These were the typical wavelength windows used to measure the equivalent widths in both the APO and Gemini data. The windows were selected with reference to Table 2 of Walkowicz & Hawley (2009) but not strictly followed. Some exposures required minor modifications to the wavelength windows shown here and the tables associated with all equivalent width measurements are available in the linked data repository.

Spectral Line	Vacuum Wavelength [Å]	Wavelength Window Width*[Å]	Blue Continuum	Red Continuum
Hα	6562.79	2 – 14	6500 – 6575	6575 – 6625
Hβ	4861.35	14	4840 – 4850	4875 – 4885
Hγ	4340.72	10	4270 – 4320	4320 – 4360
Hδ	4101.7	9	4060 – 4080	4120 – 4140
Ca II H + Hϵ	3968.47, 3970.1	12	3952.8 – 3956	3975.8 – 3982
Ca II K	3933.6	8	3922.8 – 3926	3943 – 3946
Hζ	3889.1	8	3850 – 3880	3900 – 3910
Hη	3835.4	8	3801 – 3810	3845 – 3854
H10	3797.7	6	3779 – 3785.6	3806 – 3814

*Varied depending on the width of the line, typically 14 Å but less for cases of narrow absorption

Hα, Ca II K, and Hδ emission lines. The black lines and errorbars shows the median value of the continuum normalized flux density across all exposures and the corresponding error. The blue and red shaded regions span the gap between the median and the 16th and 84th percentiles values respectively. Note that this is variability in the emission line relative to the continuum, so this indicates variability in the ratio between chromospheric and photospheric emission that carries forward to the measurements of equivalent widths. Photospheric emission varies by less than a few percent over the course of a full rotation period for low-mass stars like those in our sample (Newton et al., 2016), and can therefore be neglected in these observations taken over the course of a single night. Normalizing to the continuum removes variations due to observational constraints like seeing, transparency, and instrumental effects.

The line profiles show measurable variation in both amplitude and width over the course of the observation. LP 247-13 was shown as a representative example, and similar variations were observed for the other FUMES stars where we were able to measure lines other than Hα. Figure 3.2 shows the time series of equivalent width measurements for all Balmer lines up to H10 and the Ca II H and K lines for HIP 23309, and Figure 3.3 shows the time series of equivalent width measurements for three emission lines (Hα, Hη, and Ca II K) across the entire sample analyzed in this work. While analyzing the equivalent width time series of Gemini data, we noticed that some of the series showed offsets after the break in the middle corresponding to time spent shifting the central wavelength setting of the grating. We attribute this offset to using only one setting when measuring a standard star spectrum for flux calibration. The offsets vary from 1$-$10% depending on the target and spectral line and can be seen most clearly in the right panel of Figure 3.2 where the median equivalent width of Ca II K shifts from -10 to -11 Å after the gap.

In Figure 3.1 the variability of Hα is small, only slightly exceeding the errorbars and a small absolute magnitude of variation between the 16^{th} and 84^{th} percentile boundaries of the continuum normalized spectrum. This behavior is also apparent in the time series for the Hα equivalent width measurements of HIP 23309 shown as dark red in Figure 3.2, and again mirrored by nearly every star in the bottom panel of Figure 3.3.

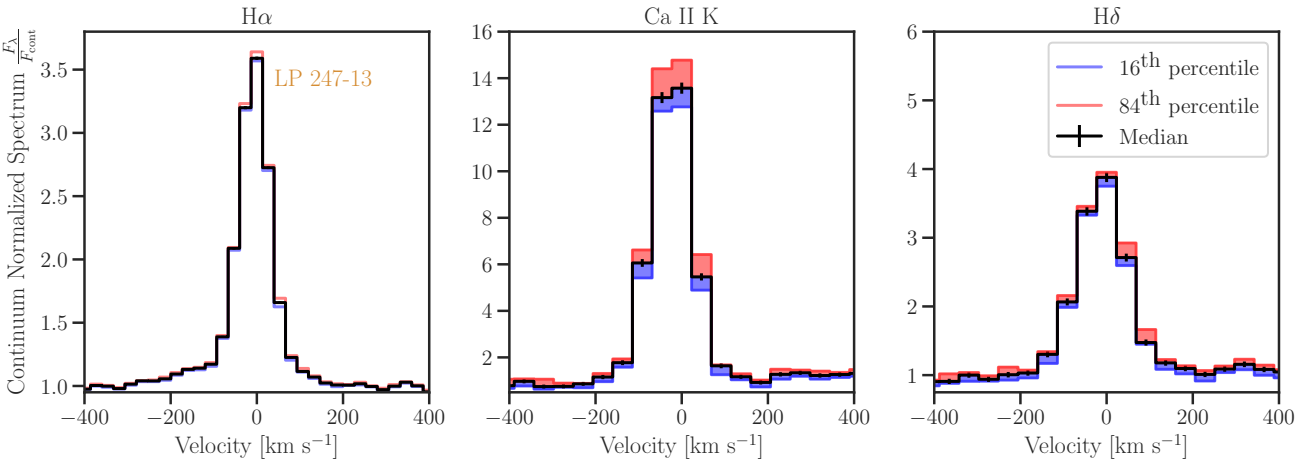

Figure 3.1: Using LP 247-13 as an example, we demonstrate the variability of three optical emission lines in individual panels; Hα on the left, Ca II K in the middle, and Hδ on the right. We first normalized the spectra from each individual exposure, then resampled them onto a common wavelength grid, and then identified the median spectrum with associated error bars and boundaries for the 16$^{\text{th}}$ and 84$^{\text{th}}$ percentile values of the spectrum in each wavelength bin. The median spectra and their errors are drawn in solid black while the gaps between the median and 16/84$^{\text{th}}$ percentile boundaries are filled in with blue/red respectively. The variability exceeds the error bars in each panel but the magnitude of variation relative to the continuum is higher for Ca II K and Hδ than for Hα, following a trend shared by the remainder of the sample where we measured lines other than Hα.

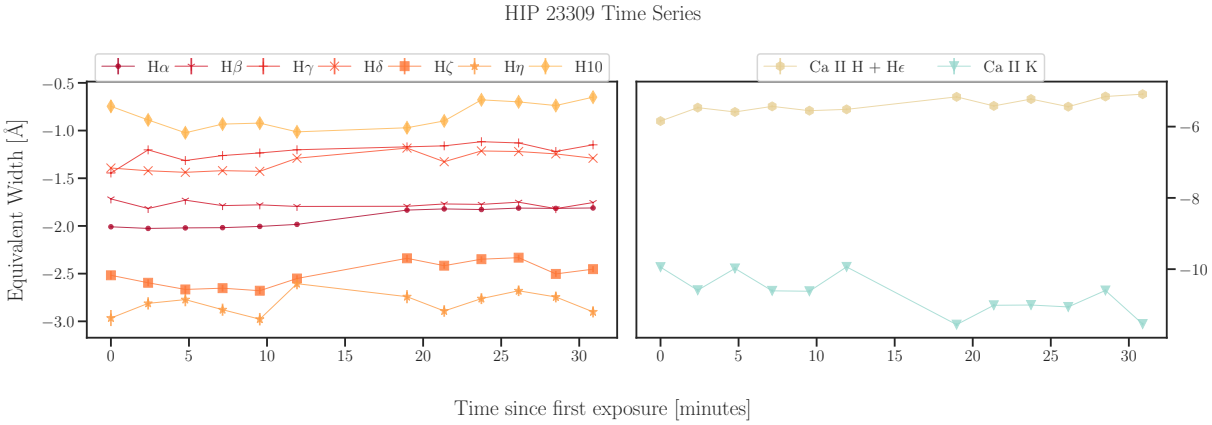

Figure 3.2: HIP 23309 is one of the more active, UV-bright stars in our sample, and as a result its spectra have signal-to-noise making them ideal for variability analysis on the shortest time scales. Each line's time series is represented by a unique marker shape and color with errorbars, although the errors are minuscule and rarely extend beyond the marker itself. The time series for Hα's equivalent width, shown in the darkest red line here, is nearly perfectly flat with no observable long-term trend or short-term variability exceeding the error bars of individual measurements. The lines with the greatest variability are the Ca II H and K lines which have been plotted in a separate panel for visual clarity, although some of this variability is an offset between grating settings that we attribute to flux calibrating with a standard star spectrum taken with just one of the two settings.

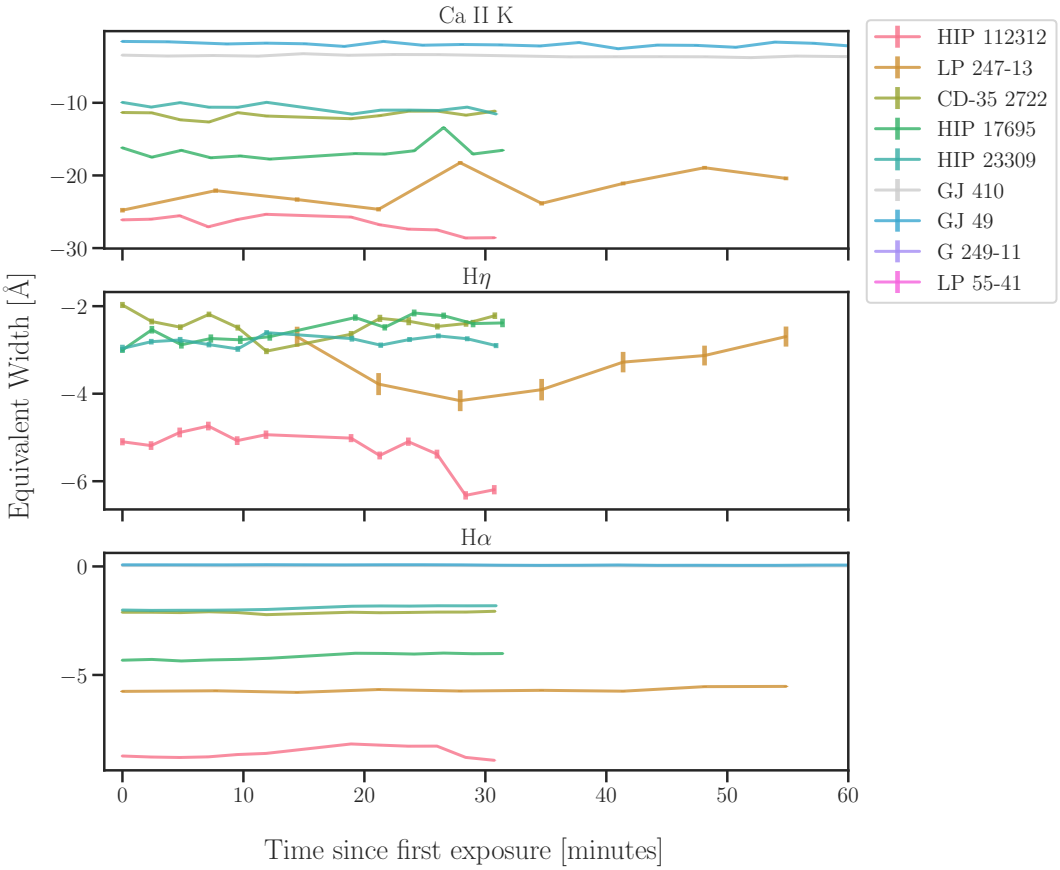

Figure 3.3: This figure shows the time series measurements for the equivalent widths of Ca II K (top panel), Hη (middle panel), and Hα (bottom panel) for every star in the sample with measurements of those respective lines. No variability is seen in Hα except for one star, HIP 112312. Ca II and Hη both exhibit significant variability in all targets. Note that all lightcurves are plotted with errorbars, but that the scale of the error is minuscule, even in Figure 3.2 which focuses on the optical time series data for just one star.

3.3.2.3 Balmer Decrements

The Balmer decrement is the flux ratio of each Balmer line (numerically integrated in our equivalent width analysis) relative to either Hβ or Hγ and can be used to distinguish between the different photoelectric processes forming the Balmer lines (Woolley, 1936). Beyond the limiting cases of pure recombination or collisional excitation, radiative transfer models of stellar atmospheres can be tuned to best match the available data and infer the physical conditions of the photosphere and chromosphere (Houdebine & Doyle, 1994; Allred et al., 2006; Kowalski et al., 2017). Our measurements of the Balmer series up to H10 provide a valuable dataset to test models of active low-mass stars, bolstered by the measurements of Ca II H and K which are formed purely by collisional excitation and provide useful points of comparison to the Balmer series (Cram & Giampapa, 1987). Furthermore, our measurements of the short-term variability of the Balmer series presents opportunities to test models of the inhomogeneity of stellar surfaces and magnetic activity that contribute to this observed variability as perturbations to a steady-state model stellar atmosphere.

We compare the ratio of numerically integrated fluxes for the Balmer lines within individual flux-calibrated exposures to the exposure's integrated flux measurement of Hβ to calculate the decrement for each line in each exposure. We do not apply any correction from the photospheric contribution to the Hα flux in the decrement analysis to be consistent with the past literature (Hawley et al., 1996; Walkowicz & Hawley, 2009; West et al., 2011). Figure 3.4 shows the time series of decrements (except Hβ which is unity by definition) for CD-35 2722 as a representative example while Figure 3.5 shows the decrement values of all FUMES stars for which we were able to measure the higher order Balmer lines. Figure 3.5 also shows the variability of the decrements with errorbars indicating the maximum range of decrement values. The most variable decrement for most stars is Hα, which is a consequence of the high variability of Hβ relative to the mostly constant Hα (see Figure 3.3).

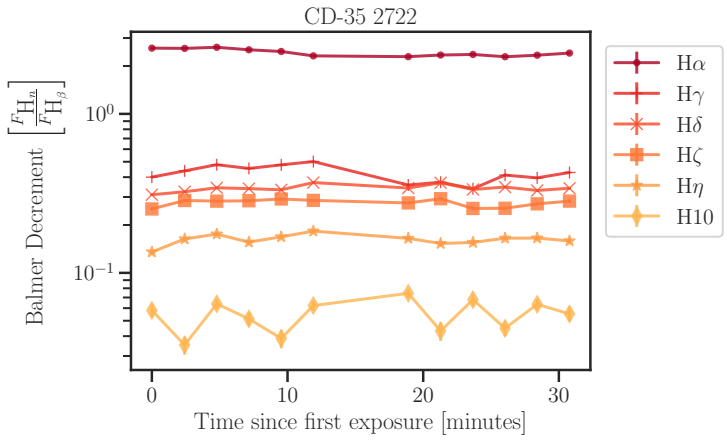

Figure 3.4: On a logarithmic scale, the time series of CD-35 2722's Balmer decrements show variations exceeding the error bars of individual measurements. A stellar atmosphere model allowed to vary over time with different magnetic heating processes could compare the scale of its decrement variability to this dataset.

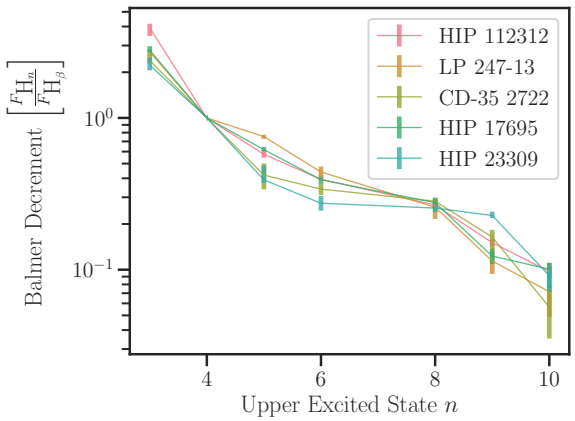

Figure 3.5: This figure shows the Balmer decrements for all stars in the FUMES sample for which we were able to measure the higher order Balmer lines. The errorbars on the points represent the maximum range of values for the decrement across the time series for that emission line. The values of the Balmer decrements are also recorded in Table 3.3.2.3.

Table 3.5. This table list the median, minimum, and maximum values of the Balmer decrements relative to Hβ for the stars where we were able to measure the higher order lines. The stars are ordered by Rossby number with the lowest/fastest Rossby number on top, corresponding to the most active star.

Star	Hα	Hγ	Hδ	Hζ	Hη	H10
HIP 112312	$3.924^{+0.249}_{-0.456}$	$0.576^{+0.039}_{-0.030}$	$0.394^{+0.027}_{-0.006}$	$0.267^{+0.018}_{-0.007}$	$0.151^{+0.008}_{-0.009}$	$0.097^{+0.014}_{-0.008}$
LP 247-13	$2.723^{+0.097}_{-0.168}$	$0.752^{+0.023}_{-0.025}$	$0.440^{+0.038}_{-0.030}$	$0.258^{+0.035}_{-0.042}$	$0.114^{+0.025}_{-0.020}$	$0.072^{+0.007}_{-0.023}$
CD-35 2722	$2.389^{+0.235}_{-0.101}$	$0.420^{+0.081}_{-0.082}$	$0.340^{+0.030}_{-0.030}$	$0.283^{+0.010}_{-0.030}$	$0.164^{+0.019}_{-0.029}$	$0.057^{+0.018}_{-0.021}$
HIP 17695	$2.793^{+0.174}_{-0.096}$	$0.618^{+0.026}_{-0.014}$	$0.392^{+0.018}_{-0.023}$	$0.276^{+0.023}_{-0.024}$	$0.123^{+0.013}_{-0.014}$	$0.101^{+0.010}_{-0.025}$
HIP 23309	$2.228^{+0.274}_{-0.169}$	$0.391^{+0.095}_{-0.018}$	$0.274^{+0.031}_{-0.029}$	$0.255^{+0.020}_{-0.015}$	$0.228^{+0.014}_{-0.009}$	$0.091^{+0.014}_{-0.020}$

3.4 UV Spectra

The brightest far ultraviolet lines are formed in the upper chromosphere (Lyman-α, C II) and transition region (C IV, N V, Si III, Si IV). The transition region is a physically thin structure that spans a wide range of temperatures, bridging the 10^4 K chromosphere and 10^6 K corona. FUV emission lines formed here can be used to trace the strength of magnetic heating across this structure, and Linsky et al. (2020) and Pineda et al. (2021a) show possible trends in the luminosity of these lines as a function of Rossby number that imply the decline of magnetic heating as stars spin down is first apparent in the corona, then progressively moves inward through the transition region to the chromosphere. We succeed this work to see if the variability of the FUV emission sheds further light on the nature of stellar magnetism and spin-down.

3.4.1 HST Data and Analysis

The FUMES program collected UV spectra using the Space Telescope Imaging Spectrograph (STIS) on *Hubble Space Telescope* (*HST*). Spectra were obtained using the FUV-MAMA detector and the G140L grating for the majority of the targets except HIP 112312 and HIP 17695, for which we used the echelle E140M grating instead. All spectra were taken using the TIME-TAG mode to assess the variability of UV transition region emission lines. See Pineda et al. (2021a) for a complete description of the observations.

We use `spectralphoton` (Loyd et al., 2018b,a) to divide the photon events into time bins of equal duration chosen for each star such that we are able to measure the flux of the N V doublet to 30% precision in an individual time bin's spectrum. This criterion was chosen because N V is one of the weaker lines and 30% seemed like a reasonable compromise between S/N and lightcurve cadence. The durations for each star are listed in Table 3.4.1. We observe two significant flares from GJ 4334 and GJ 410 where the count rate changed by a factor > 5. The GJ 4334 flare was observed simultaneously by *HST* and from APO. The analysis of both of these flares is left to future work and our analysis of the short-term stochastic UV variability excludes these high-energy events.

With these obvious flares excised, we measured the integrated line fluxes of the N V, Si IV, C IV doublets, the C II 1335 Å multiplet, and the He II 1640 Å multiplet for each time bin. We convolve the linespread functions of the observing modes associated with each spectrum during the linefitting process[2] . We fit the lines as Gaussian profiles atop a sloped continuum within windows listed in Table 3.4.1. The C II and He II multiplets were both fit using single Gaussian profiles because we lacked the resolution and S/N to distinguish multiple components. For the N V, Si IV, and C IV doublets we performed a joint fit of both lines in the doublet using Gaussian profiles for each. We used the `astropy.models` framework to optimize the fit using the Levenberg-Marquardt non-linear least-squares method (Levenberg, 1944; Marquardt, 1963). Figure 3.6 shows an example best-fit to the C II multiplet and N V doublet for the first time bin spectrum of CD-35 2722.

3.4.1.1 Ultraviolet Emission Line Variability

Pineda et al. (2021a) discusses a long-term trend in the countrate lightcurve for HIP 23309, uniform across the entire FUV spectrum and possibly caused by guiding issues affecting the fraction of starlight that fell on the slit. We follow the method described in Pineda et al. (2021a) by fitting a third-order polynomial to the trend and dividing it out. The maximum deviation of the countrate from the mean before correcting the trend was $< 20\%$.

[2] https://www.stsci.edu/hst/instrumentation/stis/performance/spectral-resolution

Table 3.6. The duration of time bins to divide up UV photon events, mimicking exposures, chosen for each star.

Name	Time Bin Duration [s]
HIP 112312	500
LP 247-13	200
CD-35 2722	150
HIP 17695	500
HIP 23309	100
GJ 49	300

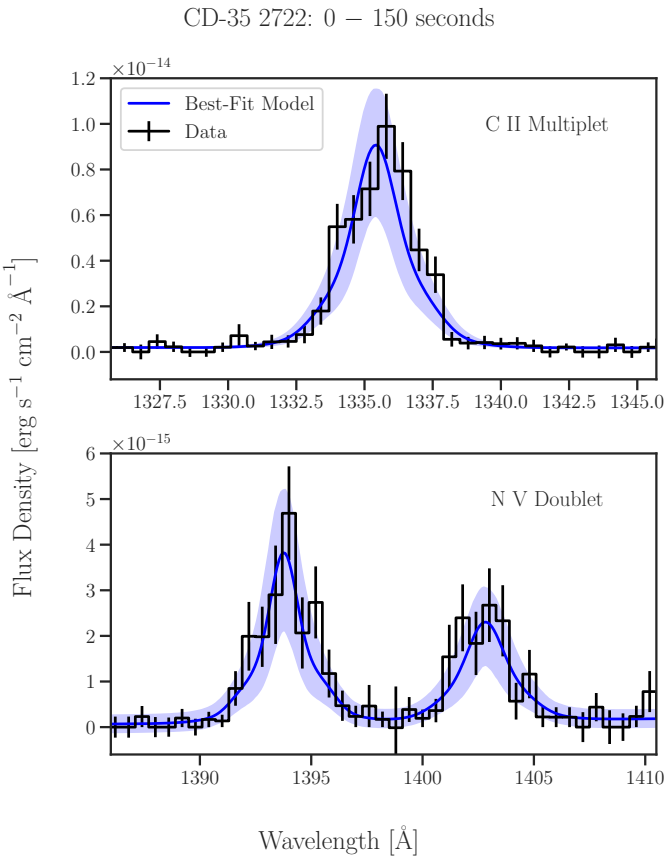

Figure 3.6: This figure demonstrates the line-fitting process for the first time bin spectrum of CD-35 2722, including photon events that occurred during the first 150 seconds of observation. The panels show the data in black and best-fit model in blue for the C II multiplet on top and the N V doublet on the bottom. The blue swath represents the 1σ boundaries of the model fit. Both fits include a sloped continuum, although the slope is very shallow, and the C II multiplet is fit with a single Gaussian while the N V doublet is fit using two Gaussians. The models are convolved with the linespread function before evaluating the fit-statistic.

Table 3.7. These ultraviolet lines are formed in the transition regions of low-mass stars (France et al., 2016). We fit them as Gaussian profiles convolved with the instrumental line-spread function.

Spectral Line	Vacuum Wavelength(s) [Å]	Wavelength Window [Å]
N V doublet	1238.82, 1242.806	1227.6 – 1254.0
C II 1335 multiplet	1334.53, 1335.66, 1335.71	1324.0 – 1347.4
Si IV doublet	1393.76, 1402.77	1381.8 – 1414.8
C IV doublet	1548.19, 1550.78	1535.5 – 1558.6
He II 1640 multiplet	1640.33 – 1640.54	1627.9 – 1653.7

After correcting for these long-term trends and fitting line profiles, we prepare light curves of the integrated flux for all the measured lines, analogous to the optical line light curves (with the caveat that now a higher value indicates more emission). Figure 3.7 shows all the light curves for emission lines measured in the spectrum of HIP 23309, one of the more active and UV-bright stars in the sample. While there is significant point to point scatter, the changes are roughly the same scale as the error bars associated with each datapoint. Figure 3.8 shows all measured line light curves for three emission lines: N V on top, Si IV in the middle, and C IV on the bottom. The light curves for other stars also show scatter consistent with the error bars. To meaningfully compare the variability between lines with statements about statistical significance, we need to quantify the intrinsic variability of line light curves in both the optical and ultraviolet datasets.

3.5 Quantifying and Comparing Variability

Our data lack the cadence or baseline required to model the variability with a sophisticated functional form or analyze a frequency power spectrum. To quantify the variability we model each light curve as a Gaussian distribution with the mean fixed at the median value of each light curve and a variance that is the quadrature sum of the measurement uncertainty and an intrinsic variability term. Assuming the underlying photospheric continuum has not changed between exposures,

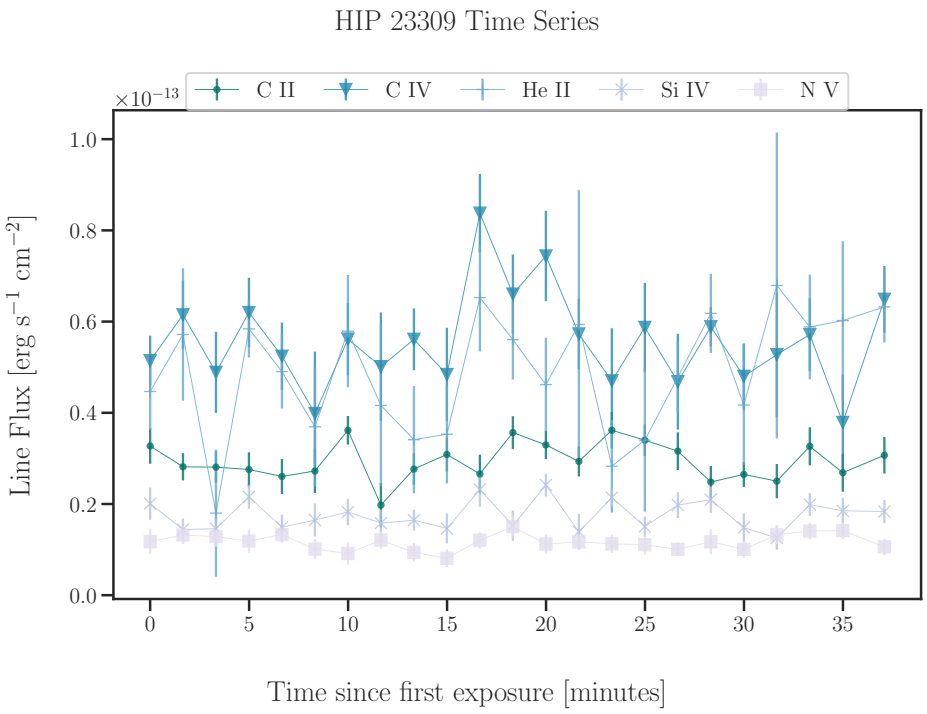

Figure 3.7: This figure shows the time series of UV line flux measurements for HIP 23309. Unlike Figure 3.2, the point-to-point variability is not visibly distinguishable from the photometric uncertainty.

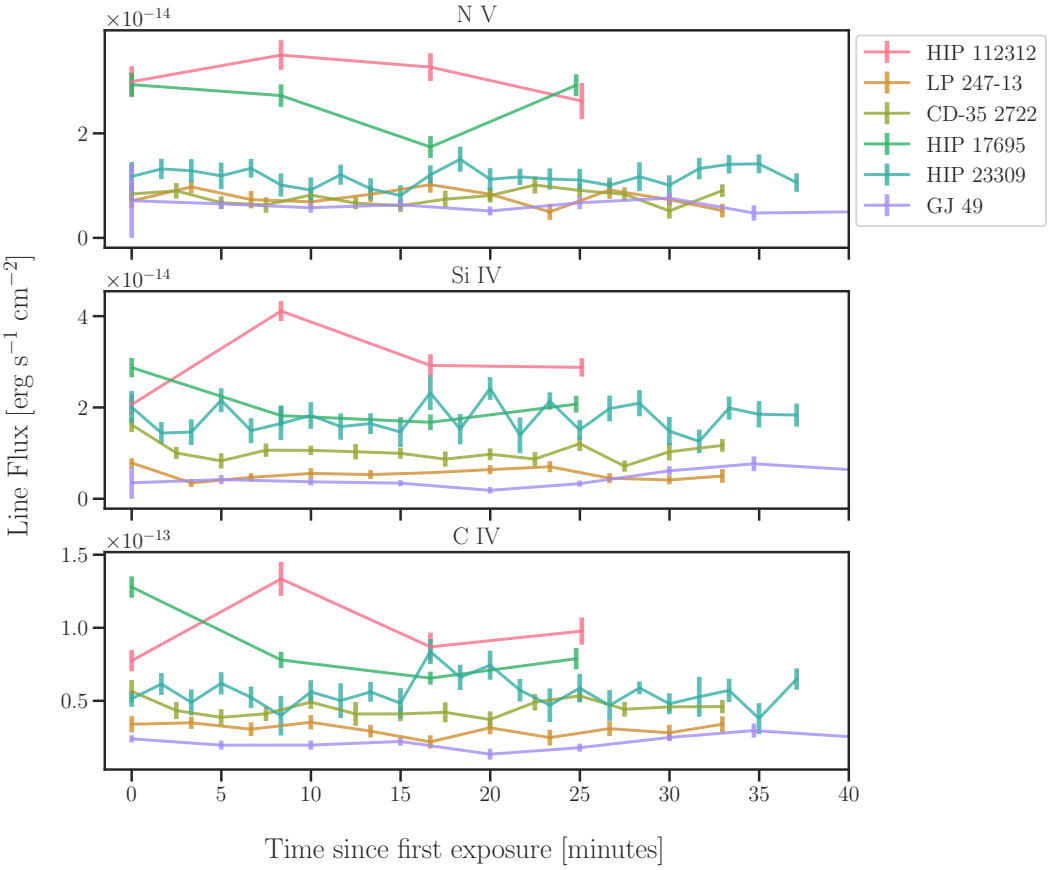

Figure 3.8: This figure shows the time series measurements of the line fluxes for three UV emission features: N V in the bottom panel, C IV in the middle panel, and Si IV in the top panel. No clear stochastic or long-term trends are apparent in these time series.

$$\frac{d\mathrm{EW}}{\mathrm{EW}} \approx -\frac{dF_\lambda}{F_\lambda} \tag{3.2}$$

meaning that the fractional change in equivalent width corresponds to a fractional change in flux. We analyze both the optical and UV lightcurves in this common framework of dimensionless fractional flux, but also look at the optical lightcurves in absolute equivalent width space and the UV lightcurves in absolute flux space. The fractional flux framework controls for the intrinsic activity of the star and allows comparisons between stars with different activity levels, but also allows comparisons between lines that are intrinsically weaker or formed at different heights and temperatures. Conversely, the absolute flux or equivalent width framework puts the variability in the context of the individual line, distinguishing between a small change in a small quantity from being interpreted as equivalent to a large change in a large quantity. Since this work is focused on chromospheric variability, we use Equation 2 of Newton et al. (2017) to calculate the photospheric contribution to the Hα equivalent width of each star, subtract it off before assessing the variability, and provide the calculated quantity in Table 3.1 for reference. The photospheric contribution to the higher-order Balmer lines is less well-characterized but likely small compared to the emission line strength given that all stars where we measure the higher-order lines are active enough to show them in emission and the photospheric contribution to Hα is small.

We use the affine-invariant Markov chain Monte Carlo method implemented by `emcee` (Foreman-Mackey et al., 2013) to sample the log-likelihood function

$$\ln \mathcal{L}(y|s) = \sum_i \frac{1}{\sqrt{2\pi\left(\sigma_i^2 + s^2\right)}} - \frac{1}{2}\frac{(y_i - \mu)^2}{\sigma_i^2 + s^2} \tag{3.3}$$

where μ is the median of the series y, which can represent either the absolute equivalent width, absolute flux, or the fractional flux variation. The only parameter being fit is the intrinsic variability s which is either in units of Å, erg s^{-1} cm^{-2}, or dimensionless for the absolute equivalent width, absolute flux, and fractional cases respectively. To correct for the offset in Gemini data described earlier in Section §3.3.1 we shift the latter 6 datapoints such that their median matches that of

the first 6. We run `emcee` with 20 walkers for 30000 steps, a factor of > 10 times the largest `emcee`-estimated autocorrelation time of < 2500 steps (typical value is 100), and discard the first 5000 steps. Figure 3.9 demonstrates the four types of fit using LP 247-13 as an example: the optical Hα line in the top row, with absolute equivalent width on the left and fractional flux on the right, and the UV C IV line in the bottom row with absolute flux on the left and fractional flux on the right. The gray shaded regions represent the $\pm 1\sigma$ boundaries using the median measurement uncertainty while the purple shaded regions represent the added contribution from the intrinsic variability parameter fit for each panel. In this case, both optical panels show that the intrinsic variability is comparable to the measurement uncertainty while both of the ultraviolet panels' intrinsic variability is a barely visible purple sliver beyond the gray of the measurement uncertainty swath. The comparison between absolute and fractional for both wavelength regimes is effectively just a shift and scaling by the median, although the sign flips for the equivalent width because an increase in flux corresponds to a more negative equivalent width as outlined in Equations 3.2 and 3.3.

Comparing the posterior distribution of the intrinsic variability to the median measurement uncertainty is how we assess the significance of the detected variability. If the median measurement uncertainty exceeds the 16th percentile of the posterior distribution of the parameterized variability s, we consider that a non-detection of variability but report the 95th percentile of the posterior distribution as an upper limit. Figure 3.10 compares the measurement uncertainty to the posterior distributions for fractional flux fits to the time series of a few stars for three optical lines on the left side and three ultraviolet emission features on the right. There are only two stars that have significant detections of ultraviolet variability, HIP 112312 and HIP 23309 while most of the optical time series data shows detectable variability. We tabulate the results of all optical fits in Table 3.5 and all ultraviolet fits in 3.5. Note that the section of the table for Hα measurements have had the photospheric contribution removed and are therefore slightly shifted from the values visible in the lightcurves.

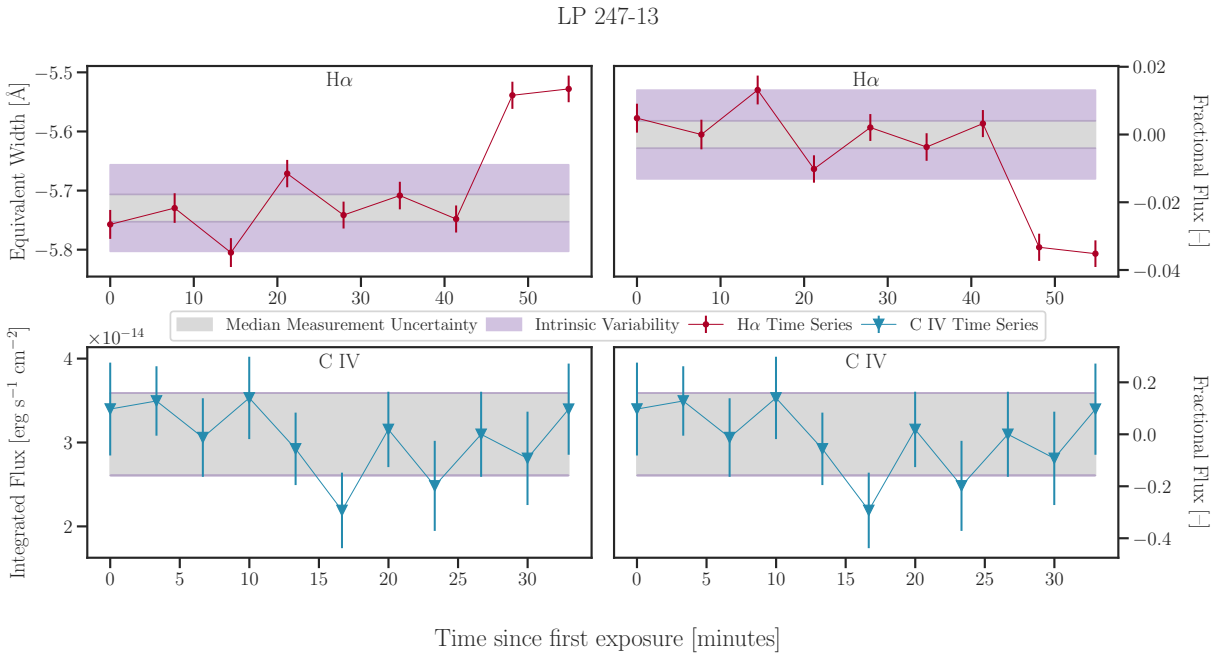

Figure 3.9: The top panels show the LP 247-13 time series data for Hα in absolute equivalent width (left) and dimensionless fractional flux (right) using red dots with error bars. The bottom panels show the LP 247-13 time series data for C IV in a similar fashion, absolute flux on the left and fraction flux on the right. In each panel we use the median measurement uncertainty (σ_{median}) of the panel's lightcurve to shade the $\pm 1\sigma$ region in gray. Each panel's plotted lightcurve has been fit individually and we use the median of the s parameter posterior distribution to shade the extra contribution in purple such that the boundaries of the shaded region are $\mu \pm \sqrt{\sigma^2_{\text{median}} + s^2}$ where μ is the median of the lightcurve. The size of the gray swath for the UV data shows how our signal-to-noise prevents us from detecting variability at the same scale as the optical.

Table 3.8. This table summarizes all the optical equivalent width measurements, absolute intrinsic variability fits, and fractional intrinsic variability fits with the + and − superscripts delineating the 16th and 84th percentile boundaries of the distributions. In cases where the significant variability is not detected, when the 16th percentile of the posterior is less than the median measurement uncertainty, we report the 95th percentile boundary of the posterior as an upper limit.

Name –	Equivalent Width [Å]	Absolute intrinsic variability [Å]	Fractional intrinsic variability –	Number of Measurements –
Chromospheric Hα				
HIP 112312	$-8.858^{+0.433}_{-0.099}$	$0.283^{+0.075}_{-0.052}$	$0.032^{+0.008}_{-0.006}$	12
LP 247-13	$-5.982^{+0.154}_{-0.025}$	$0.107^{+0.036}_{-0.024}$	$0.018^{+0.006}_{-0.004}$	9
CD-35 2722	$-2.410^{+0.012}_{-0.018}$	$0.039^{+0.010}_{-0.007}$	$0.016^{+0.004}_{-0.003}$	12
HIP 17695	$-4.360^{+0.126}_{-0.177}$	$0.071^{+0.019}_{-0.013}$	$0.016^{+0.004}_{-0.003}$	12
HIP 23309	$-2.467^{+0.093}_{-0.110}$	$0.051^{+0.014}_{-0.009}$	$0.020^{+0.005}_{-0.004}$	12
GJ 410	$-0.264^{+0.006}_{-0.007}$	$0.008^{+0.001}_{-0.001}$	$0.031^{+0.004}_{-0.003}$	40
GJ 49	$-0.210^{+0.007}_{-0.016}$	< 0.014	$0.050^{+0.009}_{-0.007}$	25
G 249-11	$-0.045^{+0.024}_{-0.019}$	< 0.058	< 1.284	5
LP 55-41	$-0.070^{+0.002}_{-0.001}$	< 0.021	< 0.297	4

Table 3.7 (cont'd)

Name	Equivalent Width	Absolute intrinsic variability	Fractional intrinsic variability	Number of Measurements
–	[Å]	[Å]	–	–
Hβ				
HIP 112312	$-8.003^{+0.074}_{-0.453}$	$0.606^{+0.159}_{-0.112}$	$0.075^{+0.020}_{-0.014}$	12
LP 247-13	$-5.771^{+0.077}_{-0.440}$	$0.307^{+0.101}_{-0.067}$	$0.053^{+0.018}_{-0.012}$	9
CD-35 2722	$-2.361^{+0.100}_{-0.081}$	$0.093^{+0.025}_{-0.017}$	$0.041^{+0.011}_{-0.008}$	12
HIP 17695	$-4.360^{+0.103}_{-0.214}$	$0.073^{+0.020}_{-0.014}$	$0.016^{+0.004}_{-0.003}$	12
HIP 23309	$-1.776^{+0.031}_{-0.024}$	$0.033^{+0.009}_{-0.006}$	$0.018^{+0.005}_{-0.003}$	12
Hγ				
HIP 112312	$-7.555^{+0.426}_{-0.437}$	$0.424^{+0.113}_{-0.078}$	$0.054^{+0.014}_{-0.010}$	12
LP 247-13	$-8.452^{+0.445}_{-0.528}$	$0.467^{+0.158}_{-0.103}$	$0.055^{+0.019}_{-0.012}$	9

Table 3.6 (cont'd)

Name	Equivalent Width	Absolute intrinsic variability	Fractional intrinsic variability	Number of Measurements
–	[Å]	[Å]	–	–
CD-35 2722	$-1.570^{+0.250}_{-0.239}$	$0.280^{+0.074}_{-0.052}$	$0.163^{+0.043}_{-0.030}$	12
HIP 17695	$-4.440^{+0.184}_{-0.309}$	$0.128^{+0.035}_{-0.024}$	$0.027^{+0.007}_{-0.005}$	12
HIP 23309	$-1.202^{+0.057}_{-0.073}$	$0.068^{+0.018}_{-0.013}$	$0.054^{+0.014}_{-0.010}$	12
Hδ				
HIP 112312	$-7.291^{+0.145}_{-0.412}$	$0.722^{+0.192}_{-0.134}$	$0.099^{+0.026}_{-0.018}$	12
LP 247-13	$-5.876^{+0.347}_{-0.337}$	$0.329^{+0.116}_{-0.078}$	$0.056^{+0.020}_{-0.013}$	9
CD-35 2722	$-2.082^{+0.076}_{-0.210}$	$0.143^{+0.039}_{-0.027}$	$0.070^{+0.019}_{-0.013}$	12
HIP 17695	$-4.238^{+0.208}_{-0.348}$	$0.124^{+0.034}_{-0.024}$	$0.027^{+0.007}_{-0.005}$	12
HIP 23309	$-1.309^{+0.090}_{-0.114}$	$0.040^{+0.011}_{-0.008}$	$0.028^{+0.008}_{-0.005}$	12

Table 3.5 (cont'd)

Name	Equivalent Width	Absolute intrinsic variability	Fractional intrinsic variability	Number of Measurements
–	[Å]	[Å]	–	–
Hζ				
HIP 112312	$-9.480^{+0.350}_{-1.060}$	$1.078^{+0.289}_{-0.202}$	$0.114^{+0.030}_{-0.021}$	12
LP 247-13	$-7.626^{+1.105}_{-0.740}$	$1.006^{+0.421}_{-0.258}$	$0.132^{+0.054}_{-0.034}$	7
CD-35 2722	$-3.461^{+0.271}_{-0.283}$	$0.273^{+0.077}_{-0.054}$	$0.077^{+0.021}_{-0.015}$	12
HIP 17695	$-6.104^{+0.553}_{-0.547}$	$0.382^{+0.106}_{-0.074}$	$0.058^{+0.016}_{-0.011}$	12
HIP 23309	$-2.510^{+0.164}_{-0.146}$	$0.070^{+0.023}_{-0.017}$	$0.026^{+0.009}_{-0.006}$	12
Hη				
HIP 112312	$-5.097^{+0.173}_{-0.502}$	$0.442^{+0.121}_{-0.086}$	$0.087^{+0.024}_{-0.017}$	12
LP 247-13	$-3.278^{+0.580}_{-0.640}$	$0.571^{+0.258}_{-0.166}$	$0.173^{+0.079}_{-0.051}$	7
CD-35 2722	$-2.373^{+0.163}_{-0.153}$	$0.254^{+0.072}_{-0.050}$	$0.108^{+0.030}_{-0.022}$	12

Table 3.4 (cont'd)

Name	Equivalent Width	Absolute intrinsic variability	Fractional intrinsic variability	Number of Measurements
–	[Å]	[Å]	–	–
HIP 17695	$-2.511^{+0.262}_{-0.285}$	$0.156^{+0.051}_{-0.038}$	$0.056^{+0.018}_{-0.014}$	12
HIP 23309	$-2.792^{+0.065}_{-0.124}$	$0.074^{+0.032}_{-0.027}$	< 0.046	12
H10				
HIP 112312	$-3.439^{+0.148}_{-0.636}$	$0.449^{+0.125}_{-0.089}$	$0.131^{+0.037}_{-0.026}$	12
LP 247-13	$-2.089^{+0.377}_{-0.357}$	$0.336^{+0.180}_{-0.125}$	$0.161^{+0.085}_{-0.060}$	7
CD-35 2722	$-0.700^{+0.151}_{-0.178}$	$0.154^{+0.047}_{-0.034}$	$0.238^{+0.073}_{-0.053}$	12
HIP 17695	$-2.125^{+0.350}_{-0.212}$	$0.212^{+0.069}_{-0.051}$	$0.091^{+0.030}_{-0.022}$	12
HIP 23309	$-0.894^{+0.200}_{-0.087}$	$0.133^{+0.039}_{-0.028}$	$0.144^{+0.043}_{-0.030}$	12

Table 3.3 (cont'd)

Name –	Equivalent Width [Å]	Absolute intrinsic variability [Å]	Fractional intrinsic variability –	Number of Measurements –
Ca II H + Hϵ				
HIP 112312	$-16.892^{+0.610}_{-0.142}$	$1.007^{+0.281}_{-0.194}$	$0.060^{+0.017}_{-0.011}$	11
LP 247-13	$-16.281^{+1.252}_{-2.240}$	$1.726^{+0.577}_{-0.375}$	$0.106^{+0.035}_{-0.023}$	9
CD-35 2722	$-6.508^{+0.383}_{-0.372}$	$0.382^{+0.101}_{-0.070}$	$0.060^{+0.016}_{-0.011}$	12
HIP 17695	$-10.594^{+0.745}_{-0.642}$	$0.476^{+0.127}_{-0.089}$	$0.042^{+0.011}_{-0.008}$	12
HIP 23309	$-5.436^{+0.274}_{-0.125}$	$0.168^{+0.046}_{-0.032}$	$0.030^{+0.008}_{-0.006}$	12
GJ 410	$-4.134^{+0.284}_{-0.228}$	$0.238^{+0.031}_{-0.025}$	$0.057^{+0.007}_{-0.006}$	39
GJ 49	$2.634^{+0.139}_{-0.124}$	$0.147^{+0.026}_{-0.020}$	$0.056^{+0.010}_{-0.008}$	25

Table 3.2 (cont'd)

Name –	Equivalent Width [Å]	Absolute intrinsic variability [Å]	Fractional intrinsic variability –	Number of Measurements –
Ca II K				
HIP 112312	$-26.451^{+0.763}_{-1.300}$	$1.050^{+0.281}_{-0.195}$	$0.040^{+0.011}_{-0.007}$	12
LP 247-13	$-22.090^{+2.741}_{-2.345}$	$2.521^{+0.818}_{-0.540}$	$0.114^{+0.037}_{-0.024}$	9
CD-35 2722	$-11.544^{+0.390}_{-0.684}$	$0.597^{+0.159}_{-0.111}$	$0.052^{+0.014}_{-0.010}$	12
HIP 17695	$-17.021^{+0.561}_{-0.486}$	$1.232^{+0.325}_{-0.227}$	$0.071^{+0.019}_{-0.013}$	12
HIP 23309	$-10.614^{+0.643}_{-0.561}$	$0.510^{+0.134}_{-0.095}$	$0.048^{+0.013}_{-0.009}$	12
GJ 410	$-3.646^{+0.147}_{-0.116}$	$0.144^{+0.019}_{-0.016}$	$0.040^{+0.005}_{-0.004}$	40
GJ 49	$-1.902^{+0.256}_{-0.314}$	$0.278^{+0.047}_{-0.038}$	$0.146^{+0.025}_{-0.020}$	25

Table 3.3. This table summarizes all the ultraviolet integrated flux measurements, absolute intrinsic variability fits, and fractional intrinsic variability fits with the + and − superscripts delineating the 16th and 84th percentile boundaries of the distributions. In cases where the significant variability is not detected, when the 16th percentile of the posterior is less than the median measurement uncertainty, we report the 95th percentile boundary of the posterior as an upper limit.

Name –	Integrated Flux [10^{-15} erg s^{-1} cm^{-2}]	Absolute Intrinsic Variability [10^{-15} erg s^{-1} cm^{-2}]	Fractional intrinsic variability –	Number of Measurements –
N V doublet				
HIP 112312	$31.28^{+2.59}_{-3.33}$	< 9.235	< 0.293	4
LP 247-13	$7.32^{+2.09}_{-1.10}$	< 2.110	< 0.286	11
CD-35 2722	$8.14^{+0.90}_{-1.83}$	< 1.566	< 0.192	14
HIP 17695	$28.21^{+1.05}_{-6.10}$	< 18.073	$0.237^{+0.174}_{-0.087}$	4
HIP 23309	$11.72^{+1.56}_{-1.66}$	< 1.452	< 0.123	23
GJ 49	$5.77^{+0.87}_{-0.57}$	< 0.678	< 0.118	19
C II multiplet				
HIP 112312	$27.02^{+2.72}_{-4.09}$	< 11.903	< 0.438	4
LP 247-13	$15.87^{+1.18}_{-1.99}$	< 2.107	< 0.132	11
CD-35 2722	$25.41^{+0.59}_{-0.66}$	< 1.604	< 0.063	14
HIP 17695	$23.37^{+0.58}_{-1.21}$	< 5.171	< 0.220	4
HIP 23309	$28.16^{+5.30}_{-1.88}$	< 4.095	< 0.146	23
GJ 49	$15.78^{+1.07}_{-0.92}$	< 1.122	< 0.071	19
Si IV doublet				
HIP 112312	$28.99^{+6.40}_{-4.45}$	< 24.346	$0.318^{+0.224}_{-0.110}$	4
LP 247-13	$5.30^{+1.34}_{-0.95}$	< 1.907	< 0.372	11
CD-35 2722	$10.16^{+1.44}_{-1.48}$	< 2.562	< 0.251	14
HIP 17695	$19.46^{+5.42}_{-2.01}$	< 15.783	$0.295^{+0.219}_{-0.111}$	4
HIP 23309	$16.49^{+4.67}_{-1.88}$	< 3.685	< 0.224	23
GJ 49	$4.32^{+1.84}_{-0.92}$	< 1.529	< 0.353	19

3.5.1 GJ 410: An Example of Intermediate Activity

GJ 410 is at an intermediate activity level where the Hα line is very close to being flat, with an equivalent width varying between 0.007 and 0.04 Å. As discussed earlier in Section §3.3.2, this is a level where the photospheric absorption is almost perfectly filled in by chromospheric emission. These changes are very small in absolute equivalent width but large in relative flux because the average is so close to zero. Figure 3.11 shows the Hα variability for this star with continuum normalized spectra. The deepest the line gets is 4% below the continuum level, with a median equivalent width of 0.025 Å. This skews the apparent variability of GJ 410 and other intermediate activity stars which is why both absolute and fractional variability should be considered in tandem.

If GJ 410 experienced a flare or other brief increase in Hα emission, it would go from being barely detectable as either absorption or emission to a definitively detected emission line and likely have a very high ratio between the minimum detected emission line flux to the maximum detected flux. This intermediate activity behavior is also observed by Kruse et al. (2010) who found that the ratio between maximum and minimum Hα equivalent width was generally higher for stars with intermittently detected Hα compared to stars where the Hα line was consistently detected.

3.5.2 Tentative Trends

To compare the variability metrics for a single line across the sample we plot them as a function of Rossby number, the ratio between the rotation period and the convective turnover timescale (Noyes et al., 1984). The Rossby numbers for the sample, listed in Table 3.1, were computed in Pineda et al. (2021a) using the mass determinations from Pineda et al. (2021b) and the methods of Wright et al. (2018). Figure 3.12 plots the posterior distribution of the equivalent width intrinsic variability fits as a function of Rossby number for a different optical line per panel. In this absolute space, faster rotators have higher intrinsic variability. Looking at the y-axis values also shows that in this absolute space, the Ca II H and K lines show more variability than the Balmer series and higher-order Balmer lines show more variability than Hα.

Table 3.2 (cont'd)

Name	Integrated Flux	Absolute Intrinsic Variability	Fractional intrinsic variability	Number of Measurements
–	[10^{-15} erg s^{-1} cm^{-2}]	[10^{-15} erg s^{-1} cm^{-2}]	–	–
C IV doublet				
HIP 112312	$92.32^{+23.96}_{-10.32}$	< 69.129	$0.263^{+0.208}_{-0.109}$	4
LP 247-13	$30.98^{+3.39}_{-4.18}$	< 5.247	< 0.172	11
CD-35 2722	$43.77^{+5.37}_{-2.72}$	< 5.695	< 0.130	14
HIP 17695	$78.39^{+25.93}_{-6.89}$	< 83.096	$0.406^{+0.285}_{-0.140}$	4
HIP 23309	$56.11^{+7.27}_{-8.59}$	< 8.313	< 0.149	23
GJ 49	$18.73^{+3.67}_{-3.00}$	< 3.983	< 0.213	19
He II multiplet				
HIP 112312	$73.97^{+12.10}_{-2.68}$	< 28.200	< 0.377	4
LP 247-13	$15.47^{+6.70}_{-3.41}$	< 7.310	< 0.470	11
CD-35 2722	$28.54^{+4.89}_{-6.02}$	< 6.000	< 0.210	14
HIP 17695	$40.87^{+9.06}_{-1.39}$	< 24.984	< 0.609	4
HIP 23309	$49.04^{+11.95}_{-14.31}$	< 11.789	< 0.241	23
GJ 49	$10.60^{+2.64}_{-2.22}$	< 2.513	< 0.238	19

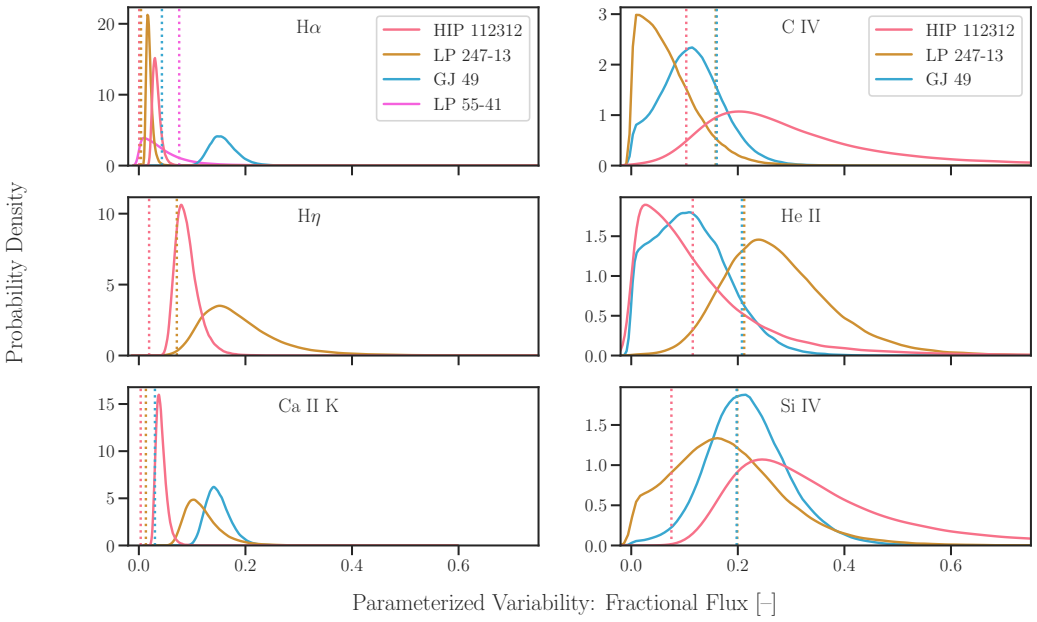

Figure 3.10: Each panel on the left side shows the posterior distribution for fitting the intrinsic variability in fractional flux for a different optical line: Hα on top, Hη in the middle, and Ca II K at the bottom. Each panel on the right side shows the posterior distribution for fitting the intrinsic variability in fractional flux for a different ultraviolet emission feature: the C IV doublet on top, He II 1640 line in the middle, and the Si IV doublet on the bottom. The distributions have been smoothed by a kernel density estimate and are color-coded by star. The median measurement uncertainty for each star's time series is also plotted as a vertical dotted line with the same color-coding although some of these vertical lines are very similar values and appear to overlap. The median measurement uncertainty falls well short of the 16th percentile for most of the optical distributions plotted here, indicating a detection of intrinsic variability that is distinguishable from photometric uncertainty. For most of the ultraviolet distributions, the opposite case is true with the median measurement uncertainty exceeding the 16th percentile and demonstrating that we are unable to detect intrinsic variability that is distinguishable from the noise of the data.

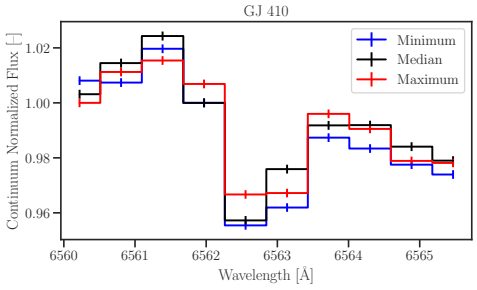

Figure 3.11: This figure shows the Hα spectra for the three exposures of GJ 410 corresponding to the minimum (blue), median (black), and maximum (red) equivalent width measurements in the GJ 410 time series.

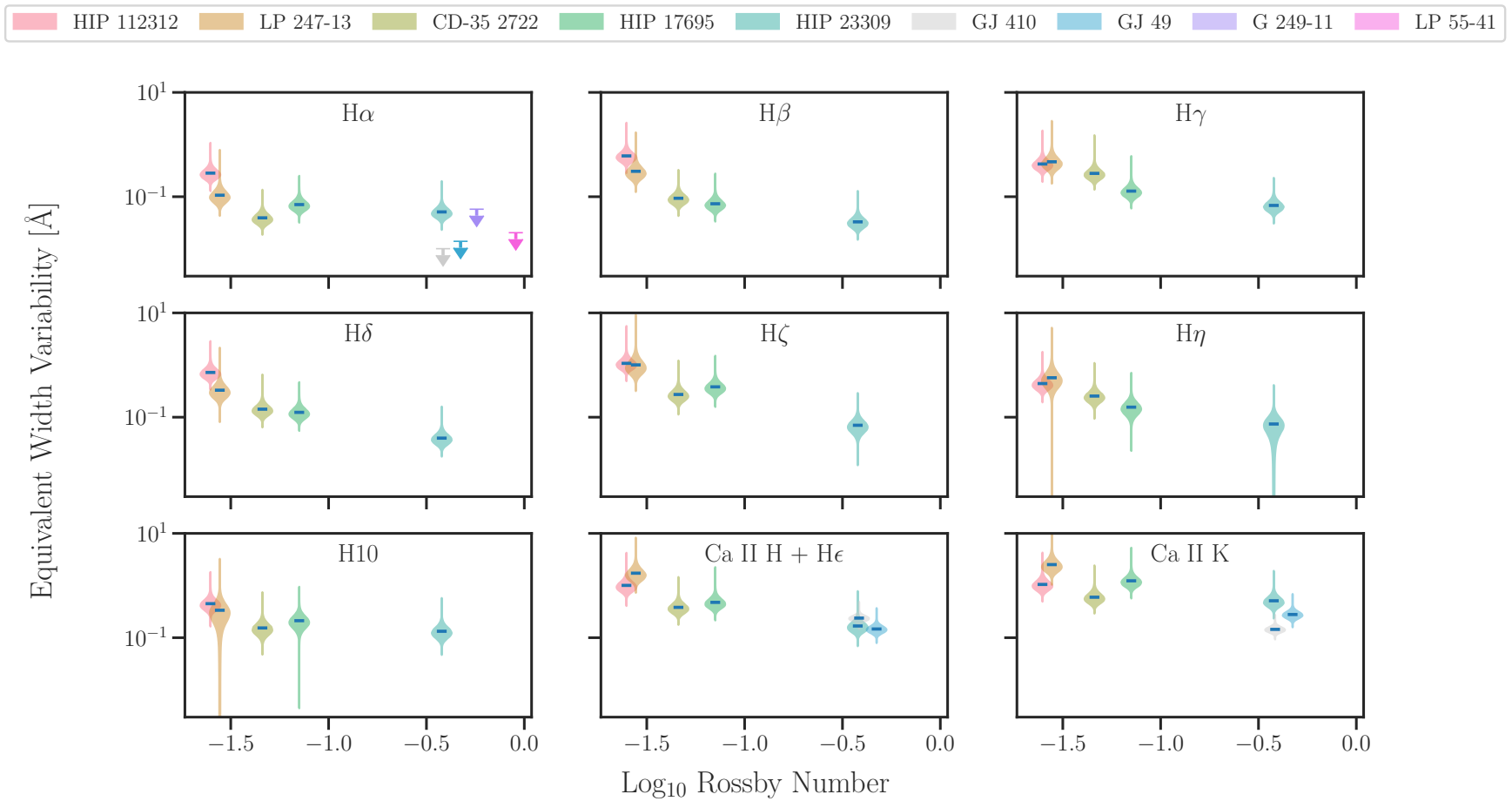

Figure 3.12: This figure shows the intrinsic variability fit distributions to the optical line equivalent width time series as a function of stellar Rossby number (as calculated in Pineda et al. 2021a). Each distribution is color-coded by star and each panel shows a different line. Smaller Rossby numbers show higher variability and the Ca II H and K lines show more variability.

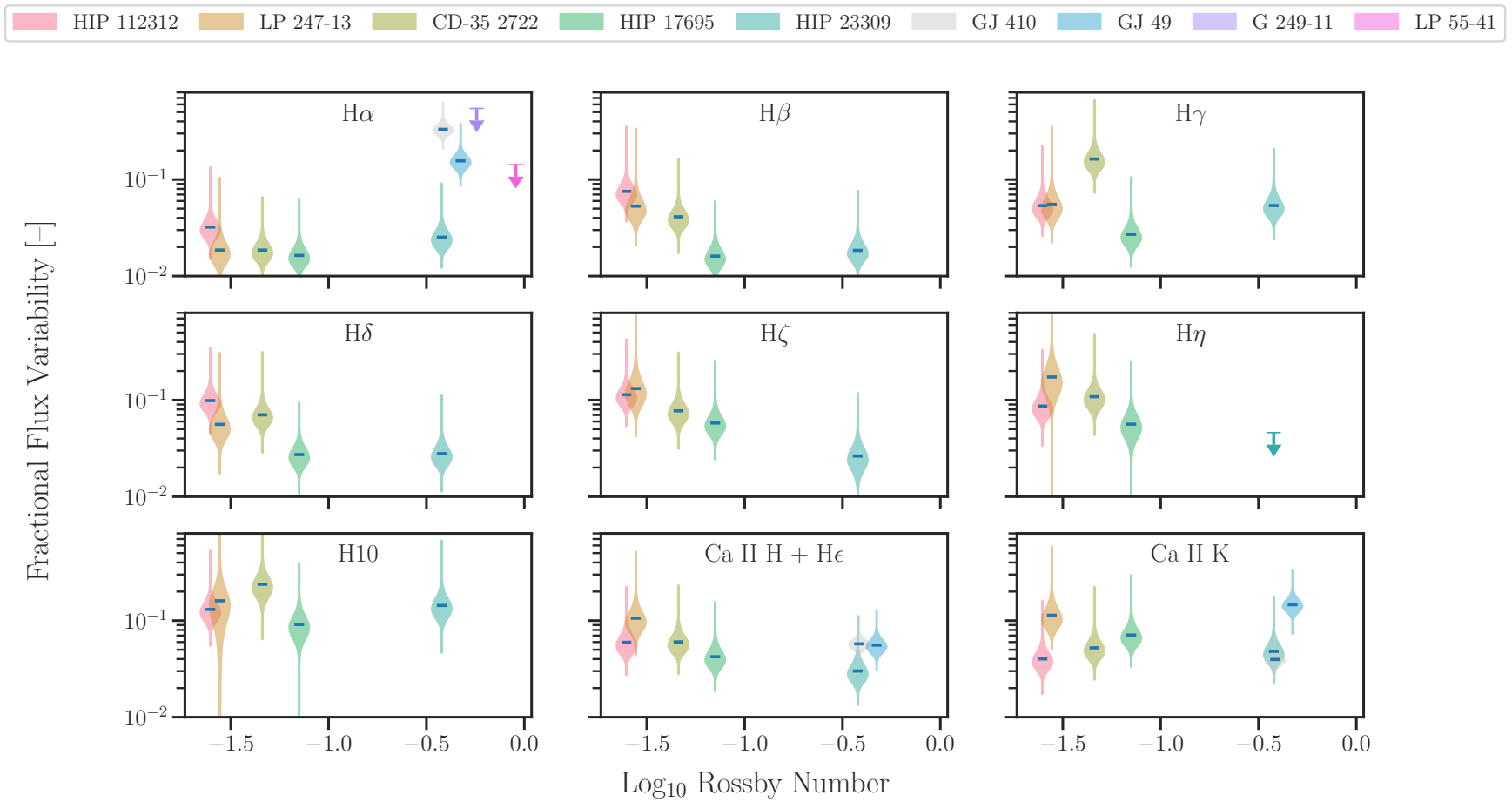

Figure 3.13: This figure shows the intrinsic variability fit distributions to the optical line fractional flux time series as a function of stellar Rossby number (as calculated in Pineda et al. 2021a). Each distribution is color-coded by star and each panel shows a different line. In this fractional space Hα is consistently less variable than the other optical chromospheric lines, but trends with Rossby number are less apparent.

Figure 3.13 is similar to 3.12 but plots the intrinsic variability of the fractional flux instead. The trends with Rossby number have mostly flattened out indicating that whatever processes contribute to the variability of a line, their behavior as a function of Rossby number is very similar to the behavior of the line's formation as a function of Rossby number. This is conceptually analogous to an observation made by Loyd et al. (2018a): flare-frequency distributions of active and inactive M dwarfs differ greatly when flares are characterized in absolute units (flare energy), but appear to coincide when the flares are characterized in relative units (equivalent flare duration, which normalizes by bandpass luminosity). In this relative space, the Hα variability is still generally the lowest, but the scatter in Ca II H and K is broadly consistent with the other Balmer lines.

For the few stars active enough to measure multiple lines in the Balmer series, the parameterized variability in fraction flux shows a tentative trend where higher order Balmer lines have a higher intrinsic variability. The sample is too small to test this rigorously, but Figure 3.14 illustrates the pattern. Each panel plots the posterior distributions of fractional variability for each Balmer line for one star. The fastest rotator, HIP 112312 shows the pattern most clearly where distributions move smoothly from left to right (increasing intrinsic variability) as the color changes from red (Hα) to yellow (H10).

Lee et al. (2010) has shown that $> 80\%$ of M3.5V to M8.5V stars are variable (amplitude $> 30\%$) over 1 hour timescales but their sample was focused on active stars with previously known Hα emission. Kruse et al. (2010) looked at a larger sample with a wider range of both spectral type and activity, but had heterogeneous numbers and cadences of measurements. The few stars with > 5 measurements were once again biased towards the most active stars. More recently, work by Medina et al. (2022) has demonstrated variability in the Hα line for a 10 star sample of M dwarfs that exceeds our measurements (50–100% equivalent width variability to our $< 30\%$), but their sample includes lower-mass stars than the FUMES sample and their work does not examine trends in the magnitude of line variability as a function of stellar rotation. This work's sample is similarly small, but by selecting a range of Rossby numbers and measuring the higher-order Balmer lines we have found evidence for trends worth examining in more detail for a larger sample of stars.

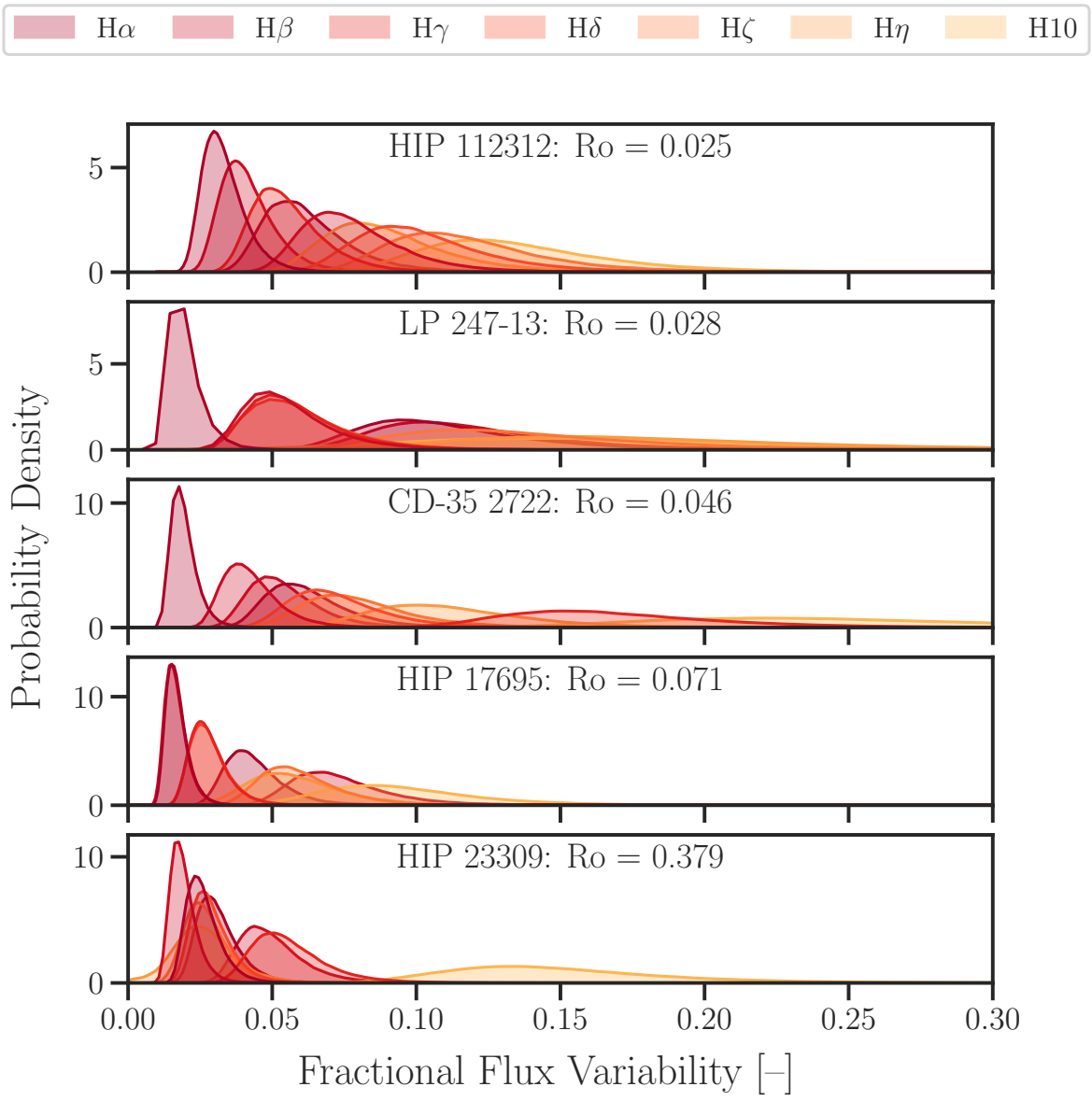

Figure 3.14: The panels correspond to individual stars, ordered by Rossby number with the lowest Rossby numbers (corresponding to faster rotating and more active stars) on top. Within the panels, the posterior distributions for fitting the intrinsic variability of the fractional flux lightcurves of the Balmer series are plotted with a color-scheme corresponding to the Balmer line order.

3.5.3 Physically Interpreting Optical Variability

Table 3.5 summarizes the optical variability analysis by listing the Balmer decrements, mean equivalent widths, $s^2_{\rm EW}$ values, and number of exposures included in analysis for each emission line. Considering the variability in terms of line formation, if the intrinsic variability in Ca II H and K is formed by the same mechanisms as the intrinsic variability in the Balmer series, then these mechanisms are related to collisional excitation which dominates the formation of Ca II H and K (Cram & Giampapa, 1987). Whatever is causing the variability, the absolute magnitude of the effect is clearly related to the rotation of the star while the relative variability may be constant across Rossby number. More tentatively, higher order Balmer lines are more sensitive to the physical processes corresponding to the variability, which could be due to the higher order lines having lower number densities making small absolute changes more apparent in a relative scale.

Some possibilities are that these trends may be a function of the total surface area of active regions, the depth of the chromosphere subject to variable energy deposition via microflares or Alfvén waves, magnetic field topology, but testing these various possibilities exceeds the scope of this work. We discuss future avenues for investigation in Section §4.6.

3.5.4 Relative Inability to Detect UV Variability

Our ability to detect intrinsic variability in the UV was limited by our need to balance time resolution with signal-to-noise ratio. We were generally sensitive to variations beyond 30% for all the features we measured but do not see evidence of intrinsic stochastic variability exceeding that threshold. This result is largely consistent with the results of Loyd & France (2014) which detected stochastic variability in a number of UV targets but few of them showed excess fluctuations $> 30\%$. We were insensitive to UV variability on the scale of what we saw for the majority of the optical line time series.

It is important to note that during the limited time baseline of the FUMES observations, we saw multiple flares, including one on the relatively slow rotator GJ 410, and so these observations

join a growing club of UV M dwarf flares (France et al., 2013, 2020b; Loyd et al., 2018b; Froning et al., 2019; Diamond-Lowe et al., 2021). M dwarfs are therefore unambiguously UV variable, but there is a need to identify whether they show additional stochastic variability that can be distinguished from flares and may have other physical causes. Loyd & France (2014) examined this problem for a much larger (and UV brighter) sample, measuring the intrinsic variability left in UV time series data after excising all identifiable flares. For AU Mic, a very active and very nearby M dwarf, Loyd & France (2014) found $< 10\%$ variability in the flare-excised data. If UV stochastic variability is caused by magnetic heating processes then one should expect the magnitude of AU Mic's variability to be among the highest in the sample, yet Loyd & France (2014) measured higher values of 13.9% and 26.4% for the fainter and less active M dwarfs GJ 832 and Proxima Centauri respectively. But if all or most stochastic variability is caused by flares too small to identify, then AU Mic appears less variable in the flare-excised data because it is much easier to identify the flares. At present this is just supposition, but a carefully planned UV survey with a long baseline could assess whether all M dwarfs show the same amount of stochastic variability after controlling for flare detection completeness.

3.6 Conclusion

This chapter has collated measurements of the Ca II H and K and Balmer optical emission lines from Hα through H10 for a subset of the FUMES sample, a group of low-mass stars spanning a range of rotation periods observed by *HST* Proposal 14640, and analyzed the variability of both the optical and UV chromospheric emission for this sample. Our measurements of the variability of the optical chromospheric emission indicate stochastic changes to line formation in the chromosphere that correlate to the Rossby number. The Hα line is least variable in both an absolute (< 0.3 Å) and relative ($< 5\%$, except for GJ 410) sense, while Ca II H and K vary up to 15% during a single observing night. For the cases where we are able to measure the higher order Balmer lines, their intrinsic variability is $> 5\%$ for all stars except the least active (GJ 410). We see 10–30% variability in most of the Balmer lines for the lowest Rossby numbers.

Previous studies of Hα and Ca II H and K emission have noted rotational modulation on weekly timescales and activity cycle variations on decadal timescales so rotation-activity relations using these lines have often used the mean equivalent width averaged over archival measurements from multiple nights and attributed the remaining scatter to stellar properties like metallicity (Baliunas et al., 1995; Houdebine, 2012; Houdebine et al., 2017). Our work and Medina et al. (2022) show that the short-term variation is also a significant contributor that needs to be accounted for and averaging the Hα and Ca II H and K emission over multiple exposures and/or long integration times is necessary to get an accurate measurement of the stellar activity on any given night. This intrinsic variability may also impede studies that try to use these lines to detect star-planet-interactions.

The stochastic optical variability does not coincide with any apparent optical flare continuum emission and no significant stochastic variability is observed in the UV emission lines on similar timescales, only occasional flares where count rate changes significantly ($>$ a factor of 2) across the entire UV spectrum. We are not sensitive to stochastic variability less than 30% in the ultraviolet data which limits our ability to compare the chromospheric variability to the transition region. There are significant discrepancies between the UV and optical flare behavior of low mass stars, namely that UV flares are frequently detected on optically inactive M dwarfs (France et al., 2013, 2020b; Loyd et al., 2018b; Froning et al., 2019; Diamond-Lowe et al., 2021). If flares on these optically inactive stars skew towards temperatures significantly hotter than 9000 K, then low energy flares may result in observations of optical stochastic variability coincident with UV flares.

We consider two plausible explanations for stochastic variability in the optical line emission that does not observably propagate to the higher layers of the transition region associated with the UV lines we have measured. Medina et al. (2022) use injection tests to demonstrate that the timescales for flares are consistent with the Hα variability they observe. In this scenario a flare produces a cascading beam of non-thermal electrons which collide in the chromosphere, depositing energy which propagates upwards through the transition region to the corona (Hawley & Fisher, 1994). This could lead to a stratified effect where small (and frequent) flares manifest as small

enhancements in the optical emission lines because of the extra collisions, but any flare strong enough to heat the transition region enhances the UV emission lines and continuum dramatically enough to be clearly identifiable as a flare. Another plausible mechanism is Alfvén wave heating, where magnetoacoustic oscillations perturb the local pressure, changing the collisional excitation rate, but the strength of these perturbations at different heights would depend on the properties of the stellar magnetic field and atmospheric structure, possibly stratifying to cause more variability in the chromosphere than the transition region (Sakaue & Shibata, 2021). Determining the relative contribution of each mechanism or identifying other mechanisms is not possible with the dataset we have collected here.

Simultaneous optical and UV monitoring of low mass stars could help determine whether microflaring events are causing the stochastic optical variability. Higher signal-to-noise observations of the UV would enable cross-correlating the variability between the chromosphere and transition region, helping to determine whether the processes involved affect both layers and test for a time lag. A higher cadence and longer baseline survey of the Balmer series for a small sample would enable analysis of the frequency and amplitude of the variability and a comparison between Balmer lines would diagnose the magnitude of energy perturbations. These measurements may be able to disentangle the two heating mechanisms we have described. A theoretical complement to this dataset could be a 3D and time-variable model of the stellar atmosphere where different heating mechanisms can be tuned and trends observed in the simulations can be compared to the available data, applying the techniques of Kowalski et al. (2017) to stars other than the Sun. A sample structured similarly to FUMES for hotter dwarf stars should also be assembled to determine whether the trends with Rossby number observed here apply to them as well. Following up on existing studies of stochastic variability in one wavelength regime can guide the sample selection, for example getting optical spectroscopic time series data for the Loyd & France (2014) UV sample. Magnetic activity is a time-variable phenomenon and time series observations of chromospheric, transition region, and coronal emission of stars across a range of rotation periods and effective temperatures are necessary to understand stellar magnetic structure and evolution.

Chapter 4

The High-Energy Emission of A Young Sun-like Star

4.1 Preface

This chapter is a lightly edited version of a paper in preparation to be submitted to the Astronomical Journal, using data from *Hubble* guest observing program GO #16163 Cauley et al. (2020) and *NICER* GO #3041 (PI: Co-author P. Wilson Cauley) . For this paper, in addition to advice and input, co-authors performed a significant portion of the analysis and provided text that was included and/or adapted in this chapter. We are currently re-analyzing the X-ray data to account for some discrepancies and so specific values described here may change although the structure and broad conclusions of the chapter are not expected to change. Co-author Roy Kilgard analyzed the *NICER* X-ray data and provided text for the discussion in Section §4.4.1, co-author Kevin France measured the strengths of far ultraviolet emission lines and provided text to describe this process in Section §4.4.2, co-author Fernando Cruz-Aguirre subtracted the airglow in the Lyman-α emission line according to the method described in Cruz Aguirre et al. (2023) and described for this particular case in Section §4.4.3, and co-author P. Wilson Cauley was PI of the observing programs for this work and provided the portions of the panchromatic spectrum beyond 1700 Å using a combination of *Hubble* STIS data and an appropriate `PHOENIX` model atmosphere spectrum (Husser et al., 2013).

4.2 Introduction

V1298 Tau is a K0-1.5 pre-main sequence star that hosts 4 known transiting exoplanets (David et al., 2019). The star is bright (d = 108.5 pc, $m_{\rm Gaia}$ = 10.1, Gaia Collaboration et al., 2018b), similar to the young Sun ($M_\star = 1.101 M_\odot$, $R_\star = 1.345 R_\odot$), and younger than 100 Myr (David et al., 2019), making the V1298 Tau planets prime targets for transmission spectroscopy. Both the star and its planets will change significantly over the lifetime of the system: the star will spin down, contract, and emit less high-energy radiation while the planets will contract as they cool but also lose mass from their H/He envelopes. The majority of planetary atmospheric escape is expected to take place within the first Gyr of the system's lifetime (King & Wheatley, 2021) and studying the physics of atmospheric evolution is necessary to understand exoplanet demographics and habitability. A major open question in this area is whether formation conditions or evolutionary processes like photoevaporative mass loss and core-powered heating are primarily responsible for the "radius valley": an apparent sparsity of exoplanets with radii near 1.8 $R_\oplus$ (Fulton et al., 2017). Statistical experiments have been proposed to compare predictions from both atmospheric loss mechanisms to the observed exoplanet population, but these approaches rely on input assumptions of the initial high-energy fluxes of young stars and their subsequent evolution (Rogers et al., 2021). Determining the high-energy irradiation and atmospheric escape of young exoplanets like those orbiting V1298 Tau is necessary to assess the accuracy and precision of those input assumptions.

This work describes the creation of a panchromatic spectrum of V1298 Tau presented in Figure 4.1 for the community to model this planetary system and interpret observations of atmospheric escape. Section §4.3 lists the X-ray and ultraviolet observations contributing to the spectrum, Section §4.4 describes our analysis of the far ultraviolet emission lines and determination of the star's coronal properties, and Section §4.5 explains the method used to predict the unobserved extreme ultraviolet flux. Section §4.6 concludes by calculating a simplified energy-limited mass loss rate for the innermost planet V1298 Tau c and using the V1298 Tau spectrum to characterize the lifetime high-energy irradiation of exoplanets orbiting solar-mass stars.

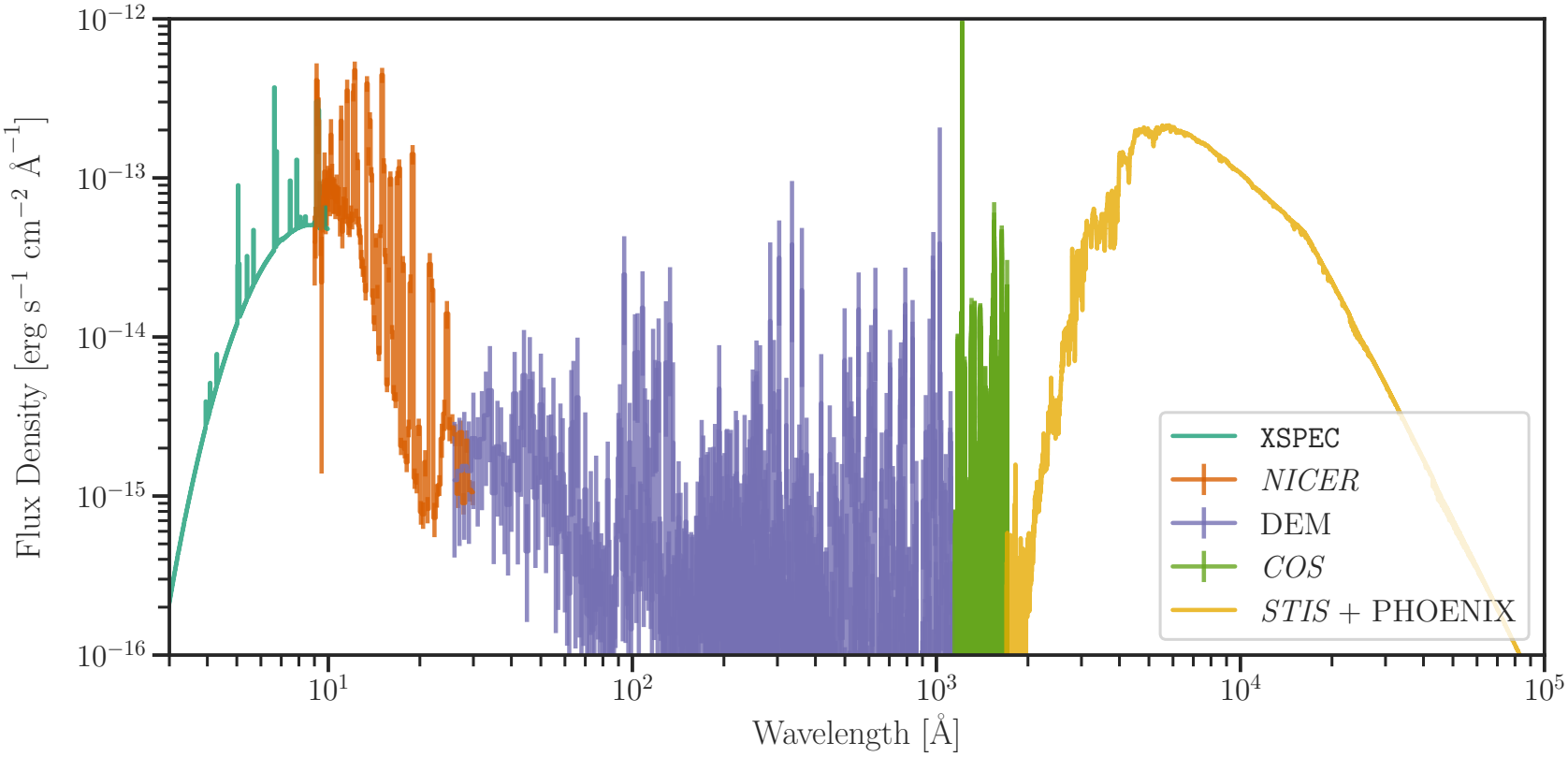

Figure 4.1: The composite spectrum is plotted with each component covering a specific wavelength interval, using data where available and supplemented by empirically constrained models. The components and their respective wavelength intervals are: `XSPEC` model (teal), 5 – 9 Å; *NICER* data (dark orange), 9 – 25 Å; DEM model (dark purple), 25 – 1150 Å; *HST* COS data (green), 1150 – 1700 Å, with a sub-interval 1214.63 – 1216.78 Å for Lyman-α replaced with a scaled reconstruction from ϵ Eridani; *HST* STIS data (yellow), 1700 – 3100 Å; PHOENIX model (yellow), 3100 – 10^5 Å.

Table 4.1. Summary of *NICER* and *HST* observations

Telescope	Instrument setting	Date (UT)	Starting time (UT)	Exposure time (seconds)	λ_{start} (Å)	λ_{end} (Å)	Resolution† (Å)
NICER	···	2020-09-13	11:06	1880	5	55	0.9
NICER	···	2020-10-18	23:37	2134	5	55	0.9
HST	STIS G230L	2020-11-07	06:44	2200	1600	3150	3.0
HST	COS G160M	2020-10-17	14:54	1997	1350	1710	0.09
HST	COS G130M	2021-12-23	10:44	9892	1140	1420	0.09
HST	COS G130M	2022-01-17	03:18	12030	1140	1420	0.09

†Resolutions vary across the free spectral range. We report the approximate value at the central wavelength of the recorded spectrum.

⋆Inclination measured from the line-of-sight.

4.3 Observations

From 2020 through early 2022 we obtained observations of V1298 Tau's high-energy spectrum using the Space Telescope Imaging Spectrograph (STIS, Woodgate et al., 1998) and Cosmic Origins Spectrograph (COS, Green et al., 2012) instruments on the *Hubble Space Telescope (HST)* and NASA's *Neutron Star Interior Composition ExploreR (NICER)* mission aboard the International Space Station (Gendreau et al., 2016). The ultraviolet observations cover the wavelength range 1140 Å - 3100 Å and the X-ray observations span the energy range 0.1 - 10 keV (≈ 5 Å - 55 Å). We give details on the individual instrument settings and observations in the two subsections below, including a summary in Table 4.1.

4.3.1 Hubble Space Telescope

The *HST* observations were designed to cover the far ultraviolet (FUV, 1100 – 1700 Å) and near ultraviolet (NUV, 1700 – 3100 Å) spectral range with two COS settings and a single STIS setting. The COS observations were obtained with the G130M and G160M gratings and cover the FUV wavelengths; the STIS observations were performed with the G230L grating to cover the NUV spectral range. We note that the COS G130M observations were executed during transits of V1298 Tau c with the goal of measuring mass loss from the planet's atmosphere. The transit observations will be detailed in an upcoming paper. Here, we combine the first two G130M visits

into a high-quality FUV spectrum to be included in the final composite high-energy spectrum data product.

4.3.2 NICER

NICER is a soft X-ray telescope whose primary purpose is to investigate the equation of state of the interiors of neutron stars. *NICER* was designed to have high photon arrival time accuracy and is able to record events with a precision of < 300 nanoseconds, but its excellent soft X-ray sensitivity also makes it useful for observing the high-energy emission from stellar coronae. *NICER* only has a single configuration so we do not specify the instrument Grating/Setting in Table 4.1.

We obtained ≈ 4 ks of exposure time through *NICER*'s Guest Observer Program Cycle 2 (proposal number 3041, PI Cauley). *NICER* observed V1298 Tau on two separate dates: 1880 seconds of exposure time on 2020-09-13 and 2134 seconds of exposure time on 2020-10-18.

4.4 Analysis

To prepare the final data product we analyzed the X-ray and FUV data to provide constraints for estimating the EUV spectrum and scaled the Lyman-α profile of ϵ Eridani as recovering the intrinsic stellar emission profile was poorly constrained given the high interstellar absorption and Earth airglow.

4.4.1 X-ray Analysis

NICER data were processed using NICERDAS 9/HEASoft 6.30 to generate cleaned event lists, extract spectra, and generate observation-specific response functions. The background levels were estimated using the nibackgen350 tool of Remillard et al. (2022). Spectra were modeled in Xspec (Arnaud, 1996) with photoelectric absorption and a Raymond-Smith optically thin thermal plasma model (Raymond & Smith, 1977). The spectral fit parameters and fluxes were nearly identical in both NICER observations (see Table 4.2), with negligible absorption, a plasma temperature of 0.79 ± 0.015 keV, and sub-Solar abundance (≈ 0.1). A plot of the X-ray spectrum and model

Table 4.2. Spectral fits to *NICER* observations

NICER ID	Temperature (keV)	Abundance	$\chi^2/D.O.F.$
3541010201	0.79 ± 0.015	0.11 ± 0.013	293.7/96
3541010301	0.79 ± 0.014	0.14 ± 0.017	109.54/82

for the second observation is shown in Figure 4.2. The plasma model appears to underpredict the low-energy emission below 5 keV, but matches the dominant emission lines and general shape of the underlying continuum well. For the final data product we use the *NICER* data between 9 and 25 Å and the `XSPEC` model below 9 Å, cutting off regions where the effective area of the detector drops off and avoiding edge effects.

4.4.2 Far-UV Emission Line Measurements of V1298 Tau

V1298 Tau was observed with the medium-resolution far-UV modes of COS (G130M and G160M; Green et al. 2012) as part of GO 16163 (PI – P. Cauley). These observations (program ID GO 16163, visits 2, 3, and 4) were acquired between 17 October 2020 and 17 January 2022. G130M observations were acquired in the CENWAVE 1291, FP-POS 4 setting, and G160M observations were acquired in the CENWAVE 1533 setting using all four FP-POS tilts. Together, these observations create a nearly continuous FUV spectrum from $\approx$ 1133 – 1709 Å, with a $\sim$ 11 Å gap around 1525 Å where the COS detector segments are physically separated, and mitigate the effects of fixed pattern noise. The one-dimensional spectra produced by the COS calibration pipeline, CALCOS, were aligned and coadded using the custom software procedure described by France et al. (2012). The final FUV spectrum has a point-source resolution of $\Delta\ v \approx 20$ km s^{-1} with 6 – 7 pixels per resolution element. A three-pixel boxcar smoothing was applied prior to fitting the emission lines. The total far-UV exposure times were 21,924s in G130M and 1,998s in G160M.

The chromospheric, transition region, and coronal emission lines in the COS spectra were fitted with an interactive multi-Gaussian line-fitting code optimized for COS emission line spectra. This code assumes a Gaussian line-shape convolved with the wavelength dependent line-spread

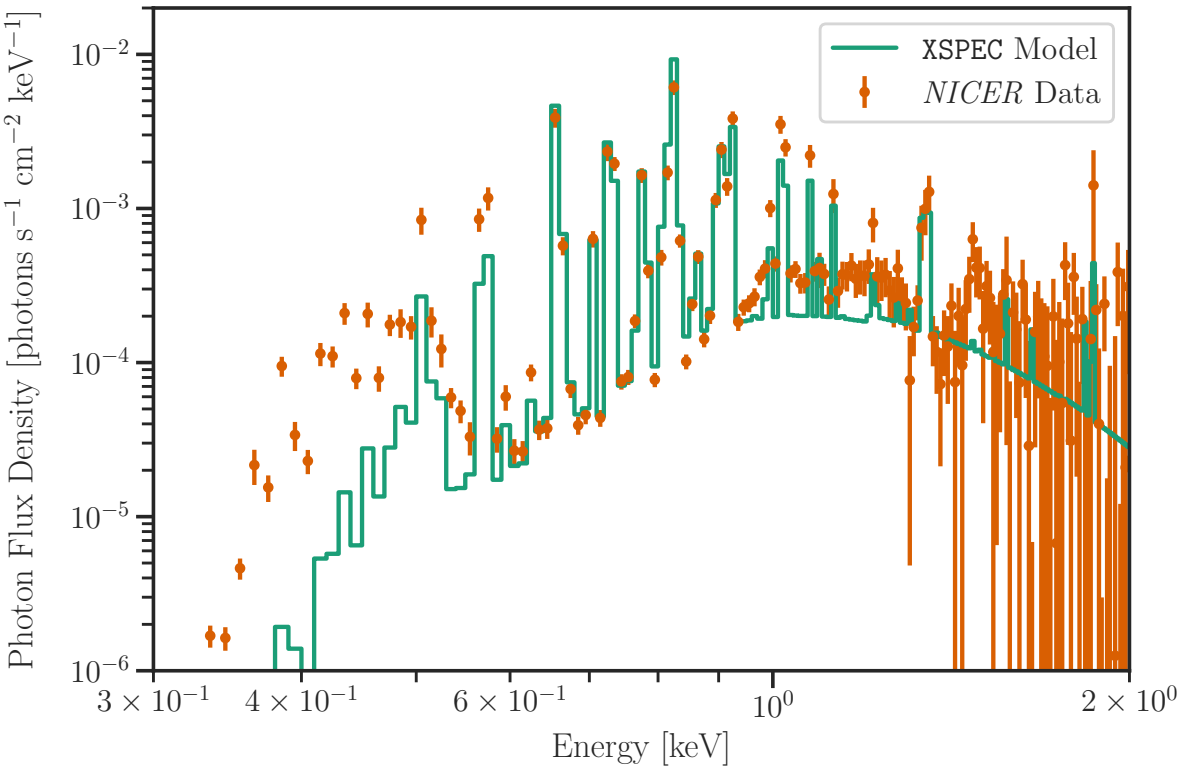

Figure 4.2: The *NICER* spectrum merged from both observations is plotted as orange circles with errorbars while the best-fit `XSPEC` model is plotted in solid green. The model fits the continuum and strong emission lines at intermediate energies well but underpredicts the emission from low energies.

function, then uses the MPFIT routine to minimize χ^2 between the fit and data (Markwardt, 2009; France et al., 2012). A second order polynomial background, the Gaussian amplitudes, and the Gaussian full-widths-at-half-maximum (FWHM) for each component are free parameters. The parameters of the underlying Gaussian emission lines are returned to the user, and the total line fluxes (Table 4.4) are used as inputs to the DEM calculations described in Section §4.5.1. Figure 4.3 presents the spectrum and line fit for the C IV emission line as an example of the data and line-fitting procedure.

4.4.3 Lyman-α Profile

Stellar Lyman-α emission is obscured by H I in the interstellar medium (ISM) which attenuates the line core. Observing Lyman-α with *HST*, whose orbit lies within the exosphere, is further complicated by geocoronal Lyman-α emission, or airglow. For COS data, the airglow signal cannot be separated from the stellar signal during the standard background subtraction routine.

Cruz Aguirre et al. (2023) (hereafter referred to as CA23) developed a tool which subtracts airglow emission from COS data to recover the underlying stellar Lyman-α emission by simultaneously fitting the intrinsic stellar emission, ISM absorption, and the contaminating airglow. While the tool was designed for main sequence F-, G-, K-, and M-type dwarf stars in the stellar neighborhood ($\lesssim$ 80 pc), we attempted to use the tool to recover the faint Lyman-α emission of V1298 Tau.

Due to the distance to V1298 Tau being larger than what the tool was optimized for, we increased the maximum H I column density to 10^{20} cm^{-2}, based on measured column densities at similar distances being $\sim$19.6 cm^{-2} (Wood et al., 2005). The spectral location of the airglow profile changes over time due to the motion of the spacecraft and the time elapsed between COS observations was large enough to require separate airglow subtractions for each individual observation.

The contaminating airglow dominates the observed spectrum, as shown in Figure 4.4, leaving behind little flux to inform the reconstruction of the intrinsic stellar emission line profile. The retrieval is further complicated by the effects of gain sag on the COS detector in the vicinity of

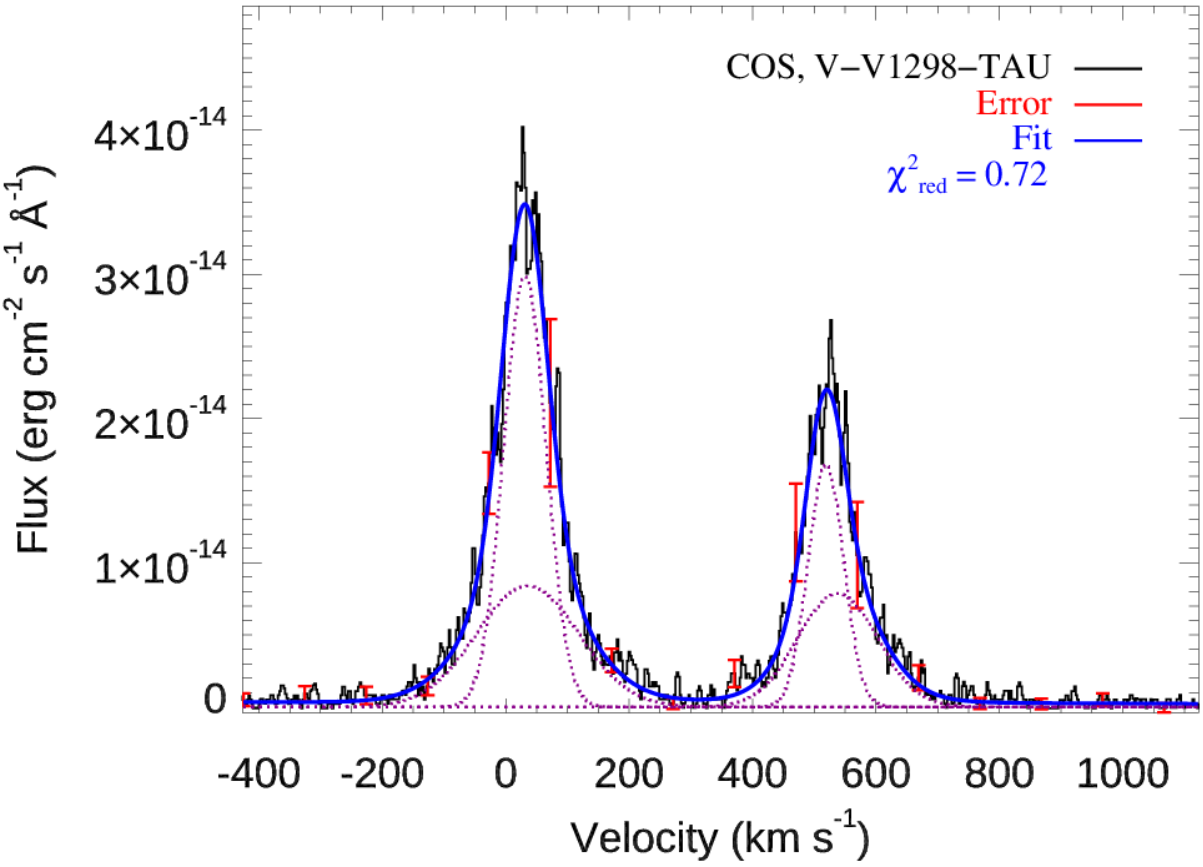

Figure 4.3: The C IV doublet from V1298 Tau. COS/G160M spectra are shown as the black histogram, with representative error bars in red. A two-component Gaussian fit is shown overplotted; individual components are in the dashed magenta lines and the overall fit is in blue.

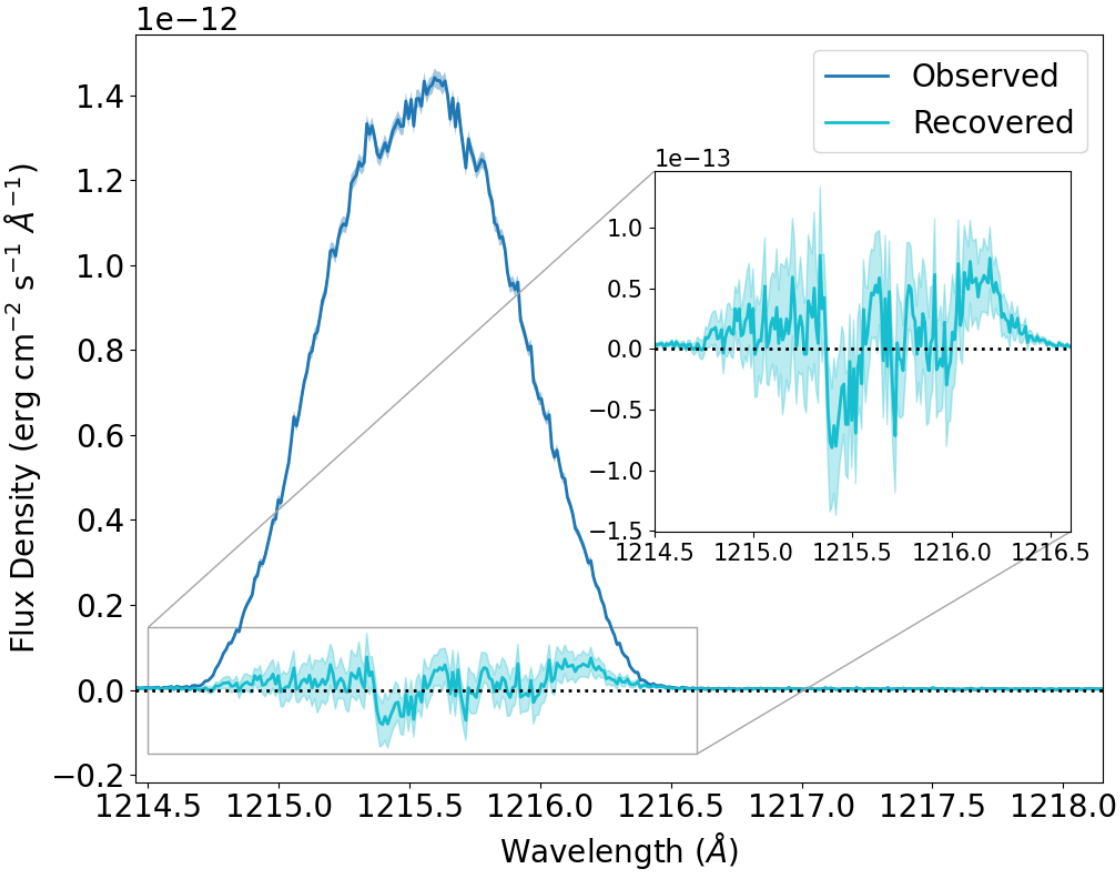

Figure 4.4: Lyman-α airglow subtraction of V1298 Tau. The spectrum as observed by COS is shown in dark blue. The CA23 tool is used to subtract the airglow, resulting in the recovered (ISM attenuated) spectrum in light blue. The recovered signal of V1298 Tau is faint, and a reliable reconstruction of the stellar emission was not possible.

geocoronal Lyman-α, which reduces the throughput of the stellar signal and was the primary cause for failed Lyman-α recoveries in CA23. Only two of the three recovered profiles were consistent in their shape, and were co-added together to try to improve the quality of the fit, but the results were poorly constrained and unstable even after multiple simplifications to the model describing the intrinsic line profile.

There are multiple correlation methods to predict the integrated Lyman-α flux using other more accessible observable quantities, divided into either measured fluxes from emission lines or stellar parameters. These correlation methods are calibrated using samples of nearby stars where Lyman-α reconstructions are more viable and these are typically main-sequence stars. Table 4.3 lists the Lyman-α flux predicted by a number of relations available in the literature, each using different activity tracers or proxies. All relations from CA23 and Wood et al. (2005) take the form of a power-law, while the Pineda et al. (2021a) prediction uses the saturation value of the Lyman-α $\frac{F_{\rm Ly\alpha}}{L_{\rm bol}}$ broken power-law relation because V1298 Tau is a fast enough rotator to be in the saturated regime. We adopt the integrated flux predicted by the Wood et al. (2005) Mg II relation because the other line-based relations are from transition region lines formed over a narrower spatial and temperature range than Lyman-α.

The Lyman-α profile provided in the final data product scales the Lyman-α reconstruction of ϵ Eridani[1] from the MUSCLES data products (France et al., 2016; Youngblood et al., 2016) by the ratio between the Lyman-α flux predicted by the Mg II relation, 1.2×10^{-13} erg cm^{-2} s^{-1}, and the integrated Lyman-α flux reported by Youngblood et al. (2016) for the ϵ Eridani reconstruction, 6.1×10^{-11} erg cm^{-2} s^{-1}. We replace the portion of the observed COS spectrum with the scaled ϵ Eridani reconstruction in the interval 1214.63 – 1216.78 Å, where the boundaries are identified by the intersection points between the original observed spectrum and the scaled reconstruction. We assign errorbars that assume an uncertainty of a factor of 2 in either direction to be conservative.

[1] https://archive.stsci.edu/prepds/muscles/

Table 4.3. Lyman-α Predictions From Correlations

Input Variable –	Input Quantity [various]	Predicted Lyman-α [10^{-13}erg s^{-1} cm^{-2}]	Reference –
$\log_{10}$ $L_{\rm Si\ III}$ /$L_{\rm bol}$	-5.61	1.0	CA23
$\log_{10}$ $L_{\rm N\ V}/L_{\rm bol}$	-5.87	3.0	CA23
Rossby Number	assumed saturation regime $<$ Ro$_c$ = 0.21	6.8	Pineda et al. (2021a)
$\log_{10}$ Mg II hk doublet Surface Flux	6.35	1.2	Wood et al. (2005)

4.5 Extreme Ultraviolet

The extreme ultraviolet (EUV, 100 – 912 Å) spectra of most stars are poorly constrained. The only facility to observe in this wavelength regime was the *Extreme Ultraviolet Explorer* (*EUVE*) which was operational from 1992 to 2001 and was not sensitive enough to obtain high signal-to-noise spectra for most main-sequence stars unless they were highly active and/or nearby. This has proven to be a significant obstacle to studying stellar magnetic activity and exoplanet atmospheric escape. In the absence of data for most stars, one must either rely on other observed quantities like the X-ray or Lyman-α flux and then use correlations between that quantity and the EUV flux of the few stars observed by EUVE (Linsky et al., 2014; Youngblood et al., 2016; France et al., 2020b), or use a model of the star's atmospheric structure above the photosphere.

4.5.1 Differential Emission Measure

We use the differential emission measure (DEM) technique, described in detail in Duvvuri et al. (2021), which has been used in a number of cases to estimate the XUV irradiation of exoplanets (Sanz-Forcada et al., 2004, 2011; Louden et al., 2017; Diamond-Lowe et al., 2021, 2022), to estimate the extreme ultraviolet spectrum of V1298 Tau and fill in the gaps between observations. The DEM method uses observed emission to constrain the density and temperature structure of the upper stellar atmosphere expressed as a one-dimensional function of temperature $\Psi(T) = n_e n_{\rm H} \frac{ds}{dT}$ (i.e. the differential emission measure), and then combines this function with atomic data to predict unobserved emission produced from the same plasma that emitted the observed flux. The DEM

function can be conceptually described as a collision or reaction rate for exciting electrons to higher states weighted by the amount of plasma along the line-of-sight at a given temperature (Duvvuri et al., 2021). The intensity of a specific emission feature can be determined by using atomic data to construct its "contribution function", weighting this function by the DEM, and then integrating over temperature (Kashyap & Drake, 1998; Craig & Brown, 1976). The peak of this integrand is the "formation temperature $T_{\rm formation}$". To constrain the DEM, it is ideal to have measurements of multiple emission features that each have very narrowly peaked contribution functions to minimize the degeneracy of DEM shapes that could produce the observed emission, and whose formation temperatures densely occupy the full temperature range of interest (10^4 – 10^8 K for stellar EUV).

We update the method described in Duvvuri et al. (2021) by using a more recent version of `CHIANTI` (`v10.0.1, Dere et al. 1997; Del Zanna et al. 2021`) and incorporating the recombination continua of hydrogen and helium species (this updated method was also used in Feinstein et al. 2022). As described in Duvvuri et al. (2021), we use a 5th order Chebyshev polynomial to describe the functional form of $\log_{10}\Psi(T)$, assume the method has a parameterized intrinsic uncertainty that is a temperature-independent fraction s of the predicted flux, and evaluate the likelihood of a given DEM function by directly comparing the observed line flux to the flux predicted by integrating the product of the DEM and emissivity function in a Markov Chain Monte-Carlo (MCMC) sampler. Our approach differs from the iterative Monte-Carlo method (Sanz-Forcada et al., 2004) by allowing a greater range of "acceptable" solutions; not just finding the "best" DEM for a given Monte-Carlo sample of line flux distributions, but any DEM that produces a likely fit to the data. Our approach also differs from the more closely related method employed by Diamond-Lowe et al. (2021) that used Chebyshev polynomials and MCMC sampling like Duvvuri et al. (2021) but evaluated the likelihood in DEM-space, using the integral of the contribution function to determine an "average DEM" value associated with a single formation temperature for each observed emission line and fitting to these averages, a method which has significant computational advantages but again restricts the range of allowed DEM shapes by neglecting the width and shape of the contribution function. We use the `emcee` (Foreman-Mackey et al., 2013) affine-invariant implementation of

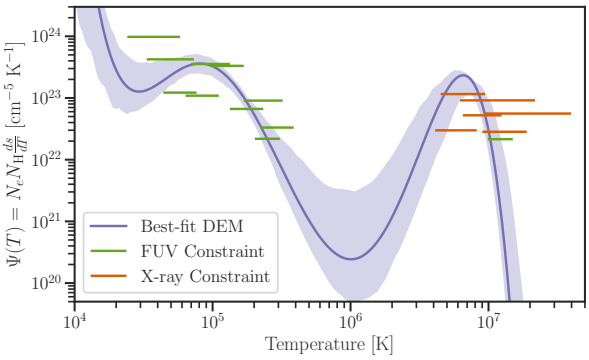

Figure 4.5: The Differential Emission Measure model fit compared to representative average DEM values derived from the observed fluxes used to constrain the fit. The uncertainty of allowed DEM shapes is greatest in the interval between 3×10^5 K – 3×10^6 K where there are no observed emission features formed at specifically those temperatures. The peak at 6×10^6 K corresponds to the corona and the DEM turning down prevents the formation of emission lines at temperatures greater than 1.5×10^7 K, which is consistent with the isothermal `XSPEC` model fit to the X-ray data. Figure 4.6 compares the fluxes predicted by the DEM model to the observed flux constraints.

the Metropolis-Hastings MCMC algorithm (Goodman & Weare, 2010) to sample the joint posterior distribution of the six polynomial coefficients and s-factor systematic uncertainty. We ran 25 chains for $2.2\times10^4 \lesssim 110\tau$ steps, where $100 < \tau < 200$ steps is the range of autocorrelation times for all parameters calculated by `emcee`, and discard the first 2×10^3 steps from all walkers.

The X-ray spectral bins used to constrain the high-temperature end of the corona were selected by downsampling the spectral resolution of the merged *NICER* spectrum to $R = \frac{\lambda}{\Delta\lambda} = 40$ to ensure all emission line profiles were contained within spectral bins, then identifying which bins had the highest integrated contributions when querying `CHIANTI`. The chosen bins correspond to the strong emission lines between 0.7 and 1.1 keV shown in Figure 4.2, but each bin contains blends from multiple emission lines which cannot be resolved. The FUV constraints are more straightforward, the summed flux from observed emission lines from different species, with integrated fluxes from the line profile fits described in Section §4.4.2, where we use lines we assume have not been significantly impacted by interstellar reddening. V1298 Tau is active enough that we were able to observe the Fe XXI 1354 Å coronal emission line, which provides a constraint at temperatures similar to the X-ray spectral bins and these appear to agree with each other.

Figure 4.5 shows the distribution of DEM shapes that fit the data, with the median DEM value represented by a solid purple line and the shaded region filling in the interval between the 16th and 84th percentile boundaries of DEM values returned by the sampled polynomial shapes. The horizontal lines represent constraints imposed by the observed fluxes, with the width encompassing the central 50% of the cumulative integral of the emissivity function and the $y-$value representing the average Ψ value obtained by dividing the flux by the integral of the emissivity function (treating the DEM Ψ as locally constant). These averages are illustrative and meant to show which temperatures are constrained by which measurements, color-coded to distinguish between the FUV lines (light green) and X-ray spectral bins (dark orange). Figure 4.6 compares the predicted fluxes from the DEM to the observed values and is a more direct visual representation of the model's goodness-of-fit while Table 4.4 compares the observations and model predictions for all flux constraints used in the DEM-fitting process.

The FUV and X-ray data were not taken simultaneously and if there were unresolved flares in either dataset the non-simultaneity would introduce discrepancies between the predicted EUV emission and the true quiescent spectrum of V1298 Tau. However, the good agreement between both X-ray observations indicates that they were at similar levels of flare activity, while no significant flares were noted in the FUV photon event lightcurve. The DEM average for the FUV Fe XXI line also agrees well with the constraints from the X-ray data, suggesting that any activity level discrepancies between the multiple observations fall within the uncertainty of the measurements and fitting process.

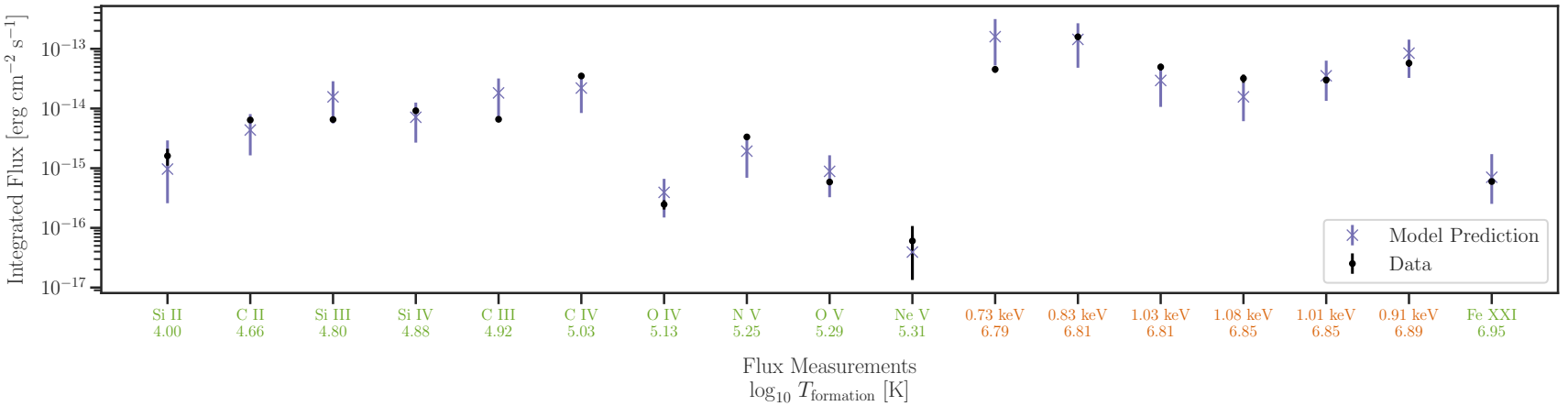

Figure 4.6: The observed flux constraints are plotted as black points with errorbars corresponding to their measurement uncertainties while the DEM model predictions are plotted as purple crosses with errorbars corresponding to the 16^{th} – 84^{th} percentile values of the distribution of fluxes predicted by drawing from the posterior of DEM shapes and the fractional flux systematic uncertainty parameter. The flux constraints are divided into two categories: ion species corresponding to integrated FUV emission line fluxes (labeled in light green) and central energies corresponding to the integrated flux of X-ray spectral bins (labeled in dark orange). Beneath each flux constraint's label is its $\log_{10} T_{\text{formation}}$ [K] value and the constraints are ordered by formation temperature increasing to the right.

4.5.2 EUV Spectrum

As mentioned above, we have improved the method of Duvvuri et al. (2021) to include recombination continua from hydrogen and helium species which adds bound-free edges most notable short of 912 Å. In addition to the increased opportunities for statistical rigor and specificity to individual stars, an advantage of the DEM over scaling relations is the ability to synthesize an actual spectrum with higher resolution than 100 Å bandpasses. While the DEM cannot predict line-shapes, predicting the flux from individual optically thin emission lines allows spectral synthesis at a resolution where the width of a line is entirely captured in a single spectral bin. This is especially important for modelling atmospheric escape from the exospheres of irradiated exoplanets with methods more sophisticated than energy-limited escape. As observations of the He I 10830 Å line become increasingly accessible for exoplanets, Oklopčić (2019) demonstrates the necessity of well-characterized EUV and mid-UV spectra with uncertainties to interpret those observations.

One set of parameters from the posterior distribution describes the shape of the DEM and the intrinsic uncertainty on fluxes predicted by that DEM. For each sample draw from the posterior we calculate Ψ using the Chebyshev coefficients, predict the flux f in 1 Å bins from 1 to 1500 Å using the emissivity functions of all lines that `CHIANTI` lists within the wavelength bin, and then sample from a Gaussian $\mathcal{N}(\mu = f, \sigma = s \cdot f)$. This creates one spectrum output corresponding to the single draw of parameters from the posterior distribution. After 10^6 such draws we record the 16th, 50th, and 84th percentile values of the flux in each wavelength bin to infer the EUV spectrum and the uncertainty of the inference. Figure 4.7 shows the EUV portion of the predicted spectrum which is enhanced relative to the Sun across the entire EUV regime. The integrated XUV (X-ray + EUV, $<$ 912 Å) flux from V1298 Tau using our combination of `XSPEC`, *NICER*, and the DEM-generated EUV spectra is $1.74 \pm 0.14 \times 10^{-12}$ erg s^{-1} cm^{-2}.

Table 4.4. Integrated fluxes of optically thin FUV emission lines and X-ray spectral bins compared to the DEM predictions

Emission Feature	Wavelengths [Å]	$\log_{10} T_{\rm formation}$ $\log_{10}([\rm K])$	Observed Flux $[10^{-15}\ \rm erg\,s^{-1}\,cm^{-2}]$	DEM Prediction $[10^{-15}\ \rm erg\,s^{-1}\,cm^{-2}]$
Si II	1260.4, 1264.7	4.40	1.61 ± 0.51	$0.981^{+0.97}_{-0.724}$
C II	1335 multiplet	4.66	6.42 ± 0.436	$4.40^{+3.82}_{-2.80}$
Si III	1294.5, 1301.1	4.80	6.53 ± 0.314	$15.5^{+13.2}_{-9.90}$
Si IV	1393.7, 1402.7	4.88	9.18 ± 0.751	$7.14^{+5.62}_{-4.50}$
C III	1175 multiplet	4.92	6.6 ± 0.314	$18.5^{+13.6}_{-11.8}$
C IV	1548.1, 1550.7	5.03	35.1 ± 3.02	$22.4^{+16.2}_{-14.2}$
O IV	1401.1	5.13	0.247 ± 0.044	$0.398^{+0.278}_{-0.246}$
N V	1238.8, 1242.8	5.25	3.34 ± 0.244	$1.98^{+1.40}_{-1.26}$
O V	1371.3	5.29	$0.587 \pm 0.05.84$	$0.896^{+0.747}_{-0.582}$
Ne V	1145.6	5.31	0.0604 ± 0.047	$0.0391^{+0.0376}_{-0.0249}$
0.73 keV	17.0 ± 0.21	6.79	45.3 ± 5.45	159^{+152}_{-109}
0.83 keV	15.0 ± 0.19	6.81	159 ± 17.3	$144^{+124}_{-94.5}$
1.03 keV	12.0 ± 0.15	6.81	49.7 ± 6.39	$29.3^{+20.9}_{-18.6}$
1.08 keV	11.5 ± 0.14	6.85	32.0 ± 5.06	$15.8^{+11.4}_{-9.92}$
1.01 keV	12.3 ± 0.15	6.85	30.0 ± 3.68	$35.4^{+28.2}_{-21.2}$
0.91 keV	13.6 ± 0.17	6.89	57.6 ± 7.25	$83.2^{+59.5}_{-52.2}$
Fe XXI	1354.0	6.95	0.598 ± 0.0576	$0.699^{+1.01}_{-0.0459}$

Note. — In cases where multiple transitions are listed for the same ion, the reported flux is the summed flux across all listed transitions. For X-ray spectral bins, we list the central energy, wavelength, and wavelength bin width.

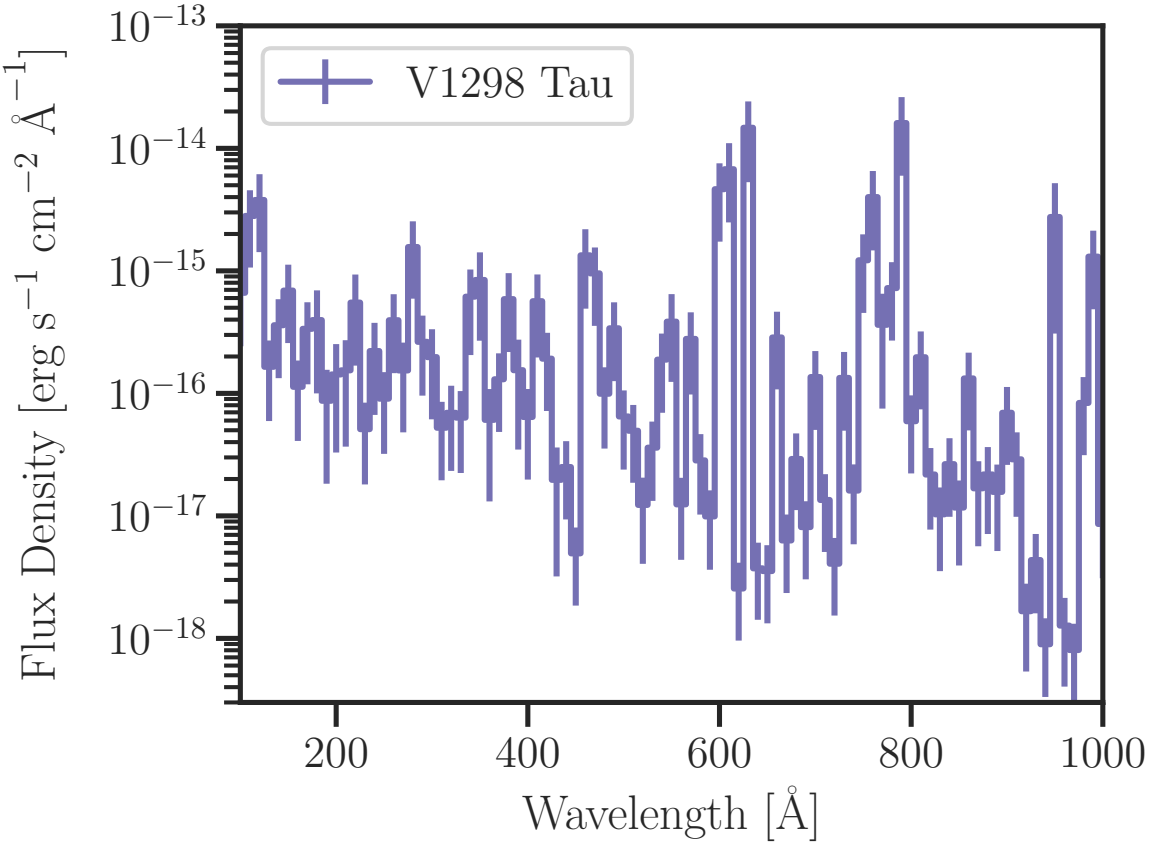

Figure 4.7: The EUV spectrum of V1298 Tau.

4.6 Conclusion

To complete the spectrum we use a PHOENIX model with $T_{\rm eff=5000}$ K, $\log_{10} g = 4.0$, M/H=0.0 (Husser et al., 2013), resampled to a wavelength resolution of 1.5 Å and rotationally broadened to 23 km s^{-1}. After scaling the PHOENIX model to match the STIS data at 3100 Å, the model and data showed good agreement between 2800 and 3100 Å, indicating that this model is a good approximation for this star's spectrum at longer wavelengths.

As the star spins down, the non-thermal heating of the star's upper atmosphere will decrease over time and reduce the high-energy emission from V1298 Tau, but not necessarily by a constant value across this wavelength regime depending on how the evolution varies at different stellar atmospheric heights/temperatures. The long-term fate of V1298 Tau's planets will depend on how the photoevaporative mass-loss changes over the lifetime of the system. Ribas et al. (2005) assembled spectra of solar-mass stars across a wide range of ages, including *EUVE* data, to characterize these stars' evolution of high-energy emission over time. Ribas et al. (2005) fit power-laws to the integrated flux for 3 XUV bandpasses: 1 – 20, 20 – 100, and 100 – 360 Å and assigned a power-law for the 360 – 920 Å bandpass. More recent work like Wright et al. (2011) has favored a broken power-law for X-ray emission, observing that for the youngest stars, the X-ray emission clusters around a saturation value. Applying the Ribas et al. (2005) power-laws to V1298 Tau drastically overestimates the observed and predicted fluxes for the individual XUV bandpasses. By taking V1298 Tau to be representative of the saturation flux for young solar-mass stars, we modify the Ribas et al. (2005) power-laws to be broken power-laws that follow

$$F_i = \left\{ \begin{array}{ll} F_{\rm V1298\ Tau,}i, & \text{if } t < t_{{\rm crit},i} \\ \alpha_i \left(\frac{t}{1\ {\rm Gyr}} \right)^{\beta_i} & \text{if } t \geq t_{{\rm crit},i} \end{array} \right\} \tag{4.1}$$

where i represents the bandpass intervals, $F_{\rm V1298\ Tau,}i$ is the flux of V1298 Tau scaled to a distance of 1 AU and integrated over the bandpass i, α_i and β_i are taken from Table 5 of Ribas et al. (2005), and we solve for the breakpoint of the power-law $t_{{\rm crit},i} = \sqrt[\beta_i]{\frac{F_{\rm V1298\ Tau,}i}{\alpha_i}}$ by requiring the function to be continuous. The parameters are listed in Table 4.5 and the functions are plotted in Figure 4.8.

The combination of transit surveys and *Gaia* has made it possible to identify exoplanet systems in moving groups and associations with known ages, increasing the number of systems with precisely known ages. We queried the Exoplanet Archive[2] for all confirmed exoplanets with known radii and orbital periods orbiting stars with $1 < M_\star < 1.2 M_\odot$ (similar to V1298 Tau $M_\star = 1.1 M_\odot$) and a known age with an uncertainty less than a factor of 2, then applied the broken power-law evolution to each planetary system to determine the cumulative XUV irradiation of each planet, used to color the points in the bottom panel of Figure 4.9.

The planets of the V1298 Tau system are in a relatively sparse region of the plot, but there are a wide range of ages and XUV irradiation values represented amongst these planets' closest neighbors. Looking for trends in XUV irradiation and planet demographics will require filling out this plot and others like it with different planetary parameters by increasing the range of stellar types with well-characterized XUV evolution. As exoplanet surveys continue to detect viable systems for atmospheric characterization via transmission spectroscopy and direct-imaging, interpreting these observations and studying atmospheric evolution requires more detailed stellar characterization beyond spectral type. V1298 Tau is one of the brightest exoplanet hosts accessible within our solar neighborhood (d = 108.5 pc) and we still require model-dependent estimates of its high-energy emission. This star is an unusual case where the EUV uncertainties are more tightly constrained than the Lyman-α recovery, but both wavelength regimes need next-generation observatories to improve our understanding of stellar magnetism and the evolution of exoplanet atmospheres. This chapter presents a roadmap for calculating empirically-informed spectra of individual exoplanet host stars that can be used until those observatories become available.

[2] https://exoplanetarchive.ipac.caltech.edu/

Table 4.5. Broken power-laws describing the evolution of bandpass fluxes for solar-type stars determined by linking the Ribas et al. (2005) relations to the V1298 Tau SED collated in this work

Bandpass i [Å]	$F_{\text{V1298 Tau},i}$ [erg s^{-1} cm^{-2}]	$\alpha_i^\star$ [erg s^{-1} cm^{-2}]	$\beta_i^\star$ [–]	$t_{\text{crit},i}$ [Myr]
1 – 20	515	2.4	-1.92	61.1
20 – 100	62.1	4.45	-1.27	126
100 – 360	82.3	13.5	-1.2	222
360 – 920†	63.0	4.56	-1	72.4

*Table 5 of Ribas et al. (2005)

†No data for stars other than the Sun were available for this bandpass so Ribas et al. (2005) calibrated the power-law by assuming $\beta = -1$ and solving for α to match the observed flux from the Sun.

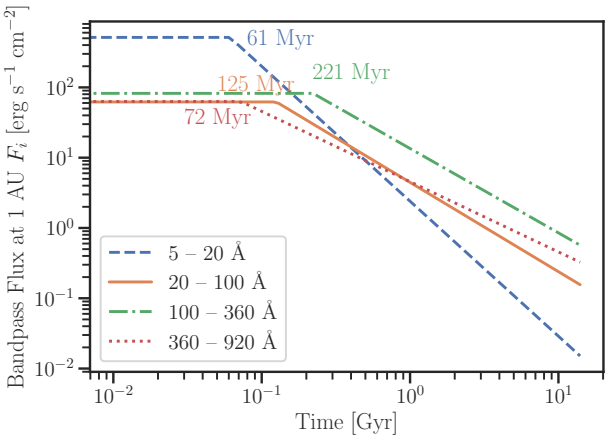

Figure 4.8: The broken-power laws describing the evolution of high-energy emission for solar-mass stars divided into 4 bandpasses, annotated with the time corresponding to the breakpoint of the power-law: 1 – 20 Å (dashed dark blue, 61 Myr), 20 – 100 Å (solid orange, 125 Myr), 100 – 360 Å (dot-dashed green, 221 Myr), 360 – 920 Å (dotted red, 72 Myr). The parameters for the broken power-laws are listed in Table 4.5.

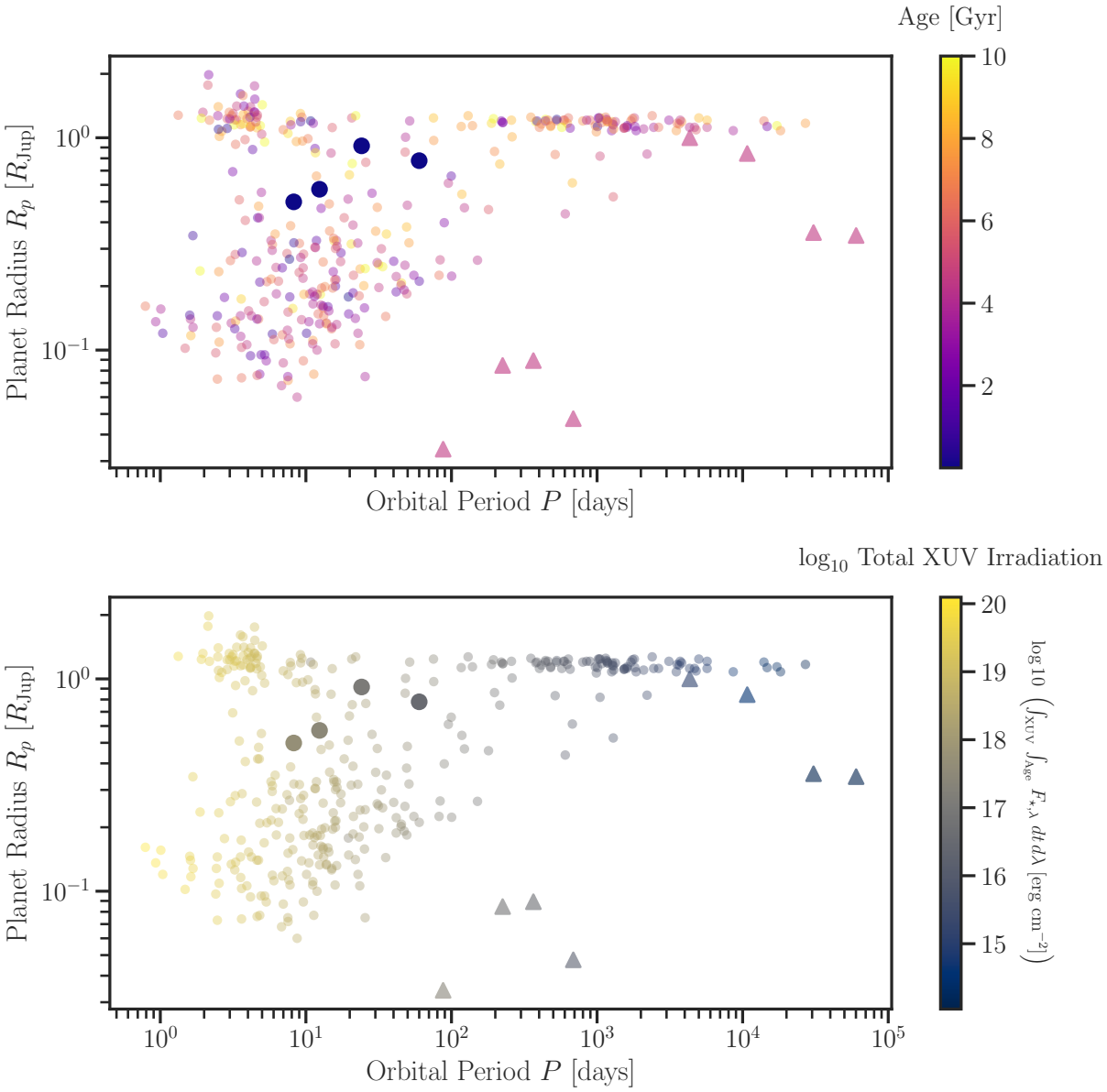

Figure 4.9: Both panels plot the planet radius against the orbital period for: a sample of confirmed exoplanets orbiting stars with a mass similar to V1298 Tau (translucent dots), the V1298 Tau planets (opaque circles), and Solar System planets (opaque triangles). The top panel colors the planet markers by the age of the star, with darker shades representing young systems and increasing brightness with age, while the bottom panel colors the planet markers by the cumulative XUV irradiation experienced by the planet assuming it has stayed at its current orbit for the entirety of the system's age, with the brightness of the color increasing with irradiation. For this sample selected by stellar mass, where all plotted planets are assumed to have experienced the same high-energy evolution, the cumulative XUV irradiation is a transformation applied to the age. In a broader sample, where different stellar hosts follow different XUV irradiation evolution behavior, other stellar parameters will be introduced into the transformation.

Chapter 5

The Evolution of High-Energy Emission for M Dwarfs

5.1 Introduction

We introduced the use of the differential emission measure to infer the unobserved extreme ultraviolet spectrum in Chapter 2, showed that the emission from the stellar upper atmosphere evolves over time in a manner correlated to rotation period or Rossby number in Chapter 3, and connected these two ideas to evolve the high-energy flux received over time from a star in Chapter 4. Chapter 4 leaned on existing parameterizations of the flux evolution from stars with a mass $M_\star = 0.8 - 1.2 M_\odot$, but the evolution of all the processes leading to high-energy emission (internal convection, magnetic energy transport, angular momentum) have a strong dependence on mass and so the scalings from Ribas et al. (2005) should not be casually applied to other spectral types. This chapter demonstrates the beginning of a much larger project to fit DEMs for as many low-mass main sequence stars as I can find sufficient data for, and then use the breadth of this sample across stellar mass and age to map the high-energy emission as a function of these two variables. Section §5.2 describes the preparation of the planned full sample and the downselection process for the subsample analysed in this chapter; Section §5.3 shows the data, DEM model fits, and inferred EUV spectra for the subsample; Section 5.4 demonstrates a crude interpolation of the DEM as a function of age for mid-M dwarfs; and Section 4.6 concludes by sketching the planned approach for a more sophisticated interpolation method using the full sample.

5.2 Sample

The sample was collated by searching the Mikulski Archive for Space Telescopes (MAST) for all GKM stars with FUV spectra that used instrument settings capable of observing the emission lines I use to constrain the DEM, and then trying to find out what X-ray data were available for these targets. Most of the identified targets were observed in the FUV as part of exoplanet host characterization programs like the Measurements of the Ultraviolet Spectral Characteristics of Low-mass Exoplanet Systems (MUSCLES, France et al., 2016), Mega-MUSCLES (Froning et al., 2019; Wilson et al., 2021), MUSCLES Extension for Atmospheric Transmission Spectroscopy (France et al., 2020a), and the follow-up characterization of JWST Early Release Science exoplanet host targets (Youngblood et al., 2021a). These programs typically included requests for X-ray data from either *Chandra* or *XMM-Newton* and therefore had X-ray spectra for the majority of their targets. Other survey programs that had relevant targets were HAZMAT (Shkolnik & Barman, 2014), FUMES (Pineda et al., 2021a), and StarCAT (Ayres, 2010).

This sample is plotted as a function of effective temperature $T_{\rm eff}$ and stellar rotation period $P_{\rm rot}$ in Figure 5.1 as purple squares, compared to grey dots representative of the broader stellar population using data from McQuillan et al. (2014) and Newton et al. (2016). A number of the plotted stars will have to be dropped because their signal-to-noise (S/N) and/or wavelength resolution ($R = \frac{\lambda}{\Delta\lambda}$) is insufficient to get good constraints for the DEM. The wavelength resolution is particularly an issue for targets where the only available X-ray data is a single band-pass flux measurement like a *ROSAT* All-Sky Survey flux which is measured across a bandpass of $0.1 - -2$ keV. However, more stars with the required data are likely to exist in the archive with a more careful search and at least a few more are likely to be added as *TESS* discovers planets orbiting stars bright enough to motivate space telescope observations.

For the interpolation demonstrated in this chapter, I wanted to illustrate the methodology with a 1-dimensional slice of the larger 2D problem, selecting stars of similar mass or effective temperature along a range of rotation periods. The MUSCLES and MegaMUSCLES programs

Table 5.1. The M dwarfs this work fits and compares DEMs for. All intrinsic stellar parameters except rotation period are from Pineda et al. (2021a) and Pineda et al. (2021b) and distances are from Gaia Collaboration et al. (2018b). Rotation periods are from Suárez Mascareño et al. (2015) unless otherwise noted.

Star –	Mass $M_\star$ [$M_\odot$]	Radius $R_\star$ [$R_\odot$]	Effective Temperature $T_{\rm eff}$ [K]	Rotation Period $P_{\rm rot}$ [days]	Distance d [pc]
AU Mic	0.667	0.80	3619	4.86 (Samus' et al., 2017)	9.7
GJ 649	0.524	0.53	3621	23.8 (Díez Alonso et al., 2019)	10.4
GJ 849	0.465	0.46	3492	39.2	8.8
GJ 436	0.425	0.43	3477	44.09	9.8
GJ 163	0.405	0.41	3460	61	15.1
GJ 15A	0.393	0.39	3601	30.52 (Newton et al., 2016)	3.6
GJ 176	0.485	0.47	3632	39.3	9.5
GJ 832	0.441	0.44	3539	45.7	5.0

followed a fairly consistent set of observing modes and target S/N, and most importantly had a consistent file format, so I started there, then used the stellar parameters tabulated in Pineda et al. (2021b), a paper that homogeneously analyzed the properties of a large sample of M dwarfs, to select a subset of similar $M_\star$ and/or $T_{\rm eff}$ M dwarfs. In the future we will use mass as the independent variable because it is more directly relevant to the physics of stellar atmospheric heating. The stars chosen for this sub-sample and their stellar parameters are listed in Table 5.1 and are plotted in Figure 5.1 as hollow red circles.

I modified the line-fitting code developed for Chapter 3 to use `emcee` (Foreman-Mackey et al., 2013), a Markov-Chain Monte-Carlo code using the Metropolis-Hastings algorithm (Goodman & Weare, 2010), to better describe the posterior distribution of line fluxes for weak lines where the previous method often failed to converge and provide a covariance matrix.

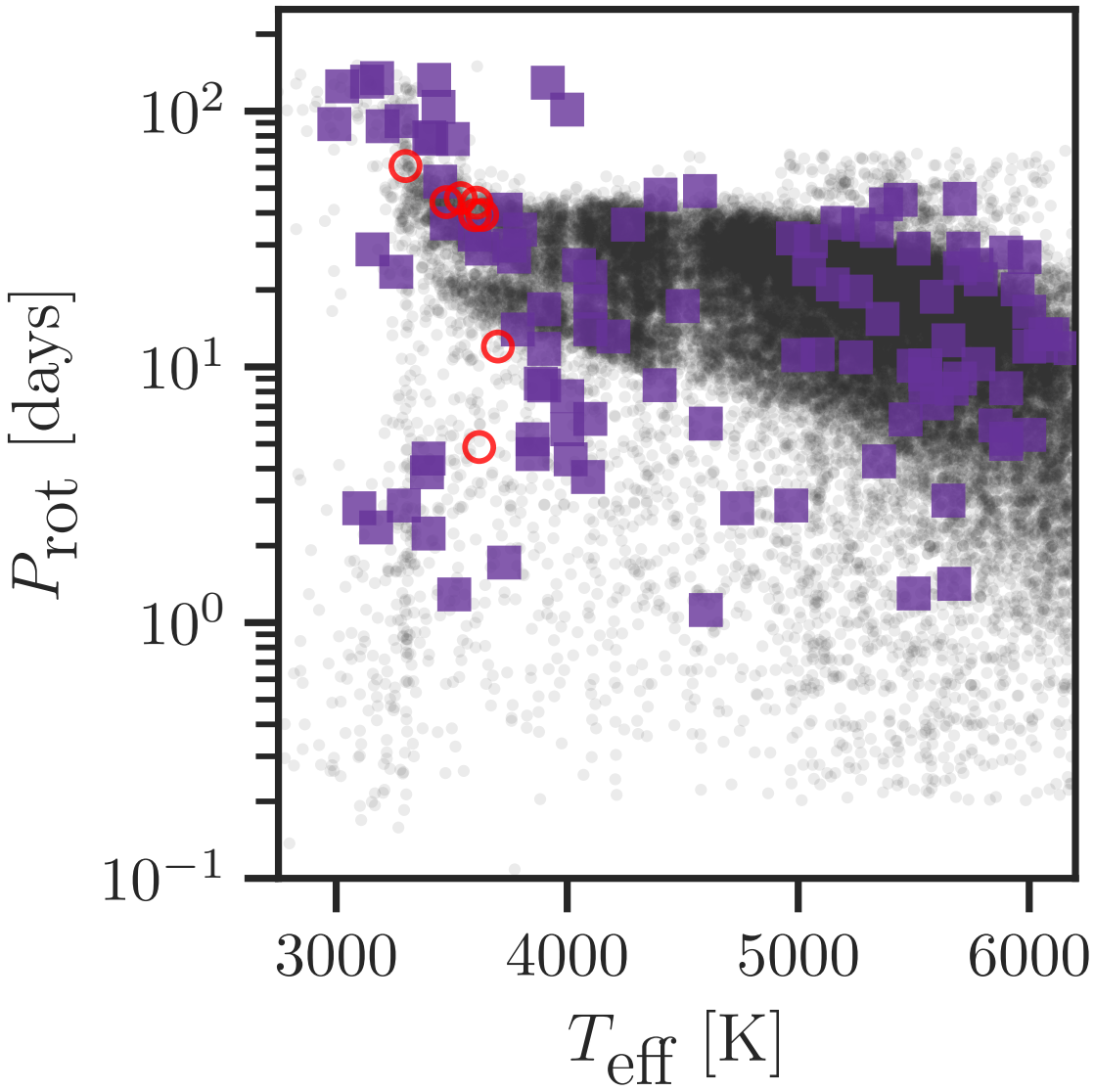

Figure 5.1: The planned sample for fitting DEMs, likely to change based on data availability.

5.3 Fit Results: DEMs and EUV Spectra

We are using the updated DEM method described in Chapter 4 where the contribution functions for X-ray spectral bins and the output EUV spectrum incorporate continua from free-free emission and the two-photon and recombination continua of H I, H II, He I, He II, and He III. The contribution functions for all stars are calculated using the same default electron density $P_e = 10^{17}\,\mathrm{cm}^{-3}\ k_\mathrm{B}T$ for $10^4 < T < 10^8\,\mathrm{K}$, the same solar coronal abundances from Schmelz et al. (2012), and the same default ionization equilibrium from `CHIANTI 10.0.1` (Dere et al., 1997; Del Zanna et al., 2021). This means that all differences in the shape of the output spectrum are from the shape of the DEM, collapsing all subtleties of the differences in temperature-pressure profile, abundances, and species ionization from star to star within the uncertainty parameter. As a specific example, if the abundance of a single element like C relative to H varies with temperature in a manner different from Fe, that will increase the systematic uncertainty when trying to fit emission from both species because moving the DEM up or down will affect all species equally.

Figure 5.2 – 5.9 are "summary figures" developed to look at a single star's DEM fitting and EUV output at a glance, enabling easier comparison between targets. The summary figure is divided into four panels, referred to in this explanation as "DEM" (top left), "EUV" (bottom left), "FIT" (top right), "SAMPLE" (bottom right). The title of the summary figure at the top shows the star's name in **boldface**, followed by the star's "T_eff [K]; $M_\star\,[M_\odot]$; $R_\star\,[R_\odot]$; P_rot [days]; d [pc]". The DEM panel shows the maximum-likelihood sample DEM for the star with a dashed blue line, flanked on either side by a blue swath enclosing the 16^th – 84^th percentile values of all the samples' DEM values at that temperature. The DEM averages associated with each flux constraint are also plotted, where the width of the line describes the central 50% of the cumulative integral of the contribution function for the flux constraint, and the y-axis position reflects the DEM value required to produce the observed flux if the DEM was a constant across the entire temperature domain. The broader the line and the more the shape of the DEM varies within the line's boundaries, the less meaningful the plotted average becomes. The EUV panel shows the output EUV spectrum as

observed at 1 AU with a step-style blue line, with 16^{th} – 84^{th} percentile boundaries of 10^6 draws from the combination of sampling from the DEM posterior and the Gaussian $\mathcal{N}(\mu = f_\lambda, \sigma = s \cdot f_\lambda)$ to incorporate the systematic uncertainty parameter. The FIT panel is a direct representation of the model's goodness-of-fit, where the x-axis is the flux of a measured emission feature scaled to a distance of 1 AU and the y-axis separates each flux constraint by tick marks and is ordered by formation temperature increasing from top to bottom. The black dot and its errorbars are the measurement used to inform the fit (but plotted with the 1 AU scaling applied, the fit uses the value as measured in the data) while the blue cross and its errorbars are the median model prediction for that emission feature and the 16^{th} – 84^{th} percentile boundaries for that prediction while incorporating the systematic uncertainty as described earlier. Finally, the SAMPLE panel is a miniaturized modification of Figure 5.1 to plot the T_{eff} and P_{rot} of the the planned full sample (purple squares), the subsample studied in this chapter (red circles), and the subject of the summary figure (solid navy blue star).

While keeping in mind that these are not strict quantitative comparisons because the DEM shapes are conditional to the assumed contribution functions, having a number of them together makes it possible to compare structural features between stars, with the additional caveat that this is a very limited sample to make strong claims with. Starting from the knowledge that the low temperature end is the base of the chromosphere while the high temperature end is the corona, the peak at high temperatures corresponds to the highest temperature at which there is a significant amount of material in the corona, conceptually related to the coronal temperature reported by single-temperature model fits commonly used in X-ray spectral analysis. The gradient of the DEM at the low temperature end is somehow related to the combination of the temperature and density gradient across the chromosphere. The link between these two features is the transition region, where a high DEM translates to physically thicker transition region.

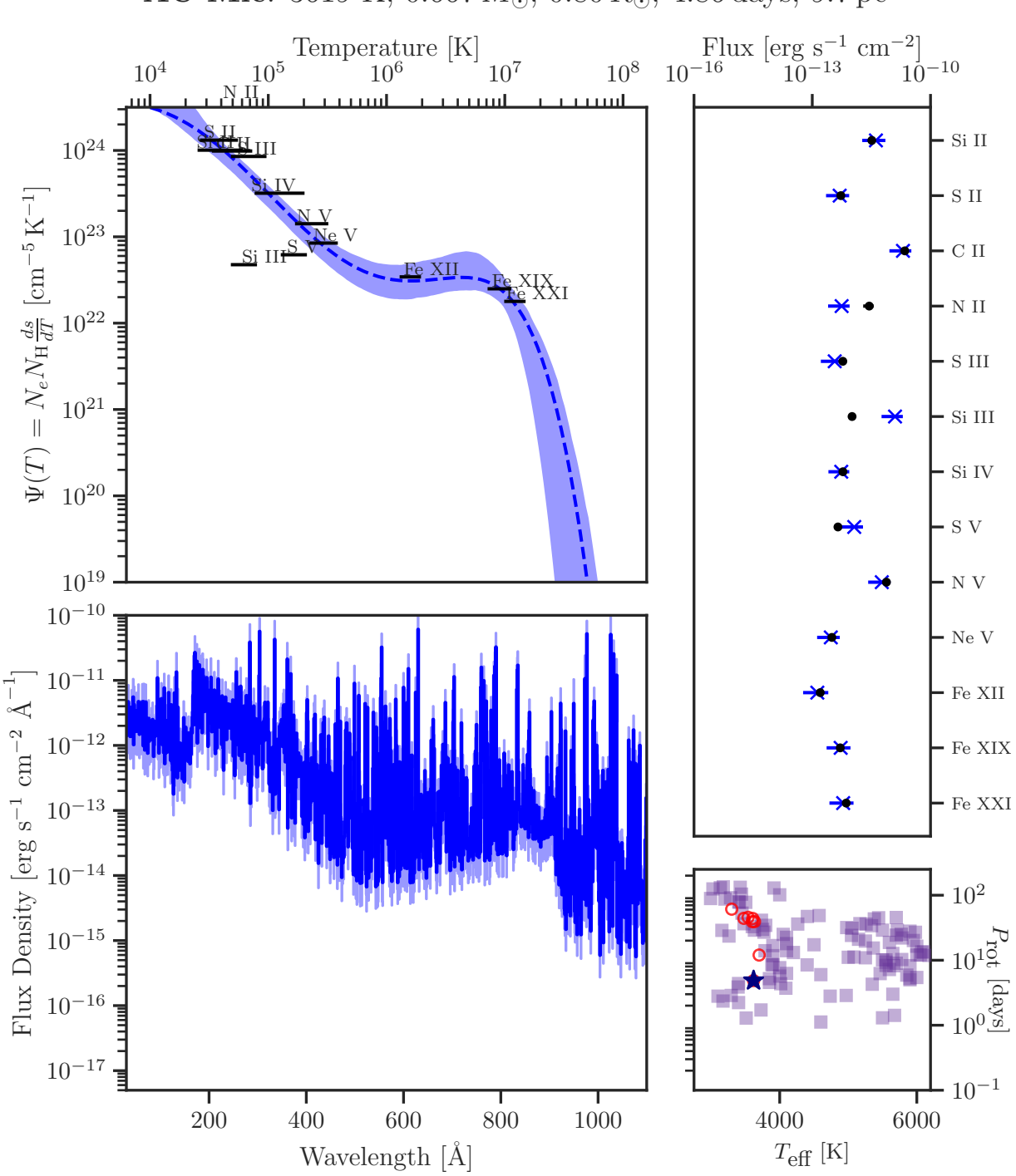

Figure 5.2: AU Mic

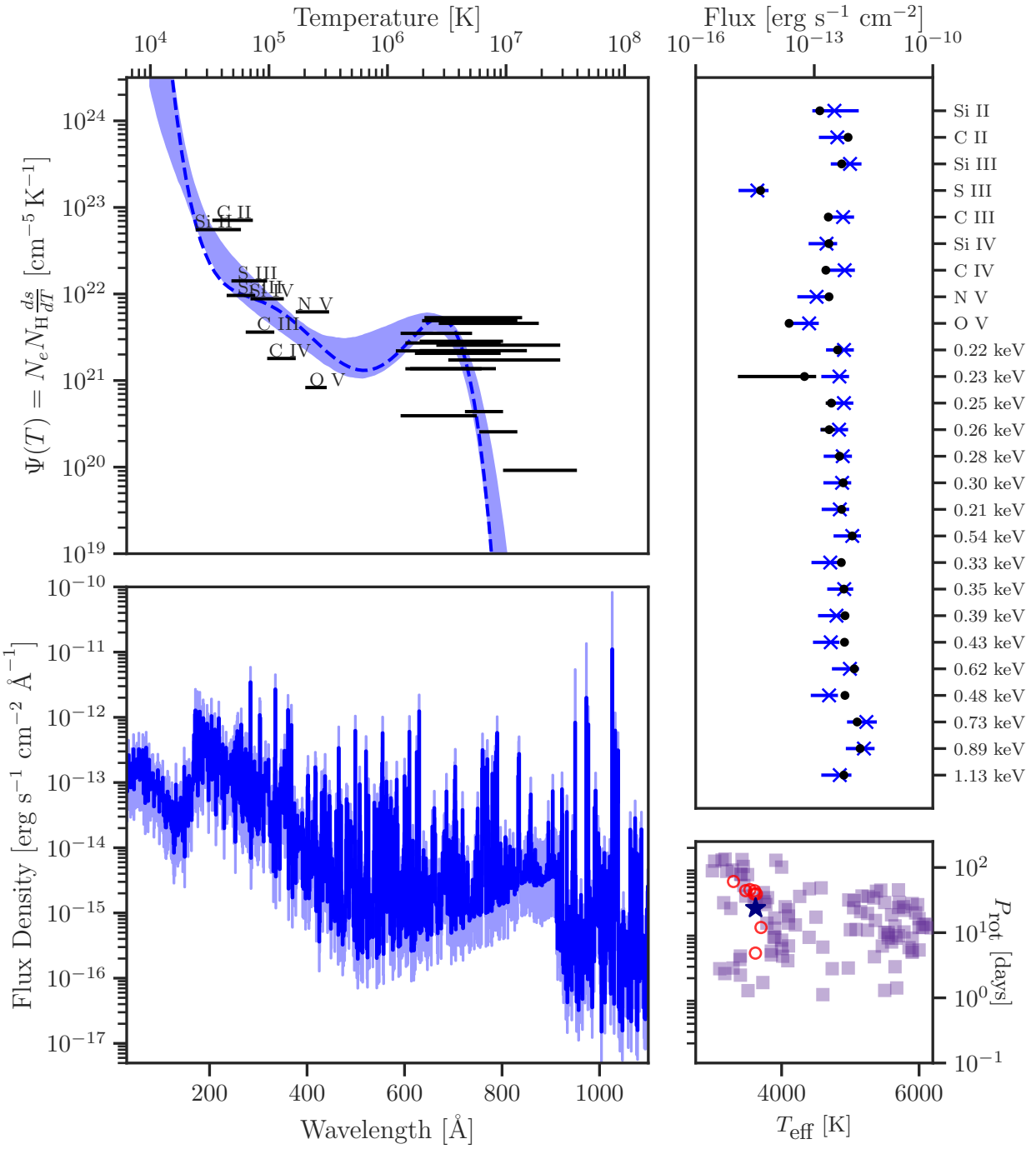

Figure 5.3: GJ 649

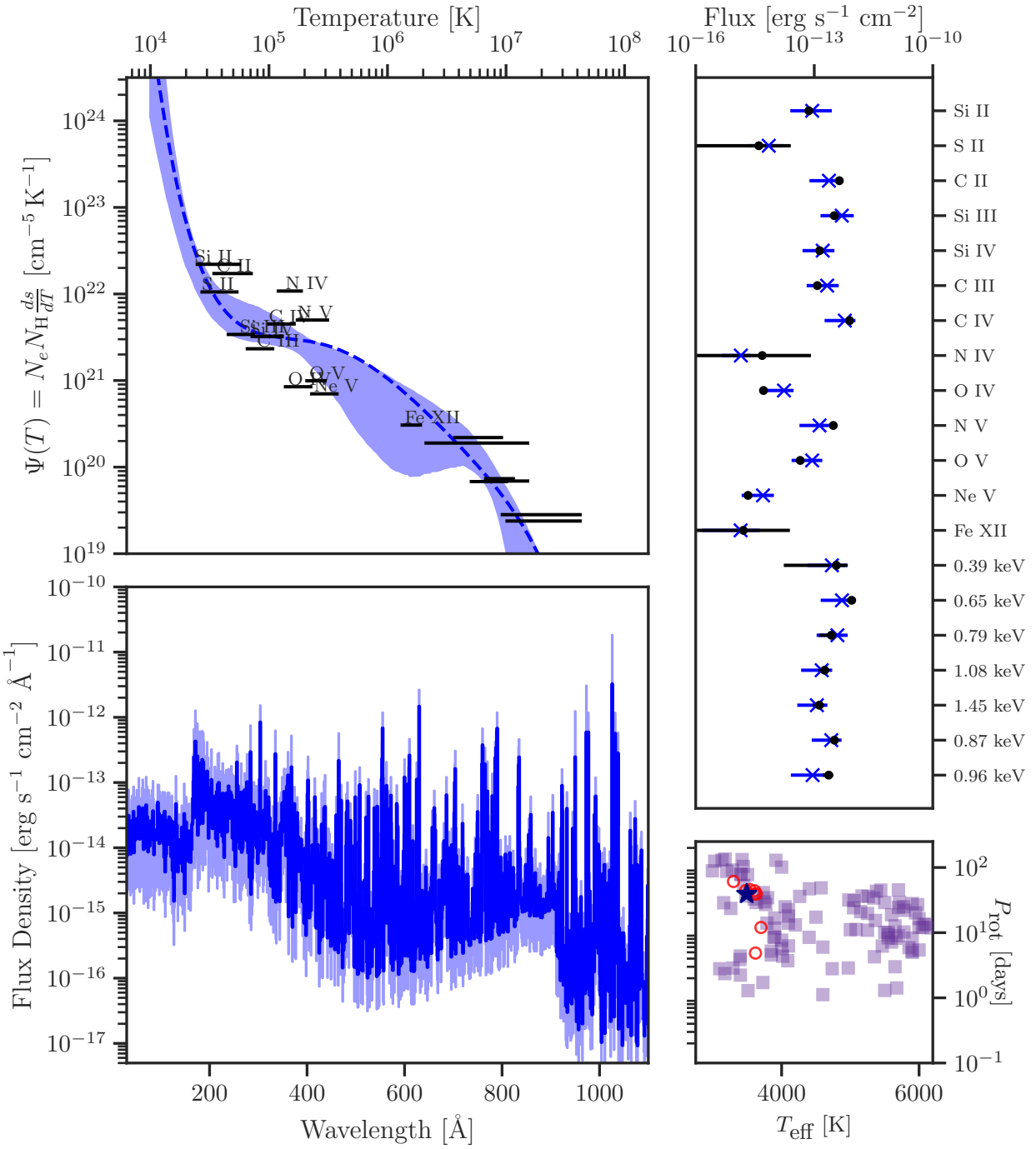

Figure 5.4: GJ 849

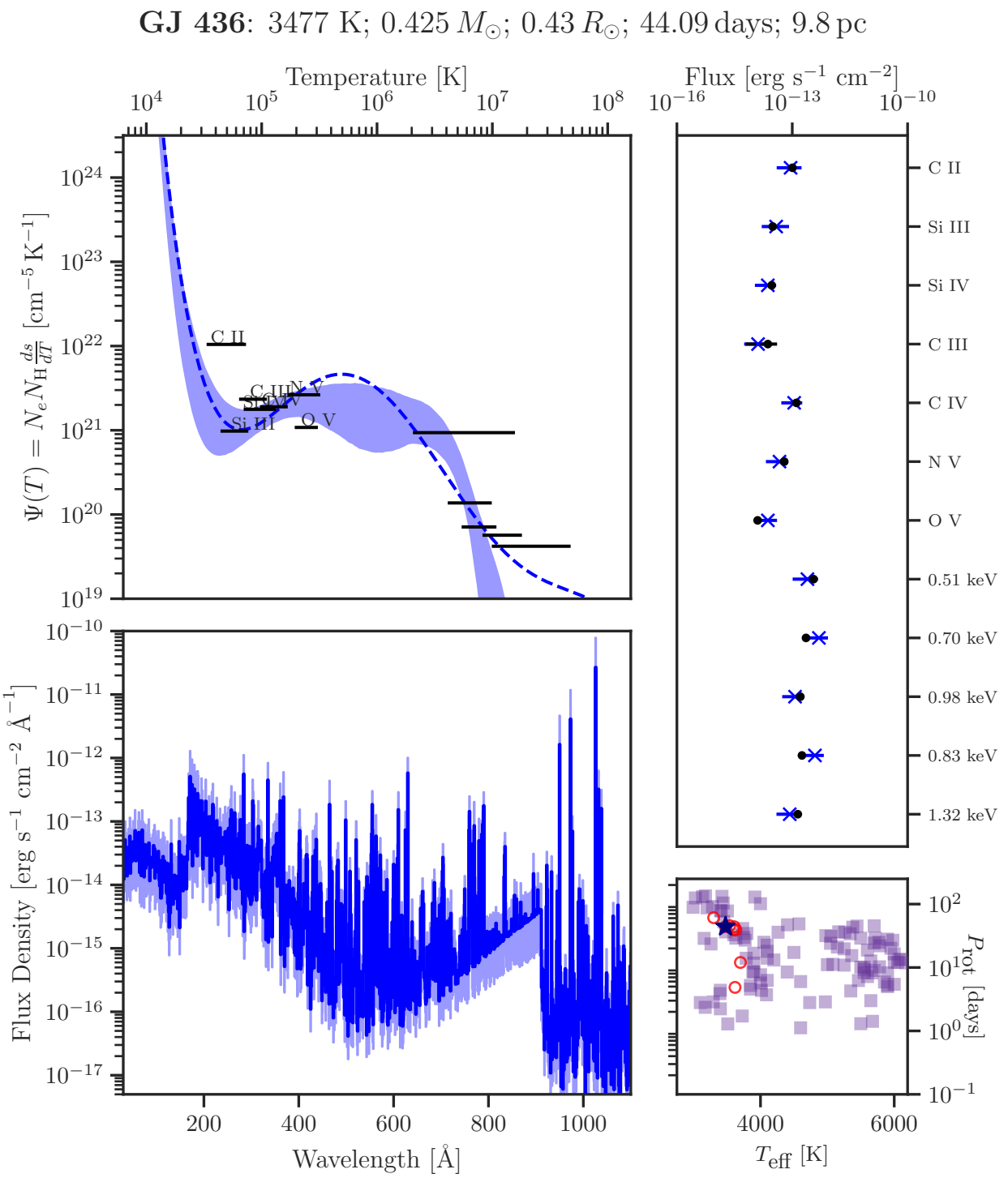

Figure 5.5: GJ 436

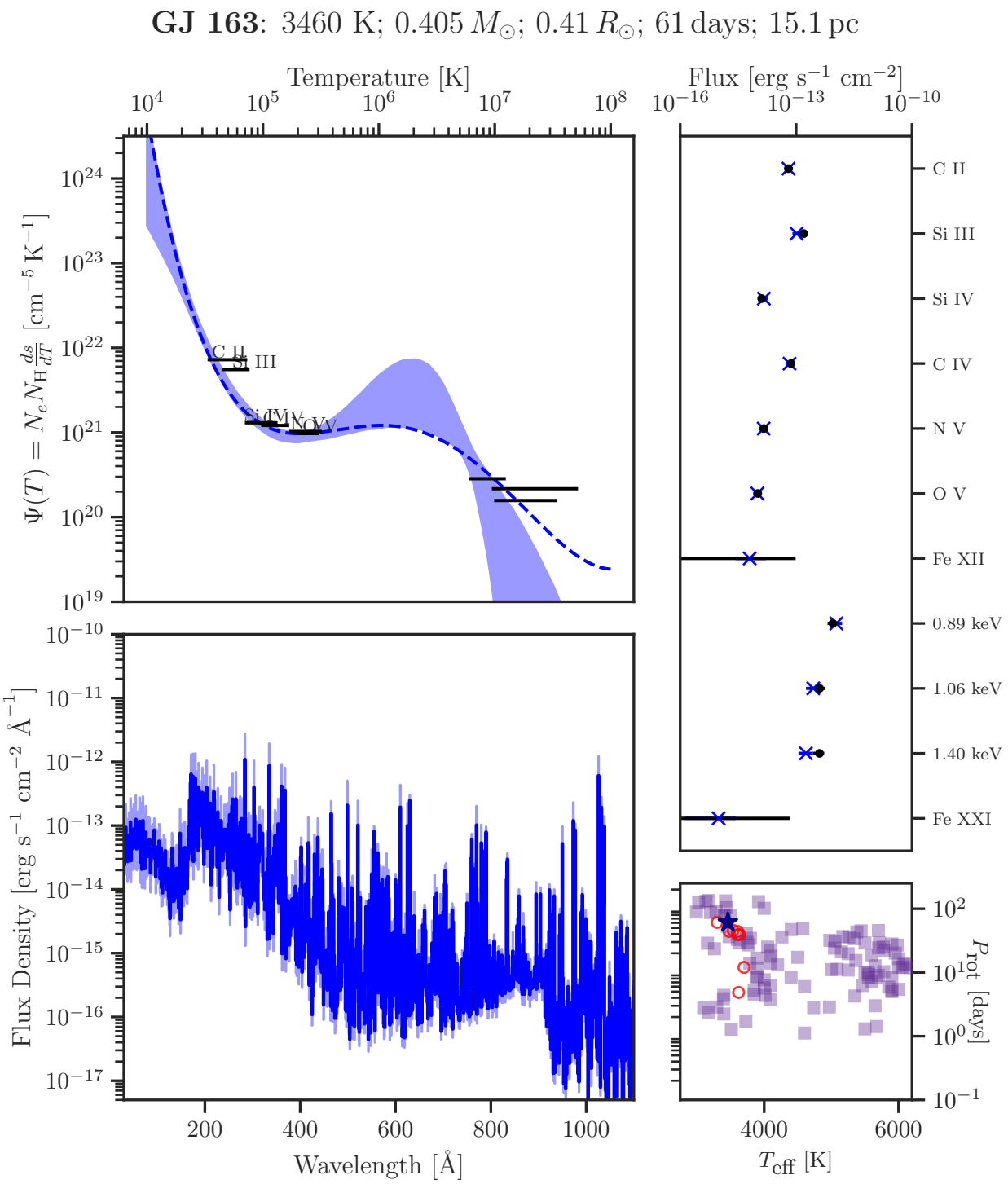

Figure 5.6: GJ 163

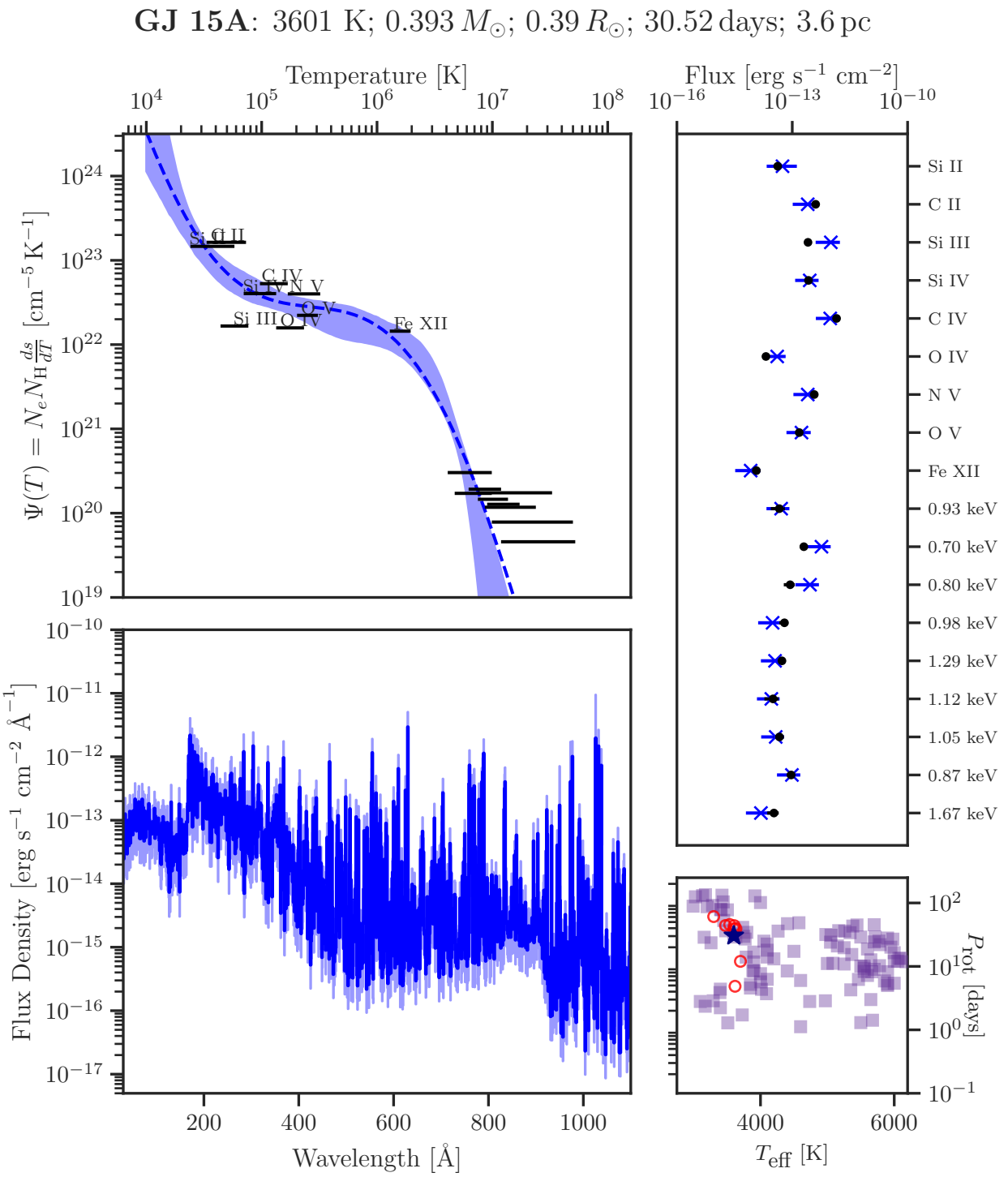

Figure 5.7: GJ 15A

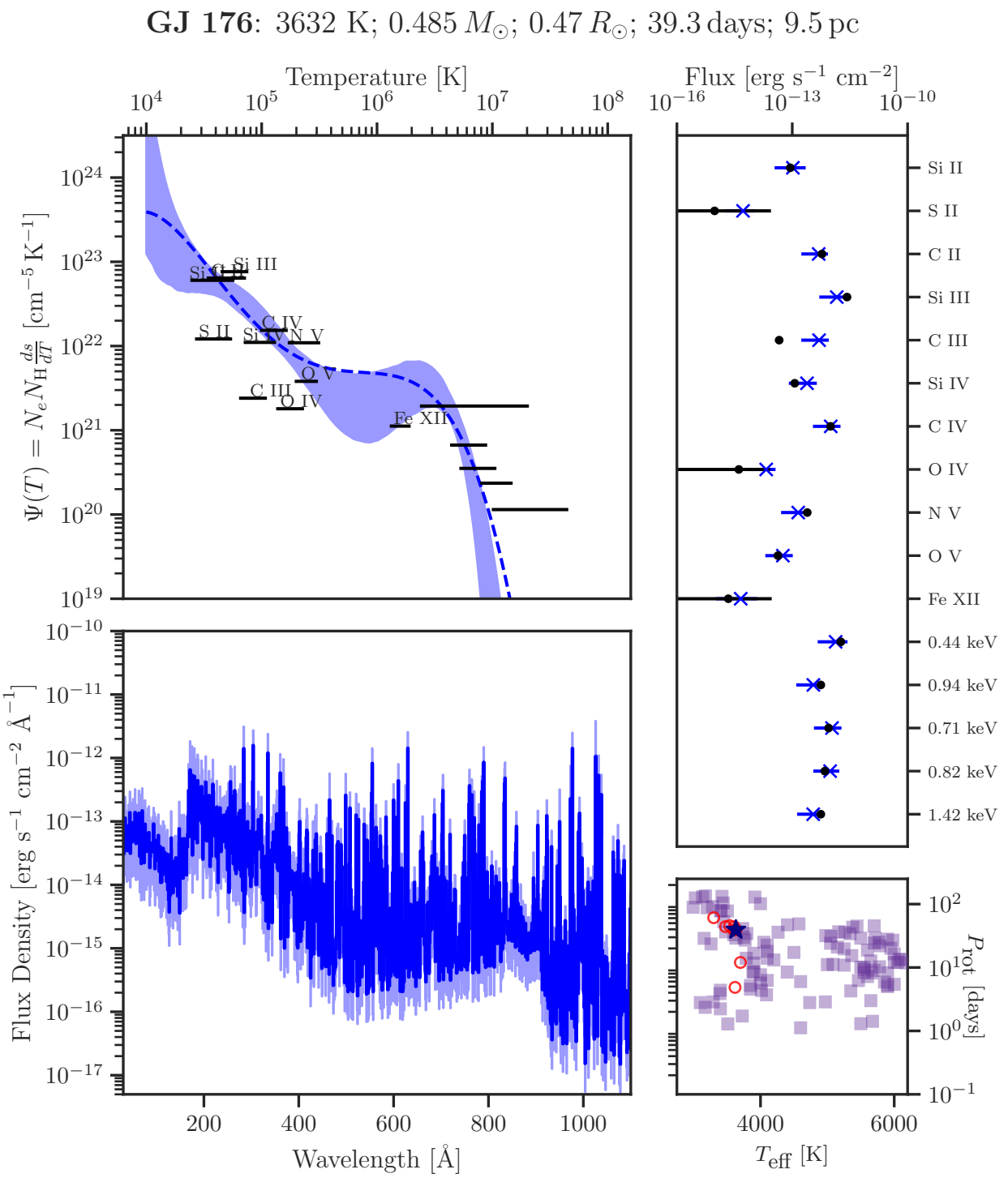

Figure 5.8: GJ 176: known flaring reported in Loyd et al. (2018b)

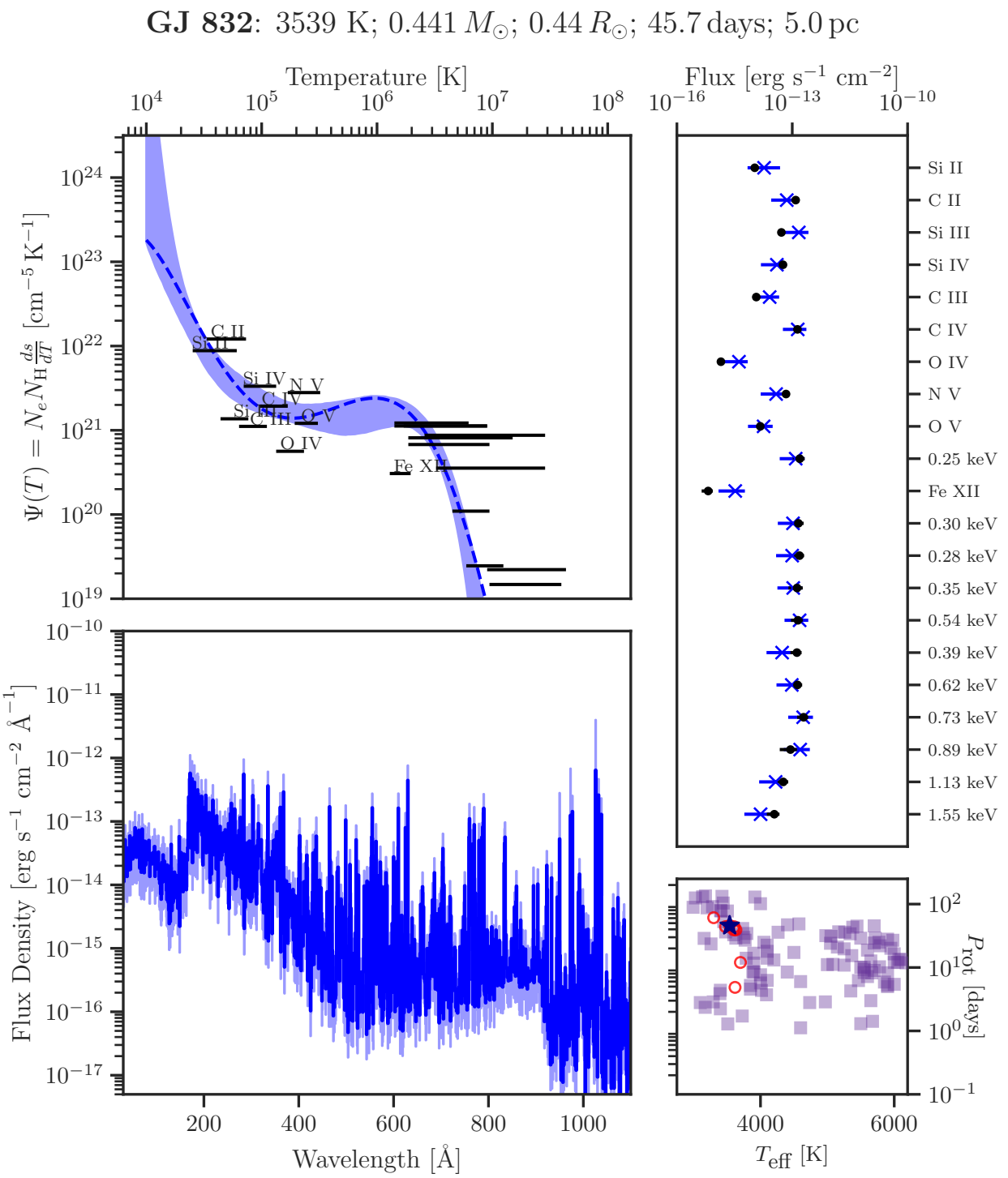

Figure 5.9: GJ 832: known flaring reported in Loyd et al. (2018b)

5.4 Interpolating the DEM and EUV Spectrum

Excluding GJ 15A (which has the lowest mass of the stars above) and the flare-contaminated stars GJ 176 and GJ 832, we are left with five stars: AU Mic, GJ 649, GJ 849, GJ 436, and GJ 163. For AU Mic we assign the literature age of 22 Myr (Plavchan et al., 2020), and for the others we use Equation 1 of Engle & Guinan (2018) to convert their rotation periods to an age estimate $\tau_\star$, marked by the annotations to the red vertical lines in the top panel of Figure 5.10. Then we use the median DEM shape from these 5 stars, plotted in the second row of panels in Figure 5.10 to linearly interpolate the DEM as a function of $\log_{10}\tau$, showing three example interpolated DEMs in the bottom row of panels in Figure 5.10, associated with the ages marked by the annotations to the grey vertical lines in the top panel of Figure 5.10.

We use this interpolated function to calculate the cumulative irradiation over an arbitrary time and wavelength bandpass

$$I_{\lambda_l-\lambda_u}(t) = \int_{0\,\mathrm{Gyr}}^{t\,\mathrm{Gyr}} \int_{\lambda_l}^{\lambda_u} F_\lambda(t')d\lambda dt' \tag{5.1}$$

for a hypothetical M2V dwarf with properties that are some average over those of the five stars used to determine the interpolant ($R_\star = 0.5R_\odot$, $T_{\mathrm{eff}} = 3600\,\mathrm{K}$). We plot the cumulative irradiation of a planet orbiting at 1 AU as a function of stellar age in Figure 5.11.

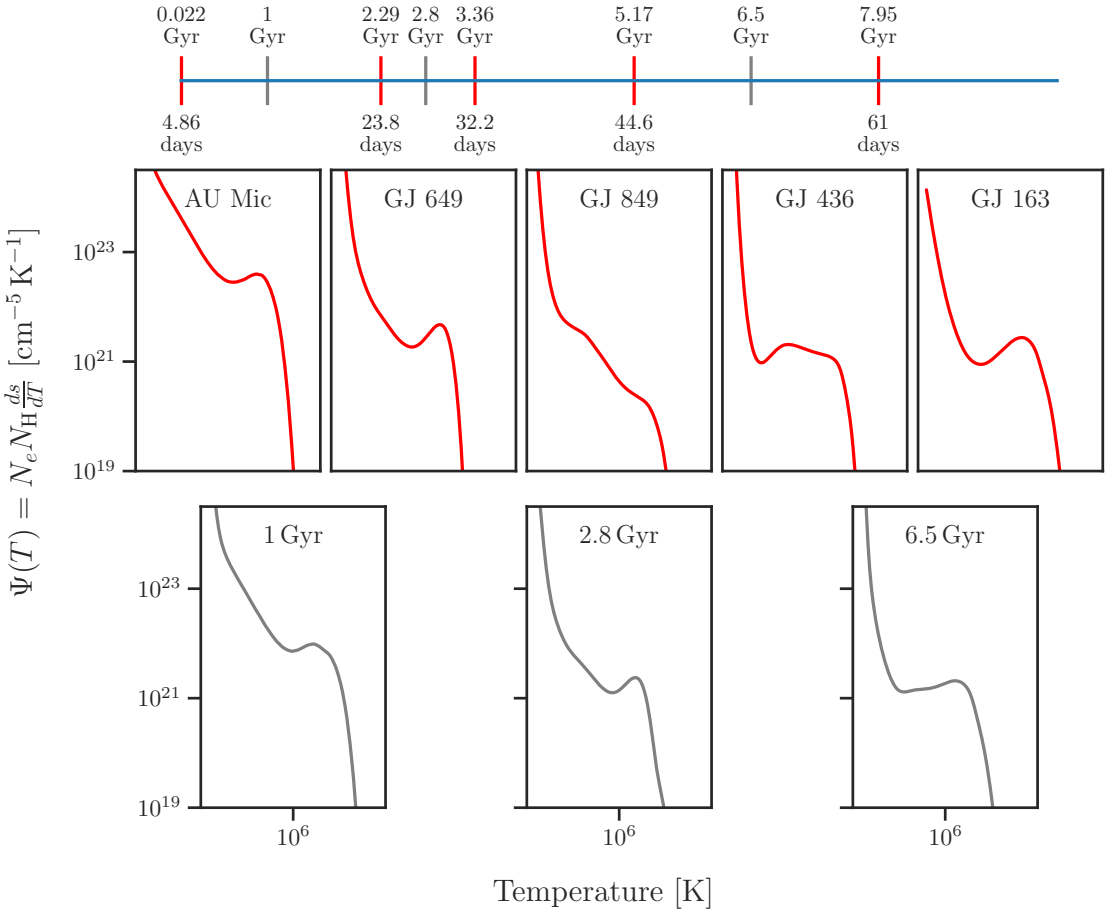

Figure 5.10: The top row is a number line showing the ages and rotation periods of the stars used to determine the interpolation with red lines, plotting their DEMs in the middle row, while the grey lines in the top row mark the ages associated with the interpolated DEMs plotted in the bottom row.

5.5 Future (of this) Work

The interpolation method described in Section §5.4 is crude, discounting uncertainties in every step of the process and lumping together a wide range of masses, but demonstrates the principle of a powerful tool to study exoplanet atmospheres by describing the time-evolution of high-energy emission. The first step is to fit DEMs to the broader sample, dropping stars where the DEMs are too unconstrained to be useful and adding stars with a more careful look at the archive and upcoming observing programs. Once the sample is populated enough for some subspace of stellar mass and age (or age proxy), we can test different interpolation schemes and incorporate the uncertainty of all inputs by drawing randomly from the posterior of DEMs for sample stars in tandem with random draws of the stellar parameters we are interpolating over. Then for whatever specific interpolation method we use for the DEM across the stellar parameters, we can parameterize the systematic uncertainty of the interpolation by iteratively testing its ability to replicate the original DEM fits for some randomly selected test subset excluded from the DEMs used to inform the interpolation. I plan to do this for M dwarfs first by completing fits for all the MUSCLES, MegaMUSCLES, and FUMES targets with sufficient data. The fits for these M dwarfs and a slightly more sophisticated version of the 1D interpolation done here will be an expanded version of this chapter that I plan to submit for publication, leaving the complete sample and 2D interpolation to future work.

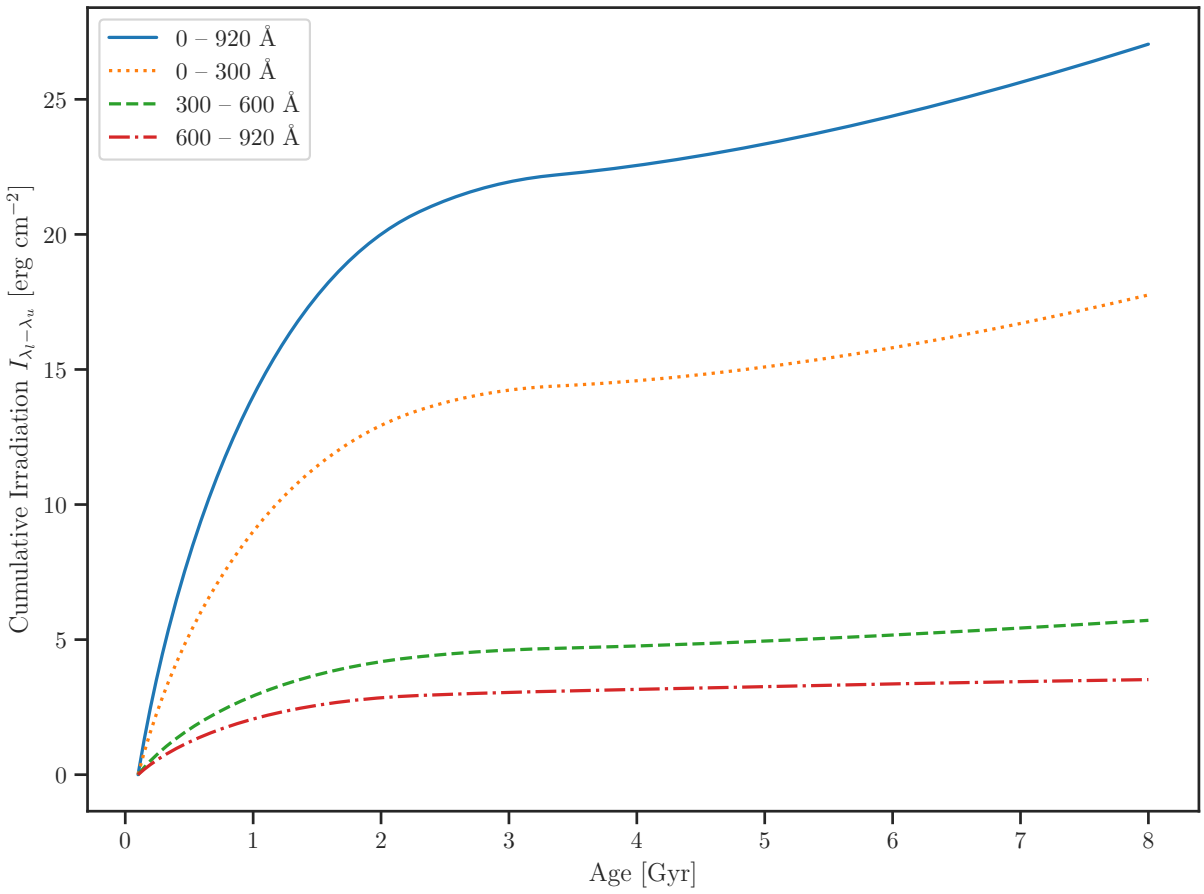

Figure 5.11: The share of EUV flux is dominated by emission from < 300 Å for this hypothetical star, with most of the cumulative irradiation being emitted when the star < 2 Gyr. If a planet outgassed a significant mass to the atmosphere after that point, it would be much more likely to be habitable.

Chapter 6

Future Work

The organizing principle of this thesis, the characterization of high-energy emission from low-mass stars, is very much a post hoc summary of the work done during my graduate school experience, but that does not make it untrue. The primary motivation for most of this work was to be able to inform studies of exoplanetary systems and learning about stellar magnetism was at first a means to that end. In this case, familiarity has bred curiosity rather than contempt, and many of the questions I want to explore in the future are directly concerned with stellar magnetic heating while my interest in exoplanetary systems persists.

There are many improvements to the differential emission measure approach that remain to be made, particularly in using semi-empirical stellar atmosphere models to refine the calculation of contribution functions and add more physical information to the prior constraints on the DEM functional form as well as using the DEM as a starting point to tune semi-empirical models. Of course the hope is that with more well-tuned semi-empirical model atmospheres to look at, we can improve our understanding of the physical processes in real stars. The observational tests of stochastic variability described in Chapter 3 are worth doing and as spectroscopic observations improve in resolution, readout time, and sensitivity across all wavelengths we can directly link the variability observed in disk-integrated stellar spectra to more local observations of the Sun. My time here has made it clear that Sun as a star observations need to be extended to shorter wavelengths and considered in terms beyond mitigating stellar activity signals in radial velocity observations.

The data collation for my planned interpolation project presents many more opportunities beyond a library of inferred EUV spectra; there are many lines formed in more complicated ways than pure collisional excitation and studying their behavior across that large sample may prove a more direct test of the trends in magnetic heating required to produce patterns we might see in recombination features which are particularly sensitive to the velocity distribution of free electrons. Every flare spectrum I set aside from the DEM work is a flare worth looking at on its own terms and applying the principle of different lines as probing different heights/temperatures may allow us to track the flare in motion as individual lines skew red or blue, with a sign change in the skew marking the passing of the chromospheric condensation layer at that line's formation temperature.

On the planetary side, it would be nice to move beyond providing inputs for exoplanet atmosphere models and interpreting observations of transmission spectroscopy to start doing those things myself. France et al. (2020b) used DEM-generated EUV spectra of Barnard's Star during both flare and quiescence to inform a long-term atmospheric escape model that included planetary magnetic field effects, while Feinstein et al. (2022) used the DEM-generated spectrum of AU Mic to calculate an energy-limited escape rate for planets orbiting AU Mic. There is a lot of open space between those two applications of EUV spectra; for example modelling the escape from a toy model single or double molecule composition atmosphere that incorporates the absorption cross-section of those species to test whether the maximum depth reached by EUV photons changes significantly over a planetary lifetime for a particular choice of dominant molecular species. Inferences of escape rates from He I 1083 nm transmission spectroscopy depend on both the model assumptions for the hydrodynamic outflow and the assumed high-energy spectrum to determine the population of the metastable state of the emission line. I would like my future research program to broadly speaking be the study of exoplanetary systems over system lifetimes, making connections between the changes of the star, planet, and their shared environment.

Bibliography

Allred, J. C., Hawley, S. L., Abbett, W. P., & Carlsson, M., 2006, Radiative Hydrodynamic Models of Optical and Ultraviolet Emission from M Dwarf Flares, *ApJ*, 644(1), 484–496.

Amerstorfer, U. V., Gröller, H., Lichtenegger, H., Lammer, H., Tian, F., Noack, L., Scherf, M., Johnstone, C., Tu, L., & Güdel, M., 2017, Escape and evolution of Mars's CO_2 atmosphere: Influence of suprathermal atoms, *Journal of Geophysical Research (Planets)*, 122(6), 1321–1337.

Arnaud, K. A., 1996, XSPEC: The First Ten Years, *in* Jacoby, G. H. & Barnes, J. (eds), *Astronomical Data Analysis Software and Systems V*, Vol. 101 of *Astronomical Society of the Pacific Conference Series*, p. 17.

Athay, R. G., 1976, *The solar chromosphere and corona: Quiet sun*, Vol. 53.

Ayres, T. R., 2010, StarCAT: A Catalog of Space Telescope Imaging Spectrograph Ultraviolet Echelle Spectra of Stars, *ApJS*, 187(1), 149–171.

Ayres, T. R., 2014, The Ups and Downs of α Centauri, *AJ*, 147(3), 59.

Ayres, T. R. & Rabin, D., 1996, Observations of Solar Carbon Monoxide with an Imaging Infrared Spectrograph. I. Thermal Bifurcation Revisited, *ApJ*, 460, 1042.

Bailey, J., Butler, R. P., Tinney, C. G., Jones, H. R. A., O'Toole, S., Carter, B. D., & Marcy, G. W., 2009, A Jupiter-Like Planet Orbiting the Nearby M dwarf GJ 832, *ApJ*, 690(1), 743–747.

Baliunas, S. L., Donahue, R. A., Soon, W. H., Horne, J. H., Frazer, J., Woodard-Eklund, L., Bradford, M., Rao, L. M., Wilson, O. C., Zhang, Q., Bennett, W., Briggs, J., Carroll, S. M., Duncan, D. K., Figueroa, D., Lanning, H. H., Misch, T., Mueller, J., Noyes, R. W., Poppe, D., Porter, A. C., Robinson, C. R., Russell, J., Shelton, J. C., Soyumer, T., Vaughan, A. H., & Whitney, J. H., 1995, Chromospheric Variations in Main-Sequence Stars. II., *ApJ*, 438, 269.

Ballard, S., 2019, Predicted Number, Multiplicity, and Orbital Dynamics of TESS M-dwarf Exoplanets, *AJ*, 157(3), 113.

Barclay, T., Pepper, J., & Quintana, E. V., 2018, A Revised Exoplanet Yield from the Transiting Exoplanet Survey Satellite (TESS), *ApJS*, 239(1), 2.

Baron, E. & Hauschildt, P. H., 2007, A 3D radiative transfer framework. II. Line transfer problems, *A&A*, 468(1), 255–261.

Basri, G. & Shah, R., 2020, The Information Content in Analytic Spot Models of Broadband Precision Light Curves. II. Spot Distributions and Lifetimes and Global and Differential Rotation, *ApJ*, 901(1), 14.

Baum, A. C., Wright, J. T., Luhn, J. K., & Isaacson, H., 2022, Five Decades of Chromospheric Activity in 59 Sun-like Stars and New Maunder Minimum Candidate HD 166620, *AJ*, 163(4), 183.

Bryson, S., Kunimoto, M., Kopparapu, R. K., Coughlin, J. L., Borucki, W. J., Koch, D., Aguirre, V. S., Allen, C., Barentsen, G., Batalha, N. M., Berger, T., Boss, A., Buchhave, L. A., Burke, C. J., Caldwell, D. A., Campbell, J. R., Catanzarite, J., Chandrasekaran, H., Chaplin, W. J., Christiansen, J. L., Christensen-Dalsgaard, J., Ciardi, D. R., Clarke, B. D., Cochran, W. D., Dotson, J. L., Doyle, L. R., Duarte, E. S., Dunham, E. W., Dupree, A. K., Endl, M., Fanson, J. L., Ford, E. B., Fujieh, M., Gautier, Thomas N., I., Geary, J. C., Gilliland, R. L., Girouard, F. R., Gould, A., Haas, M. R., Henze, C. E., Holman, M. J., Howard, A. W., Howell, S. B., Huber, D., Hunter, R. C., Jenkins, J. M., Kjeldsen, H., Kolodziejczak, J., Larson, K., Latham, D. W., Li, J., Mathur, S., Meibom, S., Middour, C., Morris, R. L., Morton, T. D., Mullally, F.,

Mullally, S. E., Pletcher, D., Prsa, A., Quinn, S. N., Quintana, E. V., Ragozzine, D., Ramirez, S. V., Sanderfer, D. T., Sasselov, D., Seader, S. E., Shabram, M., Shporer, A., Smith, J. C., Steffen, J. H., Still, M., Torres, G., Troeltzsch, J., Twicken, J. D., Uddin, A. K., Van Cleve, J. E., Voss, J., Weiss, L. M., Welsh, W. F., Wohler, B., & Zamudio, K. A., 2021, The Occurrence of Rocky Habitable-zone Planets around Solar-like Stars from Kepler Data, *AJ*, 161(1), 36.

Cargill, P. J. & Priest, E. R., 1983, The heating of postflare loops, *ApJ*, 266, 383–389.

Cauley, P. W., Bean, J. L., David, T., Duvvuri, G., France, K., Johns-Krull, C. M., Kilgard, R. E., & Stahl, A., 2020, Planetary mass loss and the high-energy spectrum of V1298 Tau, HST Proposal. Cycle 28, ID. #16163.

Chadney, J. M., Galand, M., Unruh, Y. C., Koskinen, T. T., & Sanz-Forcada, J., 2015, XUV-driven mass loss from extrasolar giant planets orbiting active stars, *Icarus*, 250, 357–367.

Claire, M. W., Sheets, J., Cohen, M., Ribas, I., Meadows, V. S., & Catling, D. C., 2012, The Evolution of Solar Flux from 0.1 nm to 160 μm: Quantitative Estimates for Planetary Studies, *ApJ*, 757(1), 95.

Cox, D. P. & Reynolds, R. J., 1987, The local interstellar medium., *ARA&A*, 25, 303–344.

Craig, I. J. D. & Brown, J. C., 1976, Fundamental limitations of X-ray spectra as diagnostics of plasma temperature structure., *A&A*, 49(2), 239–250.

Craig, N., Abbott, M., Finley, D., Jessop, H., Howell, S. B., Mathioudakis, M., Sommers, J., Vallerga, J. V., & Malina, R. F., 1997, The Extreme Ultraviolet Explorer Stellar Spectral Atlas, *ApJS*, 113(1), 131–193.

Cram, L. E. & Giampapa, M. S., 1987, Formation of Chromospheric Lines in Cool Dwarf Stars, *ApJ*, 323, 316.

Cranmer, S. R., Asgari-Targhi, M., Miralles, M. P., Raymond, J. C., Strachan, L., Tian, H., & Woolsey, L. N., 2015, The role of turbulence in coronal heating and solar wind expansion, *Philosophical Transactions of the Royal Society of London Series A*, 373(2041), 20140148–20140148.

Cruz Aguirre, F., Youngblood, A., France, K., & Bourrier, V., 2023, Disentangling Stellar and Airglow Emission Lines from HST-COS Spectra, *arXiv e-prints*, p. arXiv:2301.08452.

Cully, S. L., Siegmund, O. H. W., Vedder, P. W., & Vallerga, J. V., 1993, Extreme Ultraviolet Explorer Deep Survey Observations of a Large Flare on AU Microscopii, *ApJ*, 414, L49.

Davenport, J., de Val-Borro, M., & Wilkinson, T. D., 2016, Pydis: Possibly Useful, Zenodo.

David, T. J., Petigura, E. A., Luger, R., Foreman-Mackey, D., Livingston, J. H., Mamajek, E. E., & Hillenbrand, L. A., 2019, Four Newborn Planets Transiting the Young Solar Analog V1298 Tau, *ApJ*, 885(1), L12.

Del Zanna, G., Dere, K. P., Young, P. R., & Landi, E., 2021, CHIANTI—An Atomic Database for Emission Lines. XVI. Version 10, Further Extensions, *ApJ*, 909(1), 38.

Del Zanna, G., Dere, K. P., Young, P. R., Landi, E., & Mason, H. E., 2015, CHIANTI - An atomic database for emission lines. Version 8, *A&A*, 582, A56.

Del Zanna, G., Landini, M., & Mason, H. E., 2002, Spectroscopic diagnostics of stellar transition regions and coronae in the XUV: AU Mic in quiescence, *A&A*, 385, 968–985.

den Herder, J. W., Brinkman, A. C., Kahn, S. M., Branduardi-Raymont, G., Thomsen, K., Aarts, H., Audard, M., Bixler, J. V., den Boggende, A. J., Cottam, J., Decker, T., Dubbeldam, L., Erd, C., Goulooze, H., Güdel, M., Guttridge, P., Hailey, C. J., Janabi, K. A., Kaastra, J. S., de Korte, P. A. J., van Leeuwen, B. J., Mauche, C., McCalden, A. J., Mewe, R., Naber, A., Paerels, F. B., Peterson, J. R., Rasmussen, A. P., Rees, K., Sakelliou, I., Sako, M., Spodek, J., Stern, M., Tamura, T., Tandy, J., de Vries, C. P., Welch, S., & Zehnder, A., 2001, The Reflection Grating Spectrometer on board XMM-Newton, *A&A*, 365, L7–L17.

Dere, K. P., Landi, E., Mason, H. E., Monsignori Fossi, B. C., & Young, P. R., 1997, CHIANTI - an atomic database for emission lines, *A&AS*, 125, 149–173.

Diamond-Lowe, H., Kreidberg, L., Harman, C. E., Kempton, E. M. R., Rogers, L. A., Joyce, S. R. G., Eastman, J. D., King, G. W., Kopparapu, R., Youngblood, A., Kosiarek, M. R., Livingston, J. H., Hardegree-Ullman, K. K., & Crossfield, I. J. M., 2022, The K2-3 System Revisited: Testing Photoevaporation and Core-powered Mass Loss with Three Small Planets Spanning the Radius Valley, *AJ*, 164(5), 172.

Diamond-Lowe, H., Youngblood, A., Charbonneau, D., King, G., Teal, D. J., Bastelberger, S., Corrales, L., & Kempton, E. M. R., 2021, The high-energy spectrum of the nearby planet-hosting inactive mid-M dwarf LHS 3844, *arXiv e-prints*, p. arXiv:2104.10522.

Díez Alonso, E., Caballero, J. A., Montes, D., de Cos Juez, F. J., Dreizler, S., Dubois, F., Jeffers, S. V., Lalitha, S., Naves, R., Reiners, A., Ribas, I., Vanaverbeke, S., Amado, P. J., Béjar, V. J. S., Cortés-Contreras, M., Herrero, E., Hidalgo, D., Kürster, M., Logie, L., Quirrenbach, A., Rau, S., Seifert, W., Schöfer, P., & Tal-Or, L., 2019, CARMENES input catalogue of M dwarfs. IV. New rotation periods from photometric time series, *A&A*, 621, A126.

Drake, J. J., Laming, J. M., & Widing, K. G., 1995, Stellar Coronal Abundances. II. The First Ionization Potential Effect and Its Absence in the Corona of Procyon, *ApJ*, 443, 393.

Dressing, C. D. & Charbonneau, D., 2015, The Occurrence of Potentially Habitable Planets Orbiting M Dwarfs Estimated from the Full Kepler Dataset and an Empirical Measurement of the Detection Sensitivity, *ApJ*, 807(1), 45.

Duvvuri, G. M., Pineda, J. S., Berta-Thompson, Z. K., France, K., & Youngblood, A., 2023, FUMES. III. Ultraviolet and Optical Variability of M-dwarf Chromospheres, *AJ*, 165(1), 12.

Duvvuri, G. M., Sebastian Pineda, J., Berta-Thompson, Z. K., Brown, A., France, K., Kowalski, A. F., Redfield, S., Tilipman, D., Vieytes, M. C., Wilson, D. J., Youngblood, A., Froning, C. S.,

Linsky, J., Parke Loyd, R. O., Mauas, P., Miguel, Y., Newton, E. R., Rugheimer, S., & Christian Schneider, P., 2021, Reconstructing the Extreme Ultraviolet Emission of Cool Dwarfs Using Differential Emission Measure Polynomials, *ApJ*, 913(1), 40.

Engle, S. G. & Guinan, E. F., 2018, The Rotation-Age Relationship of M Dwarfs: A Progress Report of the Living with a Red Dwarf Program, *Research Notes of the American Astronomical Society*, 2(1), 34.

Erkaev, N. V., Kulikov, Y. N., Lammer, H., Selsis, F., Langmayr, D., Jaritz, G. F., & Biernat, H. K., 2007, Roche lobe effects on the atmospheric loss from "Hot Jupiters", *A&A*, 472(1), 329–334.

European Organization For Nuclear Research & OpenAIRE, 2013, Zenodo.
URL: *https://www.zenodo.org/*

Feinstein, A. D., France, K., Youngblood, A., Duvvuri, G. M., Teal, D. J., Cauley, P. W., Seligman, D. Z., Gaidos, E., Kempton, E. M. R., Bean, J. L., Diamond-Lowe, H., Newton, E., Ginzburg, S., Plavchan, P., Gao, P., & Schlichting, H., 2022, AU Microscopii in the Far-UV: Observations in Quiescence, during Flares, and Implications for AU Mic b and c, *AJ*, 164(3), 110.

Fontenla, J. M., Linsky, J. L., Witbrod, J., France, K., Buccino, A., Mauas, P., Vieytes, M., & Walkowicz, L. M., 2016, Semi-empirical Modeling of the Photosphere, Chromosphere, Transition Region, and Corona of the M-dwarf Host Star GJ 832, *ApJ*, 830(2), 154.

Foreman-Mackey, D., Hogg, D. W., Lang, D., & Goodman, J., 2013, emcee: The MCMC Hammer, *PASP*, 125(925), 306.

France, K., Arulanantham, N., Fossati, L., Lanza, A. F., Loyd, R. O. P., Redfield, S., & Schneider, P. C., 2018, Far-ultraviolet Activity Levels of F, G, K, and M Dwarf Exoplanet Host Stars, *ApJS*, 239(1), 16.

France, K., Bean, J. L., Berta-Thompson, Z. K., Brown, A., Duvvuri, G., Froning, C. S., Miguel, Y., Pineda, J. S., & Youngblood, A., 2020a, MUSCLES Extension for Atmospheric Transmission

Spectroscopy: Essential Ultraviolet Stellar Characterization for Guaranteed JWST Transiting Planet Targets, HST Proposal.

France, K., Duvvuri, G., Egan, H., Koskinen, T., Wilson, D. J., Youngblood, A., Froning, C. S., Brown, A., Alvarado-Gómez, J. D., Berta-Thompson, Z. K., Drake, J. J., Garraffo, C., Kaltenegger, L., Kowalski, A. F., Linsky, J. L., Loyd, R. O. P., Mauas, P. J. D., Miguel, Y., Pineda, J. S., Rugheimer, S., Schneider, P. C., Tian, F., & Vieytes, M., 2020b, The High-energy Radiation Environment around a 10 Gyr M Dwarf: Habitable at Last?, *AJ*, 160(5), 237.

France, K., Fleming, B. T., Drake, J. J., Mason, J. P., Youngblood, A., Bourrier, V., Fossati, L., Froning, C. S., Koskinen, T., Kruczek, N., Lipscy, S., McEntaffer, R., Romaine, S., Siegmund, O. H. W., & Wilkinson, E., 2019, The extreme-ultraviolet stellar characterization for atmospheric physics and evolution (ESCAPE) mission concept, *Proc. SPIE*, Vol. 11118 of *Society of Photo-Optical Instrumentation Engineers (SPIE) Conference Series*, p. 1111808.

France, K., Froning, C. S., Linsky, J. L., Roberge, A., Stocke, J. T., Tian, F., Bushinsky, R., Désert, J.-M., Mauas, P., Vieytes, M., & Walkowicz, L. M., 2013, The Ultraviolet Radiation Environment around M dwarf Exoplanet Host Stars, *ApJ*, 763(2), 149.

France, K., Loyd, R. O. P., Youngblood, A., Brown, A., Schneider, P. C., Hawley, S. L., Froning, C. S., Linsky, J. L., Roberge, A., Buccino, A. P., Davenport, J. R. A., Fontenla, J. M., Kaltenegger, L., Kowalski, A. F., Mauas, P. J. D., Miguel, Y., Redfield, S., Rugheimer, S., Tian, F., Vieytes, M. C., Walkowicz, L. M., & Weisenburger, K. L., 2016, The MUSCLES Treasury Survey. I. Motivation and Overview, *ApJ*, 820(2), 89.

France, K., Schindhelm, R., Herczeg, G. J., Brown, A., Abgrall, H., Alexander, R. D., Bergin, E. A., Brown, J. M., Linsky, J. L., Roueff, E., & Yang, H., 2012, A Hubble Space Telescope Survey of H_2 Emission in the Circumstellar Environments of Young Stars, *ApJ*, 756(2), 171.

Froning, C. S., Kowalski, A., France, K., Loyd, R. O. P., Schneider, P. C., Youngblood, A., Wilson, D., Brown, A., Berta-Thompson, Z., Pineda, J. S., Linsky, J., Rugheimer, S., & Miguel, Y., 2019, A Hot Ultraviolet Flare on the M Dwarf Star GJ 674, *ApJ*, 871(2), L26.

Fulton, B. J., Petigura, E. A., Howard, A. W., Isaacson, H., Marcy, G. W., Cargile, P. A., Hebb, L., Weiss, L. M., Johnson, J. A., Morton, T. D., Sinukoff, E., Crossfield, I. J. M., & Hirsch, L. A., 2017, The California-Kepler Survey. III. A Gap in the Radius Distribution of Small Planets, *AJ*, 154(3), 109.

Gaia Collaboration, 2018, VizieR Online Data Catalog: Gaia DR2 (Gaia Collaboration, 2018), *VizieR Online Data Catalog*, p. I/345.

Gaia Collaboration, Babusiaux, C., van Leeuwen, F., Barstow, M. A., Jordi, C., Vallenari, A., Bossini, D., Bressan, A., Cantat-Gaudin, T., van Leeuwen, M., & et al., 2018a, Gaia Data Release 2. Observational Hertzsprung-Russell diagrams, *A&A*, 616, A10.

Gaia Collaboration, Brown, A. G. A., Vallenari, A., Prusti, T., de Bruijne, J. H. J., Babusiaux, C., Bailer-Jones, C. A. L., Biermann, M., Evans, D. W., Eyer, L., & et al., 2018b, Gaia Data Release 2. Summary of the contents and survey properties, *A&A*, 616, A1.

Gendreau, K. C., Arzoumanian, Z., Adkins, P. W., Albert, C. L., Anders, J. F., Aylward, A. T., Baker, C. L., Balsamo, E. R., Bamford, W. A., Benegalrao, S. S., Berry, D. L., Bhalwani, S., Black, J. K., Blaurock, C., Bronke, G. M., Brown, G. L., Budinoff, J. G., Cantwell, J. D., Cazeau, T., Chen, P. T., Clement, T. G., Colangelo, A. T., Coleman, J. S., Coopersmith, J. D., Dehaven, W. E., Doty, J. P., Egan, M. D., Enoto, T., Fan, T. W., Ferro, D. M., Foster, R., Galassi, N. M., Gallo, L. D., Green, C. M., Grosh, D., Ha, K. Q., Hasouneh, M. A., Heefner, K. B., Hestnes, P., Hoge, L. J., Jacobs, T. M., Jørgensen, J. L., Kaiser, M. A., Kellogg, J. W., Kenyon, S. J., Koenecke, R. G., Kozon, R. P., LaMarr, B., Lambertson, M. D., Larson, A. M., Lentine, S., Lewis, J. H., Lilly, M. G., Liu, K. A., Malonis, A., Manthripragada, S. S., Markwardt, C. B., Matonak, B. D., Mcginnis, I. E., Miller, R. L., Mitchell, A. L., Mitchell, J. W., Mohammed,

J. S., Monroe, C. A., Montt de Garcia, K. M., Mulé, P. D., Nagao, L. T., Ngo, S. N., Norris, E. D., Norwood, D. A., Novotka, J., Okajima, T., Olsen, L. G., Onyeachu, C. O., Orosco, H. Y., Peterson, J. R., Pevear, K. N., Pham, K. K., Pollard, S. E., Pope, J. S., Powers, D. F., Powers, C. E., Price, S. R., Prigozhin, G. Y., Ramirez, J. B., Reid, W. J., Remillard, R. A., Rogstad, E. M., Rosecrans, G. P., Rowe, J. N., Sager, J. A., Sanders, C. A., Savadkin, B., Saylor, M. R., Schaeffer, A. F., Schweiss, N. S., Semper, S. R., Serlemitsos, P. J., Shackelford, L. V., Soong, Y., Struebel, J., Vezie, M. L., Villasenor, J. S., Winternitz, L. B., Wofford, G. I., Wright, M. R., Yang, M. Y., & Yu, W. H., 2016, The Neutron star Interior Composition Explorer (NICER): design and development, *in* den Herder, J.-W. A., Takahashi, T., & Bautz, M. (eds), *Space Telescopes and Instrumentation 2016: Ultraviolet to Gamma Ray*, Vol. 9905 of *Society of Photo-Optical Instrumentation Engineers (SPIE) Conference Series*, p. 99051H.

Gillon, M., Jehin, E., Lederer, S. M., Delrez, L., de Wit, J., Burdanov, A., Van Grootel, V., Burgasser, A. J., Triaud, A. H. M. J., Opitom, C., Demory, B.-O., Sahu, D. K., Bardalez Gagliuffi, D., Magain, P., & Queloz, D., 2016, Temperate Earth-sized planets transiting a nearby ultracool dwarf star, *Nature*, 533(7602), 221–224.

Gillon, M., Triaud, A. H. M. J., Demory, B.-O., Jehin, E., Agol, E., Deck, K. M., Lederer, S. M., de Wit, J., Burdanov, A., Ingalls, J. G., Bolmont, E., Leconte, J., Raymond, S. N., Selsis, F., Turbet, M., Barkaoui, K., Burgasser, A., Burleigh, M. R., Carey, S. J., Chaushev, A., Copperwheat, C. M., Delrez, L., Fernandes, C. S., Holdsworth, D. L., Kotze, E. J., Van Grootel, V., Almleaky, Y., Benkhaldoun, Z., Magain, P., & Queloz, D., 2017, Seven temperate terrestrial planets around the nearby ultracool dwarf star TRAPPIST-1, *Nature*, 542(7642), 456–460.

Gonzales, E. C., Faherty, J. K., Gagné, J., Teske, J., McWilliam, A., & Cruz, K., 2019, A Reanalysis of the Fundamental Parameters and Age of TRAPPIST-1, *ApJ*, 886(2), 131.

Goodman, J. & Weare, J., 2010, Ensemble samplers with affine invariance, *Communications in Applied Mathematics and Computational Science*, 5(1), 65–80.

Green, J. C., Froning, C. S., Osterman, S., Ebbets, D., Heap, S. H., Leitherer, C., Linsky, J. L., Savage, B. D., Sembach, K., Shull, J. M., Siegmund, O. H. W., Snow, T. P., Spencer, J., Stern, S. A., Stocke, J., Welsh, B., Béland, S., Burgh, E. B., Danforth, C., France, K., Keeney, B., McPhate, J., Penton, S. V., Andrews, J., Brownsberger, K., Morse, J., & Wilkinson, E., 2012, The Cosmic Origins Spectrograph, *ApJ*, 744(1), 60.

Hauschildt, P. H., 1993, Multi-level non-LTE radiative transfer in expanding shells., *J. Quant. Spec. Radiat. Transf.*, 50(3), 301–318.

Hauschildt, P. H. & Baron, E., 2006, A 3D radiative transfer framework. I. Non-local operator splitting and continuum scattering problems, *A&A*, 451(1), 273–284.

Hawley, S. L., 1993, Magnetic Activity in Low-Mass Stars, *PASP*, 105, 955.

Hawley, S. L. & Fisher, G. H., 1994, Solar Flare Model Atmospheres, *ApJ*, 426, 387.

Hawley, S. L., Gizis, J. E., & Reid, I. N., 1996, The Palomar/MSU Nearby Star Spectroscopic Survey.II.The Southern M Dwarfs and Investigation of Magnetic Activity, *AJ*, 112, 2799.

Henry, T. J., Jao, W.-C., Subasavage, J. P., Beaulieu, T. D., Ianna, P. A., Costa, E., & Méndez, R. A., 2006, The Solar Neighborhood. XVII. Parallax Results from the CTIOPI 0.9 m Program: 20 New Members of the RECONS 10 Parsec Sample, *AJ*, 132(6), 2360–2371.

Hertzsprung, E., 1911, Number 63. Zweiundzwanzigsten Bandes Erstes Stuck. Uber die verwendung photographischer effecktiver wellenlangen zur bestimmung von farbenaquivalenten, *Publikationen des Astrophysikalischen Observatoriums zu Potsdam*, 22, A1–A40.1.

Hill, M. L., Bott, K., Dalba, P. A., Fetherolf, T., Kane, S. R., Kopparapu, R., Li, Z., & Ostberg, C., 2023, A Catalog of Habitable Zone Exoplanets, *AJ*, 165(2), 34.

Houdebine, E. R., 2010, Observation and modelling of main-sequence star chromospheres - XIV. Rotation of dM1 stars, *MNRAS*, 407(3), 1657–1673.

Houdebine, E. R., 2012, Observation and modelling of main-sequence star chromospheres - XVIII. Observations of the Ca II resonance lines and Hα line for dM4 stars and dK5 stars, *MNRAS*, 421(4), 3189–3205.

Houdebine, E. R. & Doyle, J. G., 1994, Observation and modelling of main sequence star chromospheres II. Modelling of the AU MIC (dM2.5e) hydrogen spectrum., *A&A*, 289, 185–201.

Houdebine, E. R., Mullan, D. J., Bercu, B., Paletou, F., & Gebran, M., 2017, The Rotation-Activity Correlations in K and M Dwarfs. II. New Constraints on the Dynamo Mechanisms in Late-K and M Dwarfs Before and At the Transition to Complete Convection, *ApJ*, 837(1), 96.

Hsu, D. C., Ford, E. B., & Terrien, R., 2020, Occurrence rates of planets orbiting M Stars: applying ABC to Kepler DR25, Gaia DR2, and 2MASS data, *MNRAS*, 498(2), 2249–2262.

Husser, T. O., Wende-von Berg, S., Dreizler, S., Homeier, D., Reiners, A., Barman, T., & Hauschildt, P. H., 2013, A new extensive library of PHOENIX stellar atmospheres and synthetic spectra, *A&A*, 553, A6.

Ibañez Bustos, R. V., Buccino, A. P., Flores, M., Martinez, C. I., Maizel, D., Messina, S., & Mauas, P. J. D., 2019, First long-term activity study of AU Microscopii: a possible chromospheric cycle, *MNRAS*, 483(1), 1159–1167.

Jeans, J., 1904, *The Dynamical Theory of Gases*.

Jones, D. O. & West, A. A., 2016, A Catalog of GALEX Ultraviolet Emission from Spectroscopically Confirmed M Dwarfs, *ApJ*, 817(1), 1.

Kashyap, V. & Drake, J. J., 1998, Markov-Chain Monte Carlo Reconstruction of Emission Measure Distributions: Application to Solar Extreme-Ultraviolet Spectra, *ApJ*, 503(1), 450–466.

Kass, R. E. & Raftery, A. E., 1995, Bayes factors, *Journal of the American Statistical Association*, 90(430), 773–795.

URL: *http://www.jstor.org/stable/2291091*

King, G. W. & Wheatley, P. J., 2021, EUV irradiation of exoplanet atmospheres occurs on Gyr time-scales, *MNRAS*, 501(1), L28–L32.

Kopparapu, R. K., Ramirez, R., Kasting, J. F., Eymet, V., Robinson, T. D., Mahadevan, S., Terrien, R. C., Domagal-Goldman, S., Meadows, V., & Deshpande, R., 2013, Habitable Zones around Main-sequence Stars: New Estimates, *ApJ*, 765(2), 131.

Kopparapu, R. K., Ramirez, R. M., SchottelKotte, J., Kasting, J. F., Domagal-Goldman, S., & Eymet, V., 2014, Habitable Zones around Main-sequence Stars: Dependence on Planetary Mass, *ApJ*, 787(2), L29.

Kowalski, A. F., Allred, J., Axelson, R., Brown, A., Carter, B., Grady, C. A., Henry, T., Hinojosa, R., Jao, W.-C., Lomax, J. L., Neff, J. E., Osten, R., Paredes, L., Soutter, J., Schneider, G., Vrijmoet, E. H., White, G., & Wisniewski, J., 2019, A 7-Day, Multiwavelength Flare Monitoring Campaign on AU Mic, *American Astronomical Society Meeting Abstracts #233*, Vol. 233 of *American Astronomical Society Meeting Abstracts*, p. 360.14.

Kowalski, A. F., Allred, J. C., Uitenbroek, H., Tremblay, P.-E., Brown, S., Carlsson, M., Osten, R. A., Wisniewski, J. P., & Hawley, S. L., 2017, Hydrogen Balmer Line Broadening in Solar and Stellar Flares, *ApJ*, 837(2), 125.

Kowalski, A. F., Hawley, S. L., Hilton, E. J., Becker, A. C., West, A. A., Bochanski, J. J., & Sesar, B., 2009, M Dwarfs in Sloan Digital Sky Survey Stripe 82: Photometric Light Curves and Flare Rate Analysis, *AJ*, 138(2), 633–648.

Kowalski, A. F., Hawley, S. L., Wisniewski, J. P., Osten, R. A., Hilton, E. J., Holtzman, J. A., Schmidt, S. J., & Davenport, J. R. A., 2013, Time-resolved Properties and Global Trends in dMe Flares from Simultaneous Photometry and Spectra, *ApJS*, 207(1), 15.

Kruse, E. A., Berger, E., Knapp, G. R., Laskar, T., Gunn, J. E., Loomis, C. P., Lupton, R. H., & Schlegel, D. J., 2010, Chromospheric Variability in Sloan Digital Sky Survey M Dwarfs. II. Short-timescale Hα Variability, *ApJ*, 722(2), 1352–1359.

Kubyshkina, D., Fossati, L., Erkaev, N. V., Cubillos, P. E., Johnstone, C. P., Kislyakova, K. G., Lammer, H., Lendl, M., & Odert, P., 2018, Overcoming the Limitations of the Energy-limited Approximation for Planet Atmospheric Escape, *ApJ*, 866(2), L18.

Kurucz, R. L., Peytremann, E., & Avrett, E. H., 1974, *Blanketed model atmospheres for early-type stars*.

Laming, J. M., 2015, The FIP and Inverse FIP Effects in Solar and Stellar Coronae, *Living Reviews in Solar Physics*, 12(1), 2.

Lavvas, P., Galand, M., Yelle, R. V., Heays, A. N., Lewis, B. R., Lewis, G. R., & Coates, A. J., 2011, Energy deposition and primary chemical products in Titan's upper atmosphere, *Icarus*, 213(1), 233–251.

Lee, K.-G., Berger, E., & Knapp, G. R., 2010, Short-term Hα Variability in M Dwarfs, *ApJ*, 708(2), 1482–1491.

Levenberg, K., 1944, A method for the solution of certain problems in least squares., *Quaterly Journal on Applied Mathematics*, (2), 164–168.

Linsky, J. L., 1980, Stellar chromospheres, *ARA&A*, 18, 439–488.

Linsky, J. L., 2017, Stellar Model Chromospheres and Spectroscopic Diagnostics, *ARA&A*, 55(1), 159–211.

Linsky, J. L., Fontenla, J., & France, K., 2014, The Intrinsic Extreme Ultraviolet Fluxes of F5 V TO M5 V Stars, *ApJ*, 780(1), 61.

Linsky, J. L., Wood, B. E., Youngblood, A., Brown, A., Froning, C. S., France, K., Buccino, A. P., Cranmer, S. R., Mauas, P., Miguel, Y., Pineda, J. S., Rugheimer, S., Vieytes, M., Wheatley, P. J., & Wilson, D. J., 2020, The Relative Emission from Chromospheres and Coronae: Dependence on Spectral Type and Age, *ApJ*, 902(1), 3.

Llama, J. & Shkolnik, E. L., 2015, Transiting the Sun: the Impact of Stellar Activity on X-Ray and Ultraviolet Transits, *ApJ*, 802(1), 41.

Lockyer, J. N., 1868, Spectroscopic Observation of the Sun, No. II., *Proceedings of the Royal Society of London Series I*, 17, 131–132.

Louden, T., Wheatley, P. J., & Briggs, K., 2017, Reconstructing the high-energy irradiation of the evaporating hot Jupiter HD 209458b, *MNRAS*, 464(2), 2396–2402.

Loyd, R. O. P. & France, K., 2014, Fluctuations and Flares in the Ultraviolet Line Emission of Cool Stars: Implications for Exoplanet Transit Observations, *ApJS*, 211(1), 9.

Loyd, R. O. P., France, K., Youngblood, A., Schneider, C., Brown, A., Hu, R., Linsky, J., Froning, C. S., Redfield, S., Rugheimer, S., & Tian, F., 2016, The MUSCLES Treasury Survey. III. X-Ray to Infrared Spectra of 11 M and K Stars Hosting Planets, *ApJ*, 824(2), 102.

Loyd, R. O. P., France, K., Youngblood, A., Schneider, C., Brown, A., Hu, R., Segura, A., Linsky, J., Redfield, S., Tian, F., Rugheimer, S., Miguel, Y., & Froning, C. S., 2018a, The MUSCLES Treasury Survey. V. FUV Flares on Active and Inactive M Dwarfs, *ApJ*, 867(1), 71.

Loyd, R. O. P., Shkolnik, E. L., Schneider, A. C., Barman, T. S., Meadows, V. S., Pagano, I., & Peacock, S., 2018b, HAZMAT. IV. Flares and Superflares on Young M Stars in the Far Ultraviolet, *ApJ*, 867(1), 70.

MacGregor, M. A., Weinberger, A. J., Loyd, R. O. P., Shkolnik, E., Barclay, T., Howard, W. S., Zic, A., Osten, R. A., Cranmer, S. R., Kowalski, A. F., Lenc, E., Youngblood, A., Estes, A., Wilner, D. J., Forbrich, J., Hughes, A., Law, N. M., Murphy, T., Boley, A., & Matthews, J., 2021, Discovery of an Extremely Short Duration Flare from Proxima Centauri Using Millimeter through Far-ultraviolet Observations, *ApJ*, 911(2), L25.

MacGregor, M. A., Wilner, D. J., Rosenfeld, K. A., Andrews, S. M., Matthews, B., Hughes, A. M.,

Booth, M., Chiang, E., Graham, J. R., Kalas, P., Kennedy, G., & Sibthorpe, B., 2013, Millimeter Emission Structure in the First ALMA Image of the AU Mic Debris Disk, *ApJ*, 762(2), L21.

Mamajek, E. E., Prsa, A., Torres, G., Harmanec, P., Asplund, M., Bennett, P. D., Capitaine, N., Christensen-Dalsgaard, J., Depagne, E., Folkner, W. M., Haberreiter, M., Hekker, S., Hilton, J. L., Kostov, V., Kurtz, D. W., Laskar, J., Mason, B. D., Milone, E. F., Montgomery, M. M., Richards, M. T., Schou, J., & Stewart, S. G., 2015, IAU 2015 Resolution B3 on Recommended Nominal Conversion Constants for Selected Solar and Planetary Properties, *arXiv e-prints*, p. arXiv:1510.07674.

Mariska, J. T., 1992, *The Solar Transition Region*, Cambridge University Press.

Markwardt, C. B., 2009, Non-linear Least-squares Fitting in IDL with MPFIT, *in* Bohlender, D. A., Durand, D., & Dowler, P. (eds), *Astronomical Data Analysis Software and Systems XVIII*, Vol. 411 of *Astronomical Society of the Pacific Conference Series*, p. 251.

Marquardt, D. W., 1963, An algorithm for least-squares estimation of nonlinear parameters, *Journal of the Society for Industrial and Applied Mathematics*, 11(2), 431–441.
URL: *https://doi.org/10.1137/0111030*

Maunder, E. W., 1904, Note on the Distribution of Sun-spots in Heliographic Latitude, 1874-1902, *MNRAS*, 64, 747–761.

McQuillan, A., Mazeh, T., & Aigrain, S., 2014, Rotation Periods of 34,030 Kepler Main-sequence Stars: The Full Autocorrelation Sample, *ApJS*, 211(2), 24.

Meadows, V. S., 2017, Reflections on O_2 as a Biosignature in Exoplanetary Atmospheres, *Astrobiology*, 17(10), 1022–1052.

Medina, A. A., Charbonneau, D., Winters, J. G., Irwin, J., & Mink, J., 2022, Variability Timescales of Hα on Active Mid-to-Late M dwarfs, *arXiv e-prints*, p. arXiv:2203.01344.

Mendoza, G. T., Davenport, J. R. A., Agol, E., Jackman, J. A. G., & Hawley, S. L., 2022, Llamaradas Estelares: Modeling the Morphology of White-light Flares, *AJ*, 164(1), 17.

Mestel, L., 1953, Rotation and stellar evolution, *MNRAS*, 113, 716.

Mihalas, D., 1978, *Stellar atmospheres*.

Monsignori Fossi, B. C., Landini, M., Del Zanna, G., & Bowyer, S., 1996, A Time-resolved Extreme-Ultraviolet Spectroscopic Study of the Quiescent and Flaring Corona of the Flare Star AU Microscopii, *ApJ*, 466, 427.

Newton, E. R., Irwin, J., Charbonneau, D., Berlind, P., Calkins, M. L., & Mink, J., 2017, The Hα Emission of Nearby M Dwarfs and its Relation to Stellar Rotation, *ApJ*, 834(1), 85.

Newton, E. R., Irwin, J., Charbonneau, D., Berta-Thompson, Z. K., Dittmann, J. A., & West, A. A., 2016, The Rotation and Galactic Kinematics of Mid M Dwarfs in the Solar Neighborhood, *ApJ*, 821(2), 93.

Noyes, R. W., Hartmann, L. W., Baliunas, S. L., Duncan, D. K., & Vaughan, A. H., 1984, Rotation, convection, and magnetic activity in lower main-sequence stars., *ApJ*, 279, 763–777.

Oklopčić, A., 2019, Helium Absorption at 1083 nm from Extended Exoplanet Atmospheres: Dependence on Stellar Radiation, *ApJ*, 881(2), 133.

Owen, J. E. & Jackson, A. P., 2012, Planetary evaporation by UV &; X-ray radiation: basic hydrodynamics, *MNRAS*, 425(4), 2931–2947.

Pagano, I., Linsky, J. L., Carkner, L., Robinson, R. D., Woodgate, B., & Timothy, G., 2000, HST/STIS Echelle Spectra of the dM1e Star AU Microscopii Outside of Flares, *ApJ*, 532(1), 497–513.

Paulson, D. B., Allred, J. C., Anderson, R. B., Hawley, S. L., Cochran, W. D., & Yelda, S., 2006, Optical Spectroscopy of a Flare on Barnard's Star, *PASP*, 118(840), 227–235.

Peacock, S., Barman, T., Shkolnik, E. L., Hauschildt, P. H., & Baron, E., 2019a, Predicting the Extreme Ultraviolet Radiation Environment of Exoplanets around Low-mass Stars: The TRAPPIST-1 System, *ApJ*, 871(2), 235.

Peacock, S., Barman, T., Shkolnik, E. L., Hauschildt, P. H., Baron, E., & Fuhrmeister, B., 2019b, Predicting the Extreme Ultraviolet Radiation Environment of Exoplanets around Low-mass Stars: GJ 832, GJ 176, and GJ 436, *ApJ*, 886(2), 77.

Peacock, S., Barman, T., Shkolnik, E. L., Loyd, R. O. P., Schneider, A. C., Pagano, I., & Meadows, V. S., 2020, HAZMAT VI: The Evolution of Extreme Ultraviolet Radiation Emitted from Early M Stars, *ApJ*, 895(1), 5.

Penz, T. & Micela, G., 2008, X-ray induced mass loss effects on exoplanets orbiting dM stars, *A&A*, 479(2), 579–584.

Philip, A. G. D., Hayes, D. S., & Crawford, D. C., 1975, Multicolor photometry and the theoretical HR diagram. Proceedings of a conference held at the State University of New York at Albany, October, 1974., *Dudley Observatory Reports*, 9.

Pineda, J. S., Youngblood, A., & France, K., 2021a, The Far Ultraviolet M-dwarf Evolution Survey. I. The Rotational Evolution of High-energy Emissions, *ApJ*, 911(2), 111.

Pineda, J. S., Youngblood, A., & France, K., 2021b, The M-dwarf Ultraviolet Spectroscopic Sample. I. Determining Stellar Parameters for Field Stars, *ApJ*, 918(1), 40.

Planck, M., 1901, Ueber das Gesetz der Energieverteilung im Normalspectrum, *Annalen der Physik*, 309(3), 553–563.

Plavchan, P., Barclay, T., Gagné, J., Gao, P., Cale, B., Matzko, W., Dragomir, D., Quinn, S., Feliz, D., Stassun, K., Crossfield, I. J. M., Berardo, D. A., Latham, D. W., Tieu, B., Anglada-Escudé, G., Ricker, G., Vanderspek, R., Seager, S., Winn, J. N., Jenkins, J. M., Rinehart, S., Krishnamurthy, A., Dynes, S., Doty, J., Adams, F., Afanasev, D. A., Beichman, C., Bottom, M.,

Bowler, B. P., Brinkworth, C., Brown, C. J., Cancino, A., Ciardi, D. R., Clampin, M., Clark, J. T., Collins, K., Davison, C., Foreman-Mackey, D., Furlan, E., Gaidos, E. J., Geneser, C., Giddens, F., Gilbert, E., Hall, R., Hellier, C., Henry, T., Horner, J., Howard, A. W., Huang, C., Huber, J., Kane, S. R., Kenworthy, M., Kielkopf, J., Kipping, D., Klenke, C., Kruse, E., Latouf, N., Lowrance, P., Mennesson, B., Mengel, M., Mills, S. M., Morton, T., Narita, N., Newton, E., Nishimoto, A., Okumura, J., Palle, E., Pepper, J., Quintana, E. V., Roberge, A., Roccatagliata, V., Schlieder, J. E., Tanner, A., Teske, J., Tinney, C. G., Vanderburg, A., von Braun, K., Walp, B., Wang, J., Wang, S. X., Weigand, D., White, R., Wittenmyer, R. A., Wright, D. J., Youngblood, A., Zhang, H., & Zilberman, P., 2020, A planet within the debris disk around the pre-main-sequence star AU Microscopii, *Nature*, 582(7813), 497–500.

Pottasch, S. R., 1963, The Lower Solar Corona: Interpretation of the Ultraviolet Spectrum., *ApJ*, 137, 945.

Rackham, B. V., Apai, D., & Giampapa, M. S., 2018, The Transit Light Source Effect: False Spectral Features and Incorrect Densities for M-dwarf Transiting Planets, *ApJ*, 853(2), 122.

Rackham, B. V., Apai, D., & Giampapa, M. S., 2019, The Transit Light Source Effect. II. The Impact of Stellar Heterogeneity on Transmission Spectra of Planets Orbiting Broadly Sun-like Stars, *AJ*, 157(3), 96.

Ranjan, S., Wordsworth, R., & Sasselov, D. D., 2017, The Surface UV Environment on Planets Orbiting M Dwarfs: Implications for Prebiotic Chemistry and the Need for Experimental Follow-up, *ApJ*, 843(2), 110.

Raymond, J. C. & Smith, B. W., 1977, Soft X-ray spectrum of a hot plasma., *ApJS*, 35, 419–439.

Redfield, S., Ayres, T. R., Linsky, J. L., Ake, T. B., Dupree, A. K., Robinson, R. D., & Young, P. R., 2003, A Far Ultraviolet Spectroscopic Explorer Survey of Coronal Forbidden Lines in Late-Type Stars, *ApJ*, 585(2), 993–1006.

Redfield, S., Linsky, J. L., Ake, T. B., Ayres, T. R., Dupree, A. K., Robinson, R. D., Wood, B. E., & Young, P. R., 2002, A Far Ultraviolet Spectroscopic Explorer Survey of Late-Type Dwarf Stars, *ApJ*, 581(1), 626–653.

Remillard, R. A., Loewenstein, M., Steiner, J. F., Prigozhin, G. Y., LaMarr, B., Enoto, T., Gendreau, K. C., Arzoumanian, Z., Markwardt, C., Basak, A., Stevens, A. L., Ray, P. S., Altamirano, D., & Buisson, D. J. K., 2022, An empirical background model for the nicer x-ray timing instrument, *The Astronomical Journal*, 163(3), 130.
URL: *https://dx.doi.org/10.3847/1538-3881/ac4ae6*

Ribas, I., Guinan, E. F., Güdel, M., & Audard, M., 2005, Evolution of the Solar Activity over Time and Effects on Planetary Atmospheres. I. High-Energy Irradiances (1-1700 Å), *ApJ*, 622(1), 680–694.

Ribas, I., Tuomi, M., Reiners, A., Butler, R. P., Morales, J. C., Perger, M., Dreizler, S., Rodríguez-López, C., González Hernández, J. I., Rosich, A., Feng, F., Trifonov, T., Vogt, S. S., Caballero, J. A., Hatzes, A., Herrero, E., Jeffers, S. V., Lafarga, M., Murgas, F., Nelson, R. P., Rodríguez, E., Strachan, J. B. P., Tal-Or, L., Teske, J., Toledo-Padrón, B., Zechmeister, M., Quirrenbach, A., Amado, P. J., Azzaro, M., Béjar, V. J. S., Barnes, J. R., Berdiñas, Z. M., Burt, J., Coleman, G., Cortés-Contreras, M., Crane, J., Engle, S. G., Guinan, E. F., Haswell, C. A., Henning, T., Holden, B., Jenkins, J., Jones, H. R. A., Kaminski, A., Kiraga, M., Kürster, M., Lee, M. H., López-González, M. J., Montes, D., Morin, J., Ofir, A., Pallé, E., Rebolo, R., Reffert, S., Schweitzer, A., Seifert, W., Shectman, S. A., Staab, D., Street, R. A., Suárez Mascareño, A., Tsapras, Y., Wang, S. X., & Anglada-Escudé, G., 2018, A candidate super-Earth planet orbiting near the snow line of Barnard's star, *Nature*, 563(7731), 365–368.

Richey-Yowell, T., Shkolnik, E. L., Loyd, R. O. P., Jackman, J. A. G., Schneider, A. C., Agüeros, M. A., Barman, T., Meadows, V. S., Gibson, R., & Douglas, S. T., 2022, HAZMAT. VIII. A

Spectroscopic Analysis of the Ultraviolet Evolution of K Stars: Additional Evidence for K Dwarf Rotational Stalling in the First Gigayear, *ApJ*, 929(2), 169.

Rogers, J. G., Gupta, A., Owen, J. E., & Schlichting, H. E., 2021, Photoevaporation vs. core-powered mass-loss: model comparison with the 3D radius gap, *arXiv e-prints*, p. arXiv:2105.03443.

Russell, H. N., 1913, "Giant" and "dwarf" stars, *The Observatory*, 36, 324–329.

Rybicki, G. B. & Lightman, A. P., 1986, *Radiative Processes in Astrophysics*.

Saha, M. N., 1920, Ionisation in the Solar Chromosphere., *Nature*, 105(2634), 232–233.

Saha, M. N., 1921, On a Physical Theory of Stellar Spectra, *Proceedings of the Royal Society of London Series A*, 99(697), 135–153.

Sakaue, T. & Shibata, K., 2021, An M Dwarf's Chromosphere, Corona, and Wind Connection via Nonlinear Alfvén Waves, *ApJ*, 919(1), 29.

Samus', N. N., Kazarovets, E. V., Durlevich, O. V., Kireeva, N. N., & Pastukhova, E. N., 2017, General catalogue of variable stars: Version GCVS 5.1, *Astronomy Reports*, 61(1), 80–88.

Sanz-Forcada, J., Favata, F., & Micela, G., 2004, Coronal versus photospheric abundances of stars with different activity levels, *A&A*, 416, 281–290.

Sanz-Forcada, J., Micela, G., Ribas, I., Pollock, A. M. T., Eiroa, C., Velasco, A., Solano, E., & García-Álvarez, D., 2011, Estimation of the XUV radiation onto close planets and their evaporation, *A&A*, 532, A6.

Sanz-Forcada, J., Ribas, I., Micela, G., Pollock, A. M. T., García-Álvarez, D., Solano, E., & Eiroa, C., 2010, A scenario of planet erosion by coronal radiation, *A&A*, 511, L8.

Scalo, J., Kaltenegger, L., Segura, A. G., Fridlund, M., Ribas, I., Kulikov, Y. N., Grenfell, J. L., Rauer, H., Odert, P., Leitzinger, M., Selsis, F., Khodachenko, M. L., Eiroa, C., Kasting, J.,

& Lammer, H., 2007, M Stars as Targets for Terrestrial Exoplanet Searches And Biosignature Detection, *Astrobiology*, 7(1), 85–166.

Schmelz, J. T., Reames, D. V., von Steiger, R., & Basu, S., 2012, Composition of the Solar Corona, Solar Wind, and Solar Energetic Particles, *ApJ*, 755(1), 33.

Schwarz, G., 1978, Estimating the Dimension of a Model, *Annals of Statistics*, 6(2), 461–464.

Sekiya, M., Nakazawa, K., & Hayashi, C., 1980, Dissipation of the Primordial Terrestrial Atmosphere Due to Irradiation of the Solar EUV, *Progress of Theoretical Physics*, 64(6), 1968–1985.

Shields, A. L., Ballard, S., & Johnson, J. A., 2016, The habitability of planets orbiting M-dwarf stars, *Phys. Rep.*, 663, 1.

Shkolnik, E. L. & Barman, T. S., 2014, HAZMAT. I. The Evolution of Far-UV and Near-UV Emission from Early M Stars, *AJ*, 148(4), 64.

Skumanich, A., 1972, Time Scales for Ca II Emission Decay, Rotational Braking, and Lithium Depletion, *ApJ*, 171, 565.

Spoerer, F. W. G. & Maunder, E. W., 1890, Prof. Spoerer's researches on Sun-spots, *MNRAS*, 50, 251.

Spruit, H. C., 1999, Differential rotation and magnetic fields in stellar interiors, *A&A*, 349, 189–202.

Stauffer, J. R. & Hartmann, L. W., 1986, Chromospheric Activity, Kinematics, and Metallicities of Nearby M Dwarfs, *ApJS*, 61, 531.

Stefan, J., 1897, Über die Beziehung zwischen der Wärmestrahlung und der Temperatur.

Suárez Mascareño, A., Rebolo, R., González Hernández, J. I., & Esposito, M., 2015, Rotation periods of late-type dwarf stars from time series high-resolution spectroscopy of chromospheric indicators, *MNRAS*, 452(3), 2745–2756.

Tian, F. & Ida, S., 2015, Water contents of Earth-mass planets around M dwarfs, *Nature Geoscience*, 8(3), 177–180.

Tilipman, D., Vieytes, M., Linsky, J. L., Buccino, A. P., & France, K., 2020, Semi-Empirical Modeling of the Atmospheres of the M Dwarf Exoplanet Hosts GJ 832 and GJ 581, *arXiv e-prints*, p. arXiv:2012.11738.

Van Grootel, V., Fernandes, C. S., Gillon, M., Jehin, E., Manfroid, J., Scuflaire, R., Burgasser, A. J., Barkaoui, K., Benkhaldoun, Z., Burdanov, A., Delrez, L., Demory, B.-O., de Wit, J., Queloz, D., & Triaud, A. H. M. J., 2018, Stellar Parameters for Trappist-1, *ApJ*, 853(1), 30.

Vernazza, J. E. & Reeves, E. M., 1978, Extreme ultraviolet composite spectra of representative solar features., *ApJS*, 37, 485–513.

Vernazza, J. E., Avrett, E. H., & Loeser, R., 1973, Structure of the Solar Chromosphere. Basic Computations and Summary of the Results, *ApJ*, 184, 605–632.

Walkowicz, L. M. & Hawley, S. L., 2009, Tracers of Chromospheric Structure. I. Observations of Ca II K and Hα in M Dwarfs, *AJ*, 137(2), 3297–3313.

Warren, H. P., Mariska, J. T., & Lean, J., 1998, A new reference spectrum for the EUV irradiance of the quiet Sun 1. Emission measure formulation, *J. Geophys. Res.*, 103(A6), 12077–12090.

Watson, A. J., Donahue, T. M., & Walker, J. C. G., 1981, The dynamics of a rapidly escaping atmosphere: Applications to the evolution of Earth and Venus, *Icarus*, 48(2), 150–166.

Wedemeyer-Böhm, S., Lagg, A., & Nordlund, Å., 2009, Coupling from the Photosphere to the Chromosphere and the Corona, *Space Sci. Rev.*, 144(1-4), 317–350.

West, A. A., Hawley, S. L., Bochanski, J. J., Covey, K. R., Reid, I. N., Dhital, S., Hilton, E. J., & Masuda, M., 2008, Constraining the Age-Activity Relation for Cool Stars: The Sloan Digital Sky Survey Data Release 5 Low-Mass Star Spectroscopic Sample, *AJ*, 135(3), 785–795.

West, A. A., Hawley, S. L., Walkowicz, L. M., Covey, K. R., Silvestri, N. M., Raymond, S. N., Harris, H. C., Munn, J. A., McGehee, P. M., Ivezić, Ž., & Brinkmann, J., 2004, Spectroscopic Properties of Cool Stars in the Sloan Digital Sky Survey: An Analysis of Magnetic Activity and a Search for Subdwarfs, *AJ*, 128(1), 426–436.

West, A. A., Morgan, D. P., Bochanski, J. J., Andersen, J. M., Bell, K. J., Kowalski, A. F., Davenport, J. R. A., Hawley, S. L., Schmidt, S. J., Bernat, D., Hilton, E. J., Muirhead, P., Covey, K. R., Rojas-Ayala, B., Schlawin, E., Gooding, M., Schluns, K., Dhital, S., Pineda, J. S., & Jones, D. O., 2011, The Sloan Digital Sky Survey Data Release 7 Spectroscopic M Dwarf Catalog. I. Data, *AJ*, 141(3), 97.

Wilson, D. J., Froning, C. S., Duvvuri, G. M., France, K., Youngblood, A., Schneider, P. C., Berta-Thompson, Z., Brown, A., Buccino, A. P., Hawley, S., Irwin, J., Kaltenegger, L., Kowalski, A., Linsky, J., Parke Loyd, R. O., Miguel, Y., Pineda, J. S., Redfield, S., Roberge, A., Rugheimer, S., Tian, F., & Vieytes, M., 2021, The Mega-MUSCLES Spectral Energy Distribution of TRAPPIST-1, *ApJ*, 911(1), 18.

Wilson, O. C., 1968, Flux Measurements at the Centers of Stellar H- and K-Lines, *ApJ*, 153, 221.

Winters, J. G., Henry, T. J., Lurie, J. C., Hambly, N. C., Jao, W.-C., Bartlett, J. L., Boyd, M. R., Dieterich, S. B., Finch, C. T., Hosey, A. D., Ianna, P. A., Riedel, A. R., Slatten, K. J., & Subasavage, J. P., 2015, The Solar Neighborhood. XXXV. Distances to 1404 m Dwarf Systems Within 25 pc in the Southern Sky, *AJ*, 149(1), 5.

Wood, B. E., Laming, J. M., & Karovska, M., 2012, The Coronal Abundance Anomalies of M Dwarfs, *ApJ*, 753(1), 76.

Wood, B. E., Laming, J. M., Warren, H. P., & Poppenhaeger, K., 2018, A Chandra/LETGS Survey of Main-sequence Stars, *ApJ*, 862(1), 66.

Wood, B. E., Redfield, S., Linsky, J. L., Müller, H.-R., & Zank, G. P., 2005, Stellar Lyα Emission

Lines in the Hubble Space Telescope Archive: Intrinsic Line Fluxes and Absorption from the Heliosphere and Astrospheres, *ApJS*, 159(1), 118–140.

Woodgate, B. E., Kimble, R. A., Bowers, C. W., Kraemer, S., Kaiser, M. E., Danks, A. C., Grady, J. F., Loiacono, J. J., Brumfield, M., Feinberg, L., Gull, T. R., Heap, S. R., Maran, S. P., Lindler, D., Hood, D., Meyer, W., Vanhouten, C., Argabright, V., Franka, S., Bybee, R., Dorn, D., Bottema, M., Woodruff, R., Michika, D., Sullivan, J., Hetlinger, J., Ludtke, C., Stocker, R., Delamere, A., Rose, D., Becker, I., Garner, H., Timothy, J. G., Blouke, M., Joseph, C. L., Hartig, G., Green, R. F., Jenkins, E. B., Linsky, J. L., Hutchings, J. B., Moos, H. W., Boggess, A., Roesler, F., & Weistrop, D., 1998, The Space Telescope Imaging Spectrograph Design, *PASP*, 110(752), 1183–1204.

Woods, T. N., Chamberlin, P. C., Harder, J. W., Hock, R. A., Snow, M., Eparvier, F. G., Fontenla, J., McClintock, W. E., & Richard, E. C., 2009, Solar Irradiance Reference Spectra (SIRS) for the 2008 Whole Heliosphere Interval (WHI), *Geophys. Res. Lett.*, 36(1), L01101.

Woolley, R. V. D. R., 1936, The Balmer decrement in the spectra of prominences, *MNRAS*, 96, 515.

Wright, N. J., Drake, J. J., Mamajek, E. E., & Henry, G. W., 2011, The Stellar-activity-Rotation Relationship and the Evolution of Stellar Dynamos, *ApJ*, 743(1), 48.

Wright, N. J., Newton, E. R., Williams, P. K. G., Drake, J. J., & Yadav, R. K., 2018, The stellar rotation-activity relationship in fully convective M dwarfs, *MNRAS*, 479(2), 2351–2360.

Youngblood, A., France, K., Bean, J. L., Behr, P. R., Berta-Thompson, Z. K., Brown, A., Duvvuri, G., Froning, C. S., Kempton, E. M. R., Malik, M., Miguel, Y., Mikal-Evans, T., Pineda, J. S., Schneider, C., Teal, D. J., & Wilson, D. J., 2021a, Essential Ultraviolet Stellar Characterization for Cycle 1 JWST Transiting Planet Targets, HST Proposal. Cycle 29, ID. #16701.

Youngblood, A., France, K., Koskinen, T., Fossati, L., Amerstorfer, U., Lichtenegger, H., Drake, J., Mason, J., Fleming, B., Allred, J., Berta-Thompson, Z., Bourrier, V., Froning, C., Garraffo, C.,

Gronoff, G., Jin, M., Kowalski, A., & Osten, R., 2019, EUV influences on exoplanet atmospheric stability and evolution, *BAAS*, 51(3), 320.

Youngblood, A., France, K., Loyd, R. O. P., Brown, A., Mason, J. P., Schneider, P. C., Tilley, M. A., Berta-Thompson, Z. K., Buccino, A., Froning, C. S., Hawley, S. L., Linsky, J., Mauas, P. J. D., Redfield, S., Kowalski, A., Miguel, Y., Newton, E. R., Rugheimer, S., Segura, A., Roberge, A., & Vieytes, M., 2017, The MUSCLES Treasury Survey. IV. Scaling Relations for Ultraviolet, Ca II K, and Energetic Particle Fluxes from M Dwarfs, *ApJ*, 843(1), 31.

Youngblood, A., France, K., Loyd, R. O. P., Linsky, J. L., Redfield, S., Schneider, P. C., Wood, B. E., Brown, A., Froning, C., Miguel, Y., Rugheimer, S., & Walkowicz, L., 2016, The MUSCLES Treasury Survey. II. Intrinsic LYα and Extreme Ultraviolet Spectra of K and M Dwarfs with Exoplanets*, *ApJ*, 824(2), 101.

Youngblood, A., Pineda, J. S., & France, K., 2021b, FUMES. II. Lyα Reconstructions of Young, Active M Dwarfs, *ApJ*, 911(2), 112.

Zahnle, K. J. & Catling, D. C., 2017, The Cosmic Shoreline: The Evidence that Escape Determines which Planets Have Atmospheres, and what this May Mean for Proxima Centauri B, *ApJ*, 843(2), 122.